Faculty of Science

Department of Organic and Macromolecular Chemistry

Development of flexible methacrylate-based packaging materials towards an implantable optical glucose sensor

Elke Van De Walle

Thesis submitted as fulfillment of the requirements for the degree of Doctor of Science: Chemistry

2016

Promotors:
Prof. Dr. P. Dubruel
Prof. Dr. S. Van Vlierberghe
Prof. Dr. M. Cornelissen

ISBN:

Picture on front cover: confocal image of HUVECs (Human umbilical vascular endothelial cells) grown on top of a polydopamine (PDA) modified and VEGF/VE-cad AB biofunctionalized PLMA material. On the back cover, a PDA cluster is shown which was deposited on a PLMA surface.

Promotors:

Prof. Dr. P. Dubruel
Prof. Dr. S. Van Vlierberghe
Prof. Dr. M. Cornelissen

Examencommissie:

Prof. Dr. Du Prez, UGent (chairman)
Prof. Dr. Hoogenboom, UGent
Prof. Dr. Vlaminck, UGent
Prof. Dr. De Vos, UAntwerpen
Prof. Dr. De Vos, UGent
Prof. Dr. Demoustier, UCL, Louvain-la-Neuve
Dr. Ronny Bockstaele, UGent
Prof. Dr. Cornelissen, UGent (promotor)
Prof. Dr. Van Vlierberghe, UGent (promotor)
Prof. Dr. Dubruel, UGent (promotor)

Universiteit Gent
Faculteit Wetenschappen

Vakgroep Organische en Macromoleculaire Chemie
Krijgslaan 281- S4, B-9000 Gent, België

UNIVERSITEIT GENT

Dit werk kwam tot stand in het kader van het IWT-SBO GlucoSens project van het IWT-Vlaanderen

Dankwoord

De laatste zes jaar ben ik op ontdekkingsreis gegaan in een wetenschappelijke wereld die me heel wat kennis maar vooral heel wat unieke ontmoetingen geboden heeft. Ontmoetingen die elk hun eigen steentje hebben bijgedragen aan dit proefwerk. Graag wil ik aan elk van hen een welgemeende dankjewel uiten.

Deze tocht begon in de zomer van 2009 dankzij Prof. Peter Dubruel die me het project GlucoSens toevertrouwde en me dus de unieke kans gaf om m'n wetenschappelijke knobbel verder te ontwikkelen. Naast Prof. Dr. Dubruel wil ik ook Prof. Dr. Sandra Van Vlierberghe bedanken voor de dagdagelijkse begeleiding. Zij zette steeds weer de puntjes op de i en zorgde ervoor dat er op moeilijkere momenten knopen werden doorgehakt. Ook een dankjewel aan alle juryleden van m'n examencommissie voor de waardevolle feedback op dit doctoraat.

Tijdens de eerste vier jaar kreeg ik ook een metgezel mee. Samen trotseerden we de uitdagingen binnen het project. Daar waar ik PMMA onder de loep nam, was PDMS haar stokpaardje. Ik wil Valérie dan ook bedanken voor de leuke samenwerking en de soms late maar gezellige uurtjes die we samen naast de 'donuts' doorbrachten. Ook Ronny Bockstaele en zijn voorganger, Geert Morren wil ik uitgebreid bedanken, want door hun rol als projectleider bleef het overzicht behouden, wat soms niet gemakkelijk was in dit multi-disciplinair onderzoek, GlucoSens.

Prof. Ria Cornelissen mag ook zeker niet ontbreken in dit plaatje. Dankzij haar konden we ons uitleven in de *in vitro* en *in vivo* wereld. Verder stond ze ook steeds klaar voor een wetenschappelijke discussie of een extra woordje uitleg. Uiteraard heb ik deze testen niet allemaal zelf gedaan. Een oprechte dank wil ik dan ook geven aan Karolien Gellynck, Heidi Declercq, Johanna Aernoudt en Greet De Smet. Ook na het aflopen van het project stonden zij paraat om live/dead en MTT assays uit te voeren, alsook om mezelf te introduceren in de wondere wereld van cellen, laminaire flows en fluorescentie microscopie. Ook Lise De Moor wil ik bedanken voor de *in vivo* evaluatie van de materialen in ratten.

Later in dit doctoraatswerk kwam Prof. Winnok De Vos op ons pad en dit zorgde ervoor dat dit werk uitgebreid kon worden met immuno-assays. Graag wil ik Prof De Vos bedanken om me toe te laten zelf met de confocale fluorescentiemicroscoop te werken, alsook voor zijn grote toewijding om de optimale R-code te vinden om beeldanalyse mogelijk te maken. Een speciaal woordje van dank wil ik hier ook schenken aan Ine Van Nieuwenhove. Ondanks het feit dat ze het zelf druk had met haar eigen doctoraat, was het haar nooit te veel me bij te staan tijdens de immuno-assay experimenten. Bedankt hiervoor!

Naast ratten hebben we ook geiten getrotseerd. In deze context wil ik dan ook Prof. Lieven Vlaminck bedanken om deze *in vivo* studies mogelijk te maken, alsook om me als publiek toe te laten tijdens de operaties. Dit was een zeer leerrijke ervaring.

Voor de karakterisatie van de materialen wil ik graag Eva Ryckeboer (NIR metingen), Maaike Op de Beeck (hermiticiteitstesten), David Schaubroeck (SEM metingen), Ken Kersemans (radiolabeling experimenten), Heidi Ottevaere (profilometrie) en Prof. Joris Delanghe bedanken. Zij ontvingen mij en m'n staaltjes steeds met een glimlach en lieten me steeds gaan met een verzadiging aan wetenschappelijke informatie. Ook een speciale dank aan de 'PBM-girls' Els Vanderleyden, Valérie Kodeck, Diana Giol en Lara Misseeuw voor de XPS metingen, die vaak ook tijdens het weekend uitgevoerd werden. Bedankt ook Veerle! Jij was er altijd voor elk toestel gerelateerd probleem, maar ook voor een gezellige babbel en zoveel meer.

Marc en Mario mogen ook zeker niet in dit lijstje ontbreken. Graag wil ik hen bedanken voor de vele uren die ze besteed hebben in de ontwikkeling en het maken van de mallen. Zonder hun technische kennis en handigheid waren er geen donuts en dus ook geen *in vivo* experimenten mogelijk.
Ook m'n thesisstudenten Arn Mignon, Stéfanie Allyn en Jens Mincke wil ik bedanken voor de bijdragen die ze leverden in dit werk.
Uiteraard wil ik ook m'n PBM collega's bedanken. Werken bij PBM heeft me heel wat collega's bezorgd, maar belangrijker, ook heel wat vrienden. Els, Thomas, Miriam and Vincent, thank you for the beautiful moments and pleasant evenings! Diana M., Diana Giol, Olga and Mamoni, thank you for the nice girls nights and your friendship. Jasper, Lara, Geert-Jan, Mieke, Tim VG, Kenny, Arne, Tim and Stijn, thank you for all the laughs and beautiful moments in the lab. Birgit and Ine wil ik verder ook bedanken voor alle leuke lunch babbels en de vriendschap. To all PBM-members, thanks for being you!
Leen, Pieter, Paul, Tom, Piet, Isabel, Tom, Michael, ook een dikke dankuwel voor de fijne practicareeksen die we samen beleefd hebben! Ook m'n huidige collega's van VKC-Centexbel wil ik bedanken voor de steun en interesse en verder wil ook Elien, Eske, Jente en Bram bedanken voor de leuke studietijd samen en het gedeelde doctoraatsleed en plezier!

Op ontdekkingstocht zijn is fantastisch en leerrijk, maar kunnen thuiskomen en weten dat er mensen achter je staan die je steunen door dik en dun, is een nog veel groter geschenk. Ik wil dan ook mijn ouders, Marc en Marianne bedanken dat zij deze ontdekkingsreis voor mij mogelijk gemaakt hebben, alsook voor hun steun en raad! Op hen, alsook op m'n zus Karlijn, kan ik echt altijd rekenen. Liefste Kenny, bedankt om me te steunen, me lief te hebben en me steeds opnieuw op te monteren tijdens de moeilijkere momenten, alsook om m'n persoonlijke IT-expert te zijn. Deze wetenschappelijke ontdekkingsreis is nu misschien afgelopen, maar ik hoop dat onze reis samen voor altijd mag blijven duren…

Elke Van De Walle
17 July 2016, Gent

Table of contents

List of abbreviations

AAPBA	3-acrylamidophenylboronic acid
AB	antibody
AEMA	2-aminoethyl methacrylate
AFM	Atomic force microscopy
AIBN	Azobisisobutyronitril
BA	Boronic acid
bFGF	Basic fibroblast growth factor
BPO	Benzoylperoxide
BSA	Bovine serum albumin
BuMA	n-butyl methacrylate
CAM	Chick chorioallantoic membrane
CCA	Crystalline colloidal array
CGM	Continuous glucose monitoring
CNT	Carbon nanotube
ConA	Concanavalin A
CP	Conducting polymer
DA	Dopamine
Da	Dalton, unit
DBD	Dielectric barrier discharge
DEA	N,N-dimethylaminoethyl
DHI	5,6-dihydroxyindole
DOPA	L-3,4-dihydroxyphenylalanine
ECH	Electron conducting hydrogels
ECM	Extracellular matrix
EDC	1-ethyl-3-(3-dimethylaminopropyl) carbodiimide
EGDMA	Ethylene glycol dimethacrylate
EHMA	2-ethylhexylmethacrylate
E-modulus, E-mod	Elasticity modulus
EPC	Endothelial progenitor cell
ePTFE	Expanded poly(tetrafluoroethylene)
FA	Focal adhesion
Fab	Antigen binding fragment
FAD	Flavin adenine dinucleotide
FBC	Foreign body capsule
FBGC	Foreign body giant cells
FBS	Fetal bovine serum
Fc	Fragment crystallizable region

FDA	Food and Drug Administration
FRET	Fluorescence energy transfer
Gel B	Gelatin B
GO	Graphene oxide
GOx	Glucose oxidase
GPC	Gel permeation chromatography
H&E staining	Hematoxylin and eosin staining
HA	Hydroxyapatite
HEMA	Hydroxyethyl methacrylate
HFF	Human foreskin fibroblast
HPMA	2-hydroxypropyl methacrylate
HUVECs	Human umbilical vascular endothelial cells
I	Intensity
ICAM	Intercellular adhesion molecule
IEP	Iso-electric point
IOL	Intra-ocular lens
IR	Infrared
ISF	Interstitial fluid
K	Kelvin, unit of temperature
LMA	Lauryl methacrylate
LRP	Living radical polymerization
MAP	Mussel adhesive protein
MAS-NMR	Magic angle spinning nuclear magnetic resonance
MES	2-(N-morpholino)ethanesulfonic acid
MIP	molecularly imprinted polymer
MMA	Methyl methacrylate
MSN	Mesoporous silica nanoparticles
MTT	3-(4,5-dimethylthiazol-2-yl)-2,5-diphenyltetrazolium bromide
Mw	Molecular weight
N	Newton, measure of force
NIPAM	N-isopropylacrylamide
NIR	Near infrared
nm	Nanometer, unit
NMR	Nuclear magnetic resonance
NP	Nanoparticle
Pa	Pascal, unit
PAAm, PAM	Polyacrylamide
PANI	Polyaniline
PBA	Phenylboronic acid
PBS	Phosphate buffered saline
PC	Polycarbonate

PCA	Pyrrolecarboxylic acid
PCCA	Polymerized crystalline colloidal array
PCL	Poly-ε-caprolactone
PD	Polydispersity
PDA	Polydopamine
PDMS	Polydimethylsiloxane
PDOT	Poly(3,4-ethylenedioxythiophene)
PEG	Poly(ethylene glycol)
PEGDMA	Poly(ethylene glycol) dimethacrylate
PEGMA	Poly(ethylene glycol) n monomethyl ether monomethacrylate
PEO	Poly(ethylene oxide)
PES	Polyethersulfone
PET	Poly(ethylene terephtalate)
PGEMA	Poly(2-glucosyloxyethyl methacrylate)
PHEMA	Poly(2-hydroxyethyl methacrylate)
PLGA	Poly(lactic-co-glycolic acid)
PLMA	Poly(lauryl methacrylate)
PMMA	Poly(methyl methacrylate)
PPD	Poly(o-phenylenediamine)
PPy	Polypyrrole
PT	Polythiophene
PU	Poly(urethane)
PVA	Poly(vinyl alcohol)
PVPAA	Poly(vinylpyrrolidone-co-acrylic acid)
QCM	Quartz-crystal microbalance
RGD	Arginylglycylaspartic acid
RGO	Reduced graphene oxide
RMS	Root mean square
SCA	Static contact angle
SEM	Scanning electron microscopy
S-Hynic	Succinimidyl-6-hydrazino-nicotinamide
SPE	Serum protein electrophoresis
SS	Stainless steel
sulfo-NHS	N-hydroxysulfosuccinimide
Tg	Glass transition temperature
TGF	Transforming growth factor
UV	Ultraviolet
VE-cad AB	Vascular endothelial cadherin antibody
VEGF	Vascular endothelial growth factor
VWF	Von Willebrand factor
W	Watt, unit

XPS	X-ray photoelectron spectroscopy

Chapter 1

Introduction: Diabetes and its management

1.1. Introduction into diabetes

According to the international diabetes federation, in 2013, 382 million people suffered from diabetes worldwide. Estimates even say that by 2035, this number might be increased up to 592 million people, which corresponds to a 55% increase over two decades [1-2]. As a consequence, diabetes has been the focus of many research groups as illustrated by the number of research papers published so far (see figure 1.1).

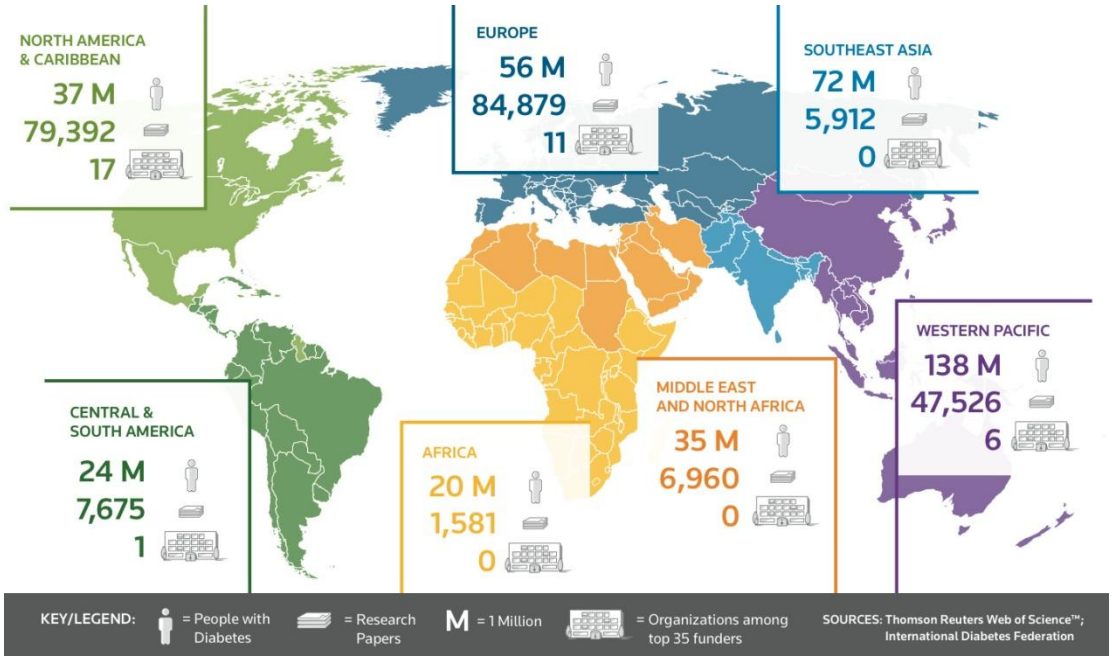

Figure 1.1: Distribution of people suffering from diabetes worldwide, the number of papers published covering this topic and the distribution of the top 35 funders worldwide [3].

To understand the main causes of diabetes, insight should be provided in the glucose household of a healthy patient. Generally, human plasma glucose levels are maintained within a very narrow range (3.5-6.5 mmol/l) via homeostasis [4]. This process involves two hormones (i.e. insulin and glucagon) which are both secreted by the endocrine pancreas. If glucose levels drop below the above-mentioned lower threshold (cfr. hypoglycemia), glucagon is secreted by the alpha cells of the pancreatic islets of Langerhans to initiate glycogenolysis. In this way, stored glucose is released from the liver and used as an energy source. Insulin on the other hand is secreted by the beta cells of the pancreas and promotes the absorption of blood glucose to skeletal muscles and fat tissue. Within the body, it is provided in a constant proportion in order to remove glucose excess (cfr. hyperglycemia) from the blood which otherwise would become toxic [4-5]. Conversely, if the patients are unable to absorb glucose properly, their blood glucose levels will remain high for a prolonged period (i.e. chronic hyperglycemia) and they will be diagnosed diabetic.

Diabetes is not a single disease entity but represents a group of diseases associated with various metabolic disorders, all related by the occurrence of chronic hyperglycemia. Its pathogenesis involves both genetic as well as environmental factors and dependent on the

origin of the disease, 3 types of diabetes can be distinguished: type I, type II and gestational diabetes, which are schematically explained in figure 1.2 [6].

Type I diabetes or insulin dependent diabetes is an auto-immune disease in which the beta-cells in the pancreas are destroyed by the body's defense system itself. As a result, the body is not able to produce its own insulin and thereby no appropriate control of blood glucose levels can be achieved. Daily injections of insulin are a prerequisite to assure the patient's life.

In case of *type II diabetes* (non-insulin dependent diabetes), the body is able to produce its own insulin but it is unable to respond to it, again resulting in glucose build-up in the blood. Type 2 diabetes comprises 90% of people with diabetes around the world and for this type, no daily insulin injections are needed to treat the disease. Adjusted diet, increased physical activity or oral medication (sometimes combined with insulin doses) are mostly sufficient in this case. However, recent studies state that genetic predisposition to obesity also leads to an increased risk of type 2 diabetes [7-8].

The third type, *gestational diabetes* is similar to diabetes type II and affects a number of women during their pregnancy. In this case, the insulin activity is again blocked, probably by hormones produced in the placenta. This type of diabetes is temporarily and normally disappears after birth. However, these women and their babies have a higher risk to develop type II diabetes in the further course of their lives [5, 9-10].

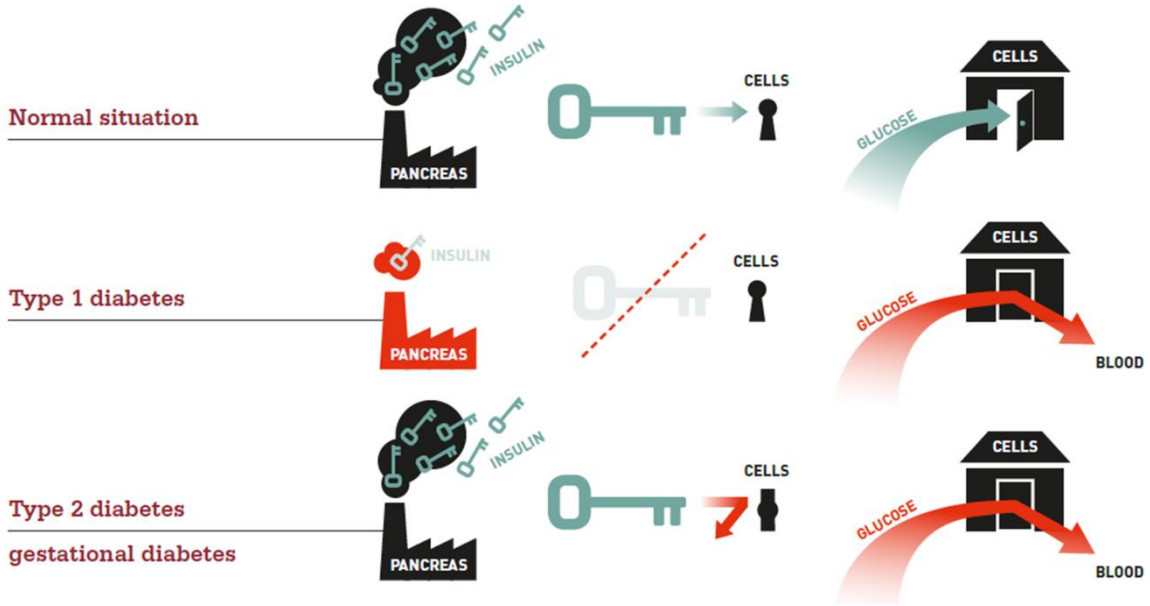

Figure 1.2: Schematic illustration of the causes of diabetes type 1, 2 and gestational diabetes [5].

Apart from short-term complications such as blurred vision, frequent urination and lack of energy, the long-term complications could be life threatening and are of great concern. Examples include heart and kidney diseases, blindness and nerve damage [11]. Because of its chronic nature and the gravity of its complications, diabetes imposes unacceptably high costs on countries at all income levels.

To date, diabetes is still not curable, however, intensive insulin therapies in diabetic patients can dramatically delay the onset of serious complications. Furthermore, it has been demonstrated that tight or continuous blood glucose control can introduce substantial reductions in overall medical care costs. In this respect, glucose sensors play a key role, as they allow the patient to maintain normal glucose values in case glucose abnormalities (i.e. too high or too low concentrations) are emerging [12]. Despite the array of tools at our disposal to tackle the disease – effective drug therapies, advanced technologies, ever-improving education and preventive strategies – the battle to protect people from diabetes and its life-threatening complications is still ongoing.

1.2. Problem statement: the need for continuous glucose monitoring (CGM)

Till today, the finger prick method includes the most common way for patients to analyze and control their glucose values at home on a daily basis. To this end, the patient places a blood droplet on top of a disposable test strip, which contains the printed electrodes including the reference and working electrode. The latter is covered with the enzyme glucose oxidase (GOx) or glucose dehydrogenase (GDH) and as a consequence, electrochemical analysis of the blood droplet is enabled after insertion of the test strip into a read-out system. Overall, this method is experienced as painful and includes a higher risk of infection. Moreover, it is characterized by a non-continuous nature. As blood is only measured periodically (4-5 times a day), periods of hypo- or hyperglycemia might occur without the patient's knowledge and without appropriate action. Especially patients suffering from diabetes type 1 fear episodes of hypoglycemia during the night. Because of this fact, researchers realized the importance to develop a system that allows for continuous glucose monitoring (CGM) via an appropriate sensor which is equipped with an alarm system to inform patients about deviations from normoglycemia [13]. Furthermore, it was proven by the 'Diabetes Control and Complications Trial of the US National Institutes of Health' that the likelihood of the occurrence of complications of diabetes such as eye disease (retinopathy), kidney disease (nephropathy), nerve disease (neuropathy) and vascular disease, decreases if diabetic patients maintain normal or near-normal glycemia [14-15].

To date, CGM devices for the *in vivo* measurement of glucose are electrochemically based and considered minimally invasive, as they are not fully but percutaneously implanted. In this respect, subcutaneously implantable needle-type electrodes have been developed and commercialized such as the CGMS units of Medtronic (i.e. Minimed) and Abbott (i.e. Freestyle Navigator). Herein, subcutaneous glucose values are measured every 1-5 minutes, during 3-7 days [12, 16]. Afterwards, the system can be replaced by the patient.
Alternatively, microdialysis sampling may be used, during which a hollow dialysis fiber is implanted subcutaneously which is perfused with isotonic fluid. In this way, glucose is able to diffuse from the tissue into the fiber and is finally pumped towards the external enzyme

electrode for detection. Commercial microdialysis probes are provided by Menarini Diagnostics (GlucoDay), which apply the electrochemical glucose sensing principle (described in §1.2.1). These systems operate for 48 hours and provide glucose values every 3 minutes [17-19].

Non-invasive CGM techniques have also been developed such as the GlucoWatch, which consists of a watch-like glucose monitor, worn around the wrist. Herein, glucose is extracted through the skin via reverse iontophoresis. To this end, a small current is passed between two skin surface electrodes, which draws ions and glucose-containing interstitial fluid (ISF) towards the surface for analysis [20]. However, due to a lack of accuracy, slow operation and the occurrence of skin irritation, the device was removed from the market in 2007. Alternatively, due to its easy and non-invasive assessment, tear fluid has also been considered as medium for glucose measurements [21-22]. To allow for continuous monitoring, glucose monitoring lenses have been developed, wherein the signal is read with the aid of an illumination and recording unit held in front of the eye [23]. Although several issues still need to be tackled, such as improved lens biocompatibility, interference control and the need for extensive calibration, Google, in a cooperation with Novartis are currently working on the development of a commercial product [24].

Apart from percutaneous sensor implants, fully implantable glucose sensors offer a minimally invasive alternative, since implantation should only be conducted once (i.e. one time invasive). In this case, the ultimate implantable CGM device should offer real-time glucose information on demand, should operate for 1 year minimally and should require minimal recalibration [25]. Unfortunately, stable, functional *in vivo* glucose sensors are not commercially available yet, which can be explained by the lack of a stable tissue-sensor interface, needed to survive complex *in vivo* events, as will be described in § 1.4.5.
As a consequence, the current work targets the development of a biocompatible packaging for an implantable single-chip optical glucose sensor, intended for long-term CGM, based on near infrared (NIR)-spectroscopy. The overall and initial concept of the CGM system, as proposed in the GlucoSens project, is presented in Figure 1.3 and discussed below.

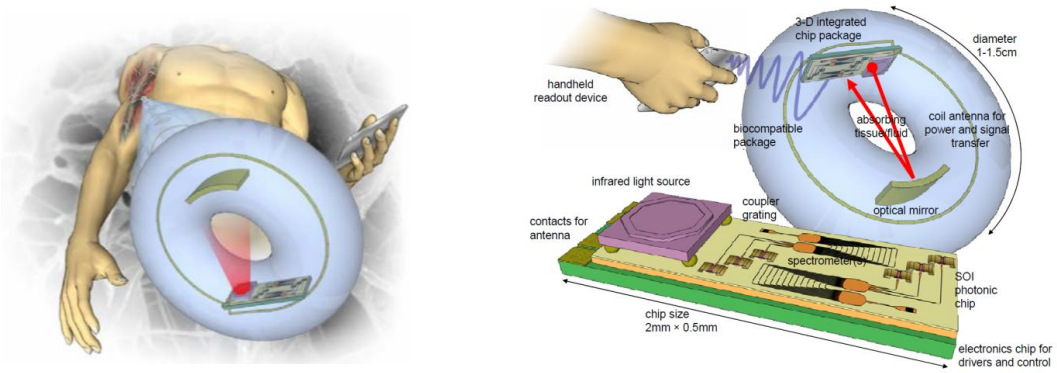

Figure 1.3: NIR-based glucose sensor, which is encapsulated in a biocompatible donut-shaped polymer packaging.

This concept describes a donut-shaped (1-1,5 cm in diameter) biocompatible packaging, which houses a single chip optical spectrometric sensor, together with inductive power and wireless data-transmission electronics. Subcutaneous implantation of the sensor e.g. in the upper arm of the patient is envisioned and glucose concentrations are measured by sending NIR-light through the cavity of the donut, where it interacts with the ISF. After reflection by a mirror, placed at the opposite side of the sensor chip, the absorption of the light can be measured by a spectrometer, which is integrated, together with the NIR source, onto the chip component. Herein, accurate measurements in a glucose concentration range of 1-33 mM is targeted. Translation and read-out of the glucose quantities are further enabled by an external wearable or portable read-out device. Since the analysis method is reagent-free, it circumvents the need for direct contact between the sensor electronics and the body environment (i.e. the ISF) and as a consequence the sensor can be fully encapsulated in a biocompatible packaging. Development of the latter comprises the subject of the current PhD.

For further information about the glucose detection system, the build-up of the integrated sensor chip and the development of a calibration model enabling the analysis of the measured NIR spectra, the following PhD manuscripts can be consulted, which cover the research results obtained in parallel with the current work:

1) Spectroscopic detection of glucose with a silicon photonic integrated circuit, by Eva Ryckeboer, Photonics Research Group (UGent).
2) GaSb/Silicon-on-insulator heterogeneous photonic integrated circuits for the short-wave infrared, by Nannicha Hattasan, Photonics Research Group (UGent).
3) Exploiting expert information in multivariate calibration of an implantable glucose sensor, by Sandeep Sharma, Biostatistics and Sensors Group (MeBioS, KULeuven).

Prior to defining the exact requirements the biocompatible packaging should fulfill, cfr. the research goals (§ 1.5), glucose sensors will first be described in a broader context. First, a brief overview is given of the glucose sensor principles typically studied and finally, an overview is provided of the role of polymer materials within the world of glucose sensors.

1.3. Glucose sensors

The basis for tight glycemic control includes frequent glucose monitoring. To this end, blood glucose concentrations are measured by means of a glucose sensor (mostly through the well-known finger-prick method) to aid in administering proper levels of insulin and to maintain homeostasis. Generally, a glucose sensor consists of three important parts [12]:

- *A (biological) recognition element* such as enzymes, proteins, antibodies or nucleic acids (i.e. biological elements) or functional units like phenyl boronic acid (PBA)-containing compounds. These elements differentiate glucose molecules from other molecules.

- *A transducer* which converts the produced chemical signal, originating from the interaction between glucose and the recognition element, into a measurable signal. Different types of transducers exist including electrochemical (amperometric and potentiometric), optical, thermometric, piezoelectric and magnetic ones. The majority of the current glucose sensors are electrochemically driven but due to some shortcomings, the current work is situated in the world of optically-based sensors as discussed below.
- *A signal processing unit* which ultimately transforms the measured signal into an interpretable read-out.

During the last 50-60 years, glucose sensor technologies have significantly improved, but as pointed out in the upcoming sections, several challenges remain to achieve accurate and reliable glucose monitoring. Generally, based on the transducer system, two main classes can be distinguished including the electrochemical and optical sensors.

1.3.1. Electrochemical sensors

Because of their good sensitivity, reproducibility and low cost, the majority of the currently applied glucose sensors are electrochemically-based and dependent on the detection principle, potentiometric, amperometric, or conductometric sensors can be distinguished [26]. Herein, the enzymatic amperometric glucose biosensor includes the most common commercially available device. In 1962, Clark and Lyons came up with the initial concept of these glucose enzyme electrodes [27]. Their first device relied on a thin layer of glucose oxidase (GOx), entrapped on an oxygen electrode, which monitored the oxygen consumed by the enzyme catalyzed reaction:

$$Glu\ \cos e + O_2 \xrightarrow{GOx} gluconic\quad acid\ + H_2O_2 \tag{1.1}$$

More precisely, upon interaction with glucose, the redox centre of the enzyme molecule, flavin adenine dinucleotide (FAD), is reduced and the redox product, gluconic acid, is formed.

$$D-Glu\ \cos e + GOx\ (FAD) \rightarrow D-Gluconic\quad acid\ + GOx\ (FADH_2) \tag{1.2}$$

$$GOx\ \ (FADH_2) + O_2 \rightarrow GOx\ \ (FAD) + H_2O_2 \tag{1.3}$$

Later on, in 1973, an enzyme electrode was developed to amperometrically monitor the produced hydrogen peroxide as a measure for blood glucose [28]:

$$H_2O_2 \longrightarrow\ O_2\ + 2H^+ + 2e^- \tag{1.4}$$

Since these inventions, a lot of research focused on the optimization and adjustment of this system and today four generations of electrochemical glucose sensors can be distinguished.

The first generation of glucose biosensors rely on the principle discussed above which is the detection of hydrogen peroxide produced in equation 1.3. A first disadvantage of these sensors includes the high potential, needed to oxidize H_2O_2. As a consequence, a minor selectivity is manifested, because at these potential values (0.7V/SCE), coexisting electro-active species such as ascorbic acid, uric acid and drugs (e.g. acetaminophen, a constituent of paracetamol®) act as interferences [29]. By the application of permselective (i.e. membranes that selectively allow the permeation of a molecule) coatings, researchers have tried to minimize the access of these interferences towards the electrode surface (see § 1.4.1) [30-32]. A second drawback of this method includes the oxygen dependency of the reactions. Fluctuations of free oxygen and its stoichiometric availability are critical factors which determine the accuracy of the glucose measurements [33].
In order to compensate for the previously mentioned shortcomings, *second generation* glucose sensors were developed. In this approach, oxygen is replaced by non-physiological electron acceptors which are able to carry electrons from the enzyme towards the surface of the working electrode. Herein, minimization of the electron-transfer distance is crucial for an optimal performance of the sensor. Examples of artificial redox mediators include ferrocene [34-35], conducting organic salts [36] and quinone-compounds [37]. In this mechanism, the mediator (M_{ox}) is reduced (M_{red}) (equation 1.5) due to the acceptance of electrons which are formed during the oxidation of $FADH_2$ to FAD (equation 1.3).

$$GOx\ (FADH_2) + M_{ox} \rightarrow GOx\ (FAD) + M_{red} \quad (1.5)$$

$$M_{red} \rightarrow M_{ox} + e^- \quad (1.6)$$

Next, the electrons generated during re-oxidation of the mediator (equation 1.6) are detected amperometrically and are a measure for the present blood glucose. In this set-up, a solution is offered to the oxygen dependency problem as well as to the selectivity problem, as lower potentials can be used that do not provoke interfering reactions from coexisting electroactive species.
Effective mediators should be stable, non-toxic, possess reversible electron transfer kinetics and should react fast with the reduced enzyme in order to minimize competition with oxygen. *In vivo*, this type of sensor is excluded due to possible leaching of the mediator molecules [12, 16, 33, 38]. On the other hand, for *in vitro* measuring set-ups, this principle is frequently used such as in the glucose test strips and the Freestyle® blood glucose monitoring system [39].
In the *third generation* of glucose biosensors, no mediators or reagents are used, but a direct transfer is created between the active site of the enzyme and the working electrode. As a consequence, this generation of sensors is characterized by a high selectivity and they allow for the development of implantable needle-type devices for continuous *in vivo* blood glucose

monitoring. To ensure direct electron transfer, organic conducting materials based on charge transfer complexes are used such as tetrathiafulvalene-tetracyanoquinodimethane (TTF-TCNQ) [40-41]. It should be noted that on normal electrode surfaces, only a few enzymes such as peroxidases exhibit direct electron transfer potential [42].

Even though improvements are made throughout the previously discussed generations, factors as temperature, humidity and interference still control the enzyme's activity strongly. Furthermore, thick enzyme layers, surrounding its redox centre, might inhibit the electron transfer process [39].

Because of the shortcomings of the previous generations of sensors, a *fourth generation* was developed which focuses on enzyme-free detection methods in which glucose is directly oxidized on the sensor surface. Research in this field focuses on the development of metal-based, composite-based and carbon micro- and nano-based electrodes for glucose sensing [39, 43-44].

Parallel to the use of GOx enzymes as glucose recognition elements and other proteins such as glucose dehydrogenase, glucokinase and lectins, a lot of attention has been paid to phenylboronic acid (PBA) as sensing unit to detect glucose. PBAs are able to bind *cis*-diol containing compounds such as carbohydrates through reversible boronate ester formation. Due to this property, they are often termed 'boronolectins', as they are recognized as a synthetic mimetic for lectins, which are natural carbohydrate binding proteins. In case of glucose, multivalent boronate ester formation is facilitated in aqueous media via the complexation scheme shown in figure 1.4. Herein, only the charged phenylboronate can form a stable complex with glucose, since the neutral complex between PBA and glucose is highly susceptible towards hydrolysis. Contribution of the latter to the represented equilibrium can thus be neglected [45].

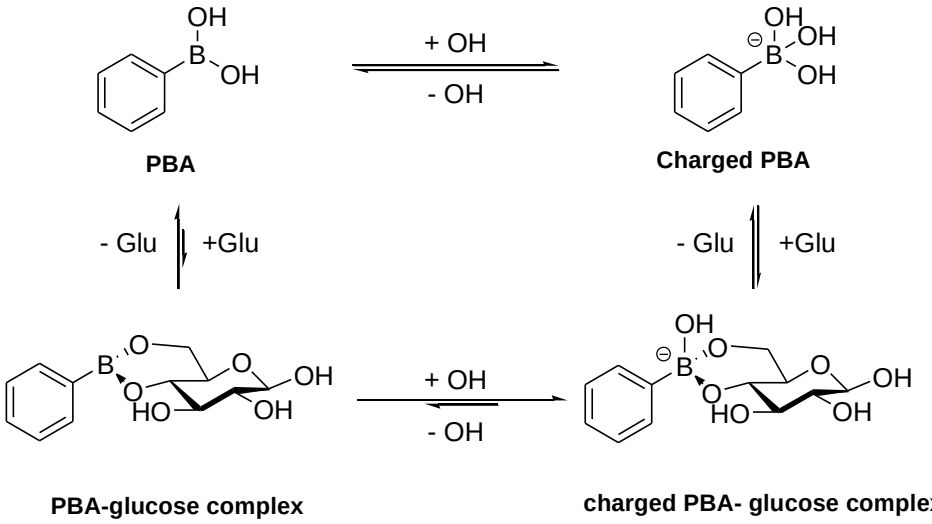

Figure 1.4: Reversible boronate ester formation with β-D-glucose in aqueous solution.

The main challenge concerning this method includes improvement of the binding affinity and selectivity [46]. Previously, it has been shown that simple monoboronic acids are

insufficient to meet these requirements, although selective glucose binding can be pursued by the initiation of multivalent glucose interactions, by using multiple boronic acid functionalities, which are properly positioned for example onto a polymer backbone [47]. In this respect, it should be mentioned that PBA-containing hydrogels only show glucose sensitivity at a pH close to the pK_a of the PBA unit. In the end, only the dissociated, charged forms of PBA are able to form a stable complex with glucose, meaning that the typically used PBA-based hydrogels (e.g. 3-(acrylamido)-phenylboronic acid (3-AAPBA); $pK_a \approx 8.2$) fail to respond to glucose at physiological pH. To solve this problem, researchers started to use PBA groups, which are characterized by a lower pK_a or they incorporated amino groups which stabilize the complex between PBA and the diol [47]. Since the applicability of this method in human physiological conditions, its use in diagnostic and therapeutic applications has been evaluated [48-50], including its application in both electrochemical and optical glucose sensors [51-52]. In the former case, the PBA-moiety is typically linked to the electrode via conducting polymers (see § 1.4.4.1) in a covalent way, whereas in the latter case, the PBA moiety is in close contact with a fluorophore.

1.3.2. Optical sensors

To date, optically based glucose sensors for *in vivo* monitoring are commercially still unavailable. Nevertheless, the interest in the development of such an optical glucose sensor has emerged, due to the availability of new technologies, such as cheap and reliable optical sources and detectors and because of their reagent-less nature [10].
Generally, optical transducers are used, which facilitate glucose detection via the use of different properties of light to interact with glucose molecules in a concentration-dependent manner. In this respect, (near)-IR- and fluorescence spectroscopy include frequently studied techniques.

1.3.2.1. IR absorption spectroscopy

In case of IR spectroscopy, glucose quantification is based on the selective absorption of light by glucose which is described by the Beer-Lambert law (equation 1.7). Herein, the transmitted intensity (I) is correlated with the glucose molar concentration (C), via the knowledge of the intensity of the incident optical radiation (I_0), the molar extinction coefficient (ε, expressed in $(mol/L)^{-1}cm^{-1}$) and the path length (L, in cm). Due to its additive character, measurements are mostly reported in absorbance, $A=\log(I_0/I)$ [10].

$$I = I_0 e^{-\varepsilon CL} \tag{1.7}$$

Both the MIR (4000-200 cm^{-1}) and NIR (14000-4000 cm^{-1}) region include attractive spectrum ranges for glucose detection. In the first case, light absorption arises from molecule specific fundamental stretching and bending modes. Despite the specific nature of the measurements, high background absorptions, especially by water, limit the applicability of this wavelength region for glucose quantification. In the second case, absorption arises due to overtone vibrations or combinations of C-H, O-H and N-H stretching vibrations. Problems

associated with this technique include substantial overlap with interferents, its temperature dependency and its sensitivity towards scattering. Due to its less specific nature (i.e. low absorption bands), several wavelengths are generally used together with multivariate analysis and calibration to calculate glucose concentrations [10, 53]. Furthermore, it has been proven that combination spectra are preferred over first-overtone spectra for the direct measurement of glucose in an aqueous environment, due to an enhanced selectivity [54]. Figure 1.5 shows the absorption peaks of glucose in the first-overtone band (FOB; 1550-1810 nm) and combination band (CB; 2070-2375 nm), together with the absorption peaks of the most important interferents.

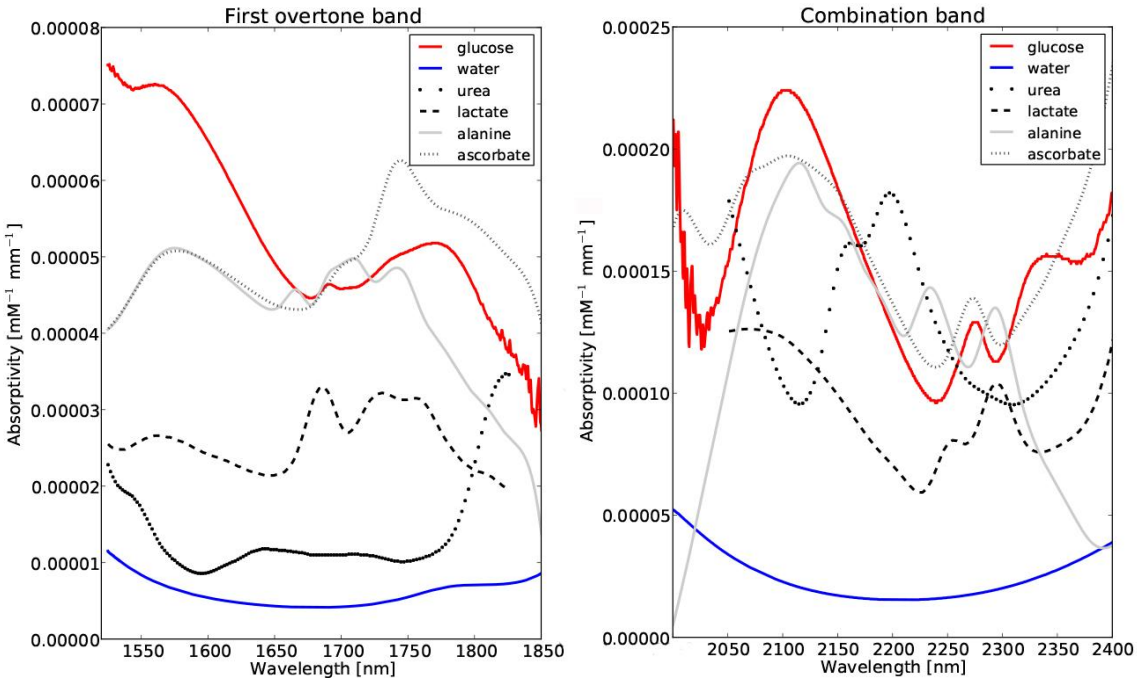

Figure 1.5: Absorptivity of glucose, water and the most important interferents in the near-infrared region. (Based on data from Amerov et al.[55], figure retrieved from Rijckeboer et al. [56])

Despite its shortcomings, NIR spectroscopy is a very attractive technology for non-invasive glucose measurements. In this respect, transcutaneous measurements occurring through the fingertip, lip, tongue, the forearm and earlobe have already been explored because of the potential of NIR light to pass through different skin layers over a distance of a few mm [57]. Nevertheless, more than 20 years of research did not yet result in the same accuracy as achieved with current invasive methods. The main reasons include the extensive light scattering induced by skin and the impact on the results of contact pressure when positioning a sensor on the skin [57].

Based on these findings, the GlucoSens project focussed on the measurement of glucose concentrations inside the body to rule out the problems associated with transcutaneous measurements. As a consequence, an implantable, NIR-light glucose sensor as presented in figure 1.3 was proposed. Further motivation for this choice was provided by previous

research that showed succesfull *in vitro* NIR glucose measurements in serum (RMSEP(root mean square error of prediction) = 1.08 mM [58]) and whole blood (RMSEP= 0.95 mM [59], 1.4 mM[60], <1mM (CB) and 1.20 mM (FOB) [61]). Furthermore, during the course of the current project similar NIR-based glucose determinations were achieved by the project partners in ISF mimicking fluid (RMSEP= 0.79 mM) and serum (RMSEP= 1.16 mM) [62-63,64].

1.3.2.2. Fluorescence spectroscopy

In fluorescent detection of glucose, light is sent through a fluorophore containing sample. Herein, the fluorophore is able to absorb light and thereby it is brought in an excited electronic state of higher energy. Upon light emission, the fluorophore loses its vibrational energy and returns to the ground electronic state. Measurement of the light emission allows determination of the glucose concentration [65].
Several fluorescence-based techniques for glucose sensing have been developed.
In a first group, *enzyme catalyzed reactions* are used to change the fluorescent status. Herein, the intrinsic fluorescence of the enzymes can be used to determine glucose quantities, due to quenching upon glucose binding. Alternatively, fluorophores, such as fluorescein, may be bound to the enzyme or an oxygen dependent fluorophore may be used. In the latter case, upon glucose oxidation, oxygen is consumed and a change in fluorescence is manifested. Apart from enzyme-based systems, PBA can also be used as glucose sensing unit. In this case, PBA is linked to a fluorophore, which couples the molecular recognition of glucose to a change in fluorescence [53, 66].

In a second group, *affinity binding sensors* are used, which use a fluorescently labeled analogue of glucose that binds competitively with a receptor site specific for both glucose and the fluorescent analogue. In this respect, Concanavalin A (Con A), a glucose-binding protein, is frequently used as the receptor molecule whereas fluorescein-labeled dextran is commonly used as a competitive binder [67]. Increased glucose concentrations displace the (quenched) dextran from the ConA sites, thereby increasing the concentration and fluorescence intensity of free dextran molecules [66, 68].

It should be mentioned that fluorescence and other optical principles were not targeted in the current PhD.

1.3.2.3. Alternative optically based sensors

Apart from IR- and fluorescence-based spectroscopic techniques, optical techniques such as Raman spectroscopy, polarimetry, scattering [69], optical coherence tomography, fluorescence energy transfer (FRET), occlusion spectroscopy and photoacoustic spectroscopy have also been studied for glucose sensing purposes. They are all based on a different optical principle but a detailed discussion is beyond the scope of this work. Nevertheless, these principles are reviewed by Oliver et al. and McNichols et al.[10, 53]

1.4. The role of polymers in glucose sensing applications

In literature, most reviews focus on the description of the different glucose sensor principles, as briefly described above. In this work, the role of polymer materials in glucose sensors will be emphasized. Over the years, they have gained tremendous recognition in the field due to several advantages. First, their chemical and physical properties may be tailored over a wide range of characteristics. Secondly, polymers may be fabricated in diverse shapes such as films, fibers, membranes, capsules and porous structures. Finally, they can be easily modified with biological compounds, which makes them ideally suitable to mimic natural sensing organs [70-71].
Based on their fulfilled function within the glucose sensor, a division is made between the different polymers described in literature.

1.4.1. Mass transport limiting membranes

As mentioned before, electrochemical detection of glucose is complicated due to the existence of other interfering electro-active species. As a consequence, a basic electrochemical sensing unit is built-up of an inner metal-based or carbon electrode, a central enzyme layer (see also §1.3.2) and an outer mass-transport limiting membrane, previously called a permselective coating. The latter coating should block interferences and enable selective glucose diffusion towards the electrode. In this respect, acetylcellulose and Nafion® are frequently used as they are known to eliminate ascorbic acid, one of the most abundant interferents [72]. Additionally, poly(urethane) (PU) includes another popular outer membrane in glucose sensor applications, due to an obtained durability, biocompatibility and long-term stability of the sensor function *in vitro*. In this respect, it was shown that the presence of hydrophilic segments inside the PU structure are responsible for an enhanced glucose transport [73]. On the other hand, to prevent the passage of interferents, polyethersulfone (PES) was in this case used as inner membrane. Since in the biomedical field, PES is widely used as blood purification membrane, it can already be mentioned that it was also selected as a barrier membrane in the current research work (see chapter 5).
More recently, Wang et al. developed electrospun PU fibers which offered an increased linearity to the glucose sensor compared to conventional epoxy-PU membranes [72]. Nevertheless, in the latter case, Yu et al. could demonstrate a successful operation of the sensor for 10-52 days in rats [74].
Other examples include the use of polycarbonate (PC) [75], polyvinylchloride [76], poly(o-phenylenediamine) [77] and hydrogels [78].

Since the sensors that apply a single polymer membrane are frequently characterized by a slow response, narrow measuring range and low current, different systems, i.e. multilayered membranes, have been proposed and evaluated. An example in this respect includes the work of Matsumoto et al., wherein the electrode is coated with respectively g-aminopropyltriethoxysilane (g-APTES), acetylcellulose, Nafion® (the inner membranes),

glucose oxidase and polydimethylsiloxane (PDMS) (the outer membrane). The sensor proved immunity towards ascorbic acid, uric acid, and *p*-acetaminophen and it showed fast responses in a broad glucose concentration range [79].

In case implantation of the sensor is targeted, it should be noted that most of the aforementioned membranes do not offer a suitable interface for an *in vivo* environment. As a consequence, an additional biocompatible coating should be applied, as discussed in § 1.4.5.

1.4.2. Polymers used as immobilization matrix

As pointed out in §1.3, dependent on the glucose sensing principle (electrochemical or optical), different compounds such as enzymes, lectines or other synthetic compounds play a crucial role within the signal generation and transduction of a glucose sensor. To allow for close contact between the electrode and the transducer, most of these compounds have been immobilized onto polymer materials.

Polymer membranes used as immobilization matrix have been studied extensively and typical examples include cuprophane [80], PU [81], redox polymers (see § 1.4.4.2) [82], copolymer hydrogels [83], poly(vinyl alcohol) (PVA) [84], polypyrrole [85-86], silica [86], etc. Apart from membranes, the use of polymer beads as immobilization matrix has also been explored, such as by Shibata et al. They developed injectable polyacrylamide hydrogel microbeads that contained fluorescent diboronic acid based monomers, which were bearing long hydrophilic spacers to maximize their mobility and opportunities for glucose binding. As this system showed sufficient fluorescent intensity during *in vivo* transdermal monitoring, it showed unique opportunities for continuous glucose monitoring (CGM) [87].

Different immobilization strategies have been developed, which are characterized by their own specific advantages and disadvantages. Generally, two classes of immobilization techniques can be distinguished, including the non-covalent immobilization protocols (physical adsorption, physical entrapment and affinity binding) and the covalent techniques. It should be clear that the performance of a biosensor is highly affected by the selected immobilization process. Further elaboration on this topic has already been performed by Guimard et al. [88], Lange et al. [89] and Rahman et al. [90], but is beyond the scope of the current work.
It should however be noted that in the design of biosensors, immobilization of biological compounds such as enzymes on the transducer surface includes a critical step. Herein, immobilization should preserve the compound's structure and function in order to maintain their biological activity after immobilization. Furthermore, to assure stability during long-term applications, immobilization should result in the formation of stable bonds and desorption of the enzyme during sensor function should be avoided.

As a last example, the more recent development of glucose sensor contact lenses could also be mentioned. Herein, polymers such as poly(ethylene terephtalate) (PET) [21, 23] and PVA [91-92] have been used to house glucose sensor electronics or other glucose sensing compounds, such as fluorophores.

A complete presentation of all polymers ever used for immobilization purposes within the world of glucose sensors would be an impossible job. Nevertheless, during the further course of this work, more examples will be given since most of these polymers exert additional functions within the glucose sensor design, as will be explained in the upcoming paragraphs.

1.4.3. Glucose sensitive polymers

1.4.3.1. Polymers used for glucose recognition, as an alternative to enzymes

As pointed out in §1.3, the recognition element constitutes one of the compounds building a glucose sensor. These elements mostly consist of biological compounds, such as enzymes, which specifically interact with glucose and induce an electrochemical reaction to quantify the glucose content. Herein, the biological compounds need to be immobilized directly onto the electrode or via an immobilization matrix such as a polymer network or hydrogel, as described above. Due to their high costs and their lack of storage and operational stability, research has focused on the development of synthetic alternatives. In this respect, molecularly imprinted polymers (MIPs) have gained a lot of interest [93]. Their synthesis is based on the polymerization of a functional monomer and a crosslinking agent, in the presence of a molecule (e.g. glucose), which acts as a template [94]. After polymerization, the template is removed, which results in the creation of recognition sites in the polymer matrix that are complementary to the analyte in its shape and positioning of functional groups. To organize the functional monomers around the template, covalent, non-covalent, electrostatic, but also metal ion coordination can be exploited [95]. Malitesta et al. were the first to synthesize poly(o-phenylenediamine) (PPD) imprinted by glucose via electrosynthesis, to be used in combination with a quartz-crystal microbalance (QCM)-based transducer [94]. The same glucose imprinted PPD polymer has also been evaluated with a capacitive transducer, which allowed for sensitive glucose detection [96]. Ersöz et al. added metal coordination in their MIP's design as a promising binding mode to prepare highly specific template polymers for the recognition of glucose and they could prove higher glucose binding affinity compared to the well-known glucose binding protein, concanavalin A [95].
Apart from PPD [97], hydrogels including poly(2-hydroxyethyl methacrylate) (PHEMA), crosslinked with poly(ethylene glycol) dimethacrylate (PEGDMA) [98], poly(allylamine) [99-100] and styrene-based polymers and micelles [101-102] have been evaluated as glucose imprinted polymers. The latter micelles were proven successful for the development of a voltammetric glucose sensor [102].

Recently, glucose selective MIPs, using boronic acids have also been explored. To this end, copolymers of phenol and 3-hydroxyphenylboronic acid have been synthesized by electropolymerization, in which D-glucose is used as a template (Figure 1.6) [103]. Alternatively, 4-vinylphenylboronic acid has been used together with methylene bisacrylamide as crosslinker [104]. Upon the application of boronic acid moieties, Manju et al. were able to synthesize a fluorescent MIP (fluorescein and PHEMA-based) which shows changes in fluorescence emission on the event of glucose binding [105].
The main disadvantage of MIPs includes the low density of imprinted sites, which often results in slow diffusion of the analyte and in longer time intervals for sensing (7-20 min). Nevertheless, response times between 3-5 minutes have been reported for PBA-based MIP-grafted electrodes. Although higher than GOx-based response times (< 1 min), these values can still be considered acceptable [104]. Figure 1.6 demonstrates the synthesis of a PBA-based MIP and offers a nice representation of the MIP's concept.

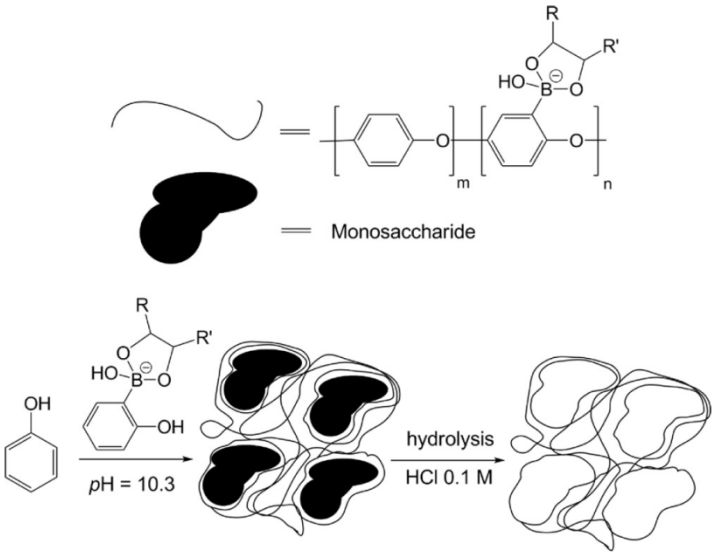

Figure 1.6: Synthesis of D-glucose imprinted poly(phenol-*co*-3-hydroxyphenylboronic acid)[52].

Apart from MIPs, boronic acid (BA)-based polymers have gained a lot of attention because of their glucose interactive nature (see also § 1.3.1) and their synthetic character. Most of these polymers are hydrogels, which are a group of water-swellable crosslinked materials. PBA-based hydrogels thus combine the merits of both BA (glucose sensitivity) and hydrogels (biocompatible, water-swellable), a concept which has been exploited for many purposes. Due to the existence of excellent reviews regarding their synthesis, properties and their applications within the world of electrochemical and optical glucose sensors [47, 52, 106], this topic is not further addressed in the current PhD.

1.4.3.2. Glucose responsive hydrogels

Hydrogels are defined as hydrophilic polymer networks which are able to absorb high amounts of water (up to thousands times their dry weight) without dissolution or loss of

their three dimensional structure. Preservation of their structure is enabled due to the existence of covalent crosslinks or physical crosslinks such as entanglements, hydrogen bonds, Vander Waals interactions, ionic or hydrophobic interactions [71]. A special class includes the stimuli-responsive hydrogel materials, which are able to undergo abrupt volume changes from a collapsed to a swollen state in response to environmental changes, such as temperature, pH or electrical stimuli. These intelligent materials possess both sensor and effector functions, as they can sense the stimulus as a signal and respond to it by inducing structural changes. Due to this combined property, glucose responsive hydrogels have gained a lot of attention for their use in glucose sensor applications but also to control insulin delivery inside the body [107-108].

The ultimate goal in diabetes control includes the development of a closed loop insulin delivery system. Herein, insulin release systems based on polymeric materials are frequently studied, also referred to as the polymeric artificial pancreas, as they try to mimic the pancreatic activity of healthy people. Initial systems consisted of polymer pellets, such as ethylene vinyl acetate copolymers [109], which were impregnated with insulin and upon implantation, a sustained release of the hormone was provided. Additionally, signal sensitive polymeric insulin release systems have been developed, wherein insulin release is activated upon application of an external impulse such as ultrasound, a magnetic field, electricity, etc. These systems have been reviewed by Uchiyama et al [110]. Nevertheless, as also stated in the latter review, these systems do not contain a regulation system that controls the insulin release according to changes in the glucose level.

To obtain the latter goal, glucose-responsive hydrogels have been studied extensively, also referred to as stimuli-responsive or intelligent materials. Based on the glucose recognition mechanism, most reviews subdivide this class of glucose responsive polymers into GOx-loaded hydrogels, lectin-loaded hydrogels and PBA-based hydrogels [107-108, 110-111]. These materials combine glucose recognition with a response signal which causes insulin release. In the next part, the general insulin-releasing principle is explained for each class, but for a detailed explanation, the above-cited references should be consulted.

In case of *GOx-based* glucose detection, pH sensitive hydrogels are mostly studied. As described in § 1.3, upon action of GOx, glucose is converted into gluconic acid, which lowers the pH inside the hydrogel. This change in pH alters the swelling behavior of the hydrogel, due to a modification of the polymer's charge density, upon capturing protons. Glucose thus triggers a volume change of the insulin-loaded gel (swelling or collapse of the gel), which enables its controlled release.

The initial system, developed by Ishihara et al. enabled insulin release upon swelling of the hydrogel. To this end, a GOx immobilized membrane was combined with a poly(amine) (copolymer of N,N-dimethylaminoethyl methacrylate (DEA) and 2-hydroxypropyl methacrylate (HPMA)) membrane and upon conversion of glucose into gluconic acid, the increased acidic conditions resulted in positively charged tertiary amino groups in the second membrane, which caused swelling of the material (due to increased hydrophilicity of the gel

and electrostatic repulsion) and subsequent insulin release [112]. To increase the insulin permeability and release rate, capsules as well as macroporous membranes have been developed [83]. In alternative systems, insulin release is enabled through contraction of the gel [113]. Recently, Chu et al. developed a closed-loop insulin system, wherein a GOx-based membrane is integrated within a silicone based insulin reservoir (Figure 1.7). Due to the GOx-catalyzed production of gluconic acid, shrinkage of the pH-responsive poly(*n*-isopropylacrylamide-co-methacrylic acid) nanoparticles, which are embedded in the bio-inorganic albumin-based membrane is caused. Because of this collapse, nanopores are created across the membrane and thereby instant insulin release is facilitated [114].

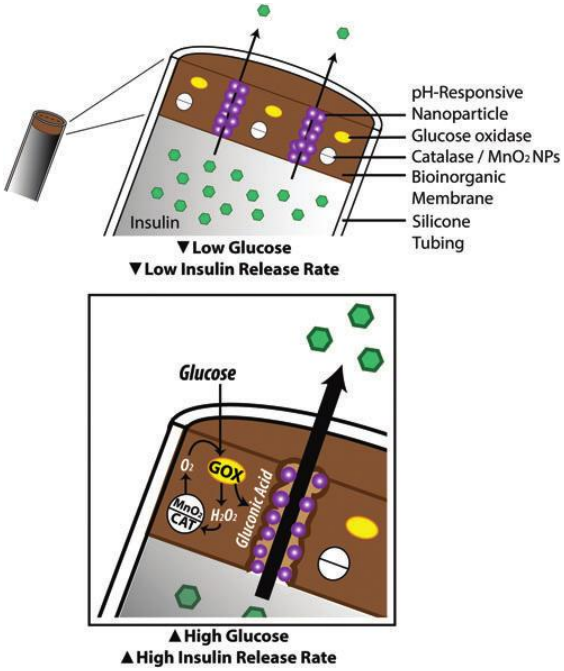

Figure 1.7: Scheme for glucose-responsive insulin microdevices: (top) polydimethylsiloxane (silicone) tubing microdevice with a bioinorganic plug and the cross-section of the device with embedded hydrogel nanoparticles (NPs) and (bottom) cross-sectional diagram of the membrane response to glucose at high glucose concentrations. CAT, catalase; GOx, glucose oxidase [114].

Apart from GOx, *lectines* are also frequently studied as glucose sensing molecules. Lectines are proteins which specifically bind to carbohydrates and in case of glucose, Con A is most frequently studied (see also § 1.2.2.2). In case insulin delivery is targeted, glycosylated insulin derivatives have been developed [115], which are bound onto hydrogel immobilized Con A. Based on the competitive and complementary binding behavior of Con A with glucose and the glycosylated insulin, insulin will be released in a proportional response to the blood glucose levels. Hydrogels used for immobilization include poly(vinylpyrrolidone-co-acrylic acid) (PVPAA) [115] and poly(2-glucosyloxyethyl methacrylate) (PGEMA) [116]. If *in vivo* use of these systems is targeted, covalent linkage of Con A with the hydrogel matrix includes a prerequisite to minimize toxic effects such as an undesirable immune effect due to leaching [108].

In case *PBA-based hydrogels* are used, similar mechanisms as for the lectine-based systems have been described. The addition of glucose will enhance swelling of the network, due to an increased hydrophilicity of the hydrogel, which is caused by the formation of negatively charged glucose-borate anion complexes. As a result, the release of insulin is facilitated in a diffusion controlled way. In case of chemically controlled release, systems make use of competitive binding between gluconic acid modified insulin and glucose onto the PBA-based hydrogel [117]. It should be mentioned that Zhang et al. could prove that the volumetric change of the PBA modified hydrogels is highly dependent on the chemical structure of the immobilized PBAs [118].

In case of the last two classes, the Con A and PBA-based hydrogels, sol-gel phase reversible hydrogel systems have also been described. In this case Con A and PBA act as crosslinking agents for respectively glucose- and polyol containing polymer chains. In both cases, the crosslinks are reversible, meaning that in case free glucose is penetrating the hydrogel, competition will exist.

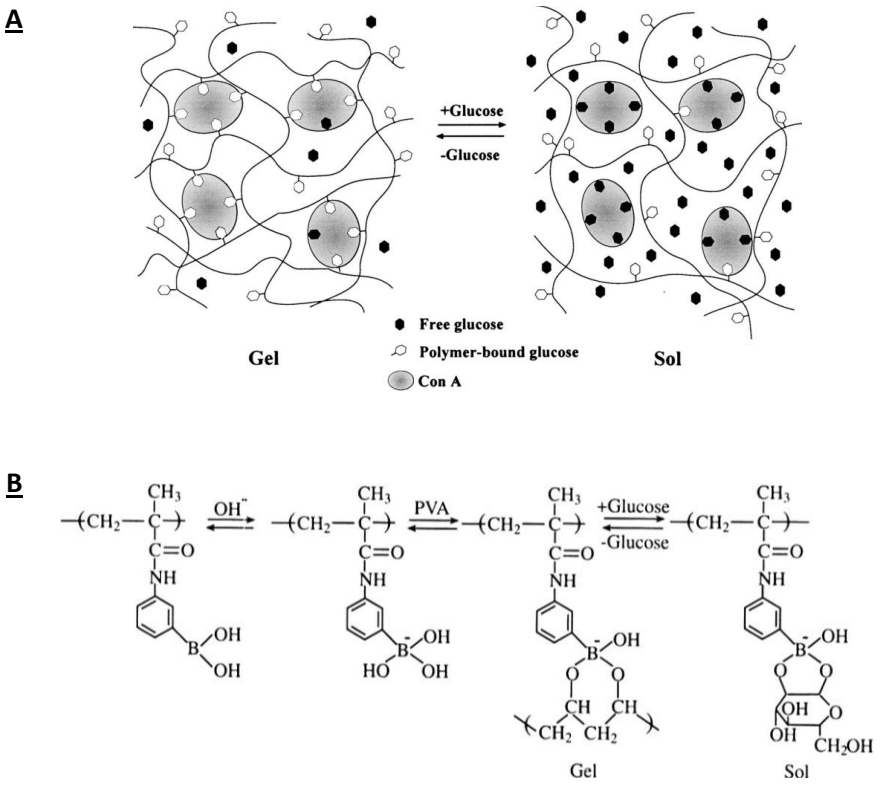

Figure 1.8: Panel A: Sol–gel phase-transition of a glucose-sensitive hydrogel. Large circles represent Con A, a glucose-binding protein. Small open and closed hexagons represent polymer-bound glucose and free glucose, respectively. Panel B: Sol–gel phase-transition of a phenylborate polymer. At alkaline pH, phenylborate polymer interacts with the polyol polymer such as poly(vinyl alcohol) to form a gel. Glucose replaces PVA to induce a transition from the gel to the sol phase [119].

In case of the Con A containing gel, competition will exist between the external glucose and the internally hydrogel-bound glucose molecules to interact with Con A (Figure 1.8, A). In

case of PBA-based hydrogels, this competition exists between the free glucose and the polyol polymer (figure 1.8, B). Since glucose only has one binding site for the borate group, it is not able to act as a crosslinker. In both cases, an increase in glucose concentration will thus result in a decreased crosslinking degree of the gel and an increased swelling, which results in a higher insulin release [119].

Apart from their use as artificial pancreas, glucose responsive hydrogels can also be applied in glucose sensor devices. In this case, the glucose-induced swelling can be read out by electrochemical methods such as conductometry [120] or optical transduction, upon the incorporation of a fluorophore inside the lectin and PBA-based hydrogel systems [47, 121]. In this respect, the development of a polymerized, crystalline colloidal array (PCCA) sensor should be mentioned, which was developed by Holtz et al [122]. Herein, highly charged monodisperse polystyrene spheres are embedded as crystalline colloidal arrays (CCA) into a glucose responsive hydrogel. Due to their dielectric periodicity, PCCA hydrogel films selectively diffract light of certain frequencies. If the glucose concentration is increased, the hydrogel (reversibly) swells and as a consequence, the lattice spacing is changed which causes a shift of the diffraction peak of the PCCA film towards longer wavelengths. Typical hydrogel examples include poly(acrylamide)/poly(ethylene glycol) with pendant PBA groups [123], acrylamide bisacrylamide hydrogels and its copolymers with *n*-hexylacrylate [124].

The main drawbacks of glucose responsive hydrogels include their slow response time towards environmental changes such as changing glucose concentrations and their lack of reproducibility. To overcome the first issue, adjustment of the hydrogel dimensions could be considered [119]. In this respect, hydrogel films with a micrometer to submicrometer thickness have been developed [125]. Furthermore, the development of injectable systems such as nanoparticles (NP) or micelles to control insulin release in the body, has gained a lot of attention. Zhao et al. developed mesoporous silica nanoparticles (MSN) as insulin reservoir, which are coated with GOx and catalase enzyme multilayers. In the presence of glucose, GOx converts glucose into gluconic acid and due to a pH decrease, the enzyme multilayer shell starts to swell and enables the subsequent insulin release [126]. As a non-enzymetic alternative, similar worm-like MSN have been developed by Sun et al. They applied both a crosslinked and non-crosslinked polymer shell onto the nanoparticles, bearing thermoresponsive N-isopropylacrylamide (NIPAM) to allow insulin loading and 3-acrylamidophenylboronic acid (AAPBA) as a glucose recognition moiety to allow insulin release [127-128].
Other recent literature examples of glucose responsive hydrogel materials, used for insulin delivery and glucose sensor applications are listed in table 1.1.

Table 1.1: Examples of responsive hydrogels used for insulin release or for glucose sensor applications, recently described in literature.

Material	Glucose recognition	Application	Ref.
Cationic chitosan hydrogel	GOx	pH-induced insulin release	129
Polymeric micelles (copolymer of MePEGA, AAPBA and NBA)*.	PBA	UV- and glucose induced insulin release	130
Amphiphilic Glycopolymer NP (p(AAPBA-r-MAGA)*)	PBA	Glucose induced insulin release	131
Biodegradable cellulose/poly(acrylic acid)	/	Oral insulin delivery (pH-induced release)	132
Poly(diethylaminoethyl methacrylate)	GOx	pH and glucose induced insulin release	133
DEAEMA/PEGDMA hydrogel particles containing GEMA/Con A complexes	Con A	Glucose induced swelling intended for insulin release and sensor applications	134
N-alkylacrylamide-based hydrogels	PBA	Glucose induced gel shrinkage	135
P(NIPAm-APBA-NBDAE-RhBEA)* microgels	PBA	Glucose sensor applications	136
polyacrylamide hydrogel microbeads	PBA	CMOS-based glucose sensor	137
PEG diglycidyl ether (PEGDGE) crosslinked polyetheramine	GOx	Impedimetric glucose sensor for tears and sweat	138
Poly (styrene-co-acrylamide-co-AAPBA*) microgels embedded in poly(acrylamide-co-2-(dimethylamino) ethylacrylate).	PBA	NIR-PCCA based glucose sensor	139
pNIPAm-co-AAc* microgels[140] AAm-AAPBA* [125]	PBA	Fabry-Perot optical glucose sensor	125, 140
Ag NP with a P(VPBA-co-DMAEA) shell	PBA	Insulin release	141

*MePEGA:poly (methoxypolyethylene glycol acrylamide); AAPBA: 3-acrylamide phenylboronic acid; NBA: 2-nitrobenzyl acrylate; p(AAPBA-r-MAGA): random copolymer of 3-acryl aminophenylboronic acid and maleimide-glucosamine; NIPAm: N-isopropylacrylamide; NBDAE: 4-(2-acryloyloxyethylamino)-7-nitro-2,1,3-benzoxadiazole (NBDAE), RhBEA: rhodamine B-based FRET acceptors; AAc: acrylic acid; AAm: acrylamide; P(VPBA-co-DMAEA): poly(4-vinylphenylboronic acid-*co*-2-(dimethylamino)ethyl acrylate)

1.4.4. Polymers used for the enhancement of electron transfer

Glucose biosensors make use of a glucose sensing unit such as an enzyme or PBA. As mentioned in §1.3.1, the greatest challenge lies in the successful immobilization of these compounds and the preservation of the sensing unit's stability and performance after immobilization, whilst being in close contact with the transducer. In the end, electrochemical detection of glucose is associated with the exchange of electrons between the sensing unit and the transducer. To improve the electrical contact, the immobilization polymers preferably function as an electron conducting interface between both components. To

realize these goals, different polymer types come into play and based on their physicochemical characteristics, composition and electron transfer mechanism, three main classes can be distinguished, including (intrinsically) conducting polymers, redox polymers and composite materials.

1.4.4.1. Conducting polymers

Conducting polymers (CP) were first recognized with the invention of iodine-doped polyacetylene in 1977 [142]. Generally, conducting polymers are described as 'synthetic metals', due to their electric, electronic, magnetic and optical properties, which are inherent to metals and semi-conductors [143]. The conducting properties of the polymers originate from the alternating double- and single-bonded sp^2 hybridized atoms which are present in their organic chains (cfr. conjugated system). A planar conformation of this system maximizes sideways overlap between the π molecular orbitals which is critical for their conductivity. In their neutral, uncharged state, conducting polymers show almost no conductivity, yet upon oxidation (*p*-doping) or reduction (*n*-doping) of the conjugated backbone and upon providing a counter anion or cation (i.e. dopant) respectively, charge carriers are formed [88, 144]. Apart from polyacetylene, typical examples of CP include polyaniline, polypyrrole, polythiophene, poly(paraphenylene), polycarbazole, polyphenol and polyfuran [89]. They can be synthesized chemically, via condensation or addition polymerization, which permits up-scaling of the materials, or electrochemically, which benefits from the deposition of polymer layers with a controlled layer thickness, going as low as 20 nm [145].

Compared to metals, semiconductors and other conductive materials, CP are favored because of their inexpensive nature, their convenient synthesis and processing and their stability in air. Furthermore, due to the availability of a broad range of molecules which can be used as a dopant, their eventual properties can be easily modeled [88].

Since 1980s, the application of conducting polymers for biomedical applications also became popular, due to the recognition in that time of their compatibility with many biomolecules, such as those used in biosensors. Herein, the mild conditions used for polymerization are ideal for the simultaneous synthesis of CP and incorporation of the biological compound [146]. Due to their biocompatibility, their ability to entrap and release biological molecules in a controlled way, their ability to transfer charge and their potential to easily change their electrical and chemical properties, next to biosensors, conducting polymers are extensively studied for their use in tissue engineering applications, neural probes, drug delivery devices and bio-actuators [88].

In sensor applications, conducting polymers act as both immobilization matrices and physicochemical transducers to convert a chemical signal into an electrical one. In this field, CP enjoy the advantage that electrochemical synthesis enables direct deposition of a polymer film with controlled thickness onto the electrode surface, followed by biomolecule immobilization. It is thus possible to deposit CP in a very precise way over defined areas of the electrode to intimately interface them with biomolecules such as enzymes. In this way,

an effective electron transfer mechanism between the enzyme and the final electrode is enabled, which enhances the sensor selectivity and sensitivity. The exact electron transfer mechanism is not yet clearly understood but the electronic phenomena in these systems can be explained by the concept of solitons, polarons and bipolarons [147].

Further improvement of electron transfer is enabled by the use of redox mediators such as ferrocene, which can be immobilized via entrapment, incorporated as dopant or immobilized via covalent linkage on the monomer [148-149]. Furthermore, to enhance the response time of the sensor, nano-fibers and nanotubes have been examined due to their porous structures [150]. Synthesis routes of these nanostructures have been reviewed by Xia et al. [151] and some recent literature examples of their use can be found in table 1.2.
In case of electrochemically based glucose sensors, cyclic polyenes have been frequently studied, including polypyrrole (PPy) [152], polythiophene (PT), poly(3,4-ethylenedioxythiophene) (PEDOT) and polyaniline (PANI) [153] (Figure 1.9) which are characterized by a good stability, conductivity and a straightforward synthesis [88, 144]. Recent literature examples of the application of these CP in glucose biosensors are listed in table 1.2. Herein, the glucose detection method is specified as well as the appearance of the CP. As sensing unit, GOx is mostly applied as specific interaction enzyme. Additionally, Welch et al. applied PEDOT/PSS (polystyrene sulfonic acid) polymers as a platform to grow combined brushes of poly(glycidyl methacrylate) and poly(2-hydroxyethyl methacrylate), to enable the subsequent covalent immobilization of GOx. In this way, leakage of the enzyme could be prevented [154].

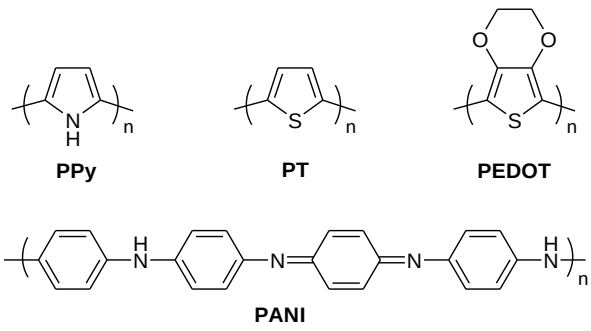

Figure 1.9: Chemical structures of conductive polymers, frequently used in electrochemical glucose sensors.

Apart from the introduction of conducting properties, upon charge injection (doping), the change in electronic band structure is also accompanied by a variation in the optical properties in the UV-VIS and NIR-region. As a consequence, CP are also studied for optical glucose sensor applications, although, to a limited extent. Nemzer et al. developed a GOx immobilized PANI-based glucose electrode, which enabled glucose detection via a GOx-catalyzed reversible redox reaction that alters the UV–VIS absorption properties of the polymer [155]. Similarly, Pringsheim et al. developed PBA-carrying PANI-based polymers, which

result in an altered NIR absorption spectrum upon interaction with saccharides. It should be noted that in this case a lower response is created for glucose compared to fructose [156]. Alternatively, Jin et al. produced an interpenetrating hydrogel network of polyacrylamide (PAAm) and PEDOT. Herein, the hydrogel microenvironment changed (i.e. hydrogel shrinkage) due to the GOx catalyzed glucose reaction and as a result, a blue shift in the reflection peak of the film was manifested [157].

Table 1.2: Recent literature examples of conducting polymers used in glucose sensor applications.

Conducting polymer	Sensing unit	Appearance	Glucose detection	Ref.
PPy	GOx	film	SPR*	158
	GOx	film	amperometry	159-161
	GOx	film	Impedimetry	162
	GOx	nanotube array	amperometry	163
PT	GOx	film	amperometry	164
PEDOT	GOx	Film	n.s.(CV)	165
	GOx	Film	voltammetry	166
	GOx	film	electrochemical/optical	167
PMB*/PEDOT	GOx	Film	amperometry	168
PSS/PEDOT	GOx	film	amperometry	169
PANI	GOx	nanofiber	amperometry	170
	p-toluenesulfonic acid	nanofiber	amperometry/impedimetry	171
	GOx	film	optical/amperometry	172-173
	GOx	nanowire	amperometry	174
	GOx	nanoparticle	electrochemical	175
		hydrogel	Amperometry	176

*SPR: surface plasmon resonance; PMB: poly(methylene blue); PSS: polystyrene sulfonic acid

1.4.4.2. Redox polymers

Apart from intrinsically conducting polymers, redox polymers are also widely applied as electron transfer media. In this case, electron motion is enabled via an electron exchange reaction (electron hopping) between neighboring redox sites, which are contained within the redox polymer. These redox sites can be oxidized or reduced and are either covalently attached (into the polymer chain or as pendant group) or electrostatically bound [177]. To enable for appropriate electron hopping, segmental motion should be enabled.

Originally, within the world of electrochemical glucose sensors, soluble redox mediators, which are non-physiological electron acceptors, such as ferrocene, have been applied (cfr. 2nd generation of glucose sensors, §1.3.1). However, these appeared inadequate for the long-term stability of devices or for *in vivo* implantation, due to possible leaching. As a consequence, in an attempt to develop reagent-less glucose biosensors, their immobilization

onto polymers has been investigated. As mentioned in the previous paragraph, their successful immobilization onto CP such as PT [178] and PPy [179] has been demonstrated as well as their use in glucose sensor applications, a topic which has been reviewed by Saleem et al. [180] Apart from CP, their immobilization on redox polymers also resulted in promising results. Polyquinones and polysiloxanes were initially studied as redox-based immobilization polymers, but due to their insolubility in aqueous media, water-swellable redox hydrogels were introduced as a superior alternative [181] (typical examples are given in figure 1.10). They were initially introduced by Heller et al. [38, 182-183] and similar to the electron conducting hydrogels (ECH), discussed under the CP, the cause for their unique properties is twofold. First, these hydrogels are able to dissolve and diffuse water soluble chemical and biochemical species at a rate almost equal as in water itself. Secondly, these hydrogels differentiate from common examples in the sense that they also possess electron-conducting properties.

Generally, they consist of a crosslinked water-swellable polymer network which possesses redox center containing tethers. Similar to the conducting polymers, the hydrogels serve to electrically connect the redox centers of enzymes to the electrode and therefore, they are referred to as 'electrically wired enzymes'. Electron-conduction in these type of materials is established by the self-exchange of electrons between their rapidly reducing and oxidizing redox functions and the exchange is enabled by collision of the involved redox centra, a process which is described by the Marcus-type collisional electron transfer theory [184]. Electron transfer in redox hydrogel films has been studied in depth by Forster et al. [185-187]

To facilitate the above-mentioned collisions, segmental mobility includes the most important prerequisite. In the end, this property will determine the electron diffusion coefficient (D_e) of the hydrogel material, which is a measure for the transport of electrons through the redox polymer. In this respect, hydration is playing a key role, meaning that it positively influences chain mobility as well as the material's D_e. Apart from chain mobility, mechanical stability of the hydrogels includes a second prerequisite. Binyamin et al. demonstrated that an adequately cross-linked redox-hydrogel should withstand shear stresses of 10^{-2} N/m^2 [188]. The mechanical strength of the hydrogels is mainly determined by the crosslinking density of the material and the molecular weight of the starting polymer. The latter property clearly enhances the segmental mobility and the hydration of the polymer accordingly, whereas crosslinking counteracts these phenomena. As a consequence, a highly crosslinked polymer backbone should preferably be combined with redox functions at the end of the tethers. Using this approach, free movement of the redox functions is facilitated and the collision probability and the GOx electron collection efficiency are enhanced. Optimally, these tethers consist of long and flexible spacers consisting of 8-15 atoms [189-190].

Typical hydrogel materials studied in this field include poly(vinylpyridine) (figure 1.10, A) [191-192], poly(N-vinylimidazole) [193-194] (figure 1.10, B) and a copolymer of 4-vinylpyridine and 4-aminostyrene. Typical redox centers tethered to the hydrogels comprise ferrocene and $Os^{2+/3+}$, which is complexed by substituted or unsubstituted pyridines.

Crosslinking of the nitrogen containing hydrogel complexes is typically done on the electrode surface itself, with the help of a diepoxide such as polyethylene glycol diglycidyl ether and in the presence of a GOx containing solution [183].
Alternatively, the UV-induced crosslinking of a ferrocene-based poly(dimethylacrylamide), containing photoreactive benzophenone groups has been reported [195-197] (figure 1.10, C).

To date, osmium-containing redox hydrogels are used in different amperometric biosensors, including the commercialized freestyle navigator system of Abbott Diabetes Care, which is a miniature subcutaneously implantable glucose sensor [198]. Rajagopalan et al. also studied $Os(bpy)_2Cl]^{+/2+}$ complexes of poly(vinylpyridine) and they could prove that quaternization of the polymer backbone with methyl iodide is able to enhance the rate of electron transport. Furthermore, due to the presence of positive charges, a superior electrostatic interaction with the negatively charged GOx enzyme is obtained, which stimulates their electrical communication [199].
Similarly, Calvo et al. synthesized poly(allylamine)-based polycationic redox hydrogels (figure 1.10, D). In this study, ferrocene was covalently attached to the polymer and crosslinked on the electrodes. Alternatively, after modification of the polymer with pyridine and crosslinking onto the electrode surface, ruthenium ($[Ru(NH_3)_5py]^{2+/3+}$) as well as iron pentacyano complexes ($[Fe(CN)_5py]^{2-/3-}$) have been immobilized [181]. Furthermore, polymer-enzyme multilayers, which are constituted via electrostatical self-assembly have been evaluated. In the latter case, the obtained films were characterized by a less random conformation compared to the crosslinked hydrogel films, which enabled a superior structural characterization of electron transfer and its kinetics. Nonetheless, they observed that only a small fraction of the enzyme was electrically wired by the attached mediators [200].

An important issue that needs to be addressed when wiring enzymes includes the enzyme's activity. Indeed, enzyme denaturation causes a loss in sensor selectivity and sensitivity. In literature, examples have been reported where precipitation occurs when mixing the redox polymers with the enzyme solution. To prevent precipitation, which is caused by electrostatic interactions, sodium dodecyl sulfate was successfully added as a surfactant [201].

More recently, Wang et al. developed branched poly(ethylenimine) nanobeads, immobilized onto ferrocene for the application in glucose biosensors. The application of hydrogel nanobeads minimizes the insulating property of a hydrogel's polymer backbone and in this respect they offer an elegant alternative for the use of composite materials (discussed in §1.3.1.3) [202].

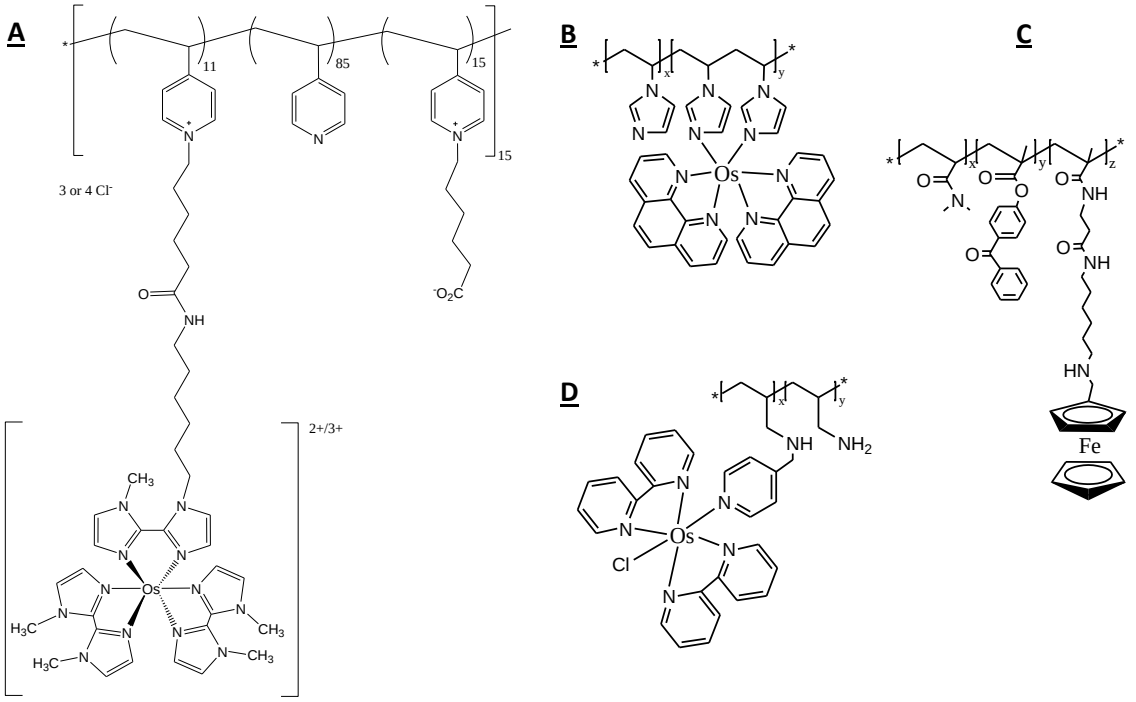

Figure 1.10: Examples of redox hydrogels: a poly(4-vinylpyridine) backbone bound to an Osmium containing redox center, via a 13 atom containing tether [182] (a), a poly(N-vinylimidazole)-based redox polymer, covalently bound to an Os-containing redox center [194] (b), a ferrocene containing poly(dimethylacrylamide) polymer containing benzophenone groups [195] (c) and poly(allylamine)-based redox hydrogel [200] (d).

1.4.4.3. Composite materials

Apart from the advantages of CP, summed above, these polymers are characterized by an inferior mechanical strength and to achieve sufficient conductivity, they have to be doped and oxidized by a counter ion. In order to enhance the mechanical properties, attempts were taken to copolymerize the CP with other polymers such as polyvinylchloride [203], but a sacrifice in conductivity is unavoidable. The same applies for the addition of dopants, which are also characterized by an insulating nature. As a consequence, the overall conductivity of CP is limited [204].

To improve the electrical conductivity, charge density, electrocatalytic activity and their strength, research has focused on the development of composite materials, wherein conductive polymers have been combined with metal nano-particles (NP), metal oxides, graphene or carbon nanotubes (CNT).

In case of glucose sensors, it was shown that metal oxides, metal nanoparticles and alloys are able to enhance the sensitivity and selectivity of glucose detection and that they act as electrochemical catalysts with high electrocatalytic activity for glucose electro-oxidation. In this context, the use of nobel metals such as Pt, Pd, Au and Ni is limited, because of their increased price and easy surface poisoning [205]. Nevertheless, in literature, Pd nanoparticles have been dispersed into nano-fibered PEDOT via a chemical or electrochemical method [206], Ni has been used in the development of cubic nickel hexacyanoferrate/polyaniline

hybrids [205] and thiolated Au NP have been evaluated as immobilization carrier of GOx [207]. Herein, the biocompatible nature of gold nanoparticles offered a compatible environment for the immobilized enzymes [208].
Carbon nanotubes, which were reported for the first time in 1991 by Iijima et al. [209], are characterized by high mechanical strength, electrical conductivity and chemical stability. Together with their minimal surface fouling and their ability of low-potential detection of hydrogen peroxide, they became very attractive for amperometric glucose sensing [210].
Next to CNT, the use of graphene has also been explored in CP composite materials. Graphene is a 2-dimensional allotrope of carbon in which the carbon atoms are held together in a honeycomb like lattice [211]. Pristine graphene, graphene oxide (GO) and reduced GO (RGO) are recognized as ideal candidates for electrochemical biosensors because of their high electrochemical activity. Their combination with CP is only a recent finding and it seems that the combination results in improved material properties due to synergetic effects. This topic and the use of these composites in sensor applications has recently been reviewed by Lei et al. [212]

As presented in table 1.3, the discussed composites are applied to enhance the electron transfer and the sensor response speed of GOx-based glucose sensors, but recently the design and the development of non-enzymatic glucose sensors have gained increasing interest (cfr. fourth generation of electrochemical glucose sensors) to meet the enzyme electrode drawbacks. Enzymatic detection usually shows good selectivity and high sensitivity, but the most common and serious problem of enzymatic glucose sensors lies in their lack of long-term stability owing to the nature of the enzymes.
As a consequence, CP composites have been studied as an alternative, wherein the enzyme's function within the glucose oxidation process is replaced by the composites electro-catalytic effect. In this way, direct oxidation of glucose at the modified electrode is enabled.
Recent literature examples of enzyme-less CP composite-based glucose sensors can also be found in table 1.3 (sensing unit is indicated by '/').

A special class of composite conducting polymers include the electroconductive hydrogels (ECH), which are polymeric blends or co-networks of inherently conductive electro-active polymers and highly hydrated hydrogels. Herein, the electrical, the electrochemical and the optical properties of the CP are combined with the *in vitro* and *in vivo* biocompatibility, the high degree of hydration and the concomitant high diffusion ability of small molecules (including glucose) inside the hydrogel material [146]. The use of these polymers have been studied for implantable biosensor applications including glucose sensors. In this respect, the combination of PHEMA and PPy have been applied in a GOx-based sensor design.[213]

Also in case of redox hydrogels, the use of composites has been studied in an attempt to increase the sensor output. In this respect, researchers have investigated the incorporation

of enzyme modified graphite particles [214] and single-walled CNT, inside redox polymer hydrogels [215].

Table 1.3: Recent literature examples of CP composites used in glucose sensor applications.

CP	Composite material	Sensing unit	Detection principle	Ref.
PPy	$CuFe_2O_4$	/	Amperometry/CV*/EIS*	216
	Fe_3O_4	GOx	Potentiometry	217
	Graphene	GOx	Amperometry	211, 218-219
	Reduced graphene oxide + Au NP*	GOx	Amperometry	220
	Au NP	/	Amperometry	221
	Carbon nanotubes	GOx	Amperometry/CV*	222
PT	Cu NP	/	Electrochemical	223
PEDOT	Graphene/PEDOT-PSS	GOx	CV	224
	Au	/	CV	225
	Carbon nanotube	/	Amperometry/voltammetry	226
	Pd NP/PEDOT nanofiber	/	Amperometry	206
PANI	Poly(styrene-sulfonic acid) MnO_2	n.s.	n.s.	227
	Graphene	GOx	CV	228
	Carbon nanotubes	GOx	CV	229
	Au NP	GOx	Amperometry	230-232
	Cu NP	/	Amperometry/CV	233
	Pt NP	GOx	Amperometry	234-235
	TiO_2	GOx	Amperometry	236

*CV: cyclic voltammetry (CV); EIS: electrochemical impedance spectroscopy; PSS: polystyrene sulfonic acid; n.s.: not specified

1.4.5. Improvement of biocompatibility for *in vivo* applications

If the developed glucose sensor is intended for *in vivo* applications, attention should be paid to the tissue-sensor interface. In other words, all sensor compounds should be characterized by a suitable biocompatibility and to realize this goal, encapsulation of the sensor compounds into a suitable packaging biomaterial includes a prerequisite [71].

Upon implantation, tissue damage will result due to incision and a host reaction will be evoked. Initially, due to blood-material interactions, proteins adsorb to the biomaterial surface, also called biofouling, and a provisional matrix forms, which constitutes the initial blood clot at the material/tissue interface [237]. Next, inflammation occurs, which is defined as the reaction of vascularized living tissue to local injury. Herein, exudation will occur wherein fluid, proteins and blood cells escape from the vascular system towards the injured tissue. In the initial stage (i.e. acute inflammation), the migrating cells mainly consist of neutrophils, whereas in the next stage of chronic inflammation, mainly monocytes, macrophages, and lymphocytes predominate. Continuation of the inflammation stage three weeks post-implantation usually indicates an infection [237]. Action of the monocytes and macrophages typically results in the initiation of the healing response. In the end, macrophages represent complex cells that secrete a large number of cytokines, which are small protein molecules

mediating immunity, inflammation and other actions. During this healing process, the formation of granulation tissue is initiated by the recruitment of fibroblasts and vascular endothelial cells towards the implantation site. As a result, new small blood vessels are created by sprouting of preexisting ones, also called angiogenesis or neo-vascularization. Furthermore, because of the action of the fibroblasts, proteoglycans are produced and in a later stage collagen, which eventually constructs a fibrous capsule around the implant. Apart from the formation of granulation tissue, the foreign body reaction is also characterized by the presence of foreign body giant cells (FBGC), which consist of fused monocytes and macrophages and which attempt to phagocytose the implanted material. Figure 1.11 summarizes the different events of inflammation and the wound-healing response. It should be noted that the tissue response is dependent on the severeness of the injury created during the implantation procedure and of the amount of provisional matrix formation. For an in depth discussion of these topics, an excellent review and book chapter of Anderson et al. can be consulted [71, 237]. Furthermore, possible mechanisms underlying the failure of subcutaneously implanted glucose sensors has been reviewed by Gerritsen et al. [238]

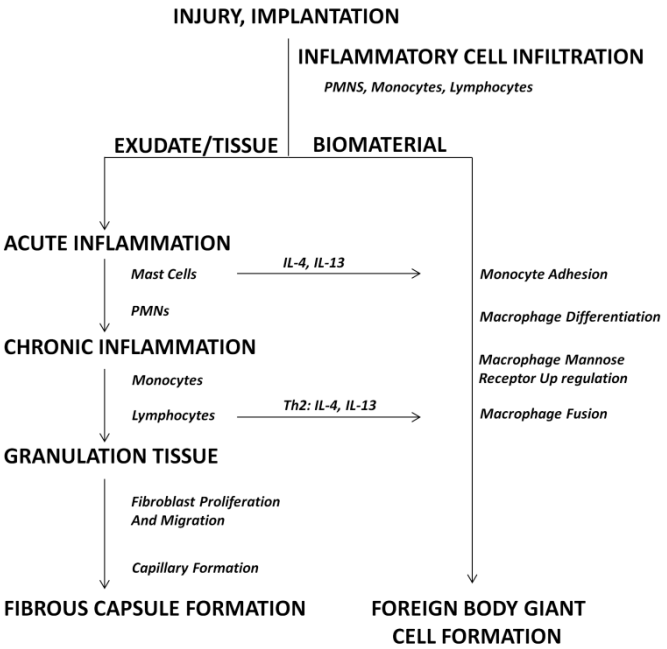

Figure 1.11: Sequence of events involved in inflammatory and wound-healing responses leading to foreign body giant cell formation and fibrous capsule formation. The important factors which direct monocyte/macrophage fusion are displayed [71, 237].

In order to prevent sensor failure, researchers have tried to control inflammation, the biofouling process and the fibrous capsule formation. The upcoming section will indicate that polymers again play a crucial role in the realization of these goals.

To control *in vivo* tissue **inflammation**, different polymer membranes have been evaluated, whether or not releasing anti-inflammatory drugs or other tissue response-modifying agents. In this respect, drug loaded poly(vinylalcohol) (PVA) and stacked layer-by-layer assembled PVA hydrogels have been evaluated [239]. Apart from a decreased inflammation, these

materials were also able to supplement the sensor's oxygen levels. Vallejo-Heligon et al. developed tubular, porous dexamethasone-releasing PU coatings which were capable of mediating the acute inflammatory response post-implantation [240].
Dexamethasone and other corticosteroids are able to impair collagen formation in post-operative wounds and as a consequence, they constitute ideal candidates for inhibiting the formation of a fibrous capsule. Conversely, caution is needed, since these hormones tend to inhibit angiogenesis by down-regulation of vascular endothelial growth factor (VEGF) [241]. In an attempt to control and localize drug delivery, a PVA hydrogel coating has been developed which contains dexamethasone-loaded poly(lactic-co-glycolic acid) (PLGA) microspheres [242-244]. Similarly, Yu et al. developed a coating for implantable glucose sensors consisting of dexamethasone loaded PLGA microspheres which were incorporated into a nordihydroguaiaretic acid (NDGA) crosslinked collagen scaffold [245]. Implantation in rats showed a significant decrease in inflammation, nevertheless, a thick fibrous capsule was still present around the implant [246].
In addition to dexamethasone, Grifford et al. suggested the use of nitric oxide to be used as inflammatory agent in biosensor devices, as it is known to play a role in wound healing by the down-regulation of mediators, active during inflammation [247]. In this respect, PU-based membranes, which are frequently used as the outer membrane in electrochemically-based glucose sensor systems are typically used as polymer carrier [248-249].

As part of the inflammation process, many researchers have focused on the reduction of **biofouling**, which describes the initial adhesion of proteins and cells onto implanted materials. This process has been indicated as the primary reason for sensitivity losses of sensors during the first 24 hours after subcutaneous implantation. Gifford et al. identified serum albumin as the primary biomolecule responsible for this fact. Additional compounds include biomolecule fragments with a molecular weight below 15 kDa, IgG (169 kDa) and fibrinogen (340 kDa). As these compounds adhere to the sensor surface, diffusion of glucose towards the sensing elements is decreased due to the formation of a diffusion barrier but also due to the consumption of glucose by attached cells [15]. Furthermore, if proteins reach the electrode itself, passivation occurs, which hampers H_2O_2 oxidation in case of enzyme-based sensors [250].
To prevent the aspecific protein binding, several polymer membranes have been evaluated as electrode coatings for their anti-biofouling potential. The most promising results have been obtained with the hydrogel-based materials, wherein poly(ethylene glycol) (PEG) is most frequently used because of its favorable biocompatibility. Due to its polar, water-swellable nature, a hydrophilic interface is created between the solid surface and aqueous bulk, which masks the underlying surfaces [251]. This hydrophilic shell is responsible for the PEG's protein-repellant nature and forms the basis of this stealth behavior. Recently, Chu et al. developed a closed loop insulin delivery system (cfr. figure 1.5) and they observed that PEGylation of the sensor surfaces with chains of 20 kDa resulted in minimal inflammation after 30 days of subcutaneous implantation in rats. Furthermore, a decreased thickness of

the fibrous capsule (<50 µm) was observed compared to the non-PEGylated surfaces and in case a lower molecular weight was applied (2 kDa) (<500 µm) [114, 252]. The biocompatible properties of PEG were further demonstrated by the subcutaneous implantation of a crosslinked 8-armed amine-terminated PEG hydrogel, since few adherent cells such as macrophages, neutrophils, foreign body giant cells, fibroblasts and collagen were observed [253]. Heo et al. developed a fluorescence based sensor, encapsulated in a PEG-bonded polyacrylamide hydrogel and implantation in the ears of mice revealed reduced inflammation compared to the non-PEGylated sensor [254].

Another hydrogel example, which is characterized by a promising *in vivo* biocompatibility includes PHEMA. In this respect, copolymers of HEMA and 2,3-dihydroxypropyl methacrylate (DHPMA) have been synthesized, in which the porosity and mechanical properties were improved by using N-vinyl-2-pyrrolidinone and EGDMA. The *in vitro* glucose diffusion coefficients were determined [255] and implantation of the hydrogel coated GOx/epoxy-PU based Pt sensors resulted in a maintained function for at least 21 days in rats. Furthermore, a reduced foreign body capsule (FBC) thickness was observed compared to the bare epoxy-PU based Pt sensors [256]. It was also shown that copolymers of PEG and PHEMA resulted in less fibrous encapsulation after subcutaneous implantation in rats [82] and that the use of dense and oriented PHEMA brushes are effective in the exclusion of proteins from the sensor surface [257].

As a short-term solution to biofouling, phospholipid-derived coatings including phosphorylcholine-based polymers [258-259], which represent a biomimitic of the cell membrane of red blood cells and Nafion membranes (i.e. perfluorosulfonic acid-based polymers) have also been studied [251].

Apart from these synthetic hydrogel materials, naturally derived coatings have also been used, such as chitosan, alginate, collagen, dextran and hyaluronic acid [260]. However, their natural variability, immunogenic nature and difficult processability include important disadvantages when considering their application in implantable devices.

As reviewed by Wisniewski et al., apart from polymer-based approaches, diamond-like carbon, surfactants and flow-based approaches could also be applied to reduce biofouling of a biosensor [251].

Apart from biofouling prevention, other researchers mainly focused on the development of modification methods to decrease or prevent fibrous capsule formation, also called the foreign body capsule (FBC). In order to realize this goal, research focused on the **stimulation of angiogenesis** in close proximity of the sensor. In this respect, based on a computational model, Novak et al. could prove that sensor lag times are mainly dependent on the thickness of the FBC, whereas the attenuation of glucose that reaches the sensor surface is mainly determined by vessel density and capsule porosity or density [261]. In other words, the creation of a well-vascularized capsule would result in an enhanced glucose sensor function because of improved glucose diffusion towards the sensor, a process which is hampered in case a fibrous avascular capsule is formed.

In order to stimulate angiogenesis around implanted glucose sensors, different strategies have been explored.

Since Ward et al. could demonstrate that the transforming growth factor β (TGFβ), a cytokine expressed by macrophages, plays an important role in the formation of FBC around subcutaneously implanted devices, they attempted to block the cytokine's action by the subcutaneous delivery of a TGFβ neutralizing antibody nearby the implanted sensor. Nevertheless, even after 28 days, they could not prove the success of this event [241]. However, they could prove that the thickness and density of the FBC increased with the thickness of the implant and decreased in case of higher material porosity. These conclusions were conducted from the comparison between, on the one hand, porous PVA sponges and expanded poly(tetrafluoroethylene) (ePTFE) and on the other hand, solid PU and a PU multipolymer containing silicone (S) and poly(ethylene oxide) (PEO) (PU-S-PEO) [262]. They also showed that the use of ePTFE resulted in an increased neovascularization, a fact which was also observed by Updike et al. They prepared an amperometric glucose sensor, which consisted of a GOx-loaded PU membrane, covered by a bioprotective membrane to prevent contact with macrophages and a ePTFE layer to enhance angiogenesis. Application of the latter porous membrane indeed resulted in stable subcutaneous glucose measurements in dogs for 5 months [263]. Additionally, Koschwanez et al. demonstrated enhanced angiogenesis around a commercial MiniMed SOF-SENSOR (Medtronics) which was encapsulated with a porous PLLA membrane [264].

Apart from varying the implant's geometry, stimulation of angiogenesis could also be triggered by the local release of angiogenic factors such as vascular endothelial growth factor (VEGF). Herein, Ward et al. could prove that local and prolonged VEGF infusion resulted in high local vascular densities around a biosensor [265].

Since the aforementioned approaches only deal with one aspect of the foreign body reaction, only a decreased intensity of this reaction is obtained for most studies. As a consequence, some researchers stressed the need for approaches, which combine different strategies. In this respect, Norton et al. and Patil et al. incorporated both Dex and VEGF in antibiofouling hydrogels to successfully lower inflammation, inhibit fibrosis and stimulate neovascularization *in vivo* [266-267]. Also Ju et al. pointed out that superior host responses could be expected upon combining their developed porous collagen scaffold, which encapsulated an electrochemical glucose sensor, with anti-inflammatory drugs or angiogenic factors [268].

Despite of all these interventions, the present commercially available glucose sensors, targeting continuous glucose monitoring, only survive for a maximum of several weeks *in vivo*, which clearly reflects the need for improved systems.

1.4.6. Conclusion

In the world of glucose sensors, the function of polymers is manifold. Different polymer classes have been identified, including classical thermoplastic polymers, conductive polymers, composites and hydrogels. In literature, their use as permselective membrane,

immobilization matrix of the sensing unit, glucose recognition element, electron transfer matrix and biocompatible coating has been described. It can be stated that each material class is valued because of its unique characteristic properties, such as hydrogels for their water swellable capacity, CP for their electron conductivity, whereas their composites, for example, combine the best of two worlds. Remarkably, if all above functions within glucose sensor applications are considered, it seems that the hydrogels are applicable in each functional category, which stresses the unique and versatile characteristics of this material class.

In case *in vivo* use of the glucose sensor is intended, the greatest challenge still includes addressing and controlling the foreign body response. In this respect, a multifaceted approach (control of polymer geometry, drug loading, etc), would be the most effective one. The current PhD mainly focuses on this subject.

1.5. Research goals and thesis outline

As mentioned in §1.2, the main goal of this PhD consists of the development of a packaging material for embedding an optical, implantable continuous glucose sensor.
Based on the proposed concept, described in § 2.1, the packaging material should fulfill the following requirements:
(1) It should offer an appropriate mechanical compatibility with subcutaneous tissue. In literature, the ideal bulk (i.e. mechanical and swelling) properties for an implantable packaging material have not yet been described. As a consequence, in the current work, a suitable range of bulk properties is targeted.
(2) It should be transparent in the NIR region to enable high signal/noise glucose measurements.
(3) It should be compatible with the sensor compounds. Herein, excellent adhesion between the polymer packaging and the sensor compounds should be pursued as well as the ability of the polymer packaging to act as a bidirectional diffusion barrier.
(4) It should enable proper *in vivo* integration. This implies that the body reaction may not alter the accuracy of the glucose measurements. A suitable surface chemistry of the packaging material is thus required which is able to control the triggered body response.

To fulfill the above-described requirements, two main goals are pursued in the current work. First, the development of a flexible packaging material is targeted. Since poly(methyl methacrylate) is known in the biomedical world as a biocompatible, FDA (Food and drug administration)-approved material, it was chosen as a starting material to develop more flexible alternatives, which could serve as a robust packaging of an optical glucose sensor. As a consequence, in *chapter 2*, an overview is given of the current use of PMMA in the biomedical world, followed by the screening of different MMA-based copolymer(s) (networks), wherein poly(ethylene glycol) (PEG) and other methacrylate-based co-

monomers are incorporated as building blocks. Apart from an extensive screening of the mechanical and swelling properties of the different candidates, the optical properties in the NIR region, the cell cytotoxicity and the compatibility with the sensor compounds are investigated.

Once implanted, the second goal of this work includes the induction of the desired body response, which is mainly determined by the sensor-tissue interface. As a consequence, a lot of attention is paid to the surface modification of the developed packaging materials. Since the developed materials are characterized by an inert character (i.e. do not contain chemically reactive functional groups), *chapter 3* focuses on the surface activation of the non-functional polymer materials. Herein, two modification strategies, including the deposition of polydopamine (PDA) and the post-plasma grafting of 2-aminoethyl methacrylate (AEMA) are described and the characterization of the surface layers via multiple surface characterization techniques is presented.

Due to the presence of surface functionalities, in a subsequent step, biofunctionalization of the polymer materials is enabled, i.e. the introduction of bioactive groups that enhance the cell interactivity of the starting materials. To this end, two strategies are followed. The first strategy mainly focuses on the improvement of tissue integration of the developed materials, in order to prevent the formation of an isolating fluid pocket around the sensor. To this end, a universal modification strategy based on gelatin has been developed, which should ensure long-term *in vivo* integration of the implant. In a second strategy, to further stimulate glucose diffusion towards the sensor, the stimulation of angiogenesis is targeted. To this end, the immobilization of VEGF and vascular endothial cadherin antibody (VE-cad AB) has been studied**.** Characterization of the different biofunctionalized surfaces is presented in *chapter 4*, as well as the *in vitro* evaluation of the different (un-)modified materials. Herein, the cell viability (live/dead assays) and cell adhesion properties (immuno-assay) are studied by the fluorescent staining of different relevant cellular compounds.

Next, in *chapter 5*, the results are presented of the *in vivo* experiments. In a first section, the sensor fabrication with the help of an 'in-house-built' mould is described. Secondly, the *in vivo* evaluation of the surface modified sensor packagings is overviewed. Next, a description is given of the attempts made for the *in vivo* administration of glucose. Finally, to gain insight in the current sensor concept, the explanted sensors are evaluated in an *in vitro* setting.

Finally, in *chapter 6*, the main principles of the used bulk and surface characterization techniques, as well as the experimental protocols are listed. In chapter 7, the main conclusions and future perspectives are summed and in chapter 8, a dutch summary is provided.

1.6. References

1. Federation, I. D. (2014) Diabetes: facts and figures, retrieved 20 September 2015, from http://www.idf.org/worlddiabetesday/toolkit/gp/facts-figures.
2. Guariguata, L., Whiting, D. R., Hambleton, I., Beagley, J., Linnenkamp, U., and Shaw, J. E. (2014) Global estimates of diabetes prevalence for 2013 and projections for 2035, *Diabetes research and clinical practice* 103, 137-149.
3. Reuters, T. (2015) Funding Diabetes Research; retrieved 11 August 2015, from http://sciencewatch.com/articles/funding-diabetes-research.
4. Turner, A., and Turner. (1985) Diabetes mellitus: biosensors for research and management, *Biosensors* 1, 85-115.
5. Federation, I. D. (2014) IDF Diabetes Atlas, 6th edition, p 160.
6. Seino, Y., Nanjo, K., Tajima, N., Kadowaki, T., Kashiwagi, A., Araki, E., Ito, C., Inagaki, N., Iwamoto, Y., Kasuga, M., Hanafusa, T., Haneda, M., Ueki, K., and Comm Japan Diabet Soc, D. (2010) Report of the Committee on the Classification and Diagnostic Criteria of Diabetes Mellitus, *Journal of Diabetes Investigation* 1, 212-228.
7. Li, S., Zhao, J. H., Luan, J., Langenberg, C., Luben, R. N., Khaw, K. T., Wareham, N. J., and Loos, R. J. F. (2011) Genetic predisposition to obesity leads to increased risk of type 2 diabetes, *Diabetologia* 54, 776-782.
8. Zhu, J., Zong, G., Lu, L., Gan, W., Ji, L., Hu, R., Ye, X., Sun, L., Loos, R. J. F., Li, H., and Lin, X. (2014) Association of genetic predisposition to obesity with type 2 diabetes risk in Han Chinese individuals, *Diabetologia* 57, 1830-1833.
9. Organization, W. H. (2014) Diabetes, retrieved 20 September 2015, from http://www.who.int/mediacentre/factsheets/fs312/en/.
10. McNichols, R. J., and Cote, G. L. (2000) Optical glucose sensing in biological fluids: an overview, *Journal of biomedical optics* 5, 5-16.
11. Turner, A. P., and Pickup, J. C. (1985) Diabetes mellitus: biosensors for research and management, *Biosensors* 1, 85-115.
12. Yoo, E.-H., and Lee, S.-Y. (2010) Glucose biosensors: an overview of use in clinical practice, *Sensors* 10, 4558-4576.
13. Pickup, J. C., Hussain, F., Evans, N. D., and Sachedina, N. (2005) In vivo glucose monitoring: the clinical reality and the promise, *Biosensors and Bioelectronics* 20, 1897-1902.
14. , D. C., and Group, C. T. R. (1995) The effect of intensive treatment of diabetes on the development and progression of long-term complications in insulin-dependent diabetes mellitus, *N Engl j Med* 329, 977-986.
15. Heller, A. (1999) Implanted electrochemical glucose sensors for the management of diabetes, *Annual Review of Biomedical Engineering* 1, 153-175.
16. Wang, J. (2008) Electrochemical glucose biosensors, *Chemical reviews* 108, 814-825.
17. Varalli, M., Marelli, G., Maran, A., Bistoni, S., Luzzana, M., Cremonesi, P., Caramenti, G., Valgimigli, F., and Poscia, A. (2003) A microdialysis technique for continuous subcutaneous glucose monitoring in diabetic patients (part 2), *Biosensors & Bioelectronics* 18, 899-905.
18. Kondepati, V. R., and Heise, H. M. (2007) Recent progress in analytical instrumentation for glycemic control in diabetic and critically ill patients, *Analytical and Bioanalytical Chemistry* 388, 545-563.
19. Poscia, A., Mascini, M., Moscone, D., Luzzana, M., Caramenti, G., Cremonesi, P., Valgimigli, F., Bongiovanni, C., and Varalli, M. (2003) A microdialysis technique for continuous subcutaneous glucose monitoring in diabetic patients (part 1), *Biosensors & Bioelectronics* 18, 891-898.
20. Pitzer, K. R., Desai, S., Dunn, T., Edelman, S., Jayalakshmi, Y., Kennedy, J., Tamada, J. A., and Potts, R. O. (2001) Detection of hypoglycemia with the GlucoWatch biographer, *Diabetes Care* 24, 881-885.

21. Lahdesmaki, I., Shum, A. J., and Parviz, B. A. (2010) Possibilities for Continuous Glucose Monitoring by a Functional Contact Lens, *Ieee Instrumentation & Measurement Magazine* 13, 14-17.
22. Baca, J. T., Finegold, D. N., and Asher, S. A. (2007) Tear glucose analysis for the noninvasive detection and monitoring of diabetes mellitus, *Ocular Surface* 5, 280-293.
23. Yao, H., Shum, A. J., Cowan, M., Laehdesmaeki, I., and Parviz, B. A. (2011) A contact lens with embedded sensor for monitoring tear glucose level, *Biosensors & Bioelectronics* 26, 3290-3296.
24. Novartis. (2014) Novartis to license Google "smart lens" technology; retrieved 20 September 2015 from https://www.novartis.com/news/media-releases/novartis-license-google-smart-lens-technology.
25. Daniloff, G. Y. (1999) Continuous glucose monitoring: long-term implantable sensor approach, *Diabetes Technology & Therapeutics* 1, 261-266.
26. Pearson, J. E., Gill, A., and Vadgama, P. (2000) Analytical aspects of biosensors, *Annals of clinical biochemistry* 37, 119-145.
27. Clark, L. C., and Lyons, C. (1962) Electrode systems for continuous monitoring in cardiovascular surgery, *Annals of the New York Academy of Sciences* 102, 29-45.
28. Guilbaul.Gg, and Lubrano, G. J. (1973) Enzyme electrode for amperometric determination of glucose, *Analytica Chimica Acta* 64, 439-455.
29. Moattisirat, D., Velho, G., and Reach, G. (1992) Evaluating in vitro and in vivo the interference of ascorbate and acetaminophen on glucose detection by a needle-type glucose sensor, *Biosensors & Bioelectronics* 7, 345-352.
30. Emr, S. A., and Yacynych, A. M. (1995) Use of polymer-films in amperometric biosensors, *Electroanalysis* 7, 913-923.
31. Sasso, S. V., Pierce, R. J., Walla, R., and Yacynych, A. M. (1990) Electropolymerized 1,2-diaminobenzene as a means to prevent interferences and fouling and to stabilize immobilized enzyme in electrochemical biosensors, *Analytical Chemistry* 62, 1111-1117.
32. Palmisano, F., Centonze, D., Guerrieri, A., and Zambonin, P. G. (1993) An interference-free biosensor based on glucose-oxidase electrochemically immobilized in a nonconducting poly(pyrrole) film for continuous subcutaneous monitoring of glucose through microdialysis sampling, *Biosensors & Bioelectronics* 8, 393-399.
33. Wang, J. (2001) Glucose biosensors: 40 years of advances and challenges, *Electroanalysis* 13, 983.
34. Cass, A. E. G., Davis, G., Francis, G. D., Hill, H. A. O., Aston, W. J., Higgins, I. J., Plotkin, E. V., Scott, L. D. L., and Turner, A. P. F. (1984) Ferrocene-mediated enzyme electrode for amperometric determination of glucose *Analytical Chemistry* 56, 667-671.
35. Sun, R., Wang, L., Yu, H., Zain ul, A., Chen, Y., Huang, J., and Tong, R. (2014) Molecular Recognition and Sensing Based on Ferrocene Derivatives and Ferrocene-Based Polymers, *Organometallics* 33, 4560-4573.
36. Ivanov, I., Vidakovic-Koch, T., and Sundmacher, K. (2013) Alternating electron transfer mechanism in the case of high-performance tetrathiafulvalene-tetracyanoquinodimethane enzymatic electrodes, *Journal of Electroanalytical Chemistry* 690, 68-73.
37. Lau, K. T., de Fortescu, S. A. L., Murphy, L. J., and Slater, J. M. (2003) Disposable glucose sensors for flow injection analysis using substituted 1,4-benzoquinone mediators, *Electroanalysis* 15, 975-981.
38. Heller, A., and Feldman, B. (2008) Electrochemical glucose sensors and their applications in diabetes management, *Chemical reviews* 108, 2482-2505.
39. Toghill, K. E., and Compton, R. G. (2010) Electrochemical non-enzymatic glucose sensors: a perspective and an evaluation, *Int. J. Electrochem. Sci* 5, 1246-1301.

40. Palmisano, F., Zambonin, P. G., Centonze, D., and Quinto, M. (2002) A disposable, reagentless, third-generation glucose biosensor based on overoxidized poly(pyrrole)/tetrathiafulvalene-tetracyanopuinodimethane composite, *Analytical Chemistry* 74, 5913-5918.
41. Khan, G. F., Ohwa, M., and Wernet, W. (1996) Design of a stable charge transfer complex electrode for a third-generation amperometric glucose sensor, *Analytical Chemistry* 68, 2939-2945.
42. Zhang, W. J., and Li, G. X. (2004) Third-generation biosensors based on the direct electron transfer of proteins, *Analytical Sciences* 20, 603-609.
43. Tian, K., Prestgard, M., and Tiwari, A. (2014) A review of recent advances in nonenzymatic glucose sensors, *Materials Science & Engineering C-Materials for Biological Applications* 41, 100-118.
44. Park, S., Boo, H., and Chung, T. D. (2006) Electrochemical non-enzymatic glucose sensors, *Analytica Chimica Acta* 556, 46-57.
45. Springsteen, G., and Wang, B. H. (2002) A detailed examination of boronic acid-diol complexation, *Tetrahedron* 58, 5291-5300.
46. Wu, X., Li, Z., Chen, X.-X., Fossey, J. S., James, T. D., and Jiang, Y.-B. (2013) Selective sensing of saccharides using simple boronic acids and their aggregates, *Chemical Society Reviews* 42, 8032-8048.
47. Guan, Y., and Zhang, Y. (2013) Boronic acid-containing hydrogels: synthesis and their applications, *Chemical Society Reviews* 42, 8106-8121.
48. Sanjoh, M., Miyahara, Y., Kataoka, K., and Matsumoto, A. (2014) Phenylboronic Acids-based Diagnostic and Therapeutic Applications, *Analytical Sciences* 30, 111-117.
49. Matsumoto, A., Kataoka, K., and Miyahara, Y. (2014) New directions in the design of phenylboronate-functionalized polymers for diagnostic and therapeutic applications, *Polymer journal* 46, 483-491.
50. Baker, S. J., Ding, C. Z., Akama, T., Zhang, Y.-K., Hernandez, V., and Xia, Y. (2009) Therapeutic potential of boron-containing compounds, *Future Medicinal Chemistry* 1, 1275-1288.
51. Egawa, Y., Seki, T., Takahashi, S., and Anzai, J.-i. (2011) Electrochemical and optical sugar sensors based on phenylboronic acid and its derivatives, *Materials Science & Engineering C-Materials for Biological Applications* 31, 1257-1264.
52. Hansen, J. S., Christensen, J. B., Petersen, J. F., Hoeg-Jensen, T., and Norrild, J. C. (2012) Arylboronic acids: A diabetic eye on glucose sensing, *Sensors and Actuators B-Chemical* 161, 45-79.
53. Oliver, N., Toumazou, C., Cass, A., and Johnston, D. (2009) Glucose sensors: a review of current and emerging technology, *Diabetic Medicine* 26, 197-210.
54. Chen, J., Arnold, M. A., and Small, G. W. (2004) Comparison of combination and first overtone spectral regions for near-infrared calibration models for glucose and other biomolecules in aqueous solutions, *Analytical Chemistry* 76, 5405-5413.
55. Amerov, A. K., Chen, J., and Arnold, M. A. (2004) Molar absorptivities of glucose and other biological molecules in aqueous solutions over the first overtone and combination regions of the near-infrared spectrum, *Applied spectroscopy* 58, 1195-1204.
56. Ryckeboer, E. (2014) Spectroscopic detection of glucose with a silicon photonic integrated circuit, Ghent University.
57. Yadav, J., Rani, A., Singh, V., and Murari, B. M. (2015) Prospects and limitations of non-invasive blood glucose monitoring using near-infrared spectroscopy, *Biomedical Signal Processing and Control* 18, 214-227.
58. Kasemsumran, S., Du, Y., Murayama, K., Huehne, M., and Ozaki, Y. (2004) Near-infrared spectroscopic determination of human serum albumin, γ-globulin, and glucose in a control serum solution with searching combination moving window partial least squares, *Analytica Chimica Acta* 512, 223-230.

59. Shen, Y., Davies, A., Linfield, E., Elsey, T., Taday, P., and Arnone, D. (2003) The use of Fourier-transform infrared spectroscopy for the quantitative determination of glucose concentration in whole blood, *Physics in medicine and biology* 48, 2023.
60. Kim, Y.-J., and Yoon, G. (2006) Prediction of glucose in whole blood by near-infrared spectroscopy: influence of wavelength region, preprocessing, and hemoglobin concentration, *Journal of biomedical optics* 11, 041128-041128-041127.
61. Amerov, A. K., Chen, J., Small, G. W., and Arnold, M. A. (2005) Scattering and absorption effects in the determination of glucose in whole blood by near-infrared spectroscopy, *Analytical Chemistry* 77, 4587-4594.
62. Sharma, S., Goodarzi, M., Wynants, L., Ramon, H., and Saeys, W. (2013) Efficient use of pure component and interferent spectra in multivariate calibration, *Analytica Chimica Acta* 778, 15-23.
63. Sharma, S. (2014) Exploiting Expert Information in Multivariate Calibration of an Implantable Glucose Sensor.
64. Sirova, M., Van Vlierberghe, S., Matyasova, V., Rossmann, P., Schacht, E., Dubruel, P., and Rihova, B. (2014) Immunocompatibility evaluation of hydrogel-coated polyimide implants for applications in regenerative medicine, *Journal of Biomedical Materials Research Part A* 102, 1982-1990.
65. Demchenko, A. P. (2006) Principles of Fluorescence Spectroscopy. Chapter: Introduction to Fluorescence; pp. 1-26, Springer, New York.
66. Pickup, J. C., Hussain, F., Evans, N. D., Rolinski, O. J., and Birch, D. J. (2005) Fluorescence-based glucose sensors, *Biosensors and Bioelectronics* 20, 2555-2565.
67. Meadows, D. L., and Schultz, J. S. (1993) Design, manufacture and characterization of an optical fiber glucose affinity sensor based on an homogeneous fluorescence energy transfer assay system, *Analytica Chimica Acta* 280, 21-30.
68. Pickup, J., McCartney, L., Rolinski, O., and Birch, D. (1999) In vivo glucose sensing for diabetes management: progress towards non-invasive monitoring, *Bmj* 319, 1289.
69. Heinemann, L., and Schmelzeisen-Redeker, G. (1998) Non-invasive continuous glucose monitoring in Type I diabetic patients with optical glucose sensors, *Diabetologia* 41, 848-854.
70. Adhikari, B., and Majumdar, S. (2004) Polymers in sensor applications, *Progress in Polymer Science* 29, 699-766.
71. Buddy D. Ratner, A. S. H., Frederick J. Schoen, Jack E. Lemons, (Ed.) (2004) *Biomaterials Science.*, Second edition ed., Elsevier.
72. Wang, N., Burugapalli, K., Song, W., Halls, J., Moussy, F., Ray, A., and Zheng, Y. (2013) Electrospun fibro-porous polyurethane coatings for implantable glucose biosensors, *Biomaterials* 34, 888-901.
73. Ward, W. K., Jansen, L. B., Anderson, E., Reach, G., Klein, J.-C., and Wilson, G. S. (2002) A new amperometric glucose microsensor: in vitro and short-term in vivo evaluation, *Biosensors and Bioelectronics* 17, 181-189.
74. Yu, B., Long, N., Moussy, Y., and Moussy, F. (2006) A long-term flexible minimally-invasive implantable glucose biosensor based on an epoxy-enhanced polyurethane membrane, *Biosensors and Bioelectronics* 21, 2275-2282.
75. Linke, B., Kerner, W., Kiwit, M., Pishko, M., and Heller, A. (1994) Amperometric biosensor for in vivo glucose sensing based on glucose oxidase immobilized in a redox hydrogel, *Biosensors and Bioelectronics* 9, 151-158.
76. Reddy, S. M., and Vadgama, P. (2002) Entrapment of glucose oxidase in non-porous poly (vinyl chloride), *Analytica Chimica Acta* 461, 57-64.
77. Moussy, F., Harrison, D., and Rajotte, R. (1994) A miniaturized Nafion-based glucose sensor: in vitro and in vivo evaluation in dogs, *The International Journal of Artificial Organs* 17, 88-94.
78. Trzebinski, J., Moniz, A. R. B., Sharma, S., Burugapalli, K., Moussy, F., and Cass, A. E. (2011) Hydrogel Membrane Improves Batch-to-Batch Reproducibility of an Enzymatic Glucose Biosensor, *Electroanalysis* 23, 2789-2795.

79. Matsumoto, T., Furusawa, M., Fujiwara, H., Matsumoto, Y., and Ito, N. (1998) A micro-planar amperometric glucose sensor unsusceptible to interference species, *Sensors and Actuators B: Chemical* 49, 68-72.
80. Newman, D. P. (1976) Membrane for enzyme electrodes, Google Patents.
81. Gilligan, B. J., Shults, M. C., Rhodes, R. K., and Updike, S. J. (1994) Evaluation of a subcutaneous glucose sensor out to 3 months in a dog model, *Diabetes Care* 17, 882-887.
82. Quinn, C. P., Pathak, C. P., Heller, A., and Hubbell, J. A. (1995) Photo-crosslinked copolymers of 2-hydroxyethyl methacrylate, poly(ethylene glycol) tetra-acrylate and ethylene dimethacrylate for improving biocompatibility of biosensors, *Biomaterials* 16, 389-396.
83. Podual, K., Doyle III, F. J., and Peppas, N. A. (2000) Glucose-sensitivity of glucose oxidase-containing cationic copolymer hydrogels having poly (ethylene glycol) grafts, *Journal of controlled release* 67, 9-17.
84. Corgier, B. P., Marquette, C. A., and Blum, L. J. (2005) Screen-printed electrode microarray for electrochemiluminescent measurements, *Analytica Chimica Acta* 538, 1-7.
85. Njagi, J., and Andreescu, S. (2007) Stable enzyme biosensors based on chemically synthesized Au–polypyrrole nanocomposites, *Biosensors and Bioelectronics* 23, 168-175.
86. Kojuharova, A., Popova, Y., Kirova, N., Klissurski, D., Simeonov, D., and Spasov, L. (1988) Characterization and application of glucose-oxidase immobilized in silica hydrogel *Journal of Chemical Technology and Biotechnology* 42, 95-104.
87. Shibata, H., Heo, Y. J., Okitsu, T., Matsunaga, Y., Kawanishi, T., and Takeuchi, S. (2010) Injectable hydrogel microbeads for fluorescence-based in vivo continuous glucose monitoring, *Proceedings of the National Academy of Sciences* 107, 17894-17898.
88. Guimard, N. K., Gomez, N., and Schmidt, C. E. (2007) Conducting polymers in biomedical engineering, *Progress in Polymer Science* 32, 876-921.
89. Lange, U., Roznyatouskaya, N. V., and Mirsky, V. M. (2008) Conducting polymers in chemical sensors and arrays, *Analytica Chimica Acta* 614, 1-26.
90. Rahman, M. A., Kumar, P., Park, D. S., and Shim, Y. B. (2008) Electrochemical sensors based on organic conjugated polymers, *Sensors* 8, 118-141.
91. Badugu, R., Lakowicz, J. R., and Geddes, C. D. (2004) Ophthalmic glucose monitoring using disposable contact lenses - A review, *Journal of fluorescence* 14, 617-633.
92. Domschke, A., March, W. F., Kabilan, S., and Lowe, C. (2006) Initial clinical testing of a holographic non-invasive contact lens glucose sensor, *Diabetes Technology & Therapeutics* 8, 89-93.
93. Kriz, D., Ramström, O., and Mosbach, K. (1997) Peer Reviewed: Molecular Imprinting: New Possibilities for Sensor Technology, *Analytical Chemistry* 69, 345A-349A.
94. Malitesta, C., Losito, I., and Zambonin, P. G. (1999) Molecularly imprinted electrosynthesized polymers: New materials for biomimetic sensors, *Analytical Chemistry* 71, 1366-1370.
95. Ersoz, A., Denizli, A., Ozcan, A., and Say, R. (2005) Molecularly imprinted ligand-exchange recognition assay of glucose by quartz crystal microbalance, *Biosensors & Bioelectronics* 20, 2197-2202.
96. Cheng, Z. L., Wang, E. K., and Yang, X. R. (2001) Capacitive detection of glucose using molecularly imprinted polymers, *Biosensors & Bioelectronics* 16, 179-185.
97. Wang, Q., Paim, L. L., Zhang, X., Wang, S., and Stradiotto, N. R. (2014) An Electrochemical Sensor for Reducing Sugars Based on a Glassy Carbon Electrode Modified with Electropolymerized Molecularly Imprinted Poly-o-phenylenediamine Film, *Electroanalysis* 26, 1612-1622.
98. Oral, E., and Peppas, N. A. (2006) Hydrophilic molecularly imprinted poly(hydroxyethyl-methacrylate) polymers, *Journal of Biomedical Materials Research Part A* 78A, 205-210.
99. Wang, J., Banerji, S., Menegazzo, N., Peng, W., Zou, Q. J., and Booksh, K. S. (2011) Glucose detection with surface plasmon resonance spectroscopy and molecularly imprinted hydrogel coatings, *Talanta* 86, 133-141.

100. Wizeman, W. J., and Kofinas, P. (2001) Molecularly imprinted polymer hydrogels displaying isomerically resolved glucose binding, *Biomaterials* 22, 1485-1491.
101. Fang, C., Yi, C., Wang, Y., Cao, Y., and Liu, X. (2009) Electrochemical sensor based on molecular imprinting by photo-sensitive polymers, *Biosensors & Bioelectronics* 24, 3164-3169.
102. Yang, Y., Yi, C., Luo, J., Liu, R., Liu, J., Jiang, J., and Liu, X. (2011) Glucose sensors based on electrodeposition of molecularly imprinted polymeric micelles: A novel strategy for MIP sensors, *Biosensors & Bioelectronics* 26, 2607-2612.
103. Granot, E., Tel-Vered, R., Lioubashevski, O., and Willner, I. (2008) Stereoselective and enantioselective electrochemical sensing of monosaccharides using imprinted boronic acid-functionalized polyphenol films, *Advanced Functional Materials* 18, 478-484.
104. Yoshimi, Y., Narimatsu, A., Nakayama, K., Sekine, S., Hattori, K., and Sakai, K. (2009) Development of an enzyme-free glucose sensor using the gate effect of a molecularly imprinted polymer, *Journal of Artificial Organs* 12, 264-270.
105. Manju, S., Hari, P. R., and Sreenivasan, K. (2010) Fluorescent molecularly imprinted polymer film binds glucose with a concomitant changes in fluorescence, *Biosensors & Bioelectronics* 26, 894-897.
106. Cambre, J. N., and Sumerlin, B. S. (2011) Biomedical applications of boronic acid polymers, *Polymer* 52, 4631-4643.
107. Miyata, T., Uragami, T., and Nakamae, K. (2002) Biomolecule-sensitive hydrogels, *Advanced Drug Delivery Reviews* 54, 79-98.
108. Ravaine, V., Ancla, C., and Catargi, B. (2008) Chemically controlled closed-loop insulin delivery, *Journal of controlled release* 132, 2-11.
109. Brown, L., Munoz, C., Siemer, L., Edelman, E., and Langer, R. (1986) Controlled release of insulin from polymer matrices: control of diabetes in rats, *Diabetes* 35, 692-697.
110. Uchiyama, T., Watanabe, J., and Ishihara, K. (2004) Implantable polymeric artificial pancreas, *Journal of Biomaterials Science-Polymer Edition* 15, 1237-1262.
111. Roy, D., Cambre, J. N., and Sumerlin, B. S. (2010) Future perspectives and recent advances in stimuli-responsive materials, *Progress in Polymer Science* 35, 278-301.
112. Ishihara, K., Kobayashi, M., Ishimaru, N., and Shinohara, I. (1984) Glucose-induced permeation control of insulin through a complex membrane consisting of immobilized glucose-oxidase and a poly(amine), *Polymer journal* 16, 625-631.
113. Dorski, C. M., Doyle, F. J., and Peppas, N. A. (1997) Preparation and characterization of glucose-sensitive P(MAA-g-EG) hydrogels, *Abstracts of Papers of the American Chemical Society* 213, 172-PMSE.
114. Chu, M. K. L., Gordijo, C. R., Li, J., Abbasi, A. Z., Giacca, A., Plettenburg, O., and Wu, X. Y. (2015) In Vivo Performance and Biocompatibility of a Subcutaneous Implant for Real-Time Glucose-Responsive Insulin Delivery, *Diabetes Technology & Therapeutics* 17, 255-267.
115. Liu, F., Song, S. C., Mix, D., Baudys, M., and Kim, S. W. (1997) Glucose-induced release of glycosylpoly(ethylene glycol) insulin bound to a soluble conjugate of concanavalin A, *Bioconjugate chemistry* 8, 664-672.
116. Nakamae, K., Miyata, T., Jikihara, A., and Hoffman, A. S. (1994) Formation of poly(glucosyloxyethyl methacrylate)-concanavalin-A complex and its glucose sensitivity, *Journal of Biomaterials Science-Polymer Edition* 6, 79-90.
117. Shiino, D., Murata, Y., Kataoka, K., Koyama, Y., Yokoyama, M., Okano, T., and Sakurai, Y. (1994) Preparation and characterization of a glucose-responsive insulin-releasing polymer device, *Biomaterials* 15, 121-128.
118. Zhang, C., Losego, M. D., and Braun, P. V. (2013) Hydrogel-Based Glucose Sensors: Effects of Phenylboronic Acid Chemical Structure on Response, *Chemistry of Materials* 25, 3239-3250.
119. Qiu, Y., and Park, K. (2012) Environment-sensitive hydrogels for drug delivery, *Advanced Drug Delivery Reviews* 64, 49-60.

120. Arnold, F. H., Zheng, W., and Michaels, A. S. (2000) A membrane-moderated, conductimetric sensor for the detection and measurement of specific organic solutes in aqueous solutions, *Journal of Membrane Science* 167, 227-239.
121. Ulijn, R. V., Bibi, N., Jayawarna, V., Thornton, P. D., Todd, S. J., Mart, R. J., Smith, A. M., and Gough, J. E. (2007) Bioresponsive hydrogels, *Materials Today* 10, 40-48.
122. Holtz, J. H., and Asher, S. A. (1997) Polymerized colloidal crystal hydrogel films as intelligent chemical sensing materials, *Nature* 389, 829-832.
123. Alexeev, V. L., Das, S., Finegold, D. N., and Asher, S. A. (2004) Photonic crystal glucose-sensing material for noninvasive monitoring of glucose in tear fluid, *Clinical Chemistry* 50, 2353-2360.
124. Ben-Moshe, M., Alexeev, V. L., and Asher, S. A. (2006) Fast responsive crystalline colloidal array photonic crystal glucose sensors, *Analytical Chemistry* 78, 5149-5157.
125. Zhang, X., Guan, Y., and Zhang, Y. (2012) Ultrathin Hydrogel Films for Rapid Optical Biosensing, *Biomacromolecules* 13, 92-97.
126. Zhao, W., Zhang, H., He, Q., Li, Y., Gu, J., Li, L., Li, H., and Shi, J. (2011) A glucose-responsive controlled release of insulin system based on enzyme multilayers-coated mesoporous silica particles, *Chemical Communications* 47, 9459-9461.
127. Sun, L., Zhang, X., Zheng, C., Wu, Z., and Li, C. (2013) A pH Gated, Glucose-Sensitive Nanoparticle Based on Worm-Like Mesoporous Silica for Controlled Insulin Release, *Journal of Physical Chemistry B* 117, 3852-3860.
128. Farooqi, Z. H., Khan, A., and Siddiq, M. (2011) Temperature-induced volume change and glucose sensitivity of poly (N-isopropylacrylamide)-co-acrylamide-co-(phenylboronic acid) microgels, *Polymer international* 60, 1481-1486.
129. Zou, X., Zhao, X., and Ye, L. (2015) Synthesis of cationic chitosan hydrogel and its controlled glucose-responsive drug release behavior, *Chemical Engineering Journal* 273, 92-100.
130. Jiang, G., Jiang, T., Chen, H., Li, L., Liu, Y., Zhou, H., Feng, Y., and Zhou, J. (2015) Preparation of multi-responsive micelles for controlled release of insulin, *Colloid and Polymer Science* 293, 209-215.
131. Jin, X., Zhang, X., Wu, Z., Teng, D., Zhang, X., Wang, Y., Wang, Z., and Li, C. (2009) Amphiphilic Random Glycopolymer Based on Phenylboronic Acid: Synthesis, Characterization, and Potential as Glucose-Sensitive Matrix, *Biomacromolecules* 10, 1337-1345.
132. Gao, X. Y., Cao, Y., Song, X. F., Zhang, Z., Zhuang, X. L., He, C. L., and Chen, X. S. (2014) Biodegradable, pH-Responsive Carboxymethyl Cellulose/Poly(Acrylic Acid) Hydrogels for Oral Insulin Delivery, *Macromol. Biosci.* 14, 565-575.
133. Marek, S. R., and Peppas, N. A. (2013) Insulin Release Dynamics from Poly(diethylaminoethyl methacrylate) Hydrogel Systems, *Aiche J.* 59, 3578-3585.
134. Kawamura, A., Hata, Y., Miyata, T., and Uragami, T. (2012) Synthesis of glucose-responsive bioconjugated gel particles using surfactant-free emulsion polymerization, *Colloids and Surfaces B-Biointerfaces* 99, 74-81.
135. Ancla, C., Lapeyre, V., Gosse, I., Catargi, B., and Ravaine, V. (2011) Designed Glucose-Responsive Microgels with Selective Shrinking Behavior, *Langmuir* 27, 12693-12701.
136. Wang, D., Liu, T., Yin, J., and Liu, S. Y. (2011) Stimuli-Responsive Fluorescent Poly(N-isopropylacrylamide) Microgels Labeled with Phenylboronic Acid Moieties as Multifunctional Ratiometric Probes for Glucose and Temperatures, *Macromolecules* 44, 2282-2290.
137. Kawamura, T., Masuda, K., Hirai, T., Ohta, Y., Motoyama, M., Takehara, H., Noda, T., Sasagawa, K., Tokuda, T., Okitsu, T., Takeuchi, S., and Ohta, J. (2015) CMOS-based implantable glucose monitoring device with improved performance and reduced invasiveness, *Electronics Letters* 51, 738-739.
138. Mac Kenna, N., Calvert, P., and Morrin, A. (2015) Impedimetric transduction of swelling in pH-responsive hydrogels, *Analyst* 140, 3003-3011.
139. Hu, Y., Jiang, X., Zhang, L., Fan, J., and Wu, W. (2013) Construction of near-infrared photonic crystal glucose-sensing materials for ratiometric sensing of glucose in tears, *Biosensors & Bioelectronics* 48, 94-99.

140. Sorrell, C. D., and Serpe, M. J. (2012) Glucose sensitive poly (N-isopropylacrylamide) microgel based etalons, *Analytical and Bioanalytical Chemistry* 402, 2385-2393.
141. Wu, W., Mitra, N., Yan, E. C. Y., and Zhou, S. (2010) Multifunctional Hybrid Nanogel for Integration of Optical Glucose Sensing and Self-Regulated Insulin Release at Physiological pH, *ACS nano* 4, 4831-4839.
142. Shirakawa, H., Louis, E. J., Macdiarmid, A. G., Chiang, C. K., and Heeger, A. J. (1977) Synthesis of electrically conducting organic polymers- halogen derivatives of polyacetylene, (CH)X, *J. Chem. Soc.-Chem. Commun.*, 578-580.
143. Ates, M. (2013) A review study of (bio)sensor systems based on conducting polymers, *Materials Science and Engineering: C* 33, 1853-1859.
144. Nambiar, S., and Yeow, J. T. W. (2011) Conductive polymer-based sensors for biomedical applications, *Biosensors & Bioelectronics* 26, 1825-1832.
145. Skotheim, T. A. (1997) *Handbook of conducting polymers*, CRC press.
146. Guiseppi-Elie, A. (2010) Electroconductive hydrogels: Synthesis, characterization and biomedical applications, *Biomaterials* 31, 2701-2716.
147. Gerard, M., Chaubey, A., and Malhotra, B. (2002) Application of conducting polymers to biosensors, *Biosensors and Bioelectronics* 17, 345-359.
148. Schuhmann, W. (1995) Electron-transfer pathways in amperometric biosensors. Ferrocene-modified enzymes entrapped in conducting-polymer layers, *Biosensors and Bioelectronics* 10, 181-193.
149. Saleem, M., Yu, H., Wang, L., Khalid, H., Akram, M., Abbasi, N. M., and Huang, J. (2015) Review on synthesis of ferrocene-based redox polymers and derivatives and their application in glucose sensing, *Analytica Chimica Acta* 876, 9-25.
150. Ates, M. (2013) A review study of (bio)sensor systems based on conducting polymers, *Materials Science & Engineering C-Materials for Biological Applications* 33, 1853-1859.
151. Xia, L., Wei, Z., and Wan, M. (2010) Conducting polymer nanostructures and their application in biosensors, *Journal of Colloid and Interface Science* 341, 1-11.
152. Ramanavicius, A., Kausaite, A., and Ramanaviciene, A. (2005) Polypyrrole-coated glucose oxidase nanoparticles for biosensor design, *Sensors and Actuators B-Chemical* 111, 532-539.
153. Dhand, C., Das, M., Datta, M., and Malhotra, B. D. (2011) Recent advances in polyaniline based biosensors, *Biosensors & Bioelectronics* 26, 2811-2821.
154. Welch, M. E., Doublet, T., Bernard, C., Malliaras, G. G., and Ober, C. K. (2015) A Glucose Sensor via Stable Immobilization of the GOx Enzyme on an Organic Transistor Using a Polymer Brush, *Journal of Polymer Science Part a-Polymer Chemistry* 53, 372-377.
155. Nemzer, L. R., and Epstein, A. J. (2010) A polyaniline-based optical biosensing platform using an entrapped oxidoreductase enzyme, *Sensors and Actuators B-Chemical* 150, 376-383.
156. Pringsheim, E., Terpetschnig, E., Piletsky, S. A., and Wolfbeis, O. S. (1999) A polyaniline with near-infrared optical response to saccharides, *Advanced Materials* 11, 865-+.
157. Jin, L., Zhao, Y. J., Liu, X., Wang, Y. L., Ye, B. F., Xie, Z. Y., and Gu, Z. Z. (2012) Dual signal glucose reporter based on inverse opal conducting hydrogel films, *Soft Matter* 8, 4911-4917.
158. Tian, L., Qiu, J., Zhou, Y.-C., and Sun, S.-G. (2010) Application of polypyrrole/GOx film to glucose biosensor based on electrochemical-surface plasmon resonance technique, *Microchimica Acta* 169, 269-275.
159. German, N., Kausaite-Minkstimiene, A., Ramanavicius, A., Semashko, T., Mikhailova, R., and Ramanaviciene, A. (2015) The use of different glucose oxidases for the development of an amperometric reagentless glucose biosensor based on gold nanoparticles covered by polypyrrole, *Electrochim. Acta* 169, 326-333.
160. Moon, B. U., de Vries, M. G., Cordeiro, C. A., Westerink, B. H. C., and Verpoorte, E. (2013) Microdialysis-Coupled Enzymatic Microreactor for in Vivo Glucose Monitoring in Rats, *Analytical Chemistry* 85, 10949-10955.
161. Pesantez, D. E., Castracane, J., and Gadre, A. P. (2012) Continuous glucose microsensor with a nanoscale conducting matrix and redox mediator, *Electrochim. Acta* 65, 196-203.

162. Zane, D., Appetecchi, G. B., Bianchini, C., Passerini, S., and Curulli, A. (2011) An Impedimetric Glucose Biosensor Based on Overoxidized Polypyrrole Thin Film, *Electroanalysis* 23, 1134-1141.
163. Ekanayake, E. M. I. M., Preethichandra, D. M. G., and Kaneto, K. (2007) Polypyrrole nanotube array sensor for enhanced adsorption of glucose oxidase in glucose biosensors, *Biosensors & Bioelectronics* 23, 107-113.
164. Senel, M., Dervisevic, M., and Cevik, E. (2013) A novel amperometric glucose biosensor based on reconstitution of glucose oxidase on thiophene-3-boronic acid polymer layer, *Current Applied Physics* 13, 1199-1204.
165. Zhao, H., Yu, S. H., Yoo, P. J., Park, J. H., and Lee, J. Y. (2013) Glucose Sensing by Glucose Oxidase/PEDOT Thin Film Electrode, *Mol. Cryst. Liquid Cryst.* 580, 22-28.
166. Nien, P. C., Wang, J. Y., Chen, P. Y., Chen, L. C., and Ho, K. C. (2010) Encapsulating benzoquinone and glucose oxidase with a PEDOT film: Application to oxygen-independent glucose sensors and glucose/O-2 biofuel cells, *Bioresour. Technol.* 101, 5480-5486.
167. Kim, Y., Do, J., Kim, J., Yang, S. Y., Malliaras, G. G., Ober, C. K., and Kim, E. (2010) A Glucose Sensor Based on an Organic Electrochemical Transistor Structure Using a Vapor Polymerized Poly(3,4-ethylenedioxythiophene) Layer, *Japanese Journal of Applied Physics* 49.
168. Kakhki, S., Barsan, M. M., Shams, E., and Brett, C. M. A. (2013) New Robust Redox and Conducting Polymer Modified Electrodes for Ascorbate Sensing and Glucose Biosensing, *Electroanalysis* 25, 77-84.
169. Yun, Y. H., Lee, B. K., Choi, J. S., Kim, S., Yoo, B., Kim, Y. S., Park, K., and Cho, Y. W. (2011) A Glucose Sensor Fabricated by Piezoelectric Inkjet Printing of Conducting Polymers and Bienzymes, *Analytical Sciences* 27, 375-379.
170. Fang, L., Liang, B., Yang, G., Hu, Y., Zhu, Q., and Ye, X. (2014) Study of glucose biosensor lifetime improvement in 37 degrees C serum based on PANI enzyme immobilization and PLGA biodegradable membrane, *Biosensors & Bioelectronics* 56, 91-96.
171. Ramya, R., and Sangaranarayanan, M. V. (2013) Electrochemical sensing of glucose using polyaniline nanofiber dendrites-amperometric and impedimetric analysis, *Journal of Applied Polymer Science* 129, 735-747.
172. Pahurkar, V. G., Tamgadge, Y. S., Gambhire, A. B., and Muley, G. G. (2015) Glucose oxidase immobilized PANI cladding modified fiber optic intrinsic biosensor for detection of glucose, *Sensors and Actuators B-Chemical* 210, 362-368.
173. Kausaite-Minkstimiene, A., Mazeiko, V., Ramanaviciene, A., and Ramanavicius, A. (2010) Enzymatically synthesized polyaniline layer for extension of linear detection region of amperometric glucose biosensor, *Biosensors & Bioelectronics* 26, 790-797.
174. Horng, Y.-Y., Hsu, Y.-K., Ganguly, A., Chen, C.-C., Chen, L.-C., and Chen, K.-H. (2009) Direct-growth of polyaniline nanowires for enzyme-immobilization and glucose detection, *Electrochemistry Communications* 11, 850-853.
175. Thakur, B., Amarnath, C. A., and Sawant, S. N. (2014) Pectin coated polyaniline nanoparticles for an amperometric glucose biosensor, *RSC Adv.* 4, 40917-40923.
176. Pan, L., Yu, G., Zhai, D., Lee, H. R., Zhao, W., Liu, N., Wang, H., Tee, B. C. K., Shi, Y., Cui, Y., and Bao, Z. (2012) Hierarchical nanostructured conducting polymer hydrogel with high electrochemical activity, *Proceedings of the National Academy of Sciences of the United States of America* 109, 9287-9292.
177. Inzelt, G. (2012) *Conducting polymers: a new era in electrochemistry*, Springer Science & Business Media.
178. Khalid, H., Yu, H. J., Wang, L., Amer, W. A., Akram, M., Abbasi, N. M., ul-Abdin, Z., and Saleem, M. (2014) Synthesis of ferrocene-based polythiophenes and their applications, *Polymer Chemistry* 5, 6879-6892.
179. Senel, M. (2011) Construction of reagentless glucose biosensor based on ferrocene conjugated polypyrrole, *Synthetic Metals* 161, 1861-1868.

180. Saleem, M., Yu, H., Wang, L., Zain ul, A., Khalid, H., Akram, M., Abbasi, N. M., and Huang, J. (2015) Review on synthesis of ferrocene-based redox polymers and derivatives and their application in glucose sensing, *Analytica Chimica Acta* 876, 9-25.
181. Calvo, E. J., Etchenique, R., Danilowicz, C., and Diaz, L. (1996) Electrical communication between electrodes and enzymes mediated by redox hydrogels, *Analytical Chemistry* 68, 4186-4193.
182. Heller, A. (2006) Electron-conducting redox hydrogels: design, characteristics and synthesis, *Curr. Opin. Chem. Biol.* 10, 664-672.
183. Heller, A. (1992) Electrical connection of enzyme redox centers to electrodes, *The Journal of Physical Chemistry* 96, 3579-3587.
184. Marcus, R. A., and Sutin, N. (1985) Electron transfers in chemistry and biology, *Biochimica Et Biophysica Acta* 811, 265-322.
185. Forster, R. J., Kelly, A. J., Vos, J. G., and Lyons, M. E. G. (1989) The effect of supporting electrolyte and temperature on the rate of charge propagation through thin-films of $Os(BiPy)_2PVP_{10}Cl$ Cl coated on stationary electrodes, *Journal of Electroanalytical Chemistry* 270, 365-379.
186. Forster, R. J., and Vos, J. G. (1991) Redox site loading, electrolyte concentration and temperature effects on charge transport and electrode kinetics of electrodes modified with osmium containing poly(4-vinylpyridine) films in sulfuric acid, *Journal of Electroanalytical Chemistry* 314, 135-152.
187. Forster, R. J., and Vos, J. G. (1990) Synthesis, characterization and properties of a series of osmium-containing and ruthenium-containing metallopolymers, *Macromolecules* 23, 4372-4377.
188. Binyamin, G., and Heller, A. (1999) Stabilization of wired glucose oxidase anodes rotating at 1000 rpm at 37 degrees C, *Journal of the Electrochemical Society* 146, 2965-2967.
189. Mano, N., Mao, F., and Heller, A. (2005) On the parameters affecting the characteristics of the "wired" glucose oxidase anode, *Journal of Electroanalytical Chemistry* 574, 347-357.
190. Mao, F., Mano, N., and Heller, A. (2003) Long tethers binding redox centers to polymer backbones enhance electron transport in enzyme "wiring" hydrogels, *Journal of the American Chemical Society* 125, 4951-4957.
191. Kenausis, G., Taylor, C., Katakis, I., and Heller, A. (1996) 'Wiring' of glucose oxidase and lactate oxidase within a hydrogel made with poly(vinyl pyridine) complexed with Os(4,4'-dimehtoxy-2,2'-bipyridine)(2)Cl (+/2+), *J. Chem. Soc.-Faraday Trans.* 92, 4131-4136.
192. Jernigan, J. C., and Murray, R. W. (1987) Electron self-exchanges in an osmium polypyridine redox polymer in the absence of liquid solvents by solid-state voltammetry, *Journal of the American Chemical Society* 109, 1738-1745.
193. Kim, H. H., Mano, N., Zhang, X. C., and Heller, A. (2003) A miniature membrane-less biofuel cell operating under physiological conditions at 0.5 V, *Journal of the Electrochemical Society* 150, A209-A213.
194. Barriere, F., Kavanagh, P., and Leech, D. (2006) A laccase-glucose oxidase biofuel cell prototype operating in a physiological buffer, *Electrochim. Acta* 51, 5187-5192.
195. Bunte, C., Prucker, O., Konig, T., and Ruhe, J. (2010) Enzyme Containing Redox Polymer Networks for Biosensors or Biofuel Cells: A Photochemical Approach, *Langmuir* 26, 6019-6027.
196. Bu, H. Z., English, A. M., and Mikkelsen, S. R. (1997) Charge transport in ferrocene-containing polyacrylamide-based redox gels, *Journal of Physical Chemistry B* 101, 9593-9599.
197. Sirkar, K., and Pishko, M. V. (1998) Amperometric biosensors based on oxidoreductases immobilized in photopolymerized poly(ethylene glycol) redox polymer hydrogels, *Analytical Chemistry* 70, 2888-2894.
198. Heller, A., and Feldman, B. (2010) Electrochemistry in Diabetes Management, *Accounts of Chemical Research* 43, 963-973.

199. Rajagopalan, R., Aoki, A., and Heller, A. (1996) Effect of quaternization of the glucose oxidase ''wiring'' redox polymer on the maximum current densities of glucose electrodes, *J. Phys. Chem.* 100, 3719-3727.
200. Calvo, E. J., and Wolosiuk, A. (2005) Wiring enzymes in nanostructures built with electrostatically self-assembled thin films, *Chemphyschem* 6, 43-47.
201. Mitala, J. J., and Michael, A. C. (2006) Improving the performance of electrochemical microsensors based on enzymes entrapped in a redox hydrogel, *Analytica Chimica Acta* 556, 326-332.
202. Wang, J.-Y., Chen, L.-C., and Ho, K.-C. (2013) Synthesis of Redox Polymer Nanobeads and Nanocomposites for Glucose Biosensors, *Acs Applied Materials & Interfaces* 5, 7852-7861.
203. Waller, A. M., Hampton, A. N. S., and Compton, R. G. (1989) An alternating current impedance study of polypyrrole/poly (vinyl chloride) composites, *Journal of the Chemical Society, Faraday Transactions 1: Physical Chemistry in Condensed Phases* 85, 773-781.
204. Chen, G. Z., Shaffer, M. S. P., Coleby, D., Dixon, G., Zhou, W. Z., Fray, D. J., and Windle, A. H. (2000) Carbon nanotube and polypyrrole composites: Coating and doping, *Advanced Materials* 12, 522-+.
205. Kong, Y., Sha, Y., Tao, Y., Qin, Y., Xue, H., and Lu, M. (2014) Non-Enzymatic Glucose Sensor Based on Nickel Hexacyanoferrate/Polyaniline Hybrids on Graphene Prepared by a One-Step Process, *Journal of the Electrochemical Society* 161, B269-B274.
206. Hosseini, H., Rezaei, S. J. T., Rahmani, P., Sharifi, R., Nabid, M. R., and Bagheri, A. (2014) Nonenzymatic glucose and hydrogen peroxide sensors based on catalytic properties of palladium nanoparticles/poly(3,4-ethylenedioxythiophene) nanofibers, *Sensors and Actuators B-Chemical* 195, 85-91.
207. Pandey, P., Singh, S. P., Arya, S. K., Gupta, V., Datta, M., Singh, S., and Malhotra, B. D. (2007) Application of thiolated gold nanoparticles for the enhancement of glucose oxidase activity, *Langmuir* 23, 3333-3337.
208. Daniel, M. C., and Astruc, D. (2004) Gold nanoparticles: Assembly, supramolecular chemistry, quantum-size-related properties, and applications toward biology, catalysis, and nanotechnology, *Chemical reviews* 104, 293-346.
209. Iijima, S. (1991) Helical microtubules of graphitic carbon, *Nature* 354, 56-58.
210. Tsai, Y. C., Li, S. C., and Liao, S. W. (2006) Electrodeposition of polypyrrole-multiwalled carbon nanotube-glucose oxidase nanobiocomposite film for the detection of glucose, *Biosensors & Bioelectronics* 22, 495-500.
211. Alwarappan, S., Liu, C., Kumar, A., and Li, C.-Z. (2010) Enzyme-Doped Graphene Nanosheets for Enhanced Glucose Biosensing, *Journal of Physical Chemistry C* 114, 12920-12924.
212. Lei, W., Si, W., Xu, Y., Gu, Z., and Hao, Q. (2014) Conducting polymer composites with graphene for use in chemical sensors and biosensors, *Microchimica Acta* 181, 707-722.
213. Brahim, S., Narinesingh, D., and Guiseppi-Elie, A. (2002) Polypyrrole-hydrogel composites for the construction of clinically important biosensors, *Biosensors and Bioelectronics* 17, 53-59.
214. Binyamin, G., Cole, J., and Heller, A. (2000) Mechanical and electrochemical characteristics of composites of wired glucose oxidase and hydrophilic graphite, *Journal of the Electrochemical Society* 147, 2780-2783.
215. Joshi, P. P., Merchant, S. A., Wang, Y. D., and Schmidtke, D. W. (2005) Amperometric biosensors based on redox polymer-carbon nanotube-enzyme composites, *Analytical Chemistry* 77, 3183-3188.
216. Shahnavaz, Z., Lorestani, F., Meng, W. P., and Alias, Y. (2015) Core-shell-CuFe2O4/PPy nanocomposite enzyme-free sensor for detection of glucose, *Journal of Solid State Electrochemistry* 19, 1223-1233.
217. Yang, Z., Zhang, C., Zhang, J., and Bai, W. (2014) Potentiometric glucose biosensor based on core-shell Fe3O4-enzyme- polypyrrole nanoparticles, *Biosensors & Bioelectronics* 51, 268-273.

218. Park, J. W., Lee, C., and Jang, J. (2015) High-performance field-effect transistor-type glucose biosensor based on nanohybrids of carboxylated polypyrrole nanotube wrapped graphene sheet transducer, *Sensors and Actuators B-Chemical* 208, 532-537.
219. Lin, E.-R., Chiu, C.-J., and Tsai, Y.-C. (2014) One-Step Electrochemical Synthesis of Polypyrrole-Graphene-Glucose Oxidase Nanobiocomposite for Glucose Sensing, *Journal of the Electrochemical Society* 161, B243-B247.
220. Xue, K. W., Zhou, S. H., Shi, H. Y., Feng, X., Xin, H., and Song, W. B. (2014) A novel amperometric glucose biosensor based on ternary gold nanoparticles/polypyrrole/reduced graphene oxide nanocomposite, *Sensors and Actuators B-Chemical* 203, 412-416.
221. Li, C., Su, Y., Lv, X., Xia, H., Shi, H., Yang, X., Zhang, J., and Wang, Y. (2012) Controllable anchoring of gold nanoparticles to polypyrrole nanofibers by hydrogen bonding and their application in nonenzymatic glucose sensors, *Biosensors & Bioelectronics* 38, 402-406.
222. Goornavar, V., Jeffers, R., Biradar, S., and Ramesh, G. T. (2014) Utilization of highly purified single wall carbon nanotubes dispersed in polymer thin films for an improved performance of an electrochemical glucose sensor, *Materials Science & Engineering C-Materials for Biological Applications* 40, 299-307.
223. Malitesta, C., Guascito, M. R., Mazzotta, E., Siciliano, T., and Tepore, A. (2013) Copper nanoparticles/poly-3-methylthiophene composite: Synthesis, characterization and catalytic application to enzyme-less glucose detecting, *Sensors and Actuators B-Chemical* 184, 70-77.
224. Wisitsoraat, A., Pakapongpan, S., Sriprachuabwong, C., Phokharatkul, D., Sritongkham, P., Lomas, T., and Tuantranont, A. (2013) Graphene-PEDOT:PSS on screen printed carbon electrode for enzymatic biosensing, *Journal of Electroanalytical Chemistry* 704, 208-213.
225. Dash, S., and Munichandraiah, N. (2013) Non-Enzymatic Electroanalysis of Glucose on Electrodeposited Au-PEDOT Dendrites, *Ecs Electrochemistry Letters* 2, B17-B20.
226. Lin, K.-C., Tsai, T.-H., and Chen, S.-M. (2010) Performing enzyme-free H2O2 biosensor and simultaneous determination for AA, DA, and UA by MWCNT-PEDOT film, *Biosensors & Bioelectronics* 26, 608-614.
227. Liu, F.-J. (2009) One-Step Synthesis of MnO(2) Particles Distributed Polyaniline-Poly(styrene-sulfonic acid), *Synthetic Metals* 159, 1896-1899.
228. Qiu, J.-D., Shi, L., Liang, R.-P., Wang, G.-C., and Xia, X.-H. (2012) Controllable Deposition of a Platinum Nanoparticle Ensemble on a Polyaniline/Graphene Hybrid as a Novel Electrode Material for Electrochemical Sensing, *Chemistry-a European Journal* 18, 7950-7959.
229. Poorahong, S., Thammakhet, C., Thavarungkul, P., and Kanatharana, P. (2012) Cauliflower polyaniline/multiwalled carbon nanotube electrode and its applications to hydrogen peroxide and glucose detection*, *Pure and Applied Chemistry* 84, 2055-2063.
230. Mazeiko, V., Kausaite-Minkstimiene, A., Ramanaviciene, A., Balevicius, Z., and Ramanavicius, A. (2013) Gold nanoparticle and conducting polymer-polyaniline-based nanocomposites for glucose biosensor design, *Sensors and Actuators B-Chemical* 189, 187-193.
231. Chowdhury, A. D., Gangopadhyay, R., and De, A. (2014) Highly sensitive electrochemical biosensor for glucose, DNA and protein using gold-polyaniline nanocomposites as a common matrix, *Sensors and Actuators B-Chemical* 190, 348-356.
232. Yan, W., Feng, X., Chen, X., Hou, W., and Zhu, J.-J. (2008) A super highly sensitive glucose biosensor based on Au nanoparticles-AgCl@polyaniline hybrid material, *Biosensors & Bioelectronics* 23, 925-931.
233. Prathap, M. U. A., Pandiyan, T., and Srivastava, R. (2013) Cu nanoparticles supported mesoporous polyaniline and its applications towards non-enzymatic sensing of glucose and electrocatalytic oxidation of methanol, *Journal of Polymer Research* 20.
234. Zhai, D., Liu, B., Shi, Y., Pan, L., Wang, Y., Li, W., Zhang, R., and Yu, G. (2013) Highly sensitive glucose sensor based on Pt nanoparticle/polyaniline hydrogel heterostructures, *ACS nano* 7, 3540-3546.

235. Wu, J., and Yin, L. (2011) Platinum Nanoparticle Modified Polyaniline-Functionalized Boron Nitride Nanotubes for Amperometric Glucose Enzyme Biosensor, *Acs Applied Materials & Interfaces* 3, 4354-4362.
236. Tang, W., Li, L., and Zeng, X. (2015) A glucose biosensor based on the synergistic action of nanometer-sized TiO2 and polyaniline, *Talanta* 131, 417-423.
237. Anderson, J. M., Rodriguez, A., and Chang, D. T. (2008) Foreign body reaction to biomaterials, *Seminars in Immunology* 20, 86-100.
238. Gerritsen, M., Jansen, J. A., Kros, A., Nolte, R. J. M., and Lutterman, J. A. (1998) Performance of subcutaneously implanted glucose sensors: A review, *Journal of Investigative Surgery* 11, 163-174.
239. Vaddiraju, S. S., Singh, H., Burgess, D. J., Jain, F. C., and Papadimitrakopoulos, F. (2009) Enhanced Glucose Sensor Linearity Using Poly (Vinyl Alcohol) Hydrogels, *Journal of diabetes science and technology (Online)* 3, 863.
240. Vallejo-Heligon, S. G., Klitzman, B., and Reichert, W. M. (2014) Characterization of porous, dexamethasone-releasing polyurethane coatings for glucose sensors, *Acta Biomaterialia* 10, 4629-4638.
241. Ward, W. K. (2008) A review of the foreign-body response to subcutaneously-implanted devices: the role of macrophages and cytokines in biofouling and fibrosis, *Journal of Diabetes Science and Technology* 2, 768-777.
242. Patil, S. D., Papadimitrakopoulos, F., and Burgess, D. J. (2004) Dexamethasone-loaded poly (lactic-co-glycolic) acid microspheres/poly (vinyl alcohol) hydrogel composite coatings for inflammation control, *Diabetes Technology & Therapeutics* 6, 887-897.
243. Bhardwaj, U., Sura, R., Papadimitrakopoulos, F., and Burgess, D. J. (2010) PLGA/PVA hydrogel composites for long-term inflammation control following sc implantation, *International Journal of Pharmaceutics* 384, 78-86.
244. Wang, Y., Papadimitrakopoulos, F., and Burgess, D. J. (2013) Polymeric "smart" coatings to prevent foreign body response to implantable biosensors, *Journal of controlled release* 169, 341-347.
245. Ju, Y. M., Yu, B. Z., Koob, T. J., Moussy, Y., and Moussy, F. (2008) A novel porous collagen scaffold around an implantable biosensor for improving biocompatibility. I. In vitro/in vivo stability of the scaffold and in vitro sensitivity of the glucose sensor with scaffold, *Journal of Biomedical Materials Research Part A* 87A, 136-146.
246. Ju, Y. M., Yu, B., West, L., Moussy, Y., and Moussy, F. (2010) A dexamethasone-loaded PLGA microspheres/collagen scaffold composite for implantable glucose sensors, *Journal of Biomedical Materials Research Part A* 93, 200-210.
247. Gifford, R., Batchelor, M. M., Lee, Y., Gokulrangan, G., Meyerhoff, M. E., and Wilson, G. S. (2005) Mediation ofin vivo glucose sensor inflammatory response via nitric oxide release, *Journal of Biomedical Materials Research Part A* 75, 755-766.
248. Koh, A., Riccio, D. A., Sun, B., Carpenter, A. W., Nichols, S. P., and Schoenfisch, M. H. (2011) Fabrication of nitric oxide-releasing polyurethane glucose sensor membranes, *Biosensors and Bioelectronics* 28, 17-24.
249. Nichols, S. P., Koh, A., Brown, N. L., Rose, M. B., Sun, B., Slomberg, D. L., Riccio, D. A., Klitzman, B., and Schoenfisch, M. H. (2012) The effect of nitric oxide surface flux on the foreign body response to subcutaneous implants, *Biomaterials* 33, 6305-6312.
250. Gifford, R., Kehoe, J. J., Barnes, S. L., Kornilayev, B. A., Alterman, M. A., and Wilson, G. S. (2006) Protein interactions with subcutaneously implanted biosensors, *Biomaterials* 27, 2587-2598.
251. Wisniewski, N., and Reichert, M. (2000) Methods for reducing biosensor membrane biofouling, *Colloids and Surfaces B-Biointerfaces* 18, 197-219.

252. Gordijo, C. R., Koulajian, K., Shuhendler, A. J., Bonifacio, L. D., Huang, H. Y., Chiang, S., Ozin, G. A., Giacca, A., and Wu, X. Y. (2011) Nanotechnology-Enabled Closed Loop Insulin Delivery Device: In Vitro and In Vivo Evaluation of Glucose-Regulated Insulin Release for Diabetes Control, *Advanced Functional Materials* 21, 73-82.
253. Quinn, C. A. P., Connor, R. E., and Heller, A. (1997) Biocompatible, glucose-permeable hydrogel for in situ coating of implantable biosensors, *Biomaterials* 18, 1665-1670.
254. Heo, Y. J., Shibata, H., Okitsu, T., Kawanishi, T., and Takeuchi, S. (2011) Long-term in vivo glucose monitoring using fluorescent hydrogel fibers, *Proceedings of the National Academy of Sciences of the United States of America* 108, 13399-13403.
255. Norton, L. W., Yuan, F., and Reichert, W. M. (2007) Glucose recovery with bare and hydrogel-coated microdialysis probes: Experiment and simulation of temporal effects, *Analytical Chemistry* 79, 445-452.
256. Yu, B., Wang, C., Ju, Y. M., West, L., Harmon, J., Moussy, Y., and Moussy, F. (2008) Use of hydrogel coating to improve the performance of implanted glucose sensors, *Biosensors & Bioelectronics* 23, 1278-1284.
257. Yoshikawa, C., Hattori, S., Honda, T., Huang, C.-F., and Kobayashi, H. (2012) Non-biofouling property of well-defined concentrated poly (2-hydroxyethyl methacrylate) brush, *Materials letters* 83, 140-143.
258. Yang, Y., Zhang, S., Kingston, M., Jones, G., Wright, G., and Spencer, S. (2000) Glucose sensor with improved haemocompatibilty, *Biosensors and Bioelectronics* 15, 221-227.
259. Mang, A., Pill, J., Gretz, N., Kränzlin, B., Buck, H., Schoemaker, M., and Petrich, W. (2005) Biocompatibility of an electrochemical sensor for continuous glucose monitoring in subcutaneous tissue, *Diabetes Technology & Therapeutics* 7, 163-173.
260. Morais, J. M., Papadimitrakopoulos, F., and Burgess, D. J. (2010) Biomaterials/tissue interactions: possible solutions to overcome foreign body response, *The AAPS journal* 12, 188-196.
261. Novak, M. T., Yuan, F., and Reichert, W. M. (2010) Modeling the relative impact of capsular tissue effects on implanted glucose sensor time lag and signal attenuation, *Analytical and Bioanalytical Chemistry* 398, 1695-1705.
262. Ward, W. K., Ward, E., Slobodzian, K., Tiekotter, M., and Wood. (2002) The effect of microgeometry, implant thickness and polyurethane chemistry on the foreign body response to subcutaneous implants, *Biomaterials* 23, 4185-4192.
263. Updike, S. J., Shults, M. C., Gilligan, B. J., and Rhodes, R. K. (2000) A subcutaneous glucose sensor with improved longevity, dynamic range, and stability of calibration, *Diabetes Care* 23, 208-214.
264. Koschwanez, H. E., Reichert, W. M., and Klitzman, B. (2010) Intravital microscopy evaluation of angiogenesis and its effects on glucose sensor performance, *Journal of Biomedical Materials Research Part A* 93A, 1348-1357.
265. Ward, W. K., Quinn, M. J., Wood, M. D., Tiekotter, K. L., Pidikiti, S., and Gallagher, J. A. (2003) Vascularizing the tissue surrounding a model biosensor: how localized is the effect of a subcutaneous infusion of vascular endothelial growth factor (VEGF)?, *Biosensors & Bioelectronics* 19, 155-163.
266. Norton, L. W., Koschwanez, H. E., Wisniewski, N. A., Klitzman, B., and Reichert, W. M. (2007) Vascular endothelial growth factor and dexamethasone release from nonfouling sensor coatings affect the foreign body response, *Journal of Biomedical Materials Research Part A* 81A, 858-869.
267. Patil, S. D., Papadmitrakopoulos, F., and Burgess, D. J. (2007) Concurrent delivery of dexamethasone and VEGF for localized inflammation control and angiogenesis, *Journal of controlled release* 117, 68-79.

268. Ju, Y. M., Yu, B., West, L., Moussy, Y., and Moussy, F. (2010) A novel porous collagen scaffold around an implantable biosensor for improving biocompatibility. II. Long-term in vitro/in vivo sensitivity characteristics of sensors with NDGA- or GA-crosslinked collagen scaffolds, *Journal of Biomedical Materials Research Part A* 92A, 650-658.

Chapter 2

Synthesis and characterization of UV-curable MMA-based packaging materials

Parts of this chapter have been published in:

Van De Walle, E., Youth Views on Sustainability: PMMA, from Plexiglass Window to a Packaging for an Implantable Glucose Sensor. *Chemistry International* **2015,** *37* (3), 16-18.

Van de Walle, E.; Van Nieuwenhove, I.; Vanderleyden, E.; Declercq, H.; Gellynck, K.; Schaubroeck, D.; Ottevaere, H.; Thienpont, H.; De Vos, W. H.; Cornelissen, M.; Van Vlierberghe, S.; Dubruel, P., Polydopamine-Gelatin as Universal Cell-Interactive Coating for Methacrylate-Based Medical Device Packaging Materials: When Surface Chemistry Overrules Substrate Bulk Properties. *Biomacromolecules* **2016,** *17* (1), 56-68.

2.1. Introduction

In this chapter, focus is laid on the development of different methacrylate-based materials which should serve as packaging for an optical glucose sensor. To this end, poly(methyl methacrylate) (PMMA) was selected as a starting material, since it has already proven its utility for biomedical applications in the past. As a consequence, the first part of this chapter overviews the use and importance of PMMA, including its discovery, its applications, its production processes and its bulk modifications. In this way, the position of PMMA in the biomedical society will be demonstrated.

Since the ultimate aim implies a subcutaneous implantation, the applied material should exhibit specific mechanical properties in addition to its biocompatibility (to be discussed in chapter 4). Intuitively, from the patient's viewpoint, a certain softness and material flexibility would be required to assure the patient's comfort after sensor implantation. On the other hand, in order to enable successful glucose measurements, all components (a.o. source, detector, etc.) should remain in place during the molding procedure as well as after implantation. As a consequence, apart from softness and flexibility, the material should also exhibit a certain rigidity. To this end, the chapter focuses on the development of a series of MMA-based copolymers and networks in an attempt to fine-tune the mechanical properties of PMMA for the envisaged application. Due to the lack of literature reports that determine a defined range of bulk properties an implantable packaging material should fulfill, we aimed in the current work to gain more insight into this topic by screening a range of polymers with divergent bulk properties. To develop such a range, two strategies were pursued, including (1) the integration of hydrophilic, protein-repellant poly(ethylene glycol) (PEG) in the polymer structure (see § 2.4) and (2) the evaluation of long-tailed hydrophobic methacrylates (see § 2.5).
Since hydrophilic compounds are applied in the first strategy, the swelling behavior of the developed materials was also evaluated. Indeed, high swelling percentages might result in inferior adhesion of the polymer to the sensor surface and corrosion (see § 2.6.2) of the sensor compounds because of the influx of interstitial fluid. Furthermore, this influx might cause leaching of sensor electronic's ions which might result in the occurrence of adverse body reactions such as inflammation. As a result, polymer swelling should be minimized. Apart from the above-mentioned physical properties, the optical properties were also assessed. Transparency of the different materials in the near IR-region (NIR) of the light spectrum is a key property, as this region is used to perform glucose measurements (see § 2.6.1).
In a last part of this chapter, a preliminary evaluation of the cell interactive properties is presented (see § 2.6.3). Since implantation is targeted, minimal cell toxicities should be pursued.

2.2. PMMA as biomedical material

2.2.1. PMMA: a short history

One of the most widely studied vinyl-based polymers includes poly(methyl methacrylate) (PMMA), an amorphous material, which is known to be very hard and brittle. When PMMA was discovered (1877; patented in 1933), the use of the homopolymer was centralized and during World War II (WWII), it functioned as aircraft windows, submarine periscopes, gun turrets for airplanes, etc. In the medical world, it became very popular as hard tissue replacement because of its biocompatibility and its ability to fulfill load bearing functions [1]. Actually, its biocompatibility was discovered by the English ophthalmologist Harold Ridley. He examined WWII pilots that suffered from PMMA ocular splinters stemming from the windows of crashed airplanes. He observed that almost no rejection occurred and that healing was initiated. As a consequence, in 1949, Dr. Ridley implanted the first intra-ocular PMMA lens (IOL) in an attempt to cure cataract [2-3]. In the meantime, in 1948, Kevin Tuohey produced the first hard PMMA contact lenses, which were a replacement of the glass scleral contact lenses already used in that time [4-6] (see figure 2.1).
Apart from ophthalmology, PMMA also plays a crucial role in the world of orthopedics [7]. In 1960, Sir John Charnley developed the first total hip implant, wherein PMMA functioned as bone cement [8]. This cement interfaces the steel/PE prostheses and the human bone to minimize adverse body reactions [9] (see figure 2.1).

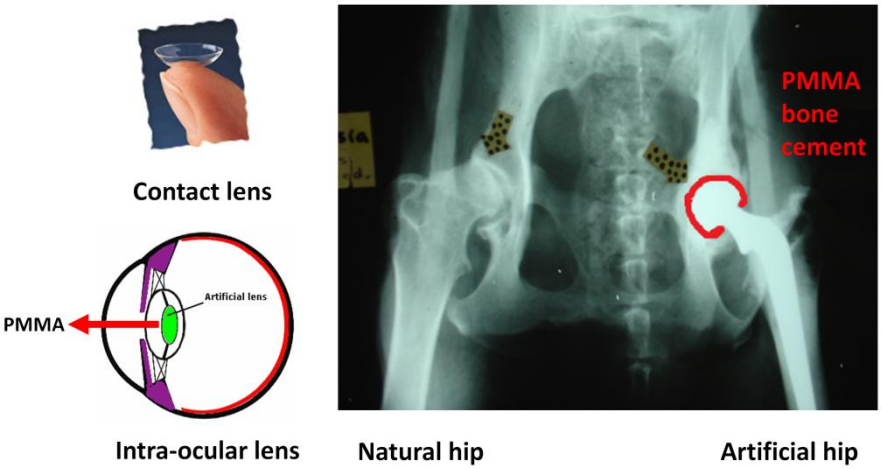

Figure 2.1: Applications of PMMA as intra-ocular lens, contact lens and bone cement.

For dentistry applications, since its early years, PMMA has also proven its utility as dental adhesive and resin [10]. More recently, micro- and nano- PMMA spheres became popular as a component in vaccine formulations, as drug carrier but also as fillers for cosmetic surgery [11-13]. Logically, in all of these fields, certain limitations were noted and continuous modifications had to be performed to produce improved materials. As a result, composite materials as well as copolymers have been developed starting from PMMA (see § 2.2.3). As an example, table 2.1 overviews some recent applications of PMMA, discussed in literature.

Table 2.1: Overview of recent applications of PMMA.

Application	References
Dentistry-related applications	*14-16*
Prevention of infection / biofilm formation on implants	*17-19*
Orthopedic applications	*20-25*
Ophtalmology	*19, 26*
Particulates for drug delivery	*11, 27-29*
Membrane filters	*30*
Microfluidics	*31-34*
Lenses (photovoltaics)	*35-37*
Batteries	*38-40*
Sensors	*41-42*

2.2.2. PMMA: production processes

Depending on the application, different polymerization processes can be applied to synthesize PMMA or MMA-based materials. Radical polymerizations are the ones mostly described in literature. These cover conventional radical polymerizations, which can be performed in solution or bulk, with the help of a thermal radical initiator such as benzoylperoxide (BPO) and Azobisisobutyronitril (AIBN) or a UV-sensitive radical initiator such as Irgacure 2959.

In case well-defined molecular weights (Mw) and Mw distributions are a prerequisite, controlled radical polymerizations can also be performed, because these processes are capable to retard chain transfer and termination. In general, an initiator, catalyst and sometimes a chain-end stabilizer will be required [43]. In order to produce well-controlled PMMA, research focuses on the evaluation of different initiating systems (i.e. initiator and catalyst) such as the use of alkylhalides (e.g. CCl_4) in the presence of ruthenium-based (e.g. $RuCl_2(PPh_3)_3$) [44-45], nickel based [46-48] copper-based [49-50] or aluminium-based complexes [51] or the use of AIBN and $FeCl_3$ in the presence of triphenylphosphine [50, 52]. The use of functional initiators permits the introduction of specific end-group functionalities into the polymer structure [48]. Furthermore, this method allows for the production of uniform and more complex polymer architectures such as MMA-based block copolymers [53-54], star shaped PMMA [55-56] and uniform stereoblock PMMA [51].

A special case of living radical polymerization (LRP) includes the surface initiated LRP. Herein, the initiator is immobilized on a surface and the polymer chains are subsequently grown in a controlled way from this surface. As a result, PMMA brushes can be created on top of different materials such as on gold films [57-58], gold nano-particles [59-60], silicon wafers [61] and silica (nano)particles [62-64]. As an example, these brushes may serve as etching barriers [61].

Apart from bulk PMMA and PMMA brushes, PMMA particles can also be produced and will mostly function as particulate carriers for drug delivery [13]. The most applied polymerization

technique in this field would be emulsion polymerization and the different variants are excellently reviewed by Bettencourt et al.[11]
Next to radical polymerizations, also anionic polymerization reactions with MMA have been reported in literature [65-66], as well as the use of click chemistry [67].
In this work, a radical UV-induced polymerization process was selected as the preferred polymer production process, as explained in paragraph 2.3.

2.2.3. PMMA-based composites and copolymers

Over the years, researchers have always tried to adjust the bulk properties of existing materials. In case of polymer materials, two main strategies co-exist:

1) Production of composites: inorganic fillers are used to fine-tune the polymer properties
2) Copolymerization strategy: the properties of different homopolymers are combined by reacting their respective building blocks.

In case of PMMA-based composites, a lot of studies have been conducted in an attempt to improve its physical properties such as its tensile strength, its heat resistance, gas permeability and even its conductivity, all with a minimum loss in transparency [68]. As a result, nanocomposites gained a lot of interest. Examples include the introduction of graphite-based compounds [69-71], (multi-walled) carbon nanotubes via in situ bulk polymerization [72-77], sulfides such as ZnS [78-79] and MoS_2 [80], clays [81-84], alumina [85] and silicium-based compounds [68, 86-87]. In the medical world, a typical example could be given by PMMA/hydroxyapatite (HA) composites. Herein, HA, a major inorganic component of bone, stimulates the adhesion of PMMA cement to bone as well as the subsequent bone growth [88-90]. Furthermore, the introduction of silver nanoparticles was studied to enhance the antibacterial properties of PMMA [91].
Apart from composites, many researchers apply the principle of copolymerization to alter material properties. A lot of MMA-based materials have already been investigated and examples of comonomers include methacrylic acid [92], styrene [93] and aldehyde-functionalized poly(ethylene oxide) (PEO) [94]. In the last case, copolymerization was facilitated by amination of PMMA.
Also in the medical world, this strategy has been applied in an attempt to adjust the material properties of PMMA. In the context of contact lenses, MMA has been copolymerized with N-vinylpyrrolidinone to create soft daily contact lenses which are characterized by a much higher oxygen permeability compared to the original hard ones [4]. For IOL's, sulfonate and carboxylate bearing monomers were used in an attempt to modulate fibroblast proliferation [95-96]. Furthermore, to apply PMMA as a stent coating, it should elicit sufficient flexibility and elasticity. In this respect, the copolymerization of MMA and hydroxyethyl methacrylate (HEMA) has already been studied [97].
It should be noted that the use of polymer blends could include a third way of altering the mechanical and physical properties of a material. In case of PMMA, examples of this strategy

include the combination of PMMA with polyaniline [98] and polystyrene [99]. Furthermore, the creation of interpenetrating networks could also be mentioned, such as with isocyanate-functionalized poly(ethylene glycol) [100].

2.3. UV-induced polymerization for the production of methacrylate-based polymers

As mentioned in §2.2.2, several techniques can be used to polymerize methacrylate-based compounds. Herein, all polymers were produced via a radical UV-induced bulk polymerization reaction of which the set-up is displayed in figure 2.2. The monomer/initiator solution is injected in a pre-shaped silicon spacer, which is placed between two teflon foil covered glass plates. The release foil prevents the monomers to interact with the glass via hydrogen bonds and ensures a straightforward release of the produced polymers.

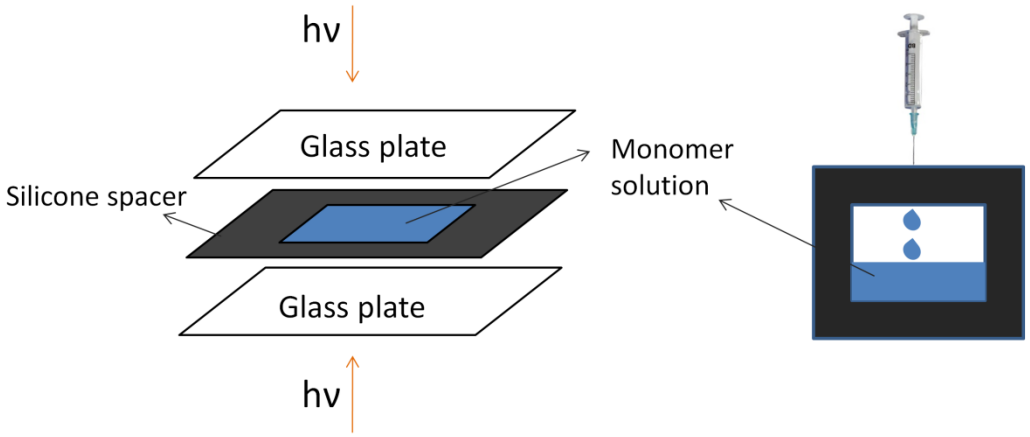

Figure 2.2: Schematic representation of the applied UV-polymerization setup. The teflon sheets covering the glass plates are not shown.

The UV-induced film casting technique is selected because of several key advantages [101]:

- low cost approach
- low energy consumption
- process feasible at ambient temperature
- solvent-free formulations are used thus excluding a drying step
- favourable reaction kinetics (< 90 minutes reaction, compared to 24 hours in case of solution polymerization)
- high yields are obtained, thus excluding purification procedures

Furthermore, since the materials should embed optical compounds, it is also desirable to immediately mold the implant in the required shape, given that an appropriate mold is developed (see chapter 5).
The main disadvantage of the bulk polymerization technique is the inferior control over the molecular weight of the final polymer obtained. In bulk, the mobility of the reacting units

will decrease because of an increasing viscosity of the reaction medium during polymerization. As a result, the active polymerizing chains become restricted in movement and thus the rate of termination becomes limited due to a limited diffusion of the growing chains. The diffusion of monomer, on the other hand is less affected by the viscosity changes and because of the limited termination, monomer consumption will increase rapidly. This autoaccelaration effect, also called Trommsdorff effect, causes a significant raise in the weight average molecular weight (Mw), but only a moderate increase in the number average molecular weight (Mn) and is thus reflected by high polydispersity values [102]. For the envisaged application, this disadvantage is clearly surpassed by the plethora of advantages listed above.

In order to conduct a UV-induced polymerization, a suitable photo-sensitive initiator is required, which is also non-toxic. Previous studies have already shown that the initiator 1-[4-(2-hydroxyethoxy)-phenyl]-2-hydroxy-2-methyl-1-propanone (i.e. Irgacure® 2959) exhibits the lowest cell toxicity throughout an extensive range of mammalian cells, compared to alternative initiators, such as Irgacure® 651 and 184 [103]. As a result, Irgacure® 2959 was selected and applied.
The conducted reactions follow a radical mechanism as depicted in figure 2.3, which illustrates the radical polymerization of a random methacrylate-based monomer using Irgacure® 2959 as an initiator.
Upon UV irradiation, Irgacure® 2959 dissociates with the formation of free radicals (cfr. the initiation step), which react with the methacrylate-based monomers to form long polymer chains (cfr. the propagation step). The chain reaction terminates when two radical species combine or disproportionate (cfr. the termination step).

In dentistry, a photopolymerization or curing is extensively used to perform dental restaurations and for sealant application [104-105], but also in the coating industry, the technique is very important for surface protection of various materials [106]. Furthermore, in the field of tissue engeering, photopolymerization is widely applied for the production of hydrogel networks to be used as tissue barriers, drug delivery systems and as cell carrier scaffolds to stimulate tissue regeneration [107]. The use of photo-initiated polymerizations in the context of biomaterials has been extensively reviewed a.o. by Fisher et al [108].

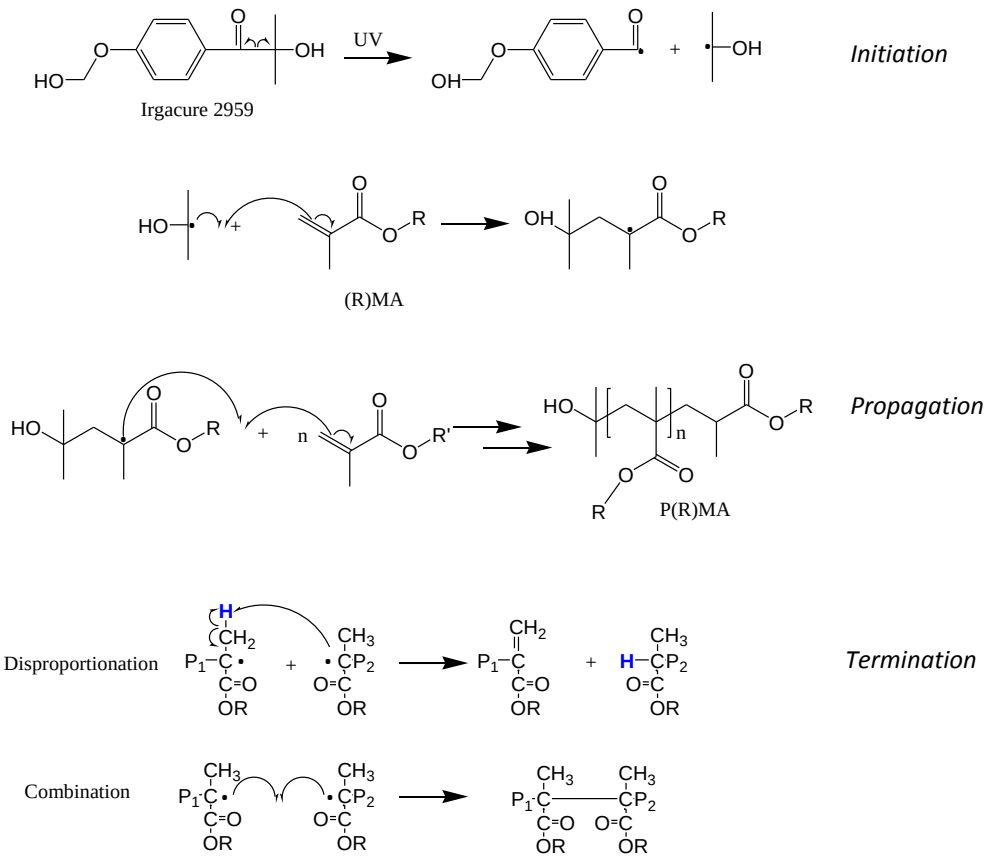

Figure 2.3: Reaction mechanism of the polymerization of a random methacrylate-based monomer, initiated by Irgacure® 2959. 'R' is referring to a random side chain (e.g. methyl, PEG,…), whereas 'P' is referring to a polymer chain which is grown according to the above-mentioned mechanism (i.e. initiation and propagation).

2.4. Development of poly(ethylene glycol)-based materials

In a first attempt to develop a suitable packaging material for an optical glucose sensor, PEG-containing macromonomers were selected and copolymerized with MMA. PEG is the most commonly applied non-ionic hydrophilic polymer and is known for its low intrinsic toxicity, which renders it ideal for biomedical applications. PEG-based coatings have already been recognized as efficient 'non-fouling' surfaces [109-113] while in the field of drug delivery, it has proven its use as an excellent shielding agent for *in vivo* delivery of various bioactive compounds including drugs and peptides [113-115]. Apart from being applied as drug excipient, PEG is approved by the Food and Drug Administration (FDA) for its use in cosmetic products [116].

In the present work, PEG is mainly selected for its protein repellent properties. As pointed out in chapter 1, proteinaceous fouling on the sensor surface or membrane is one of the main reasons why the stability and reliability of most commercially available sensors decreases after implantation. As a consequence, PEG-based copolymers were selected as

potential sensor packaging material. Variation of the PEG molecular weight, its functionality and composition enabled to fine-tune the final material properties.
Paragraph 2.4.1 will report on the different starting compounds and the production of the selected homopolymers. Next, in the following paragraphs the different PEG-based copolymers will be described and their bulk properties will be evaluated.

2.4.1. Characterization of the starting compounds and the homopolymers.

Two PEG-based methacrylates were selected for the copolymerization with MMA, including poly(ethylene glycol) monomethyl ether monomethacrylate (PEGMA) as monomer and poly(ethylene glycol) dimethacrylate (PEGDMA), as crosslinker. For both compounds, the number of ethylene glycol (EG) repeating units was varied (cfr. different molecular weights) and its effect was investigated. More specifically, for PEGMA, molecular weights of 500 g/mol (PEGMA(500)) and 1100 g/mol (PEGMA(1100)) were studied whilst for PEGDMA, the molecular weights were 550 g/mol (PEGDMA(550)), 750 (PEGDMA(750)) and 1154 g/mol (PEGDMA(1150)). The structure and proton NMR spectra of the different starting compounds are displayed in figure 2.4. These NMR spectra will form the base for structure elucidation of the to-be-developed polymers. The different peak annotations are overviewed in the experimental part (see chapter 6, § 6.2.1.1).

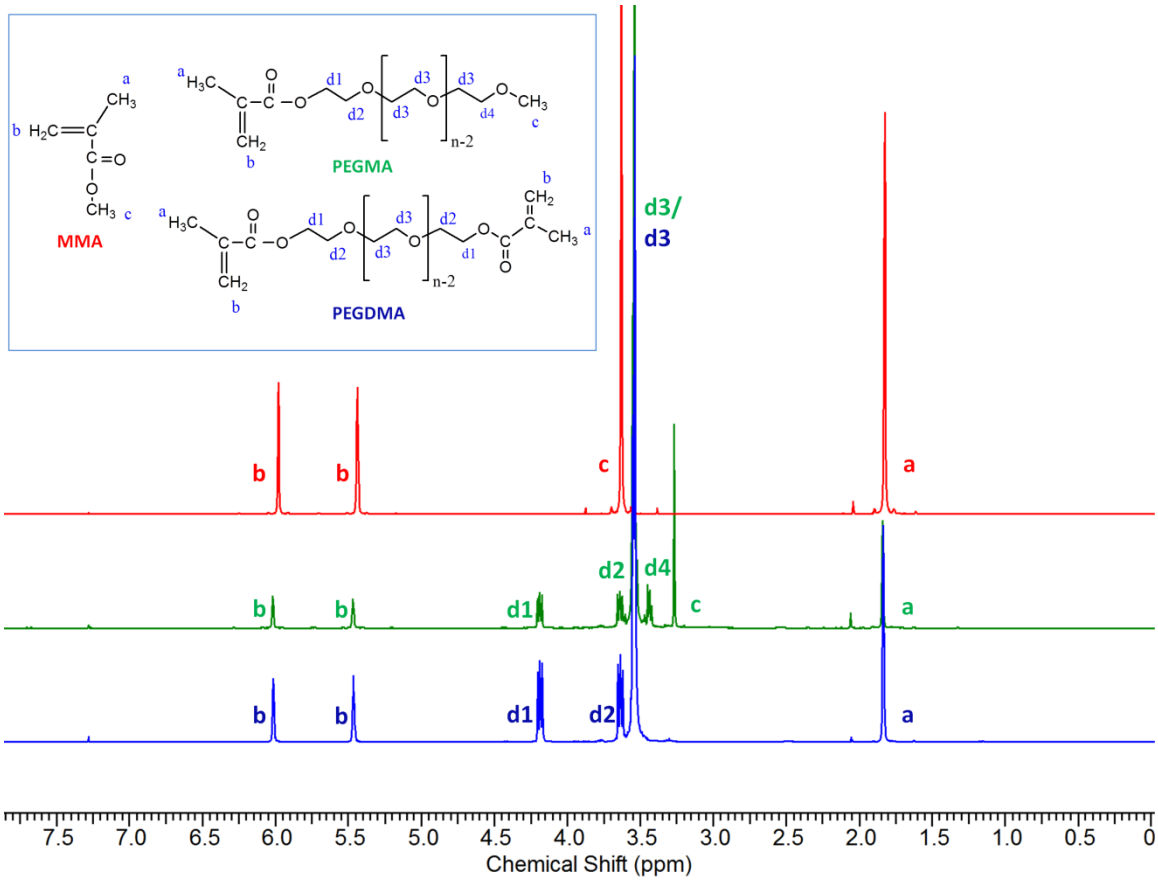

Figure 2.4: ^{1}H-NMR spectra of MMA (top), PEGMA(500) (center, n=9) and PEGDMA(550) (bottom, n=9), recorded in $CDCl_3$. The indices (a,b,c,…) link the protons with the corresponding peaks.

During the course of this work, the vinyl proton peaks were of major importance, because their disappearance indicated a successful polymerization/crosslinking. Completion of the polymerization is a prerequisite to minimize possible leaching of the starting monomers and potential inflammation *in vivo*. As a consequence, the UV irradiation time was optimized for each starting compound in order to ensure full conversion. Figure 2.5 summarizes the optimization results for MMA, PEGMA(500) and PEGDMA(550).

For MMA, as anticipated, a decrease in peak area corresponding to the double bond protons (at 5.47 and 6.02 ppm) was obtained upon increasing the irradiation time (see figure 2.5, A). Furthermore, new signals arose between 0.75 and 1 ppm, representing the protons in the polymer backbone (indicated by arrows in figure 2.5, A). Moreover, upon polymerization, a shift could be observed of the peak corresponding to the methyl-ester (H_3C-O-C=O) group from 3.53 ppm to 3.69 ppm (see spectra b and c). Figure 2.5 (A) also includes a spectrum of the initiator (spectrum d), Irgacure® 2959, in order to identify the additional peaks present in spectra b and c.

Quantification of the conversion (see figure 2.5, B and chapter 5, experimental part) was enabled by the calculation of the following ratio:

$$Conversion \quad (\%) = \frac{(I_{5.47\ ppm} + 6.02\ ppm) / 2}{(I_{3.69\ ppm}\ (monomer) + I_{3.53\ ppm}\ (polymer)) / 3} * 100 \quad \% \qquad (2.1)$$

Herein, the integration in the numerator resembles the double bond protons, whereas the integrations in the denominator resemble the methoxy protons. As a result, the PMMA synthesis in the presence of 2 mol% initiator resulted in a conversion of 98% after 90 minutes of UV irradiation.

For PEGMA, irradiation times of 2, 6, 10 and 20 minutes were evaluated and after 20 minutes, all double bond protons disappeared (figure 2.5, C). Compared to PMMA, the PEG-based oligomer is characterized by superior conversion kinetics (figure 2.5, D), due to the lower viscosity of the reaction mixture. As a consequence, the UV irradiation time of the copolymers was set between 20 and 90 minutes, depending on the PEGMA/MMA comonomer ratios (see § 2.4.2).

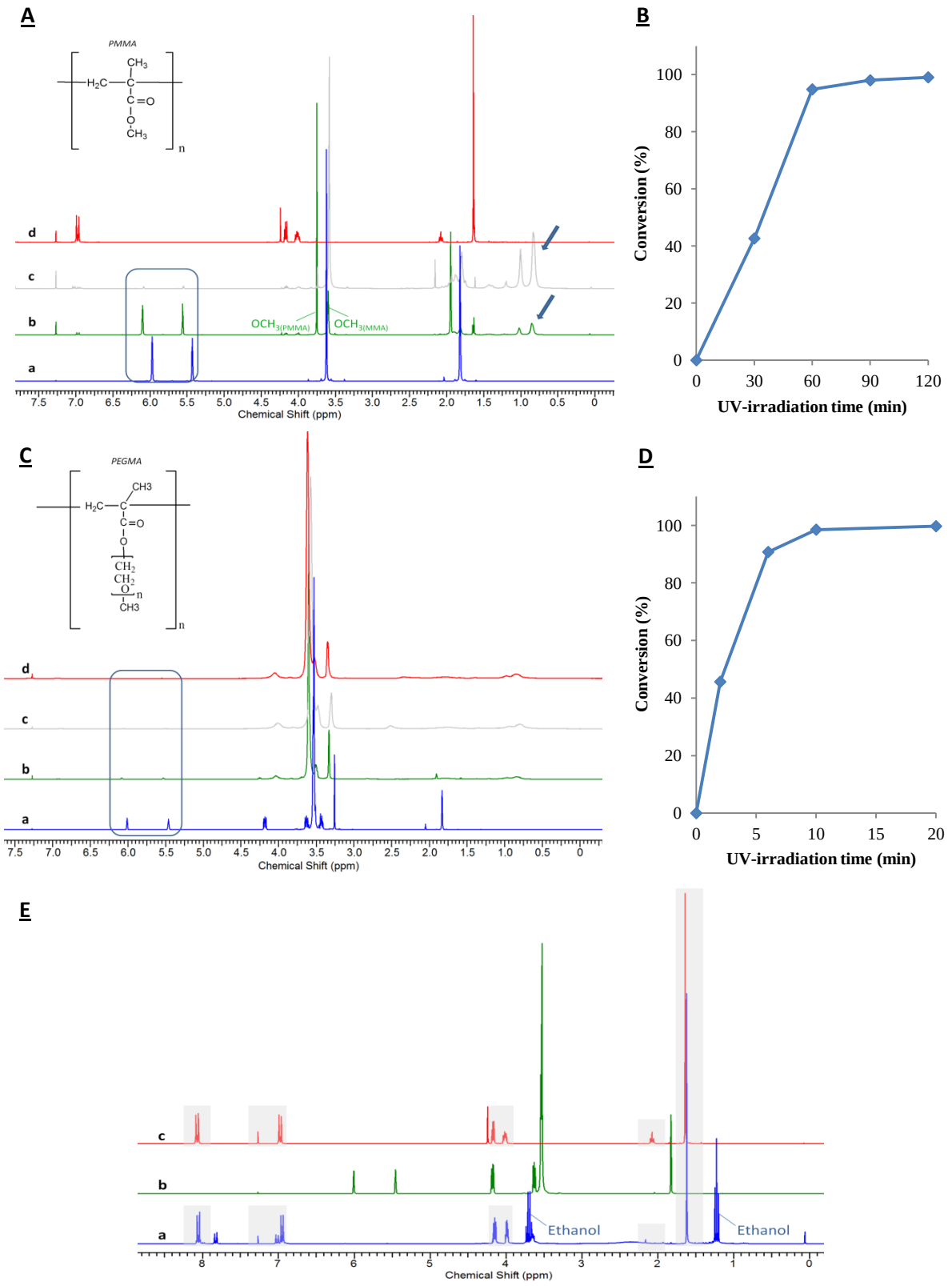

Figure 2.5: A: Overlay of the ^{1}H NMR spectra of MMA (a), PMMA after 30 minutes (b) and 90 minutes (c) of UV irradiation and Irgacure® 2959 (d). B: MMA conversion as a function of UV irradiation time (365 nm). C: Overlay of the ^{1}H NMR spectra of unreacted (a) and reacted PEGMA(500) after 6 (b), 10 (c) and 20 minutes (d) of UV irradiation. D: PEGMA conversion percentage as a function of UV irradiation time. E: ^{1}H NMR spectra of the soluble fraction obtained after soxhlet extraction in ethanol of the homopolymer PEGDMA(550) (a), the starting oligomer PEGDMA(550) (b) and Irgacure® 2959 (c). All NMR solutions were prepared in $CDCl_3$.

For PEGDMA, a similar optimization was performed. Conventional ^{1}H-NMR spectroscopy was not applicable since the homopolymer of PEGDMA is crosslinked, rendering dissolution impossible. Furthermore, HR-MAS spectroscopy measurements was neither a valid alternative because of a too high crosslinking degree [117]. Therefore, soxhlet extractions were conducted to quantify and identify the soluble fraction of the produced samples. Different irradiation times were again evaluated (10, 20 and 30 minutes). The results showed that after 10 minutes, the crosslinking reaction was completed. The soluble fraction amounted 1.6% and mainly consisted of an excess of 'leached-out initiator', as evidenced by ^{1}H NMR spectroscopy (figure 2.5, E).
As a consequence, for the production of the MMA/PEGDMA copolymer networks, the UV irradiation time was varied between 10 and 90 minutes, depending on the PEGDMA/MMA comonomer ratios (see § 2.4.3).

As PMMA was used as a reference material, the UV-polymerized sheets were fully characterized. The properties are summarized in table 2.2.
Tensile tests confirmed the fact that PMMA acts as a strong (E-mod of ± 1600 MPa) but brittle (elongation of 3%) material. In literature, the E-modulus of PMMA typically varies between 710 MPa and 5000 MPa [118-123], while the elongation is around 3 % [121]. These variations can typically be attributed to variations in polymer molecular weight, different production processes applied for sample preparation, the shape of the test specimens and the instrument settings. Furthermore, PMMA reveals a hydrophobic character since almost no swelling was obtained (i.e. 2%). By applying a UV-induced radical polymerization, a molecular weight of 30000 g/mol was obtained and the polydispersity (PD= 2.9) clearly reflected the method of synthesis, since more controlled polymerizations result in polydispersities < 1.5 or even around 1.

Table 2.2: Characteristics of PMMA, produced via UV-induced bulk polymerization

Mechanical properties	
E-modulus (Mpa)	1595 ± 357
Elongation (%)	3 ± 1
Force at break (N)	96 ± 24
Swelling properties	
Swelling (%)	2.0 ± 0.2
Molecular weight	
Mn (g/mol)	30000 ± 800
Polydispersity	2.9 ± 0.0

In the upcoming paragraphs, the results of a full screening of the different copolymer formulations is described. The initial focus will be on the PEGMA-based copolymers (§ 2.4.2), followed by the PEGDMA-based networks (§ 2.4.3). Finally, combinations of the three starting compounds will be evaluated (§ 2.4.4).

2.4.2. Development and evaluation of copolymers of MMA and poly(ethylene glycol) monomethyl ether monomethacrylate.

The first series of PEG-based copolymers were non-crosslinked and constituted of methyl methacrylate (MMA) and poly(ethylene)glycol monomethylether monomethacrylate (PEGMA) of different molecular weights. First, the maximum amount of PEGMA to be incorporated in order to produce rigid materials was determined. In case of PEGMA(500), solid materials were obtained if the incorporated percentage was lower than 20 mol%. As a consequence, 15 mol% was selected as limit. In case of PEGMA(1100), this limit was set to 7 mol% as the incorporation of higher mol% PEGMA(1100) resulted in sticky, glue-like materials. This is related to the low glass transition temperature of this polymer (Tg < -60°C). The structure of the developed copolymers was evidenced by means of ^{1}H-NMR spectroscopy. Figure 2.6 displays the spectra of a random co-polymer, together with the corresponding peak assignments.

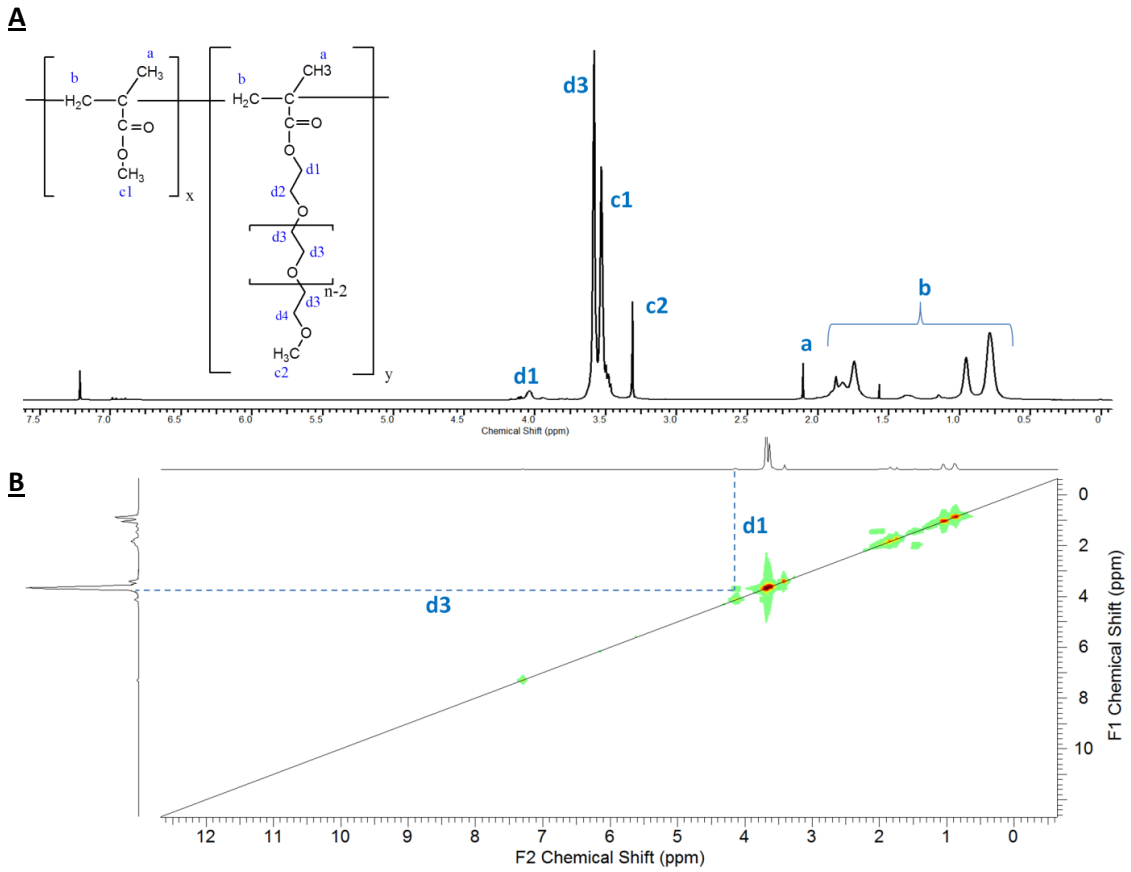

Figure 2.6: ^{1}H NMR spectrum of P(MMA-co-PEGMA(500)) recorded on a 300 MHz device (A) and the 2D cosy NMR spectrum of the same compound, recorded on a 500 MHz device (B), both in $CDCl_3$.

When comparing with figure 2.4 (a), it is clear that the peak at 3.3 ppm (i.e. peak c2) represents the methoxy protons of the PEG-units while the signal at 4 ppm (i.e. peak d1) corresponds to the -CH_2- protons adjacent to the ester functionality in the same PEG-

segment. Based on the integrations of the peaks at 3.53 (peak c1) and 3.58 ppm (peak d3) and the known composition of the synthesized polymer, the one at 3.58 ppm (i.e. peak d3) could be assigned to the ether protons in the PEG side chain, whereas the one at 3.53 ppm (i.e. peak c1) could be annotated to the methyl-ester-protons of the MMA-units. To verify these results, a 2D cosy NMR spectrum was recorded. From figure 2.6 (B), it is evident that the peak at 4.05 ppm (peak d1) and the one at 3.65 ppm (d3) couple, which implies that both proton types are part of the same building block, being the PEG-based compound.

Based on literature, it can be anticipated that an almost ideal random copolymer will be obtained, since the reactivity ratios of MMA and PEGMA are 0.95 and 1.05 respectively [124]. Nevertheless, it should be pointed out that these parameters were determined for a conventional solution polymerization and upon applying a much lower molar ratio for PEGMA compared to MMA.

Next, the molecular weight of the different copolymers, as well as their polydispersities were determined. Table 2.3 gives an overview of the copolymer compositions and the GPC results. Compared to PMMA (table 2.2), slightly higher molecular weights are obtained, which is due to the higher molecular weight of the PEG building blocks, but similar high polydispersities were obtained, which is again inherent to the used bulk polymerization technique.

Table 2.3: Copolymer compositions which were synthesized and analyzed by GPC.

Sample	MMA(mol%)	PEGMA(500)(mol%)	Mn	stdev	DP	stdev
1	95	5	43700	700	2.8	0.03
2	90	10	50200	1100	2.6	0.03
3	85	15	47700	3400	2.3	0.12
	MMA(mol%)	**PEGMA(1100)(mol%)**	**Mn**	**stdev**	**DP**	**stdev**
4	98	2	42000	600	2.7	0.11
5	96	4	44000	400	2.5	0.04
6	94	6	48300	900	2.2	0.01
7	93	7	50800	2400	2.0	0.12

In a next step, mechanical tests were performed to study the influence of PEGMA on the mechanical properties of the developed materials. Figure 2.7 (B) clearly shows that an increased amount of PEGMA resulted in a decrease of the E-modulus. This is also visualized by a less steep slope of the initial linear elastic part in the stress-strain curves (Figure 2.7, A) and was anticipated, because of the presence of long chains in the materials developed. The longer side chains increase the free volume between the polymer backbones as well as their freedom to move. As a result, a higher flexibility of the material is obtained. Furthermore, it was noted that the longer the PEG chains, the more the E-modulus decreased leading to more elastic materials.

The observed trend was also evidenced by the elongation potential of the materials. Elongations of 500 % were obtained when 15 mol% of PEGMA(400) was incorporated. On

the other hand, for PEGMA(1100), only 7 mol% was needed to realize elongations of 600%. The strength of the materials could be evaluated based on the force required for material failure. As expected, this force decreased with increasing molar percentages of PEGMA incorporated (see table 2.4).

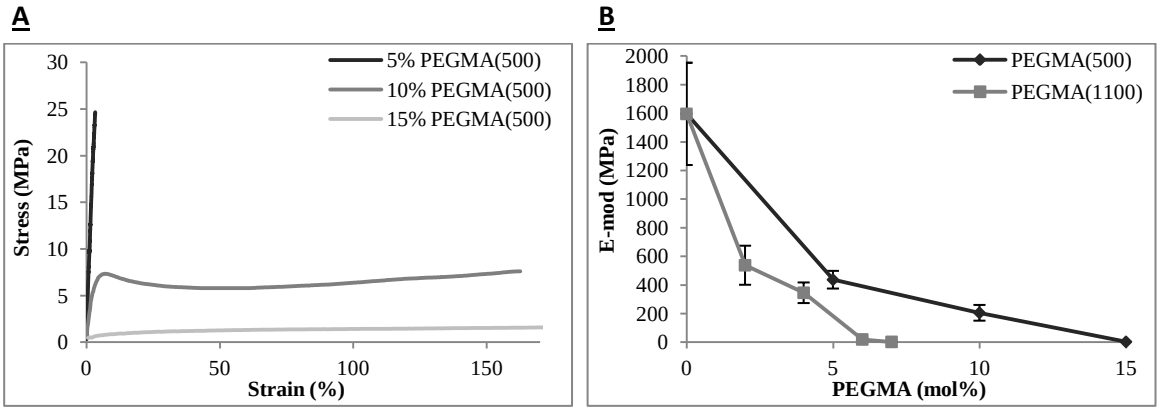

Figure 2.7: Typical stress-strain curves obtained at room temperature by tensile testing for PEGMA-based copolymers (A). Elastic modulus as a function of mol% PEGMA incorporated. Two different molecular weights of the PEG chains were studied: 400 and 1000 g/mol (B).

The trends observed for the mechanical properties are further supported by the glass transition temperatures (Tg) of the materials. In case of PMMA, a high Tg value was found (98°C) as anticipated based on its glassy state for the current test conditions (i.e. measurements at room temperature). Conversely, in case 15 mol% PEGMA(500) was introduced in the polymer structure, a negative value was obtained for the Tg (i.e. -20°C). As a consequence, the material is in its rubbery state, which is clearly reflected by the low E-modulus and the high elongation percentage.

Table 2.4: Overview of the bulk properties of the MMA and PEGMA containing copolymers. All tensile tests were performed at room temperature and the swelling experiments were conducted in water at 37°C. Furthermore, the glass transition temperature of a selection of materials are also presented, calculated based on the 2nd heating cycle.

Sample	MMA (mol%)	PEGMA(500) (mol%)	E-mod (Mpa)	Elongation (%)	Force at break (N)	Swelling (%)	Tg (°C)
Ref.	100	0	1595 ± 357	3 ± 1	96 ± 24	2 ± 0	98
1	95	5	436 ± 62	4 ± 2	44 ± 30	12 ± 4	59
2	90	10	204 ± 55	170 ± 8	39 ± 9	37 ± 4	37
3	85	15	2 ± 1	551 ± 44	10 ± 3	249 ± 27	-20
	MMA (mol%)	**PEGMA(1100) (mol%)**	**E-mod (Mpa)**	**Elongation (%)**	**Force at break (N)**	**Swelling (%)**	**Tg (°C)**
4	98	2	537 ± 136	10 ± 12	55 ± 24	12 ± 2	57
5	96	4	345 ± 72	64 ± 44	45 ± 8	33 ± 2	50
6	94	6	19 ± 7	343 ± 30	14 ± 2	105 ± 4	-
7	93	7	2 ± 0	619 ± 93	7 ± 4	107 ± 4	-

Apart from the mechanical properties, the swelling capacity of the materials was also studied. Since PEG is known to be a very hydrophilic compound, higher concentrations will result in higher swelling percentages, which is clearly visible in table 2.4. Furthermore, when comparing copolymer 1 and 5, the swelling percentage of the first polymer is twice as high as the latter one. Doubling the molecular weight of the PEG chain thus results in a doubling of the swelling capacity.

2.4.3. Development and evaluation of copolymers of MMA and poly(ethylene glycol) dimethacrylate

The second set of produced materials included a series of crosslinked polymers based on MMA and poly(ethylene glycol) dimethacrylate (PEGDMA). As stated above, dependent on the molar composition of the networks, UV irradiation times varying from 10 to 90 minutes were applied. To determine the monomer conversions, sol-gel studies were conducted in acetone. It can be concluded that high monomer conversions were obtained as gel fractions above 95% were obtained for all formulations under study (figure 2.8)

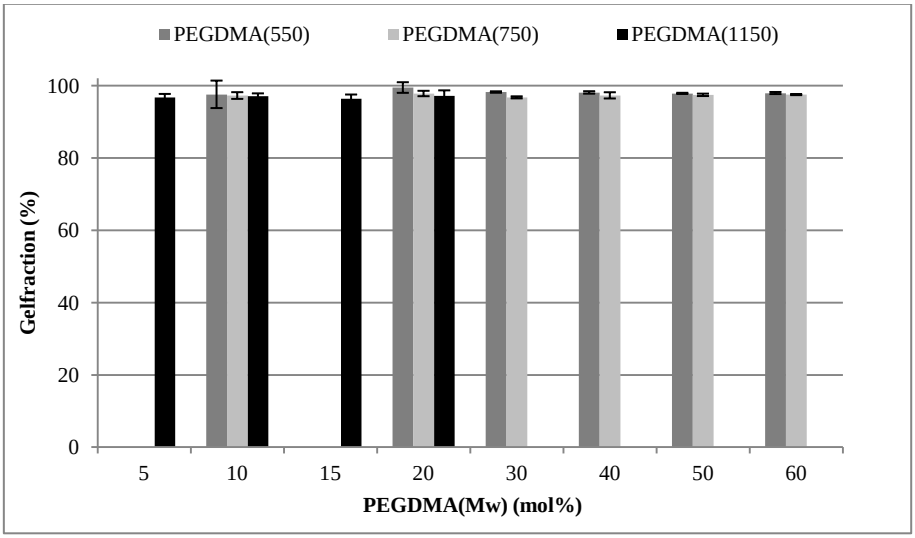

Figure 2.8: Gel fraction as a function of the mol% and the molecular weight of PEGDMA as obtained through sol-gel testing in acetone.

Figure 2.9 and table 2.5 provide an overview of the bulk properties of the obtained polymer networks. Comparison of the different E-moduli shows a similar trend for the three studied molecular weights of PEGDMA. Up to a certain level of PEGDMA, a decrease of the E-modulus is obtained with an increasing PEGDMA content. Subsequently, upon exceeding this percentage of PEGDMA (depending on the molecular weight), a plateau value is reached. This phenomenon can be explained by the counteracting effect of two factors: higher percentages of PEGDMA result in the presence of a higher amount of long and flexible chains. As a result, the free volume between the polymer chains increases and more flexible and soft materials are obtained. Conversely, an increase of the percentage of PEGDMA

results in an increase in the number of crosslinking points present in the material. These crosslinks determine the brittleness of the material.
Once the plateau value is reached, both effects compensate. At that point, the introduction of long chains in the material will be masked by the number of crosslinks introduced. As anticipated, this plateau value is reached at a lower PEGDMA(1154) content (at 10 mol%) compared to PEGDMA(750) (at 20 mol%) and PEGDMA(550) (at 50 mol%) (see arrows in figure 2.9, B).

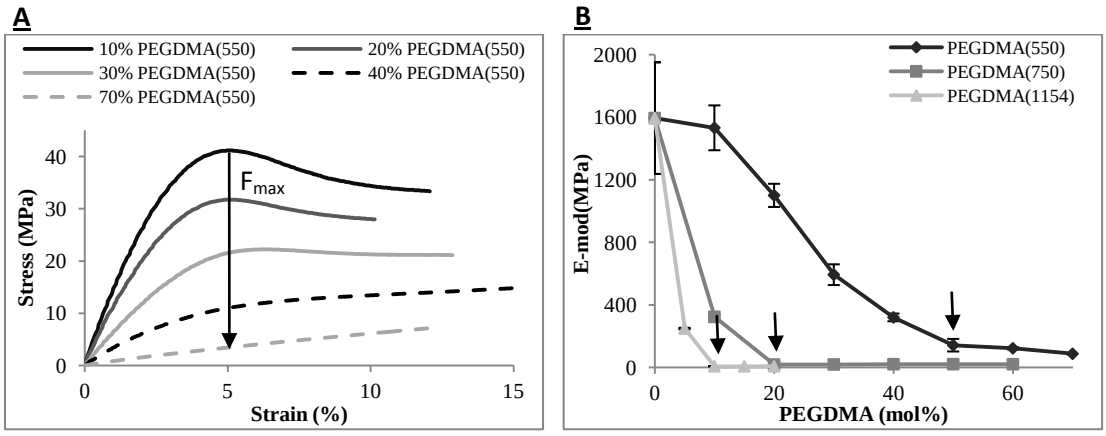

Figure 2.9: Typical stress-strain curves obtained for MMA/PEGDMA networks (A). Elastic modulus as a function of mol% PEGDMA incorporated. Three different molecular weights of PEGDMA are studied: 550, 750 and 1154 g/mol (B)

The decrease in E-modulus with increasing PEGDMA content can be noted in the stress-strain curves by a decreasing steepness of the slope in the linear elastic part. Furthermore, higher percentages of PEGDMA result in weaker materials which is represented by a decreasing F_{max} (figure 2.9(A)) and force at break (table 2.5).
The presence of crosslinks also influences the elongation percentages of the materials. A higher amount of crosslinker or crosslinking points results in lower elongation percentages. The crosslinks act as anchorage points, which freeze the polymer chains in a fixed position. In this way, the polymer chains are not able anymore to move along each other, but instead, these points will introduce a certain stress into the material. As a consequence, the crosslinks will enhance the brittle nature of the materials.
Next, the swelling behavior of the materials was studied. Table 2.5 clearly shows that an increased swelling is obtained when more PEGDMA is introduced into the material. Nevertheless, if the swelling percentages are compared with the ones obtained for the PEGMA-based materials (table 2.4), these percentages are still moderate because of the presence of crosslinks.

Table 2.5: Overview of the bulk properties of the developed copolymer networks consisting of MMA and PEGDMA. The table mentions the theoretical co-monomer ratios. All tensile tests were performed at room temperature and the swelling experiments were conducted in water at 37°C.

Sample	MMA (mol%)	PEGDMA(550) (mol%)	E-mod (Mpa)	Elongation (%)	Force at break (N)	Swelling (%)
Ref	100	0	1595 ± 357	3 ± 1	96 ± 24	2 ± 0
8	90	10	1533 ± 144	10 ± 2	121 ± 6	7 ± 1
9	80	20	1101 ± 74	9 ± 3	88 ± 7	10 ± 0
10	70	30	593 ± 66	11 ± 4	67 ± 2	13 ± 0
11	60	40	320 ± 25	21 ± 2	54 ± 4	15 ± 1
12	50	50	142 ± 40	16 ± 3	36 ± 6	17 ± 1
13	40	60	122 ± 7	17 ± 1	34 ± 3	19 ± 1
	MMA (mol%)	**PEGDMA(750) (mol%)**	**E-mod (Mpa)**	**Elongation (%)**	**Force at break (N)**	**Swelling (%)**
14	90	10	324 ± 13	30 ± 9	70 ± 3	19 ± 2
15	80	20	19 ± 4	42 ± 2	18 ± 1	30 ± 1
16	70	30	19 ± 1	18 ± 2	10 ± 1	36 ± 1
17	60	40	21 ± 2	13 ± 1	8 ± 1	43 ± 0
18	50	50	21 ± 1	11 ± 1	7 ± 1	43 ± 1
19	40	60	21 ± 1	8 ± 1	5 ± 1	46 ± 2
	MMA (mol%)	**PEGDMA(1154) (mol%)**	**E-mod (Mpa)**	**Elongation (%)**	**Force at break (N)**	**Swelling (%)**
20	95	5	249 ± 5	105 ± 1	77 ± 2	16 ± 0
21	90	10	7 ± 0	87 ± 7	20 ± 2	37 ± 1
22	85	15	7 ± 0	30 ± 9	9 ± 1	56 ± 2
23	80	20	8 ± 0	23 ± 4	7 ± 0	62 ± 2

Compared to PEGMA, the introduction of PEGDMA resulted in slightly higher E-moduli (a minimum of 8 MPa compared to 2 MPa) and lower elongation percentages (a maximum of 100% compared to 600%), due to the introduction of crosslinking points in the latter case. One remarkable result can further be highlighted. The combination of MMA with 5 mol% PEGDMA(1154) is characterized by a relatively high elongation percentage (± 105%) combined with a rather high E-modulus (± 250 MPa), which seems contradictive. The increased elongation can probably be explained by the higher molecular weight of the PEG chain, a fact which is also described in literature [125]. Regarding the higher E-modulus, it can be noted that compared to PMMA, the addition of 5 mol% PEGDMA(1154) still resulted in a significant drop of this modulus (i.e. 6 times lower). Future experiments could focus on the thermal analysis of the developed materials to gain further insight in the obtained mechanical data. As an intermediate conclusion, It can be stated that the introduction of PEG in the polymer structure has a beneficial effect on the mechanical properties (i.e. enhanced flexibility compared to PMMA). Indeed, combinations of MMA and PEGMA or PEGDMA resulted in E-moduli ranging from 2 till 1600 MPa and in elongation percentages going from 3 till 600 %.

2.4.4. Development and evaluation of copolymers based on MMA, PEGMA and PEGDMA

Tables 2.4 and 2.5 confirm that the introduction of PEG has a beneficial effect on the mechanical properties of the synthesized materials, meaning that lower E-moduli, higher flexibilities and higher elongations are obtained compared to PMMA itself. On the other hand, when the total amount of PEG is increased, the swelling of the materials increases in a proportional way, unless a crosslinking agent is used. In the latter case, crosslinking points are introduced which hamper swelling of the material. As a consequence, in a final step, both PEGMA and PEGDMA were used to finetune the properties of the starting material (i.e. PMMA). Since the molecular weight of the PEG chain also influences the swelling behavior of the material, the molecular weight of the crosslinker was fixed at 550 g/mol.

Tables 2.6 (use of PEGMA(1100)) and 2.7 (use of PEGMA(500)) overview the different combinations under evaluation as well as their mechanical and swelling properties. The E-moduli are plotted in figure 2.10. Similar trends as before were observed and are summarized below.Higher amounts of PEGMA resulted in:

- a lower E-modulus, which implies that more flexible materials are obtained
- higher elongation percentages, although the addition of a crosslinker limits this effect
- a lower strength of the materials as less force is required before failure
- higher swelling percentages, although this effect is counterbalanced by the crosslinker

Table 2.6: Overview of the bulk properties of the copolymer networks consisting of MMA, PEGMA(1100) and PEGDMA(550). All tensile tests were performed at room temperature and the swelling experiments were conducted in milli-Q water at 37°C.

Sample	MMA (mol%)	PEGDMA(550) (mol%)	PEGMA(1100) (mol%)	E-mod (Mpa)	Elongation (%)	Force at break (N)	Swelling (%)
Ref	100	0	0	1595 ± 357	3 ± 1	96 ± 24	2 ± 0
45	50	48	2	55 ± 4	14 ± 2	24 ± 3	23 ± 1
46	50	46	4	43 ± 2	13 ± 1	18 ± 1	28 ± 0
47	50	44	6	32 ± 1	11 ± 1	12 ± 1	32 ± 0
	MMA (mol%)	**PEGDMA(550) (mol%)**	**PEGMA(1100) (mol%)**	**E-mod (Mpa)**	**Elongation (%)**	**Force at break (N)**	**Swelling (%)**
48	75	23	2	270 ± 55	22 ± 3	35 ± 23	19 ± 0
49	75	21	4	50 ± 7	30 ± 2	27 ± 1	28 ± 1
50	75	19	6	20 ± 1	30 ± 2	17 ± 1	34 ± 1
	MMA (mol%)	**PEGDMA(550) (mol%)**	**PEGMA(1100) (mol%)**	**E-mod (Mpa)**	**Elongation (%)**	**Force at break (N)**	**Swelling (%)**
51	85	13	2	445 ± 13	19 ± 8	61 ± 5	16 ± 0
52	85	11	4	107 ± 55	53 ± 3	43 ± 2	32 ± 0
53	85	9	6	14 ± 4	55 ± 8	17 ±3	41 ± 1

Table 2.7: Overview of the bulk properties of the copolymers based on MMA, PEGMA(500) and PEGDMA(550). All tensile tests were performed at room temperature and the swelling experiments were conducted in milli-Q water at 37°C.

Sample	MMA (mol%)	PEGDMA(550) (mol%)	PEGMA(500) (mol%)	E-mod (Mpa)	Elongation (%)	Force at break (N)	Swelling (%)
Ref	100	0	0	1595 ± 357	3 ± 1	96 ± 24	2 ± 0
24	50	45	5	62 ± 6	16 ± 0	25 ± 1	21 ± 0
25	50	40	10	37 ± 1	13 ± 1	16 ± 2	24 ± 0
26	50	35	15	29 ± 2	11 ± 0	10 ± 0	33 ± 2
	MMA (mol%)	**PEGDMA(550) (mol%)**	**PEGMA(500) (mol%)**	**E-mod (Mpa)**	**Elongation (%)**	**Force at break (N)**	**Swelling (%)**
27	75	25	0	424 ± 80	16 ± 5	92 ± 23	12 ± 1
28	75	20	5	149 ± 12	28 ± 5	48 ± 5	15 ± 0
29	75	15	10	49 ± 10	44 ± 4	32 ± 3	21 ± 1
30	75	10	15	10 ± 1	42 ± 5	12 ± 2	34 ± 1
31	75	5	20	4 ± 0	37 ± 6	3 ± 2	65 ± 3
	MMA (mol%)	**PEGDMA(550) (mol%)**	**PEGMA(500) (mol%)**	**E-mod (Mpa)**	**Elongation (%)**	**Force at break (N)**	**Swelling (%)**
32	80	18	2	491 ± 9	26 ± 2	82 ± 2	12 ± 1
33	80	16	4	486 ± 14	24 ± 6	69 ± 3	13 ± 0
34	80	12	8	212 ± 2	49 ± 1	49 ± 2	19 ± 0
35	80	4	16	8 ± 0	108 ± 2	15 ± 0	44 ± 1
36	80	2	18	2 ± 0	153 ± 5	7 ± 5	65 ± 1
	MMA (mol%)	**PEGDMA(550) (mol%)**	**PEGMA(500) (mol%)**	**E-mod (Mpa)**	**Elongation (%)**	**Force at break (N)**	**Swelling (%)**
37	85	15	0	945 ± 63	14 ± 4	111 ± 12	9 ± 0
38	85	13	2	900 ± 39	14 ± 5	91 ± 6	9 ± 0
39	85	10	5	453 ± 57	23 ± 7	63 ± 4	14 ± 0
40	85	5	10	125 ± 35	86 ± 5	40 ± 6	23 ± 1
	MMA (mol%)	**PEGDMA(550) (mol%)**	**PEGMA(500) (mol%)**	**E-mod (Mpa)**	**Elongation (%)**	**Force at break (N)**	**Swelling (%)**
41	90	8	2	1542 ± 235	11 ± 3	120 ± 19	8 ± 1
42	90	6	4	1129 ± 124	14 ± 3	86 ± 3	9 ± 1
43	90	4	6	1081 ± 194	10 ± 2	85 ± 12	12 ± 1
44	90	2	8	678 ± 122	39 ± 22	69 ± 12	16 ± 1

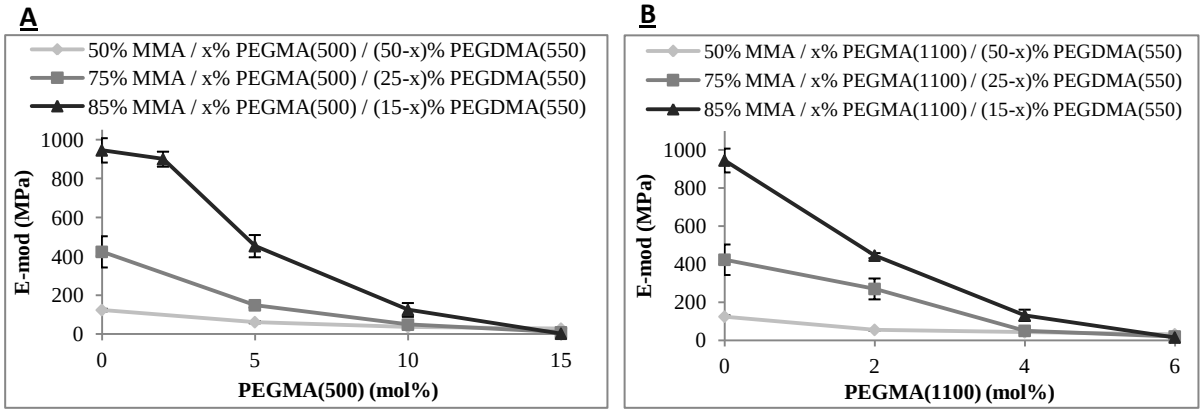

Figure 2.10: Elastic modulus as a function of mol% PEGMA incorporated for the polymers consisting of MMA, PEGMA and PEGDMA(550). Two molecular weights of PEGMA were evaluated: 500 g/mol (A) versus 1100 g/mol (B). 'x' stands for the amount of PEGMA as indicated on the x-axis.

2.4.5. Influence of PBS buffer on the polymer mechanical properties

Previous paragraphs (2.4.2-2.4.4) have shown that all materials reveal some swelling in water (percentages ranging from 2% to 250%). As the materials will be implanted subcutaneously, material swelling will occur *in vivo*. To study the effect of swelling on the mechanical behavior, a material selection was incubated at 37°C in PBS (phosphate buffered saline) buffer, a phosphate buffer, mimicking the pH and ionic strength of the *in vivo* environment. The materials were evaluated for their elastic modulus, elongation and force at break. The selection was based on minimized water swelling percentages. In the end, electronic parts need to be encapsulated into the polymer material and excessive swelling should thus be avoided. Furthermore, high swelling could introduce mechanical stress and eventually cause fracture of the polymer implant. As a consequence, combinations of MMA and PEGMA were excluded from this study as well as the PEGDMA derivatives which were characterized by a longer PEG chain (i.e. PEGDMA(750) and PEGDMA(1154)). First, the 2-component systems were evaluated (see figure 2.11) and incubation in PBS buffer resulted in a significant decrease of the E-modulus and force at break ($p<0.05$).

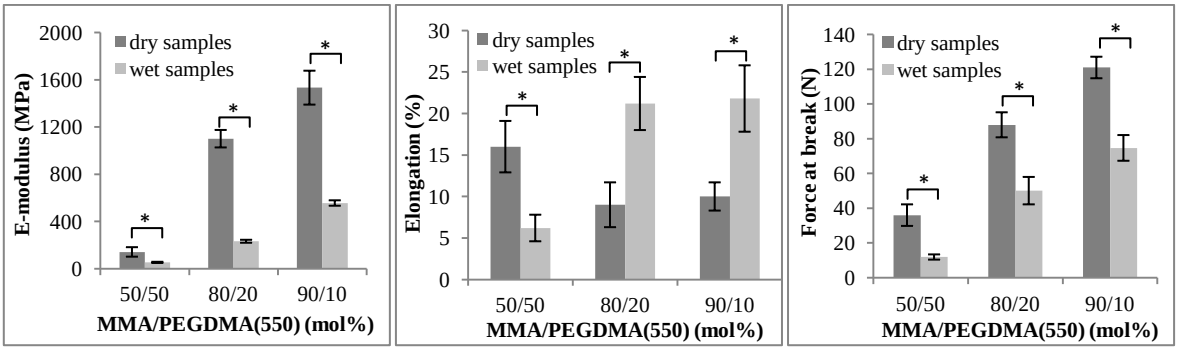

Figure 2.11: E-modulus, elongation % and force at break of materials 8, 9 and 12 (cfr. table 2.5), measured in dry state and after incubation in PBS buffer (pH 7.4) at 37°C. Samples which are statistically different are denoted by "*".

The elongation percentage on the other hand increased for the lower crosslinker percentages (10 and 20 mol% PEGDMA), but not when 50 mol% crosslinker was introduced. Due to the higher amount of hydrophilic PEG, higher swelling is manifested and it is anticipated that because of this swelling more salts, which are present in the PBS buffer, will be incorporated inside the polymer network. As a consequence, these salts alter the brittleness of the incubated materials, which is illustrated by a decreased elongation of the material.

Results of the three-component systems are summarized in figure 2.12.

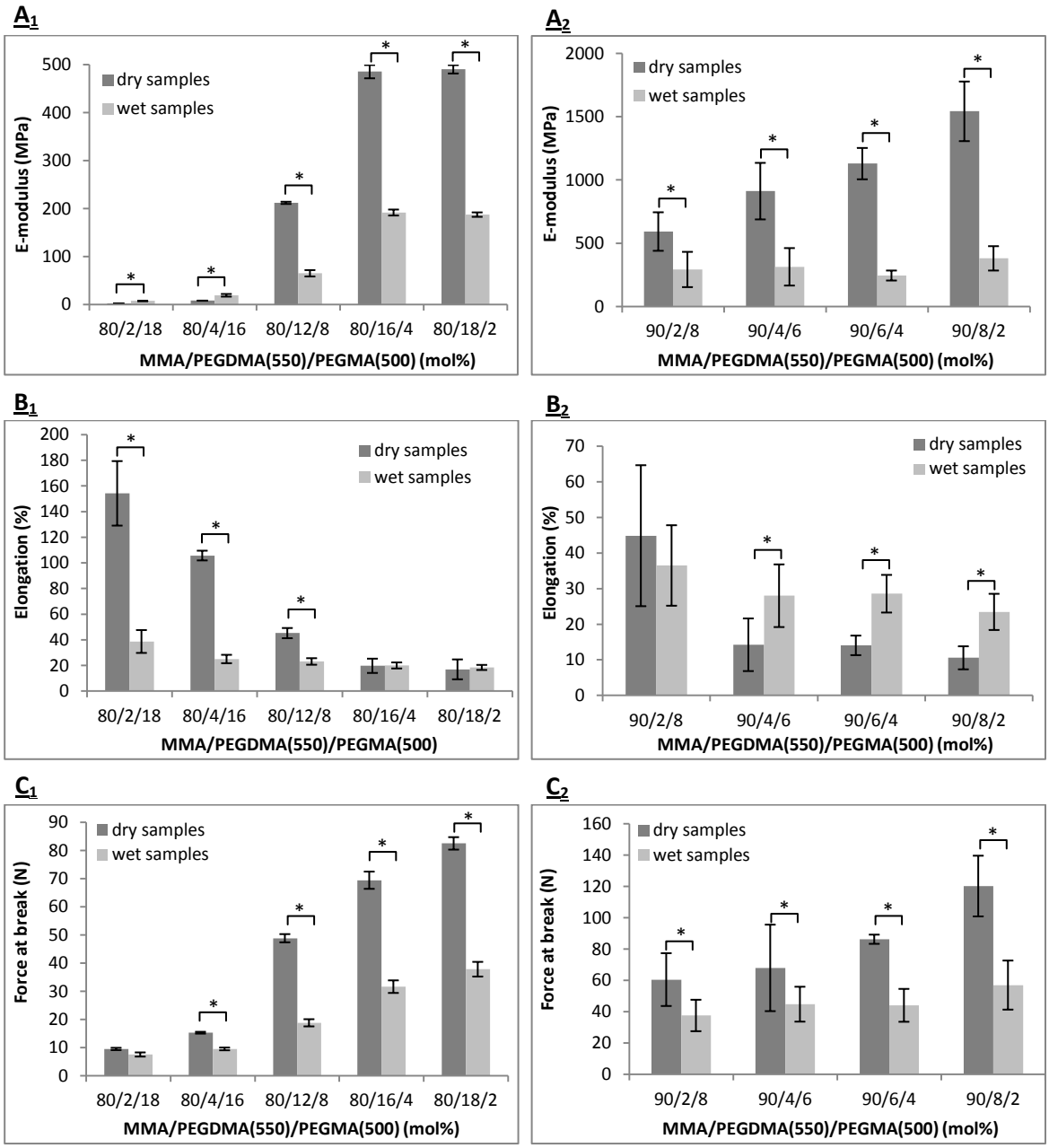

Figure 2.12: E-modulus (A), elongation % (B) and force at break (C) of materials 32-36 (left column, subscript "1") and materials 41-44 (right column, subscript "2"), measured in their dry state and after incubation in PBS buffer at 37°C (pH 7.4). Samples which are statistically different are denoted by "*".

Herein, the materials consisting of 90 mol% MMA and 10 mol% PEG (i.e. total PEG content consisting of PEGMA and PEGDMA) follow the expected trend. Upon swelling in PBS-buffer, lower E-moduli (figure 2.12, A_2), higher elongation percentages (figure 2.12, B_2) as well as lower forces at break (figure 2.12, C_2) were measured. These trends are the result of the plasticizing effect of water. On the other hand, in case the amount of PEG is increased up to 20 mol%, some unexpected findings arose. For materials consisting of 80/2/18 and 80/4/16 mol% of MMA/PEGDMA(550)/PEGMA(500), a higher E-modulus is obtained for the incubated samples compared to the dry ones (figure 2.12, A_1). This result might be explained by the high swelling percentages of these materials, being 65% and 44% respectively. Again, because of swelling, a substantial amount of salts will be incorporated inside the polymer structure, which influences the material's mechanical properties. Indeed, a higher resistance against deformation is manifested (cfr. increased E-modulus) as well as a decreased elongation of the material (figure 2.12, B_1) and a decreased force at break (figure 2.12, C_1).

2.4.6. Intermediate conclusion on the evaluation of PEG-based materials as potential packaging for an implantable glucose sensor

In a first part of this research, different copolymers were produced starting from MMA and PEG. The materials possessed different physical characteristics and depending on the envisaged application, these properties can be finetuned. Their characteristics are mostly defined by the molar ratios of the different compounds used, the molecular weight of the PEG-chains and the possible use of a crosslinker.

As stated in the introduction, when considering materials to be applied as packaging for an optical glucose sensor, they should meet certain characteristics. When screening the various result tables in previous paragraphs, various conclusions can be drawn. First, a broad range of materials ranging from hard (E-mod ≈ 1600 MPa) to soft (E-mod ≈ 2MPa) PEG-based materials could be produced. Secondly, due to the application of a hydrophilic compound, all polymers reveal a certain degree of swelling. It is clear that both properties counteract implying the need for compromises. As a consequence, the softer materials summarized in table 2.4 suffer from a too high swelling and are considered unsuited for the envisaged application. Nevertheless, for other applications including stent coatings, these materials could offer clear benefits (see chapter 7).

As the present work focuses on the development of a packaging material for an optical glucose sensor, the network consisting of 50 mol% MMA and 50 mol% PEGDMA(550) was selected as most optimal material from table 2.5. This choice was made because the material contains a high molar percentage of PEG, but still shows limited swelling (i.e. 17%) due to the presence of crosslinks in the material. Furthermore, a 10-fold lower E-modulus is obtained and a five times higher elongation percentage, compared to PMMA.

As a result, this material was selected as a first glucose sensor packaging candidate and was used as basis to fine-tune the biocompatibility (cfr. chapters 3 and 4). Alternatives comprise materials described in tables 2.6 and 2.7, including material 34 (80 mol% MMA/ 16 mol% PEGDMA(550)/ 4 mol% PEGMA(500)), material 44 (90 mol% MMA/ 4 mol% PEGDMA(550)/ 6

mol% PEGMA(500)) or material 28 (75 mol% MMA/ 20 mol% PEGDMA(550)/ 5 mol% PEGMA(500)). The former two will be discussed in chapter 5, where the *in vivo* evaluation will be centralized.

2.5. Development and characterization of butyl- , ethylhexyl- and laurylmethacrylate-based polymers

In paragraph 2.2, flexible and hydrophilic copolymers were produced and screened. For the second strategy, flexible while hydrophobic materials have been developed. More specifically, different long chained comonomers were evaluated and the resulting copolymers were characterized by different techniques such as NMR spectroscopy and tensile testing. The selected monomers include *n*-butyl methacrylate (BuMA), 2-ethylhexyl methacrylate (EHMA) and lauryl methacrylate (LMA). The above-mentioned monomers have been selected because of their larger side chain compared to MMA. As a consequence, an increased free volume between the polymer main chains is anticipated along with a decreased glass transition temperature (T_g). A T_g below room temperature ensures that the polymer is in its rubbery state at phsyiological conditions and is easily deformed at processing and body temperature.

In literature, alkylmethacrylate-based (co-)polymers are frequently studied. For example, PBuMA has already been used as a soft component in drug-eluting coatings (e.g. for stents a.o. the Cypher stent) [126]. In the same field of drug delivery, copolymers consisting of BuMA and N-vinyl pyrrolidone (NVP) have also been studied [127]. Furthermore, a combination of dextran-graft-polybutylmethacrylate has been synthesized in an attempt to enhance endothelialisation of materials [128] and in the field of sensors, electro-conductive films of PBuMA and polyaniline have been examined for their application as biosensor to detect urea and uric acid [129]. In case of PEHMA, literature examples include the use as paper coating [130] and the application of its monomer as a component in triblock copolymers with MMA as candidates for adhesives in medical tapes and labels [131].

LMA, which contains twelve C-atoms in its side chain, is a very hydrophobic monomer and because of this, it has already been studied as co-monomer in the development of oil-absorbing copolymers [132-134]. In the biomedical world, it has been copolymerized with 2-methacryloyloxyethyl phosphorylcholine (MPC) in an attempt to design polymers for *in vivo* applications such as blood-contacting devices [135].

In the following paragraph, the evaluation of different monomers and their homopolymers is described (§ 2.5.1). Subsequently, different copolymer formulations will be screened (§ 2.5.2-2.5.3).

2.5.1. Characterization of the starting compounds BuMA, EHMA and LMA and evaluation of the developed homopolymers

The structure and NMR spectra of the different starting compounds are displayed in figure 2.13. The different peak annotations are also given in the experimental part (chapter 6; § 6.2.1.2).

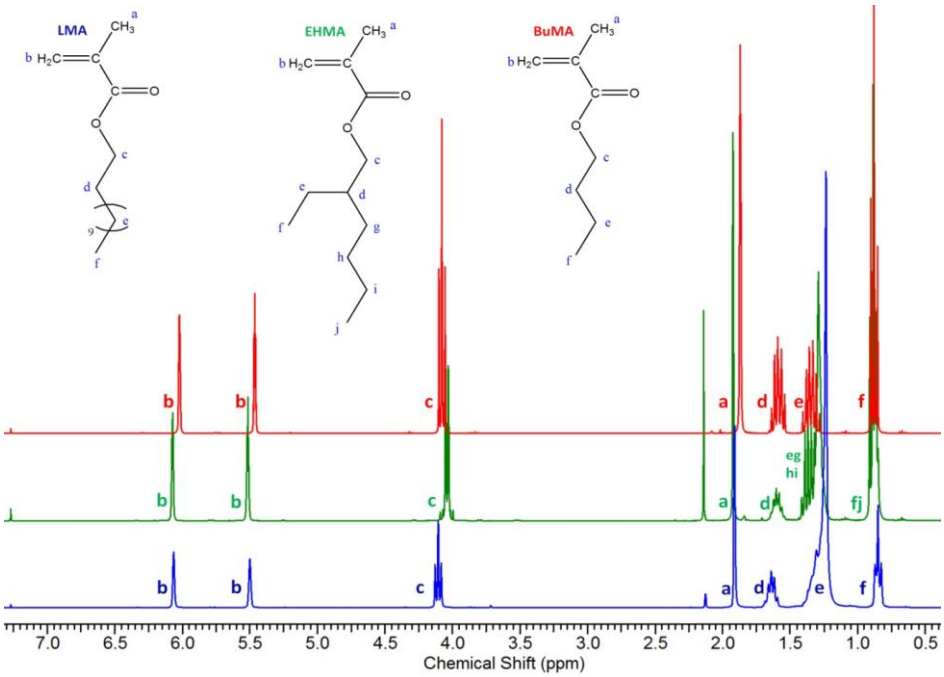

Figure 2.13: ^{1}H-NMR spectrum of BuMA (top), EHMA (middle) and LMA (bottom), recorded in $CDCl_3$. The indices (a,b,c,…) link the protons with the corresponding peaks.

To check for successful polymerization, the vinyl proton integrations were applied. Similar to the PEG-based materials, the UV irradiation time was optimized for the different methacrylate-based compounds under evaluation. Figure 2.14 summarizes the optimization results for BuMA, EHMA and LMA.

In case of PBuMA, conversions of 99% were obtained after 60 minutes irradiation time. It is anticipated that PBuMA is characterized by a higher flexibility compared to PMMA, because of its larger side chains, which is reflected by the lower glass transition temperature of PBuMA (Tg ≈ 24°C,[136]), compared to PMMA (Tg ≈ 105°C). Unfortunately, simple material inspection showed that PBuMA acted as a very stiff and brittle material, which did not possess the required flexibility. As a consequence, BuMA was excluded from further study.

For PEHMA, a solid while sticky material was obtained after 30 minutes, which was characterized by a conversion percentage above 99%. The flexible character of this polymer can be attributed to the low glass transition temperature which is around -10 °C. In

literature, this homopolymer has been described as a flexible material which possesses good adhesion properties at room temperature [137], which confirms the observed stickiness.

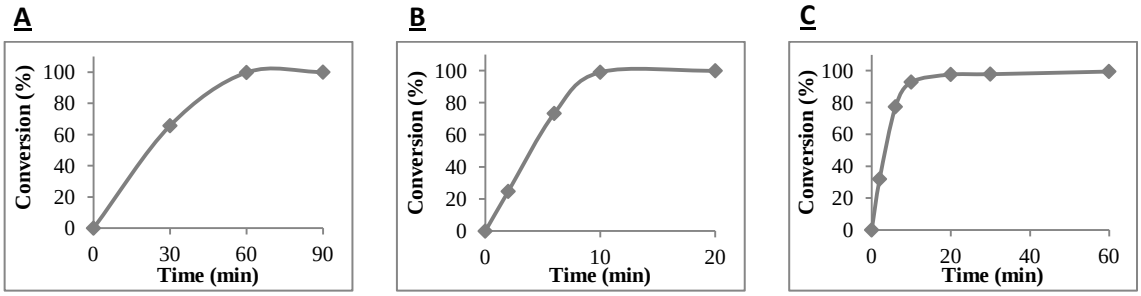

Figure 2.14: Conversion percentage of BuMA (A), EHMA (B) and LMA (C) as a function of UV irradiation time, as determined by ^{1}H NMR spectroscopy using sol-gel studies.

It should be mentioned that for the production of PEHMA, an adjustment was made in the synthesis protocol. So far, all polymers were synthesized by initiation using Irgacure® 2959. As EHMA did not enable dissolution of this initiator, an alternative UV-sensitive initiator was tested, i.e. Irgacure® 651 (2,2-dimethoxy-2-phenylacetophenone). Its structure is shown in figure 2.15.

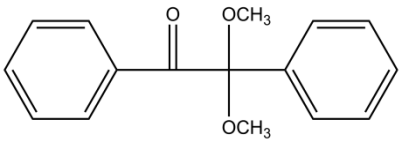

Figure 2.15: Chemical structures of Irgacure® 651

Also for LMA polymerization Irgacure® 651 was selected as initiator due to solubility reasons. Figure 2.14 (C) shows that after 30 minutes, already 97% of the monomer was incorporated into the polymer structure and after 90 minutes of UV irradiation, conversions above 99% were obtained. As a consequence, this UV irradiation time was set as the minimal time to produce the copolymers. Also in this case, the homopolymer behaved as a flexible material, which can again be understood by the low glass transition temperature (Tg) of this material. In literature, Tg's of PLMA are reported to be approximately -53°C [138] and -65°C [139].

It should be mentioned that the use of Irgacure® 651 has been reported as more toxic towards cells compared to the use of Irgacure® 2959 [103]. As a consequence, this was further studied and discussed in § 2.6.3.

2.5.2. Development and characterization of P(MMA-co-EHMA)

As already mentioned in the previous section, PEHMA behaves as a sticky polymer. In the scope of this work, this property could be detrimental towards its ease of use, such as difficulties that could arise during transfer between different sample containers, but more

importantly, the attachment of contaminants that could easily result from this stickiness. As a consequence, different MMA/EHMA copolymers were first visually screened, focusing on this specific property.

The tested MMA/EHMA ratios are summarized in table 2.8, which shows that 80 mol% of EHMA can be set as a maximum to avoid stickiness of the material. On the other hand, a minimum of 70% is required to ensure sufficient material flexibility. Due to the brittle nature of the latter material, the material consisting of 80 mol% EHMA and 20 mol% MMA was selected as initial optimum.

Table 2.8: Overview of the properties of copolymers consisting of different ratios of MMA and EHMA, as visually observed after production. The last column presents the E-moduli of the materials, as determined by tensile testing.

MMA/EHMA ratio	stickiness	flexibility	brittleness	E-mod (MPa)
75/25	-	--	++*	/
50/50	-	-	+	/
40/60	-	-	+	0.7
30/70	-	+	+	1.1
20/80	-	+	-	0.3
10/90	+	++	-	0.1

*The plus sign denotes presence of the mentioned property. A higher number of +-signs indicate a relatively higher tackiness/flexibility of the materials. A minus sign denotes absence of the mentioned poperty.

To confirm this trend and to prove the optimum of 20/80 MMA/EHMA, tensile tests were conducted on the different materials. From table 2.8, it is clear that compared to the PEG-based materials, much lower E-moduli are obtained. Furthermore, an increase of the MMA content resulted in a slight increase of the E-modulus.

Unexpectedly, upon storage of the produced materials during 1 day, the more flexible materials were transformed into very brittle ones. As a consequence, mechanical testing was made impossible. We anticipated that this phenomenon could be ascribed to hydrophobic interactions between the alkyl side chains, which induced an increased brittleness of the material. Due to this observation, EHMA was not further studied as potential comonomer of MMA, but we decided to explore a third co-monomer, lauryl methacrylate.

2.5.3. Development and characterization of P(MMA-co-LMA)

Lauryl methacrylate possesses a long linear side chain, which consists of 12 carbon atoms. For this reason, this monomer was evaluated as co-monomer of MMA. In a preliminary test, different MMA/LMA monomer ratios were evaluated and visually screened for their characteristics. Again, sticky while flexible materials were obtained. Both properties counteracted each other and as a consequence, a compromise had to be made between both.

The first visual screening resulted in the copolymer consisting of 62 mol% MMA and 38 mol% of LMA as the best compromise. Physicochemical analysis showed that the polymer was characterized by an E-modulus of ± 0.4 MPa and a swelling percentage below 1%. Unfortunately, the material again suffered from ageing which resulted in an increased brittleness over time. In order to improve the mechanical stability of the copolymers, it was decided to apply a crosslinker. Different amounts (1, 2 and 5 mol%) of poly(ethylene glycol) dimethacrylate (PEGDMA(550)), described in paragraph 2.4.3, were added to the 'optimal' composition of 62 mol% MMA and 38 mol% LMA and were evaluated.
Since the addition of the crosslinker resulted in a decrease of the material flexibility, the amount of LMA needed to be increased to again obtain more flexible polymers. The preliminary and qualitative evaluation of different material compositions are shown in table 2.9 and the optimal ratio which resulted in a flexible, non-sticky material consisted of 52.5 mol% MMA, 42.5 mol% LMA and 5 mol% PEGDMA. Since this crosslinked material did no longer suffer from ageing, it was selected for further quantitative evaluation.
It should be noted that addition of PEGDMA again enabled the use of Irgacure®2959 as an initiator. As a result, both initiators were compared to study their influence on the physical properties, as well as on the cell toxicity of the materials (see § 2.5.3).

Table 2.9: First line visual screening of copolymers consisting of MMA, LMA and PEGDMA(550).

MMA/LMA/PEGDMA(550) (mol%)	stickiness	flexibility
61.5/37.5/1	-*	+
59.5/39.5/1	+	+
57.5/41.5/1	+	++
54.5/45.5/1	+	+++
54/44/2	+	+++
52.5/42.5/5	-	+++

*The plus sign denotes presence of the mentioned property. A higher number of +-signs indicate a relatively higher tackiness/flexibility of the materials. A minus sign denotes absence of the mentioned poperty.

In a first step, the optimized material was characterized by ^{1}H-NMR spectroscopy. Since the material is crosslinked, HR-MAS NMR spectroscopy had to be performed. Comparison of the spectra of the produced polymers using both types of initiators is shown in figure 2.16. No clear differences were observed between both spectra and the most important observation involved the absence of the signals between 5 and 6.5 ppm, which confirmed a full and successful polymerization.

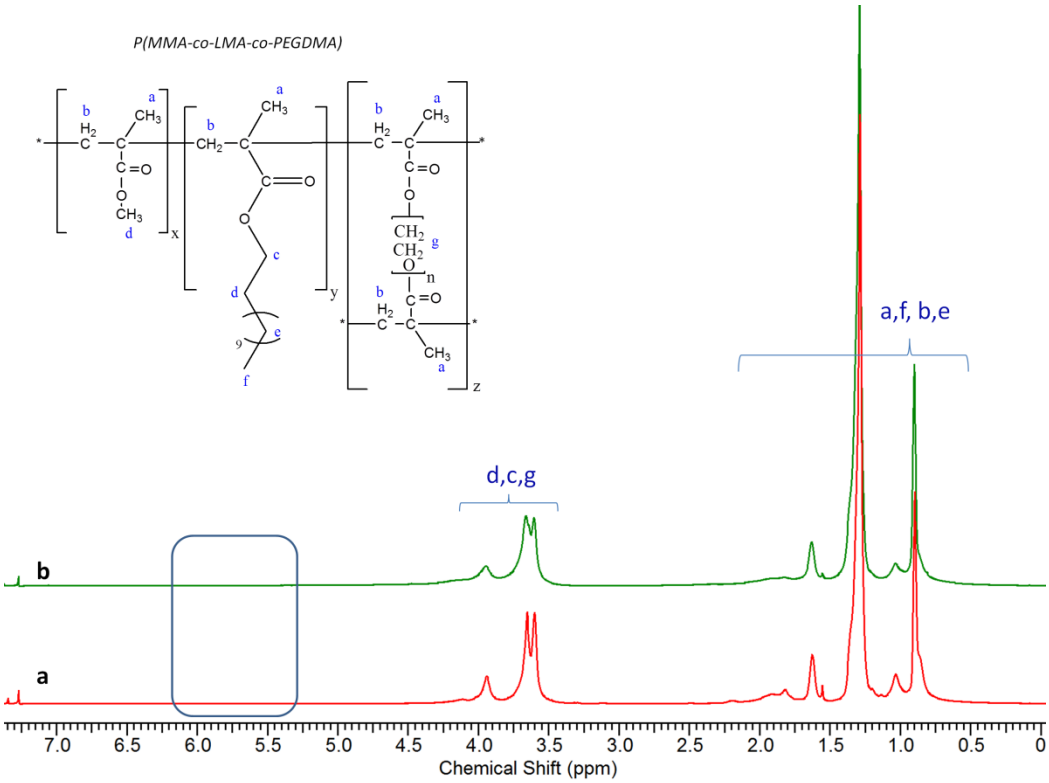

Figure 2.16: ^{1}H NMR spectra of P(MMA-co-LMA-co-PEGDMA) (52.5/42.5/5), produced using Irgacure® 651 (a) and 2959 (b)

Next, mechanical analysis was performed. During this analysis, the amount of added PEGDMA was further optimized and the impact of both initiator types, i.e. Irgacure® 651 and 2959, was evaluated. Table 2.9 showed that the addition of 5 mol% of the crosslinker is a prerequisite to avoid material stickiness. As a result, somewhat higher amounts (7 and 10 mol%) of PEGDMA were also tested for their effect on the mechanical and swelling properties of the material (see table 2.10). As anticipated, an increasing amount of crosslinker resulted in a slightly increased E-modulus ($p>0.05$), a decreased elongation percentage ($p<0.05$) and a slightly increased force at break ($p>0.05$). Indeed, the addition of a crosslinker 'freezed' the polymer chains to some extent, rendering the polymer less flexible and deformable, but more tough and rigid. The more elastic character of this new generation of materials was also apparent when comparing its stress-strain curve with the PMMA reference and the selected material from the previous section, i.e. P(MMA-co-PEGDMA(550)) 50/50 (figure 2.17).
The use of a different initiator only influenced the E-modulus significantly ($p<0.05$), whereas for the other properties, such as elongation, force at break and swelling, no significant differences were observed.

Since PEG was used as a crosslinker, the material hydrophilicity could again be increased. As a result, the swelling percentage of these materials had to be evaluated. Table 2.10 shows that an increase in the crosslinker percentage is reflected in the swelling percentage. Indeed, swelling slightly increased upon introducing higher amounts of PEG-based crosslinker.

Nevertheless, the percentages were still lower than the ones obtained for PMMA (i.e. 2.0 ± 0.2 %) and as a consequence, they could be considered negligible.

Table 2.10. Overview of the bulk properties of the copolymer networks consisting of MMA, LMA and PEGDMA(550), using different initiators (Irgacure® 651 versus 2959). Significantly different results (for 1 initiator type; p<0.05) are denoted with the same letter a,b,c,… All tensile tests were performed at room temperature and the swelling experiments were conducted in milli-Q water at 37°C.

Sample	MMA (mol%)	LMA (mol%)	PEGDMA (mol%)	Irgacure® (type)	E-mod (MPa)	Elongation (%)	Force at break (N)	Swelling (%)
54	52.5	42.5	5	651	3 ± 1^{a}	116 ± 12^{d}	10 ± 4	0.8 ± 0.3^{h}
55	52.5	42.5	7	651	5 ± 1	87 ± 6^{d}	11 ± 3	1.2 ± 0.4^{g}
56	52.5	42.5	10	651	7 ± 1^{a}	68 ± 9^{d}	13 ± 3	$1.7 \pm 0.3^{g,h}$
57	52.5	42.5	5	2959	$6 \pm 1^{b,c}$	$96 \pm 11^{e,f}$	11 ± 2	0.6 ± 0.2^{j}
58	52.5	42.5	7	2959	9 ± 3^{b}	74 ± 8^{e}	12 ± 2	1.1 ± 0.3^{i}
59	52.5	42.5	10	2959	10 ± 1^{c}	61 ± 6^{f}	15 ± 2	$1.6 \pm 0.3^{i,j}$

Also for the optical absorption properties, these low swelling percentages could be considered as a positive result, since water includes one of the major interferents in the NIR detection region. Since no extensive differences were obtained in E-modulus or force at break, the material elongation was selected to be maximized and the swelling to be minimized. As a consequence, the incorporation of only 5 mol% of crosslinker was preferred.

It can thus be concluded that a material was developed with increased flexibility and softness, but also with an improved swelling behavior compared to the PEG-based material.

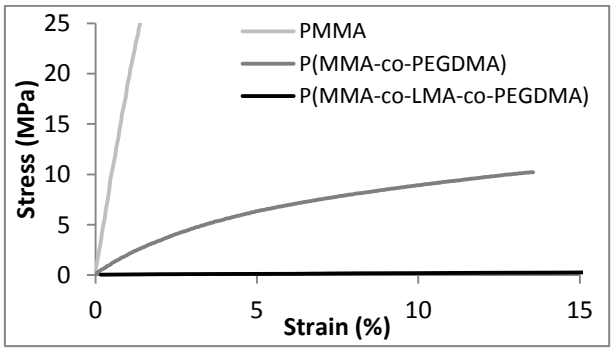

Figure 2.17: Typical stress-strain curves for PMMA, P(MMA-co-PEGDMA(550)) 50/50 and P(MMA-co-LMA-co-PEGDMA) (52.5/42.5/5) as obtained by tensile testing.

It should be noted that the materials initiated by Irgacure® 651 were characterized by a characteristic smell after production and during storage. Since no unreacted monomer was detected by HR-MAS NMR spectroscopy (figure 2.16), a soxhlet extraction was performed to extract and identify the nature of the non-covalently introduced fraction (i.e. the soluble fraction).

It appeared that only 2.52% of the material was extracted from the polymer network and that it mainly consisted of unreacted initiator as illustrated in figure 2.18. After extraction and drying of the samples, the smell disappeared. The results showed that unreacted initiator was the cause for this typical smell. It should be noted that also a small fraction of LMA was detected, as indicated by the arrows. Since no double bond protons were detected, this could refer to a leached-out PLMA fraction that was not included (i.e. covalently bound) inside the polymer network.

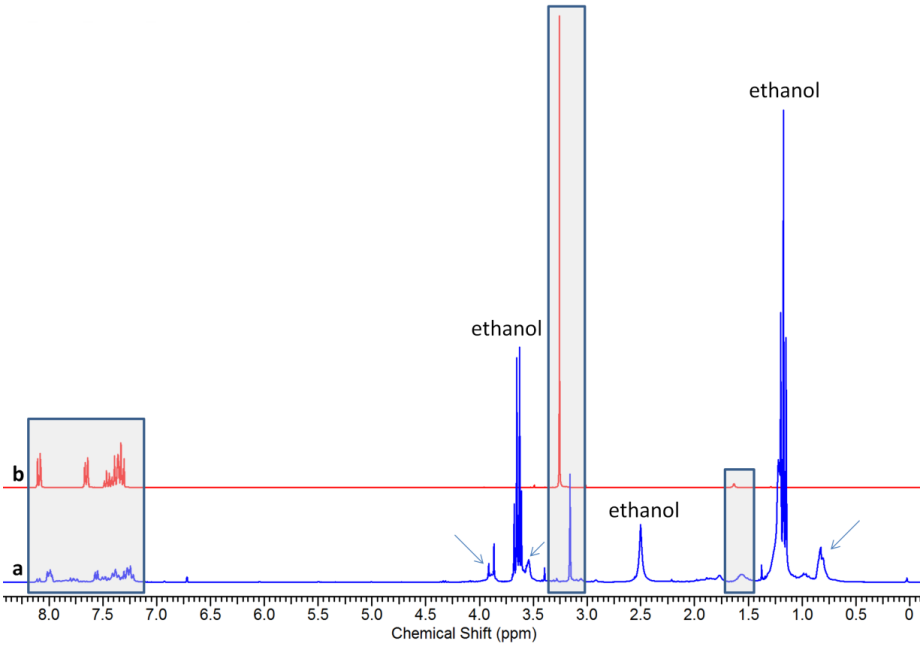

Figure 2.18: ^{1}H NMR spectra of the soluble fraction of poly(MMA(52.5)-co-LMA(42.5)-co-PEGDMA(5)) polymerized in the presence of irgacure®651, obtained after soxhlet extraction in ethanol (a) and of Irgacure® 651 (b).

2.6. Evaluation of the developed materials as packaging of glucose sensor electronics

Previous sections described the optimization of the bulk properties of methacrylate-based polymers, intended for their application as potential packaging material for a glucose sensor. Apart from exhibiting excellent mechanical and swelling properties, additional success criteria had to be fulfilled. In the upcoming paragraphs, two additional criteria are discussed. First, the optical properties of the materials are discussed and secondly, their characteristics in forming a diffusion barrier are evaluated. Finally, some preliminary cell tests will be presented, to investigate the cell toxicity of the different developed materials.

2.6.1. Evaluation of the polymer optical properties[1]

Within the current concept of a glucose sensor, near infrared light was intended to be used to detect glucose in the *in vivo* environment. Since both the laser source and the detector are supposed to be embedded in a polymer packaging, it was important to assess the spectral characteristics of the developed materials. The two wavelength regions which are commonly used to measure glucose are the so-called first overtone band (FOB) (1560-1850 nm) and the combination band (CB) (2080-2325 nm) [140]. For both selected materials (i.e. the PEG-based versus LMA-based), the absorption spectra are displayed in figure 2.19.

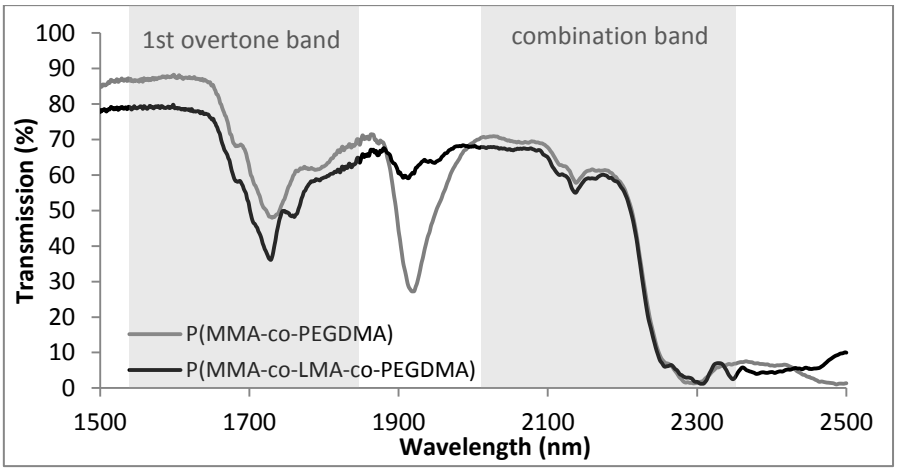

Figure 2.19: Transmission in the near infrared region, recorded for 1 mm thick P(MMA-co-PEGDMA) and P(MMA-co-LMA-co-PEGDMA).

For both materials under investigation, absorption occurred around 1700 nm in the 1st overtone band. In the combination band, strong absorption was observed starting at wavelengths of 2200 nm. These absorptions could be attributed to stretching (combination + overtone region) and bending (combination region) vibrations of C-H bonds in the polymer structures [140]. The results indicated that the strong absorptions could cause some issues, since two out of three features (2.13, 2.27 and 2.32 µm) in the combination band could not be accessed for glucose detection. Predictions based on multivariate analysis are typically more successful in case info is provided on multiple absorption bands. In the present research, only two features are left including one at 2.13 (CB) and 1.59 µm (FOB). Nevertheless, the latter corresponds with one of the least absorbing wavelength features of glucose (4-5 times lower compared to wavelengths in the CB). Furthermore, since the absorption is proportional to the path length of light (see Beer-Lambert law, chapter 1, § 1.3.2.1), a minimal thickness of the polymer packaging should be pursued. Any signal loss caused by polymer absorption will affect the final sensitivity of the glucose sensor. Alternatively, the evanescent sensor, described by Ryckeboer et al, could offer a solution since this concept eliminates light absorption by the polymer packaging [141].

[1] In cooperation with Eva Ryckeboer, from the Faculty of Engineering Sciences and Architecture; Department of Information Technology

2.6.2. Evaluation of the polymers as hermetic barrier[2]

To evaluate the developed materials as hermetic barrier, preliminary tests were executed together with IMEC ('Interuniversitair Micro-Electronica Centrum'). Hermeticity refers to the fact that the materials should be able to encapsulate all electronic compounds, which are considered non-biocompatible and the encapsulating material should function as a 2-directional diffusion barrier. In the past, rigid Ti boxes have frequently been used to package implantable electronic devices, such as pacemakers [142]. Of course, if the same strategy would be used for smaller micro-devices, a titanium packaging would enlarge the size of the final implant tremendously with the result of decreased user comfort. Furthermore, a lack of mechanical compatibility would arise between rigid titanium and the surrounding soft tissue. With respect to this shortcoming, tailored polymer materials could offer a distinct advantage. Within this scope, two of the developed polymers (i.e. P(MMA-co-PEGDMA(550)); 50/50 (PMMAPEG) and P(MMA-co-LMA-co-PEGDMA); 55.5/45.5/5) (PLMA)) were evaluated as potential hermetic coatings, by applying a copper (Cu) corrosion test. For these tests, test samples consisting of copper meanders of various line widths were covered with the barrier layer to be tested (i.e. the polymers under evaluation; see figure 2.20). Next, a glass ring was glued over the Cu meanders, creating a cavity which was filled with PBS buffer. The tests were performed at 37°C and at 70°C. The higher temperature was included to mimic stressed conditions (i.e. accelerated ageing of Copper) and to understand, whether or not, accelerated effects might occur. A good hermetic barrier is typically characterized by low corrosion of copper, which is reflected by low resistance of the Cu-meanders. For these tests, metallic copper (i.e. Cu^0) was selected because of its sufficiently fast corrosion properties, its low cost, but also its omnipresence in sensor chips.

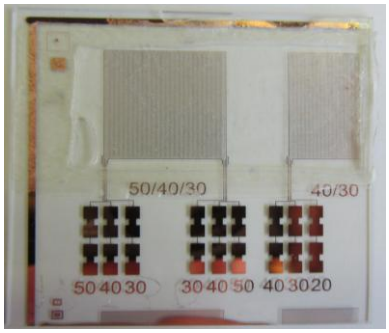

Figure 2.20: Image of the test samples consisting of copper meanders of various line widths used for Cu-corrosion testing.

In case PMMAPEG was used as potential hermetic layer, swelling was noticed and as a result, detachment from the copper samples was observed. It could be concluded that swelling of the materials induced inferior adhesion to the copper samples and as a result, PMMAPEG was identified to be insufficient as hermetic barrier. For PLMA on the other hand, no

[2] In cooperation with Maaike Op de Beeck from the Centre for Microsystems Technology (CMST), affiliated with IMEC vzw

swelling was observed and the resistance in copper meanders of different widths was measured over time in order to quantify a potential corrosion phenomenon. Figure 2.21 clearly shows that the smaller the line width of the copper meander, the faster corrosion occurred. At 70°C, the 50 µm lines started to corrode after 20 hours of incubation. Afterwards, the resistance increased steadily towards full corrosion.

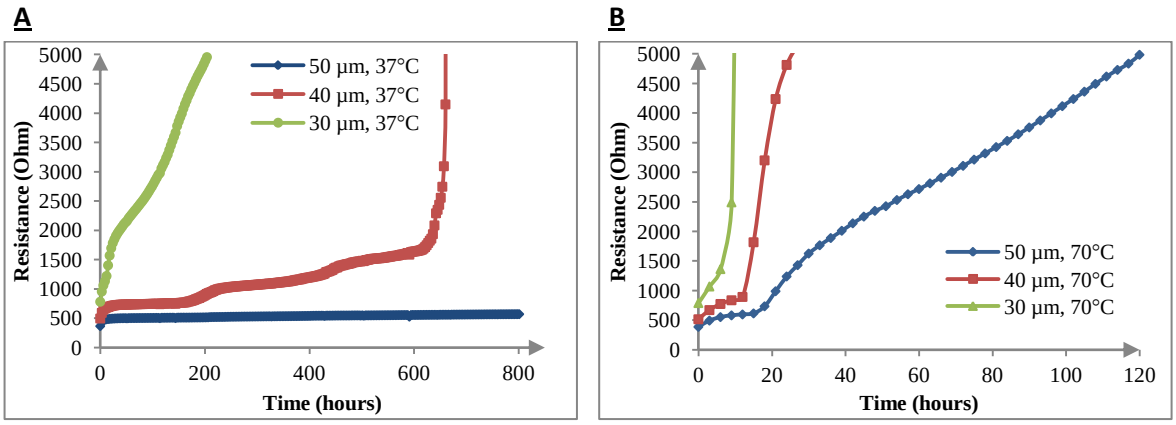

Figure 2.21: Evaluation of the resistance change of PLMA protected Cu meanders of 30, 40 and 50 µm width which are exposed to PBS buffer at 37°C (A) and 70°C (B).

When comparing these results to the ones obtained for unprotected Cu-meanders (figure 2.22, A), similar trends could be observed in case unprotected copper was measured. After 200 hours of exposure, infinite high resistances were measured for all Cu-lines, which indicated that corrosive sensitive electronics must be protected from the body environment upon implantation. Furthermore, these results showed that the LMA-based polymer was permeable for moisture, rendering it a non-ideal hermetic barrier. The underlying cause for this observation could be an inferior adhesion between the polymer and the copper substrate. Alternatively, despite the material's hydrophobic nature, these results might also suggest potential diffusion of water through the polymer network.

If a polymer is used as coating for electronic devices, it is clear that an additional barrier has to be included to avoid diffusion of body fluids. A frequently used example of such a hermetic barrier is a parylene C coating, which is a vapour-deposited poly(p-xylylene) polymer which is frequently used as a barrier for moisture and gases and as dielectric barrier [143]. Homogeneous coatings of this polymer can be obtained, even at room temperature. The barrier properties of this polymer were evaluated by IMEC (see figure 2.22, B). The results showed that the resistance remained constant for more than 600 hours, indicating delayed corrosion.

To conclude, the available polymers did not provide sufficient protection for both the implant itself against fluid penetration nor for the local tissue to avoid adverse effects upon implantation due to potential leaching of toxic substances from the electronics. Therefore, the polymer-based implant encapsulation should ideally be complemented by hermetic barriers such as parylene C in order to provide a bi-directional diffusion barrier insulating the

implanted electronics from the body. Future research should thus focus on the study and optimization of the adhesion between the developed polymers and the diffusion barrier.

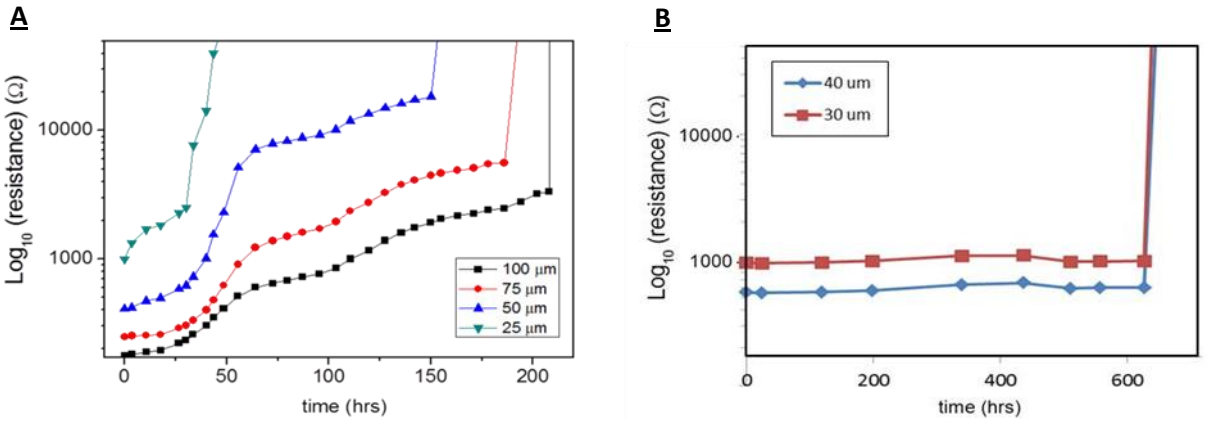

Figure 2.22: Evaluation of the resistance change of Cu meanders exposed to PBS buffer at 70°C: unprotected Cu meanders of 25, 50, 75 and 100 um width, during 200 hours (A) and parylene C-protected (5µm) Cu meanders of 30 and 40 µm width (B).

2.6.3. Preliminary cell tests: Cytotoxicity and cell interactivity of the developed materials.[3]

Since the materials are intended for implantation, possible cell toxicity needs to be considered. In order to assess preliminary information regarding the potential cytotoxicity of the selected polymers, a colorimetric assay was used, applying the tetrazolium salt 3-(4,5-dimethylthiazol-2-yl)-2,5-diphenyltetrazolium bromide (MTT). The tetrazolium salt can readily enter cells where it is reduced to the insoluble formazan by NAD(P)H-dependent oxidoreductases of metabolically active cells (see figure 2.23) [144]. The yellow MTT is hereby converted into a purple formazan, which can be analyzed quantitatively by spectrophotometry.

Figure 2.23: Enzymatic conversion of 3-(4,5-dimethylthiazol-2-yl)-2,5-diphenyltetrazolium bromide (MTT) to (*E,Z*)-5-(4,5-dimethylthiazol-2yl)-1,3-diphenylformazan (formazan)

Prior to spectroscopic analysis, the polymer samples (n = 3) were extracted with cell medium. Next, different dilutions were prepared from the extraction media and added to a

[3] In cooperation with Heidi Declercq and Johanna Aernoudt, from the Tissue Engineering Group of the Department of Basic Medical Sciences

96 well plate that contained human foreskin fibroblast (HFF) cells. After 2 days of incubation, the MTT solution was added and the cells were lysed in order to read out the absorbance. It should be noted that these tests were conducted according the ISO 10993 standard to gain initial insight in the potential of the materials and the necessity for material optimization. In case cell viabilities below 70% would have been obtained, the bulk materials would be excluded from future experiments.
From the results (see figure 2.24) it is clear that both PMMA and PMMAPEG obeyed the minimum standard, as viabilities higher than 70% were obtained (figure 2.24, A).
In case of PLMA (see figure 2.24, B), on the other hand, the undiluted and non-soxhlet-extracted samples showed cell viabilities below 70%. Nevertheless, upon further dilution of the cell media, the minimum value of 70% was reached for both initiator types. This result suggests that the studied materials could be considered as inherently non-toxic.
Extraction of the samples illustrated that the viability tends to increase, especially in case Irgacure® 2959 was used as an initiator, although no significant differences were obtained when comparing both conditions (extraction vs no extraction) ($p>0.05$). In this respect, it can be noted that soxhlet extraction of the prepared samples in ethanol affected the mechanical integrity of the materials, as illustrated by crack formation. As a consequence, the execution of such an extraction was not further considered.

If both initiators are compared, the present data show a small preference towards the use of Irgacure® 651. These data thus contradict literature reports, as previous results showed that Irgacure® 2959 offers a good cytocompatibility and a less cytotoxic nature compared to Irgacure® 651 [103, 145]. In those studies, six different mammalian cell types were exposed to certain initiator concentrations (0.03 - 0.1% w/v) while Irgacure® 2959 resulted in the lowest toxicity. It can be concluded that the different results obtained were possibly caused by the different experimental approach. Nevertheless, if only the non-extracted values are considered, similar cell viabilities were obtained for both photo-initiators and as a consequence, both of them were included in the surface modification strategies (see chapter 3).

In a next step, the cell interactivity of the pristine polymers was evaluated by means of a live/dead assay. Herein, living cells are stained with a green color, whereas dead cells are washed away or stained in red. Figure 2.24, C clearly demonstrates that on PMMAPEG almost no cells were adhering, whereas PMMA and PLMA already showed higher cell densities. Nevertheless, compared to the control, more cell clusters (i.e. agglomerated cells) were present and the natural cuboidal shape of the human umbilical vascular endothelial cells (HUVECs) was not always present for the developed materials. In the current work, cell interactivity of the sensor packaging is targeted, because in the end, after implanting the materials, the creation of a fluid pocket had to be avoided. Instead, the formation of functional and vascularized tissue had to be pursued (see chapter 4). A proper cell interactivity of the materials was thus appreciated as a good indicator for the *in vivo* success

of the developed materials. To further improve the cell interactivity of the herein developed materials, surface modifications were performed and the discussion of these results will be topic of the upcoming chapters (chapter 3 and 4).

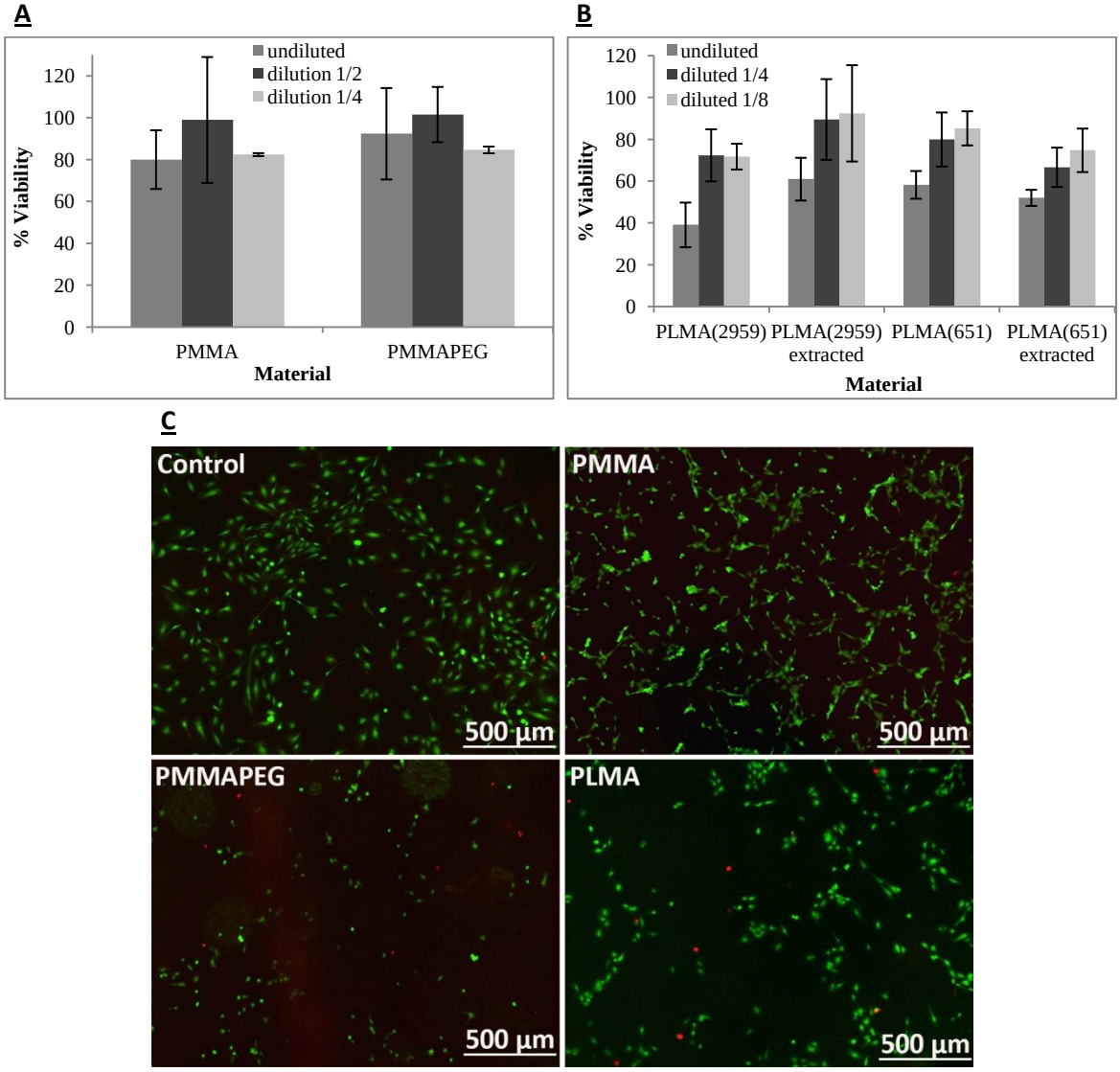

Figure 2.24: MTT assays to evaluate the cell toxicity of the developed materials, i.e. PMMAPEG (A) and PLMA (B). In case of the LMA-based materials, both the influence of the initiator and an extraction step were evaluated. A live/dead assay was performed to evaluate the cell interactivity of the pristine polymers (C).

2.7. Conclusion

In the present chapter, different MMA-based copolymers have been developed and characterized. In case of PEG incorporation, a broad range of flexible while hydrophilic materials were obtained, of which the material consisting of 50 mol% MMA and 50 mol% PEGDMA(550) (PMMAPEG) was selected as a potential candidate for packaging a glucose sensor. This material was characterized by a 10-fold lower E-modulus (142 MPa) when

compared to PMMA (1600 MPa), which was actually still an underestimation, as the body environment will cause swelling (17%) with a further decrease of the E-modulus (53 MPa) as a consequence. Furthermore, a second potential candidate was identified (i.e. the 3-component system consisting of 55.5 mol% MMA, 45.5 mol% LMA and 5 mol% PEGDMA(550)). Compared to the swollen PEG-based material, an even lower E-modulus was obtained (6 MPa) together with lower swelling percentages (0.6%). For both materials, similar absorption behavior was obtained in the near-IR region. Because of the presence of absorption peaks, the polymer packaging should preferably be as thin as possible (<< 1mm) or even excluded from the optical path. Furthermore, it was shown that none of the polymers would act as a proper barrier layer. As a consequence, combination of the polymer packaging with a superior insulating layer such as parylene C, will be a prerequisite to ensure a successful operating system. In this respect, future work should definitely focus on the optimization of the adhesion properties between this insulating layer and the polymer packaging itself.

Finally, PMMA and the PEG-based material could be considered as intrinsically non-toxic, since cell viabilities higher than 70% were obtained. On the other hand, the LMA-based materials gave rise to a slightly higher cell toxicity in case irgacure®2959 was used as initiator instead of Irgacure®651. Nevertheless, both initiators will still be considered during future experiments.

In the upcoming chapter, both materials of choice will be subjected to different surface modification strategies in order to enhance their biocompatibility.

2.8. References

1. Reynolds, M. A. (2010) Regeneration of periodontal tissue: bone replacement grafts, *Dental clinics of North America* 54, 55.
2. Apple, D. J., and Sims, J. (1996) Harold Ridley and the invention of the intraocular lens, *Surv. Ophthalmol.* 40, 279-292.
3. Mikos, J. S. T. A. G. (2008) *Biomaterials: The Intersection of Biology and Materials Science*, Pearson/Prentice Hall, 2008.
4. Lloyd, A. W., Faragher, R. G. A., and Denyer, S. P. (2001) Ocular biomaterials and implants, *Biomaterials* 22, 769-785.
5. Tan, D. T. H., Pullum, K. W., and Buckley, R. J. (1995) Medical applications of scleral contact lenses.1. A retrospective analysis of 343 cases, *Cornea* 14, 121-129.
6. Schaeffer, J., and Beiting, J. (2007) The early history of contact lenses, *Review of Optometry* 144, 3-8.
7. Mousa, W. F. (2000) Biological and mechanical properties of PMMA-based bioactive bone cements, *Biomaterials* 21, 2137.
8. Charnley, J. (1970) 2 Total Hip Replacement by Low-Friction Arthroplasty, *Clinical orthopaedics and related research* 72, 7-21.
9. Ratner, B. D., and Bryant, S. J. (2004) Biomaterials: where we have been and where we are going, *Annu. Rev. Biomed. Eng.* 6, 41-75.
10. Van Landuyt, K. L., Snauwaert, J., De Munck, J., Peurnans, M., Yoshida, Y., Poitevin, A., Coutinho, E., Suzuki, K., Lambrechtsa, P., and Van Meerbeek, B. (2007) Systematic review of the chemical composition of contemporary dental adhesives, *Biomaterials* 28, 3757-3785.

11. Bettencourt, A., and Almeida, A. J. (2012) Poly(methyl methacrylate) particulate carriers in drug delivery, *Journal of Microencapsulation* 29, 353-367.
12. Vargas, K. F., Borghetti, R. L., Moure, S. P., Salum, F. G., Cherubini, K., and de Figueiredo, M. A. Z. (2012) Use of polymethylmethacrylate as permanent filling agent in the jaw, mouth and face regions - implications for dental practice, *Gerodontology* 29, E16-E22.
13. Kluin, O. S., van der Mei, H. C., Busscher, H. J., and Neut, D. (2013) Biodegradable vs non-biodegradable antibiotic delivery devices in the treatment of osteomyelitis, *Expert Opinion on Drug Delivery* 10, 341-351.
14. Raj, P. A., and Dentino, A. R. (2013) Denture polymers with antimicrobial properties: a review of the development and current status of anionic poly(methyl methacrylate) polymers, *Future Medicinal Chemistry* 5, 1635-1645.
15. Ikemura, K., and Endo, T. (2010) A review of our development of dental adhesives - Effects of radical polymerization initiators and adhesive monomers on adhesion, *Dental Materials Journal* 29, 109-121.
16. Gautam, R., Singh, R. D., Sharma, V. P., Siddhartha, R., Chand, P., and Kumar, R. (2012) Biocompatibility of polymethylmethacrylate resins used in dentistry, *J. Biomed. Mater. Res. Part B* 100B, 1444-1450.
17. Shah, S. R., Tatara, A. M., D'Souza, R. N., Mikos, A. G., and Kasper, F. K. (2013) Evolving strategies for preventing biofilm on implantable materials, *Materials Today* 16, 177-182.
18. Ascherl, R. (2010) Infection management of megaimplants, *Orthopade* 39, 980-+.
19. Kodjikian, L., Roques, C., Pellon, G., Renaud, F., Hartmann, D., Freney, J., and Burillon, C. (2006) Bacterial adhesion to intraocular lenses and enclophthalmitis prevention: review of the literature, *Journal Francais D Ophtalmologie* 29, 74-81.
20. Ochsner, P. E. (2011) Osteointegration of orthopaedic devices, *Seminars in Immunopathology* 33, 245-256.
21. Nair, M. B., Kretlow, J. D., Mikos, A. G., and Kasper, F. K. (2011) Infection and tissue engineering in segmental bone defects - a mini review, *Current Opinion in Biotechnology* 22, 721-725.
22. Lewis, G. (2011) Viscoelastic properties of injectable bone cements for orthopaedic applications: State-of-the-art review, *J. Biomed. Mater. Res. Part B* 98B, 171-191.
23. Jaeblon, T. (2010) Polymethylmethacrylate: Properties and Contemporary Uses in Orthopaedics, *Journal of the American Academy of Orthopaedic Surgeons* 18, 297-305.
24. Tihan, T. G., Ionita, M. D., Popescu, R. G., and Iordachescu, D. (2009) Effect of hydrophilic-hydrophobic balance on biocompatibility of poly(methyl methacrylate) (PMMA)-hydroxyapatite (HA) composites, *Materials Chemistry and Physics* 118, 265-269.
25. Kenny, S. M., and Buggy, M. (2003) Bone cements and fillers: A review, *Journal of Materials Science-Materials in Medicine* 14, 923-938.
26. Findl, O., Buehl, W., Bauer, P., and Sycha, T. (2010) Interventions for preventing posterior capsule opacification, *Cochrane Database of Systematic Reviews*.
27. Nordstierna, L., Abdalla, A. A., Nordin, M., and Nyden, M. (2010) Comparison of release behaviour from microcapsules and microspheres, *Progress in Organic Coatings* 69, 49-51.
28. Barth, R. E., Vogely, H. C., Hoepelman, A. I. M., and Peters, E. J. G. (2011) 'To bead or not to bead?' Treatment of osteomyelitis and prosthetic joint-associated infections with gentamicin bead chains, *International Journal of Antimicrobial Agents* 38, 371-375.
29. Haidar, R., Boghossian, A. D., and Atiyeh, B. (2010) Duration of post-surgical antibiotics in chronic osteomyelitis: empiric or evidence-based?, *International Journal of Infectious Diseases* 14, E752-E758.
30. Niiyama, S., Yamaga, O., Nakamura, A., Takasu, O., Yamashita, N., Ushijima, K., and Sakamoto, T. (2012) An *in vitro* study of the ability of a PMMA membrane hemofilter to adsorb a high concentration of interleukin-6 in human waste ascites under a spiked recovery test., *Critical Care Medicine* 40, U66-U67.

31. Wang, Y., Vaidya, B., Farquar, H. D., Stryjewski, W., Hammer, R. P., McCarley, R. L., Soper, S. A., Cheng, Y. W., and Barany, F. (2003) Microarrays assembled in microfluidic chips fabricated from poly(methyl methacrylate) for the detection of low-abundant DNA mutations, *Analytical Chemistry* 75, 1130-1140.
32. Alrifaiy, A., Lindahl, O. A., and Ramser, K. (2012) Polymer-Based Microfluidic Devices for Pharmacy, Biology and Tissue Engineering, *Polymers* 4, 1349-1398.
33. Adams, A. A., Okagbare, P. I., Feng, J., Hupert, M. L., Patterson, D., Gottert, J., McCarley, R. L., Nikitopoulos, D., Murphy, M. C., and Soper, S. A. (2008) Highly efficient circulating tumor cell isolation from whole blood and label-free enumeration using polymer-based microfluidics with an integrated conductivity sensor, *Journal of the American Chemical Society* 130, 8633-8641.
34. Tsougeni, K., Papageorgiou, D., Tserepi, A., and Gogolides, E. (2010) "Smart'" polymeric microfluidics fabricated by plasma processing: controlled wetting, capillary filling and hydrophobic valving, *Lab on a Chip* 10, 462-469.
35. Aklalouch, M., Calleja, A., Granados, X., Ricart, S., Boffa, V., Ricci, F., Puig, T., and Obradors, X. (2014) Hybrid sol-gel layers containing CeO2 nanoparticles as UV-protection of plastic lenses for concentrated photovoltaics, *Solar Energy Materials and Solar Cells* 120, 175-182.
36. Miller, D. C., and Kurtz, S. R. (2011) Durability of Fresnel lenses: A review specific to the concentrating photovoltaic application, *Solar Energy Materials and Solar Cells* 95, 2037-2068.
37. Languy, F., Fleury, K., Lenaerts, C., Loicq, J., Regaert, D., Thibert, T., and Habraken, S. (2011) Flat Fresnel doublets made of PMMA and PC: combining low cost production and very high concentration ratio for CPV, *Optics Express* 19, A280-A294.
38. Stephan, A. M., and Nahm, K. S. (2006) Review on composite polymer electrolytes for lithium batteries, *Polymer* 47, 5952-5964.
39. Stephan, A. M. (2006) Review on gel polymer electrolytes for lithium batteries, *European polymer journal* 42, 21-42.
40. Song, J. Y., Wang, Y. Y., and Wan, C. C. (1999) Review of gel-type polymer electrolytes for lithium-ion batteries, *Journal of Power Sources* 77, 183-197.
41. Nicho, M. E., Trejo, M., Garcia-Valenzuela, A., Saniger, J. M., Palacios, J., and Hu, H. (2001) Polyaniline composite coatings interrogated by a nulling optical-transmittance bridge for sensing low concentrations of ammonia gas, *Sensors and Actuators B-Chemical* 76, 18-24.
42. Daneshkhah, A., Shrestha, S., Agarwal, M., and Varahramyan, K. (2014) PPy/PMMA/PEG-based sensor for low-concentration acetone detection, *Smart Biomedical and Physiological Sensor Technology Xi* 9107.
43. Webster, O. W. (1991) LIVING POLYMERIZATION METHODS, *Science* 251, 887-893.
44. Kato, M., Kamigaito, M., Sawamoto, T., and Higashimura. (1995) Polymerization of Methyl Methacrylate with the Carbon Tetrachloride/Dichlorotris-(triphenylphosphine)ruthenium(II)/Methylaluminum Bis(2,6-di-tert-butylphenoxide) Initiating System: Possibility of Living Radical Polymerization, *Macromolecules* 28, 1721-1723.
45. Ando, T., Kato, M., Kamigaito, M., and Sawamoto, M. (1996) Living radical polymerization of methyl methacrylate with ruthenium complex: Formation of polymers with controlled molecular weights and very narrow distributions, *Macromolecules* 29, 1070-1072.
46. Granel, C., Dubois, P., Jerome, R., and Teyssie, P. (1996) Controlled radical polymerization of methacrylic monomers in the presence of a bis(ortho-chelated) arylnickel(II) complex and different activated alkyl halides, *Macromolecules* 29, 8576-8582.
47. Uegaki, H., Kotani, Y., Kamigaito, M., and Sawamoto, M. (1998) NiBr2(Pn-Bu-3)(2)-mediated living radical polymerization of methacrylates and acrylates and their block or random copolymerizations, *Macromolecules* 31, 6756-6761.
48. Moineau, G., Minet, M., Dubois, P., Teyssie, P., Senninger, T., and Jerome, R. (1999) Controlled radical polymerization of (meth)acrylates by ATRP with NiBr2(PPh3)(2) as catalyst, *Macromolecules* 32, 27-35.

49. Grimaud, T., and Matyjaszewski, K. (1997) Controlled/''living'' radical polymerization of methyl methacrylate by atom transfer radical polymerization, *Macromolecules* 30, 2216-2218.
50. Haddleton, D. M., Jasieczek, C. B., Hannon, M. J., and Shooter, A. J. (1997) Atom transfer radical polymerization of methyl methacrylate initiated by alkyl bromide and 2-pyridinecarbaldehyde imine copper(I) complexes, *Macromolecules* 30, 2190-2193.
51. Hatada, K., and Kitayama, T. (2000) Structurally controlled polymerizations of methacrylates and acrylates, *Polymer international* 49, 11-47.
52. Moineau, G., Dubois, P., Jerome, R., Senninger, T., and Teyssie, P. (1998) Alternative atom transfer radical polymerization for MMA using FeCl3 and AIBN in the presence of triphenylphosphine: An easy way to well-controlled PMMA, *Macromolecules* 31, 545-547.
53. Kotani, Y., Kato, M., Kamigaito, M., and Sawamoto, M. (1996) Living radical polymerization of alkyl methacrylates with ruthenium complex and synthesis of their block copolymers, *Macromolecules* 29, 6979-6982.
54. Kotani, Y., Kamigaito, M., and Sawamoto, M. (1998) Living random copolymerization of styrene and methyl methacrylate with a Ru(II) complex and synthesis of ABC-Type "Block-Random" copolymers, *Macromolecules* 31, 5582-5587.
55. Costa, R. O. R., Vasconcelos, W. L., Tamaki, R., and Laine, R. M. (2001) Organic/inorganic nanocomposite star polymers via atom transfer radical polymerization of methyl methacrylate using octafunctional silsesquioxane cores, *Macromolecules* 34, 5398-5407.
56. Xu, Y. J., and Pan, C. Y. (2000) Block and star-block copolymers by mechanism transformation. 3. S-(PTHF-PSt)(4) and S-(PTHF-PSt-PMMA)(4) from living CROP to ATRP, *Macromolecules* 33, 4750-4756.
57. Shah, R. R., Merreceyes, D., Husemann, M., Rees, I., Abbott, N. L., Hawker, C. J., and Hedrick, J. L. (2000) Using atom transfer radical polymerization to amplify monolayers of initiators patterned by microcontact printing into polymer brushes for pattern transfer, *Macromolecules* 33, 597-605.
58. Jones, D. M., Brown, A. A., and Huck, W. T. S. (2002) Surface-initiated polymerizations in aqueous media: Effect of initiator density, *Langmuir* 18, 1265-1269.
59. Ohno, K., Koh, K., Tsujii, Y., and Fukuda, T. (2002) Synthesis of gold nanoparticles coated with well-defined, high-density polymer brushes by surface-initiated living radical polymerization, *Macromolecules* 35, 8989-8993.
60. Mandal, T. K., Fleming, M. S., and Walt, D. R. (2002) Preparation of polymer coated gold nanoparticles by surface-confined living radical polymerization at ambient temperature, *Nano Letters* 2, 3-7.
61. Kong, X. X., Kawai, T., Abe, J., and Iyoda, T. (2001) Amphiphilic polymer brushes grown from the silicon surface by atom transfer radical polymerization, *Macromolecules* 34, 1837-1844.
62. Pyun, J., Jia, S. J., Kowalewski, T., Patterson, G. D., and Matyjaszewski, K. (2003) Synthesis and characterization of organic/inorganic hybrid nanoparticles: Kinetics of surface-initiated atom transfer radical polymerization and morphology of hybrid nanoparticle ultrathin films, *Macromolecules* 36, 5094-5104.
63. Ohno, K., Morinaga, T., Koh, K., Tsujii, Y., and Fukuda, T. (2005) Synthesis of monodisperse silica particles coated with well-defined, high-density polymer brushes by surface-initiated atom transfer radical polymerization, *Macromolecules* 38, 2137-2142.
64. Li, C., Han, J., Ryu, C. Y., and Benicewicz, B. C. (2006) A versatile method to prepare RAFT agent anchored substrates and the preparation of PMMA grafted nanoparticles, *Macromolecules* 39, 3175-3183.
65. Kokubo, H., and Watanabe, M. (2008) Anionic polymerization of methyl methacrylate in an ionic liquid, *Polymers for Advanced Technologies* 19, 1441-1444.
66. Dhara, M. G., Sivaram, S., and Baskaran, D. (2009) Synthesis of hydroxy-functionalized star-branched PMMA by anionic polymerization, *Polymer Bulletin* 63, 185-196.

67. Pangilinan, K., and Advincula, R. (2013) Synthesis of PS-PMMA polymer 2 catenane block copolymer by "click" reaction, *Abstracts of Papers of the American Chemical Society* 246.
68. Huang, X. Y., and Brittain, W. J. (2001) Synthesis and characterization of PMMA nanocomposites by suspension and emulsion polymerization, *Macromolecules* 34, 3255-3260.
69. Zheng, W., and Wong, S. C. (2003) Electrical conductivity and dielectric properties of PMMA/expanded graphite composites, *Composites Science and Technology* 63, 225-235.
70. Chen, G. H., Weng, W. G., Wu, D. J., and Wu, C. L. (2003) PMMA/graphite nanosheets composite and its conducting properties, *European polymer journal* 39, 2329-2335.
71. Mishra, S. K., Tripathi, S. N., Choudhary, V., and Gupta, B. D. (2014) SPR based fibre optic ammonia gas sensor utilizing nanocomposite film of PMMA/reduced graphene oxide prepared by in situ polymerization, *Sensors and Actuators B-Chemical* 199, 190-200.
72. Wang, T., Shen, J.-n., Wu, L.-g., and Van der Bruggen, B. (2014) Improvement in the permeation performance of hybrid membranes by the incorporation of functional multi-walled carbon nanotubes, *Journal of Membrane Science* 466, 338-347.
73. Park, S. J., Cho, M. S., Lim, S. T., Choi, H. J., and Jhon, M. S. (2003) Synthesis and dispersion characteristics of multi-walled carbon nanotube composites with poly(methyl methacrylate) prepared by in-situ bulk polymerization, *Macromol. Rapid Commun.* 24, 1070-1073.
74. Sung, J. H., Kim, H. S., Jin, H. J., Choi, H. J., and Chin, I. J. (2004) Nanofibrous membranes prepared by multiwalled carbon nanotube/poly(methyl methacrylate) composites, *Macromolecules* 37, 9899-9902.
75. Jia, Z. J., Wang, Z. Y., Xu, C. L., Liang, J., Wei, B. Q., Wu, D. H., and Zhu, S. W. (1999) Study on poly(methyl methacrylate)/carbon nanotube composites, *Materials Science and Engineering a-Structural Materials Properties Microstructure and Processing* 271, 395-400.
76. Hammer, P., dos Santos, F. C., Cerrutti, B. M., Pulcinelli, S. H., and Santilli, C. V. (2013) Carbon nanotube-reinforced siloxane-PMMA hybrid coatings with high corrosion resistance, *Progress in Organic Coatings* 76, 601-608.
77. Weng, B., Xu, F., Salinas, A., and Lozano, K. (2014) Mass production of carbon nanotube reinforced poly(methyl methacrylate) nonwoven nanofiber mats, *Carbon* 75, 217-226.
78. Wang, B., Zhou, K., Jiang, S., Shi, Y., Wang, B., Gui, Z., and Hu, Y. (2014) Poly(methyl methacrylate)/layered zinc sulfide nanocomposites: Preparation, characterization and the improvements in thermal stability, flame retardant and optical properties, *Materials Research Bulletin* 56, 107-112.
79. Li, Y., Zhang, S., Gao, L., Chen, W., Gao, L., Zhang, W., Cui, J., and Yan, S. (2014) The Preparation and Characterization of ZnS/PMMA Nanocomposites, *Synthesis and Reactivity in Inorganic Metal-Organic and Nano-Metal Chemistry* 44, 942-945.
80. Zhou, K., Liu, J., Wang, B., Zhang, Q., Shi, Y., Jiang, S., Hu, Y., and Gui, Z. (2014) Facile preparation of poly(methyl methacrylate)/MoS2 nanocomposites via in situ emulsion polymerization, *Materials letters* 126, 159-161.
81. Okamoto, M., Morita, S., Taguchi, H., Kim, Y. H., Kotaka, T., and Tateyama, H. (2000) Synthesis and structure of smectic clay/poly(methyl methacrylate) and clay/polystyrene nanocomposites via in situ intercalative polymerization, *Polymer* 41, 3887-3890.
82. Biasci, L., Aglietto, M., Ruggeri, G., and Ciardelli, F. (1994) Functionalization of montmorillonite by methyl-methacrylate polymers containing side-chain ammonium cations., *Polymer* 35, 3296-3304.
83. Lee, D. C., and Jang, L. W. (1996) Preparation and characterization of PMMA-clay hybrid composite by emulsion polymerization, *Journal of Applied Polymer Science* 61, 1117-1122.
84. Zeng, C. C., and Lee, L. J. (2001) Poly(methyl methacrylate) and polystyrene/clay nanocomposites prepared by in-situ polymerization, *Macromolecules* 34, 4098-4103.
85. Ash, B. J., Schadler, L. S., and Siegel, R. W. (2002) Glass transition behavior of alumina/polymethylmethacrylate nanocomposites, *Materials letters* 55, 83-87.

86. Landry, C. J. T., Coltrain, B. K., and Brady, B. K. (1992) In situ polymerization of tetraethoxysilane in poly(methyl methacrylate) - morphology and dynamic mechanical properties. , *Polymer* 33, 1486-1495.
87. Mu, J., Zhou, Y. M., Bu, X. H., and Zhang, T. (2014) Preparation and Characterization of Micron-Sized PMMA/SiO2 Composite Microspheres, *J. Inorg. Organomet. Polym. Mater.* 24, 776-779.
88. Morales Nieto, V., Navarro, C. H., Moreno, K. J., Arizmendi Morquecho, A., Chavez Valdez, A., Chávez Valdez, A., García Miranda, S., and Louvier Hernández, J. F. (2013) Poly(methyl methacrylate)/carbonated hydroxyapatite composite applied as coating on ultra high molecular weight polyethylene, *Progress in Organic Coatings* 76, 204-208.
89. Rao, M., Su, Q., Liu, Z., Liang, P., Wu, N., Quan, C., and Jiang, Q. (2014) Preparation and Characterization of a Poly(methyl methacrylate) Based Composite Bone Cement Containing Poly(acrylate-co-silane) Modified Hydroxyapatite Nanoparticles, *Journal of Applied Polymer Science* 131.
90. Mano, J. F., Sousa, R. A., Boesel, L. F., Neves, N. M., and Reis, R. L. (2004) Bioinert, biodegradable and injectable polymeric matrix composites for hard tissue replacement: state of the art and recent developments, *Composites Science and Technology* 64, 789-817.
91. Kong, H., and Jang, J. (2008) Antibacterial properties of novel poly(methyl methacrylate) nanofiber containing silver nanoparticles, *Langmuir* 24, 2051-2056.
92. Araújo, E., Hage Jr, E., and Carvalho, A. (2003) Morphological, mechanical and rheological properties of nylon 6/acrylonitrile-butadiene-styrene blends compatibilized with MMA/MA copolymers, *Journal of Materials Science* 38, 3515-3520.
93. Fukuda, T., Ma, Y. D., and Inagaki, H. (1987) Free-radical copolymerization, 6. New interpretation for the propagation rate versus composition curve, *Die Makromolekulare Chemie, Rapid Communications* 8, 495-499.
94. Eisa, T., and Sefton, M. V. (1993) Towards the preparation of a MMA-PEO block copolymer for the microencapsulation of mammalian cells, *Biomaterials* 14, 755-761.
95. El Khadali, F., Helary, G., Pavon-Djavid, G., and Migonney, V. (2002) Modulating fibroblast cell proliferation with functionalized poly(methyl methacrylate) based copolymers: Chemical composition and monomer distribution effect, *Biomacromolecules* 3, 51-56.
96. Evans, M. D. M., Pavon-Djavid, G., Helary, G., Legeais, J. M., and Migonney, W. (2004) Vitronectin is significant in the adhesion of lens epithelial cells to PMMA polymers, *Journal of Biomedical Materials Research Part A* 69A, 469-476.
97. Bar, F. W., van der Veen, F. H., Benzina, A., Habets, J., and Koole, L. H. (2000) New biocompatible polymer surface coating for stents results in a low neointimal response, *Journal of biomedical materials research* 52, 193-198.
98. Yang, C. Y., Cao, Y., Smith, P., and Heeger, A. J. (1993) Morphology of conductive, solution-processed blends of polyanailine and poly(methyl methacrylate), *Synthetic Metals* 53, 293-301.
99. Tanaka, K., Takahara, A., and Kajiyama, T. (1996) Film thickness dependence of the surface structure of immiscible polystyrene/poly(methyl methacrylate) blends, *Macromolecules* 29, 3232-3239.
100. Jian, X.-x., Xiao, L.-q., Zhou, W.-l., and Xu, F.-m. (2009) Synthesis and characterization of PMMA/PEG-TPE semi-interpenetrating polymer networks, *Polymer Bulletin* 63, 225-233.
101. Decker, C. (1998) The use of UV irradiation in polymerization, *Polymer international* 45, 133-141.
102. Trommsdorff, V. E., Köhle, H., and Lagally, P. (1948) Zur polymerisation des methacrylsäuremethylesters1, *Die Makromolekulare Chemie* 1, 169-198.
103. Williams, C., Williams, A., Malik, T., Kim, P., Manson, J., and Elisseeff. (2005) Variable cytocompatibility of six cell lines with photoinitiators used for polymerizing hydrogels and cell encapsulation, *Biomaterials* 26, 1211-1218.

104. Lovell, L. G., Lu, H., Elliott, J. E., Stansbury, J. W., and Bowman, C. N. (2001) The effect of cure rate on the mechanical properties of dental resins, *Dental Materials* 17, 504-511.
105. Maffezzoli, A., Dellapietra, A., Rengo, S., Nicolais, L., and Valletta, G. (1994) Photopolymerization of dental composite matrices, *Biomaterials* 15, 1221-1228.
106. Decker, C. (2002) Kinetic study and new applications of UV radiation curing, *Macromol. Rapid Commun.* 23, 1067-1093.
107. Nguyen, K., Nguyen, J., and West. (2002) Photopolymerizable hydrogels for tissue engineering applications, *Biomaterials* 23, 4307-4314.
108. Fisher, J. P., Dean, D., Engel, P. S., and Mikos, A. G. (2001) Photoinitiated polymerization of biomaterials, *Annual review of materials research* 31, 171-181.
109. Patel, S., Thakar, R. G., Wong, J., McLeod, S. D., and Li, S. (2006) Control of cell adhesion on poly(methyl methacrylate), *Biomaterials* 27, 2890-2897.
110. Norde, W., and Gage, D. (2004) Interaction of Bovine Serum Albumin and Human Blood Plasma with PEO-Tethered Surfaces: Influence of PEO Chain Length, Grafting Density, and Temperature, *Langmuir* 20, 4162-4167.
111. D'Sa, R., and Meenan, B. J. (2010) Chemical Grafting of Poly(ethylene glycol) Methyl Ether Methacrylate onto Polymer Surfaces by Atmospheric Pressure Plasma Processing *Langmuir* 26.
112. Scott, E. A., Nichols, M. D., Cordova, L. H., George, B. J., Jun, Y.-S., and Elbert, D. L. (2008) Protein adsorption and cell adhesion on nanoscale bioactive coatings formed from poly(ethylene glycol) and albumin microgels, *Biomaterials* 29, 4481-4493.
113. Knop, K., Hoogenboom, R., Fischer, D., and Schubert, U. S. (2010) Poly(ethylene glycol) in Drug Delivery: Pros and Cons as Well as Potential Alternatives, *Angewandte Chemie-International Edition* 49, 6288-6308.
114. Veronese, F. M., and Pasut, G. (2005) PEGylation, successful approach to drug delivery, *Drug Discov. Today* 10, 1451-1458.
115. Otsuka, H., Nagasaki, Y., and Kataoka, K. (2003) PEGylated nanoparticles for biological and pharmaceutical applications, *Advanced Drug Delivery Reviews* 55, 403-419.
116. Fruijtier-Polloth, C. (2005) Safety assessment on polyethylene glycols (PEGs) and their derivatives as used in cosmetic products, *Toxicology* 214, 1-38.
117. Rueda, J., Suica, R., Komber, H., and Voit, B. (2003) Synthesis of new polymethyloxazoline hydrogels by the "macroinitiator" method, *Macromolecular Chemistry and Physics* 204, 954-960.
118. Cheang, P., and Khor, K. A. (2003) Effect of particulate morphology on the tensile behaviour of polymer-hydroxyapatite composites, *Materials Science and Engineering a-Structural Materials Properties Microstructure and Processing* 345, 47-54.
119. Ishiyama, C., and Higo, Y. (2002) Effects of humidity on Young's modulus in poly(methyl methacrylate), *J. Polym. Sci. Pt. B-Polym. Phys.* 40, 460-465.
120. Blond, D., Barron, V., Ruether, M., Ryan, K. P., Nicolosi, V., Blau, W. J., and Coleman, J. N. (2006) Enhancement of modulus, strength, and toughness in poly(methyl methacrylate)-based composites by the incorporation of poly(methyl methacrylate)-functionalized nanotubes, *Advanced Functional Materials* 16, 1608-1614.
121. Rao, K. H., Forssberg, K. S. E., and Forsling, W. (1998) Interfacial interactions and mechanical properties of mineral filled polymer composites: wollastonite in PMMA polymer matrix, *Colloids and Surfaces a-Physicochemical and Engineering Aspects* 133, 107-117.
122. Zeng, J. J., Saltysiak, B., Johnson, W. S., Schiraldi, D. A., and Kumar, S. (2004) Processing and properties of poly(methyl methacrylate)/carbon nano fiber composites, *Compos. Pt. B-Eng.* 35, 173-178.
123. Cohen, R. E., Kopesky, E. T., and McKinley, G. H. (2006) Toughened poly(methyl methacrylate) nanocomposites by incorporating polyhedral oligomeric silsesquioxanes, *Polymer* 47, 299-309.

124. Ydens, I., Degee, P., Haddleton, D. M., and Dubois, P. (2005) Reactivity ratios in conventional and nickel-mediated radical copolymerization of methyl methacrylate and functionalized methacrylate monomers, *European polymer journal* 41, 2255-2263.
125. Killion, J. A., Geeuer, L. M., Deuine, D. M., Kennedy, J. E., and Higginbotham, C. L. (2011) Mechanical properties and thermal behaviour of PEGDMA hydrogels for potential bone regeneration application, *Journal of the Mechanical Behavior of Biomedical Materials* 4, 1219-1227.
126. Wolf, K. V., Zong, Z., Meng, J., Orana, A., Rahbar, N., Balss, K. M., Papandreou, G., Maryanoff, C. A., and Soboyejo, W. (2008) An investigation of adhesion in drug-eluting stent layers, *Journal of Biomedical Materials Research Part A* 87A, 272-281.
127. Huma, F., Akhter, Z., Yasin, T., Zafar-uz-Zaman, M., and Manan, A. (2014) Crosslinking of poly(N-vinyl pyrrolidone-co-n-butyl methacrylate) copolymers for controlled drug delivery, *Polymer Bulletin* 71, 433-451.
128. Derkaoui, S. (2010) Films of dextran-graft-polybutylmethacrylate to enhance endothelialization of materials, *Acta Biomaterialia* 6, 3506-3513.
129. Castillo-Ortega, M. M., Rodriguez, D. E., Encinas, J. C., Plascencia, M., Mendez-Velarde, F. A., and Olayo, R. (2002) Conductometric uric acid and urea biosensor prepared from electroconductive polyaniline-poly(n-butyl methacrylate) composites, *Sensors and Actuators B-Chemical* 85, 19-25.
130. Itoh, Y., Ozaki, K., Sahara, F., and Teramoto, A. (2011) Quick-drying, protective coating of papers with poly(methacrylate) latices containing alkali-hydrolysable emulsifiers, *Polymer Bulletin* 67, 1367-1377.
131. Eslami, H., and Zhu, S. P. (2006) Morphological and physical properties of triblock copolymers of methyl methacrylate and 2-ethylhexyl methacrylate, *Macromol. Mater. Eng.* 291, 1104-1118.
132. Zhao, J., Xiao, C., Xu, N., and Ma, X. (2012) Preparation and properties of poly (butyl methacrylate/lauryl methacrylate) and its blend fiber, *Polymer Bulletin* 69, 733-746.
133. Jang, J., and Kim, B. S. (2000) Studies of crosslinked styrene–alkyl acrylate copolymers for oil absorbency application. II. Effects of polymerization conditions on oil absorbency, *Journal of Applied Polymer Science* 77, 914-920.
134. Feng, Y., and Xiao, C. (2006) Research on butyl methacrylate–lauryl methacrylate copolymeric fibers for oil absorbency, *Journal of Applied Polymer Science* 101, 1248-1251.
135. Clarke, S., Davies, M. C., Roberts, C. J., Tendler, S. J., Williams, P. M., O'Byrne, V., Lewis, A. L., and Russell, J. (2000) Surface mobility of 2-methacryloyloxyethyl phosphorylcholine-co-lauryl methacrylate polymers, *Langmuir* 16, 5116-5122.
136. Garwe, F., Schönhals, A., Lockwenz, H., Beiner, M., Schröter, K., and Donth, E. (1996) Influence of cooperative α dynamics on local β relaxation during the development of the dynamic glass transition in poly (n-alkyl methacrylate) s, *Macromolecules* 29, 247-253.
137. Zosel, A., and Schuler, B. (1999) The influence of surfactants on the peel strength of water-based pressure sensitive adhesives, *The Journal of Adhesion* 70, 179-195.
138. Demetriou, M., and Krasia-Christoforou, T. (2008) Synthesis and characterization of well-defined block and statistical copolymers based on lauryl methacrylate and 2-(acetoacetoxy) ethyl methacrylate using RAFT-controlled radical polymerization, *Journal of Polymer Science Part A: Polymer Chemistry* 46, 5442-5451.
139. Chatterjee, D. P., and Mandal, B. M. (2006) Triblock thermoplastic elastomers with poly (lauryl methacrylate) as the center block and poly (methyl methacrylate) or poly (tert-butyl methacrylate) as end blocks. Morphology and thermomechanical properties, *Macromolecules* 39, 9192-9200.
140. Amerov, A. K., Chen, J., Small, G. W., and Arnold, M. A. (2005) Scattering and absorption effects in the determination of glucose in whole blood by near-infrared spectroscopy, *Analytical Chemistry* 77, 4587-4594.

141. Ryckeboer, E. (2014) Spectroscopic detection of glucose with a silicon photonic integrated circuit, Ghent University.
142. Olin, C. (2001) Titanium in cardiac and cardiovascular applications, In *Titanium in Medicine*, pp 889-907, Springer.
143. Bienkiewicz, J. (2006) Plasma-Enhanced Parylene Coating, *Medical device technology* 17, 10.
144. Berridge, M. V., Herst, P. M., and Tan, A. S. (2005) Tetrazolium dyes as tools in cell biology: new insights into their cellular reduction, *Biotechnology annual review* 11, 127-152.
145. Bryant, S. J., Nuttelman, C. R., and Anseth, K. S. (2000) Cytocompatibility of UV and visible light photoinitiating systems on cultured NIH/3T3 fibroblasts in vitro, *Journal of Biomaterials Science, Polymer Edition* 11, 439-457.

Chapter 3

Surface activation and functionalization of methacrylate-based polymers

Parts of this chapter have been published in:

Van de Walle, E.; Van Nieuwenhove, I.; Vanderleyden, E.; Declercq, H.; Gellynck, K.; Schaubroeck, D.; Ottevaere, H.; Thienpont, H.; De Vos, W. H.; Cornelissen, M.; Van Vlierberghe, S.; Dubruel, P., Polydopamine-Gelatin as Universal Cell-Interactive Coating for Methacrylate-Based Medical Device Packaging Materials: When Surface Chemistry Overrules Substrate Bulk Properties. *Biomacromolecules* **2016,** *17* (1), 56-68.

3.1. Introduction

Polymers such as poly(ethylene terephtalate) (PET) [1], poly(ethylene) (PE) [2], but also PMMA [3] are characterized by inert surface properties. The latter implies that no reactive chemical functionalities are available on the surface to enable subsequent reactions, such as biofunctionalization to enhance the cell-interactive properties. In the end, as pointed out in the introduction, we aim at stimulating the growth of blood vessels in the neighborhood of the sensor [4]. Since endothelial cells build up the inner blood vessel wall, attraction of this cell type would be beneficial. In order to obtain this goal, the immobilization of biologically active compounds, such as growth factors (see chapter 4) is necessary. Therefore, the activation of the surface by the introduction of reactive functional groups should be pursued.

Previously, wet chemical modifications such as aminolysis and hydrolysis have frequently been applied on polymers containing functional groups which are susceptible towards these processes. Since PMMA contains a methylester group, aminolysis could be performed using a diamine derivative such as ethylenediamine, lithiated diamines or di-amino-PEG [5-10], whereas the introduction of carboxylic acid groups could be facilitated by hydrolysis with an acid or base [9, 11-12]. Before, it was already proven that these amine and carboxylic acid functionalities permit the subsequent reactions with biosignaling molecules such as transferrin, insulin, fibronectin and other proteins [13-15]. Since wet chemical modifications require the use of solvents and tend to affect the bulk of the materials, nowadays, less harsh and more environmental friendly methods are being evaluated which only affect the surface of the materials.

In this respect, plasma treatments of polymers have been extensively studied. With respect to PMMA, the influence of different plasma treatments has already been evaluated, including oxygen [16-17], argon [18-21] and air [22-23] plasma. These literature reports indicate that a plasma treatment results in surface oxygen enrichment and in an increased hydrophilicity of the substrate. For PMMA, a decrease in water contact angle of 30° has been obtained when treating it with Ar-plasma (going from 75° to 45°), whereas oxygen plasma results in even lower contact angles (down to 2°) [16, 24].

Even though it has been proven that a plasma treatment as such can induce an increased cell response [16, 25], it can be desirable to introduce specific chemical functionalities on the surface, which enable subsequent and permanent immobilization of biologically active compounds. In this respect, plasma has been frequently applied as a tool to graft such specific functionalities. Examples include graft polymerization of acrylamide or acrylic acid onto poly(ethylene) [26] or PMMA films [27-28] and post-plasma grafting of 2-aminoethyl methacrylate onto PCL [29].

Apart from plasma-based modifications, alternative solventless modification techniques exist including photografting, ozone oxidation and high energy radiation. In the first case, upon UV-irradiation and in the presence of an initiator, radicals are created on the polymer surface, which can subsequently react with monomers, carrying the desired functionalities.

Using this approach, PEG monoacrylate and acrylamide were previously immobilized onto PMMA polymer sheets [30-31]. In case of ozonization, surface peroxides, carbonyl and carboxyl functionalities are introduced, enabling subsequent reactions such as the immobilization of PEG [32]. In case of high energy radiation such as electron beams, degradation of PMMA is highly manifested and mainly results in chain scission with the formation of radicals or active ions, which are chemically reactive and which may result in subsequent crosslinking [33-34].

Alternatively, surface modification can also be realized by the deposition of a functionalized coating. In literature, different deposition principles are described such as Langmuir Blodgett deposition [35], self-assembled monolayers [36] or layer-by-layer deposition [37]. Since all of these methods suffer from their non-versatile nature, the use of polydopamine was more recently proposed by Messersmith et al as a universal surface functionalization strategy [38-40]. By a simple immersion step in alkaline conditions, the polymer can be applied onto a wide range of materials, including ceramics, metals and polymers [41]. In a subsequent step, this activating layer enables the subsequent biofunctionalization of the materials (see chapter 4).

The previous chapter indicated that the developed materials lack cell interactivity. As a consequence, the immobilization of biologically active compounds is required to enhance the cell response. Since the selected polymers are inert (i.e. do not contain reactive chemical functionalities), activation is necessary to subsequently link biomolecules such as antibodies and growth factors in a covalent way (see chapter 4). The biomolecules used in this work are built-up of aminoacids, implying that their main reactive groups consist of amines and carboxylic acids. As a consequence, complementary functional groups have to be immobilized onto the material surfaces to enable coupling. To this end, two strategies were elaborated. In a first strategy, amine-based functionalities were introduced by means of post-plasma grafting of 2-aminoethyl methacrylate (AEMA) (§ 3.3.2). These amine functions enable the reaction with carboxylic acids present in the biomolecules. The strategy was selected based on a previous successful report, describing the biofunctionalisation of PCL scaffolds [29]. In a second strategy, because of its universal and versatile character (as described above), polydopamine (PDA) (§ 3.3.2), a marine-based adhesive, was selected as activating coating. Furthermore, since plasma activation was used prior to functionalization, the upcoming paragraph will focus on this topic. Herein, the effect of different plasma gasses on the material properties was studied. The final selection of plasma gas was based on available literature reports and on the obtained results (see further).

Based on their superior mechanical and swell properties (see chapter 2), one PEG-based material was selected (P(MMA-co-PEGDMA), referred to as PMMAPEG), as well as one LMA-based material (P(MMA-co-LMA-co-PEGDMA), referred to as PLMA). For the latter case, two different initiators (i.e. Irgacure® 2959 and irgacure®651) were evaluated in the previous chapter, but only minor differences were obtained during evaluation of the bulk properties of the materials (i.e. PLMA(2959) and PLMA(651)). Whether the initiator selection will

influence the surface modification and properties of the materials, will be investigated in the current chapter. Figure 1 overviews the different surface modification strategies that will be discussed in the current chapter.

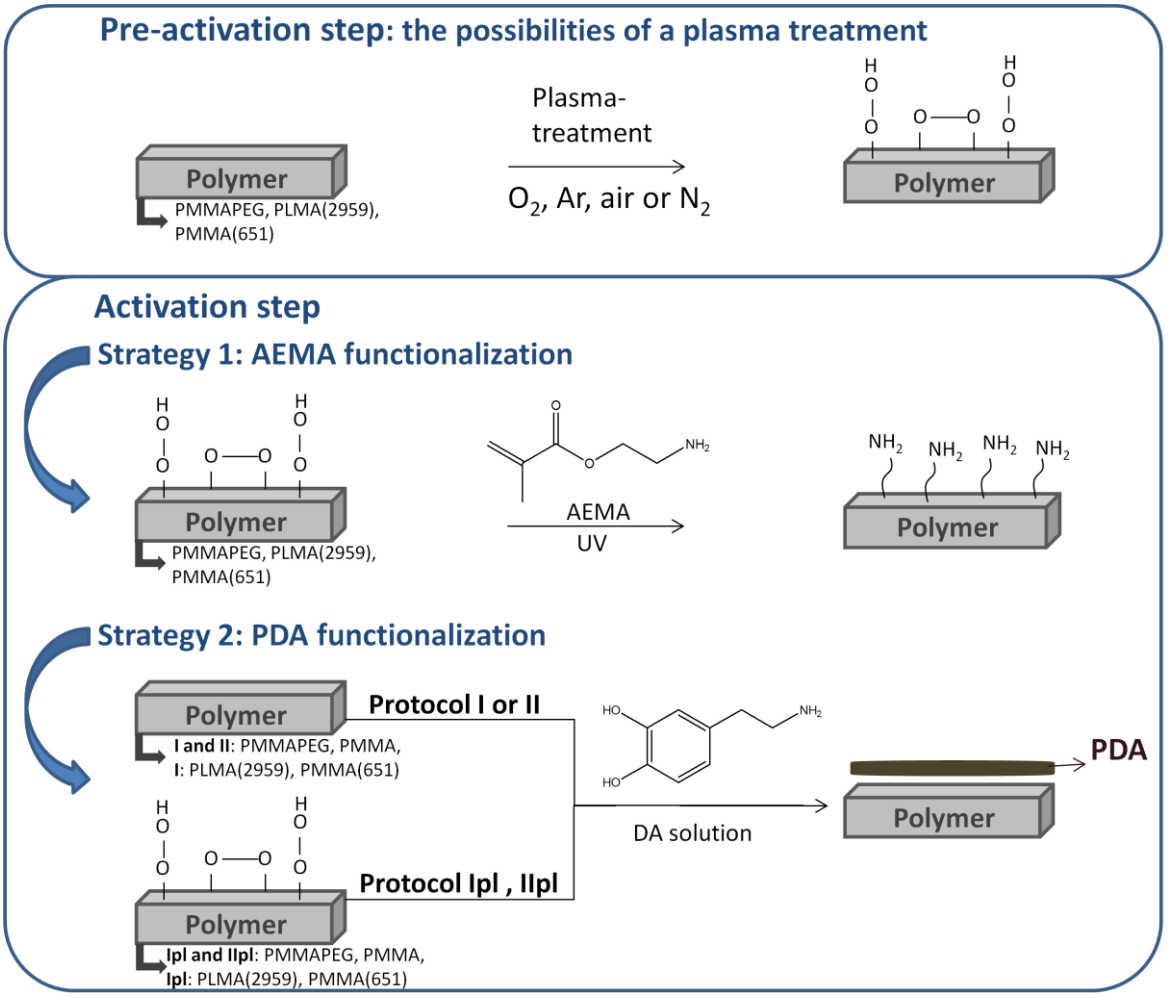

Figure 3.1: Overview of the different surface modifications that will be discussed in the current chapter. First, a plasma treatment was conducted as a pre-activation step. Next, surface functionalization was targeted via post-plasma grafting of AEMA (strategy 1) or PDA (strategy 2: protocol Ipl and IIpl). For the latter strategy, straightforward immersion of the polymer substrates in the DA solution was also evaluated (protocols I and II). The different protocols will be further explained in the upcoming paragraphs. The scheme also mentions the polymer substrates which were used during the different modification steps.

3.2. Plasma activation of the polymer surfaces

In 1929, Langmuir introduced the term plasma, which is also referred to as the fourth state of matter, in addition to the solid, liquid and gaseous state [42]. It can be defined as a 'gaseous' or fluid-like mixture consisting of ions, electrons, radicals and neutral particles such as atoms and molecules. Since some of the particles are in an excited state, relaxation to the ground state typically results in the emission of photons, which is responsible for the characteristic illumination of a plasma reactor (cfr. the purple color in figure 3.2, A).
Generally, two types of plasma can be distinguished, including thermal equilibrium and non-thermal non-equilibrium plasmas. In the former type, high temperatures are applied in order to equally distribute the energy amongst all particles present in the plasma. Since polymers do not withstand such high temperatures (up to 20000 K), the latter type is preferred to treat polymer-based biomaterials [43]. In literature, different ways are described to generate a non-thermal or cold plasma including the use of glow discharge, microwave discharge, corona discharge and dielectric barrier discharge (DBD) [43-44]. Herein, a cylindrical dielectrical discharge plasma reactor was used of which the schematic set-up is displayed in figure 3.2 (B).

A **B**

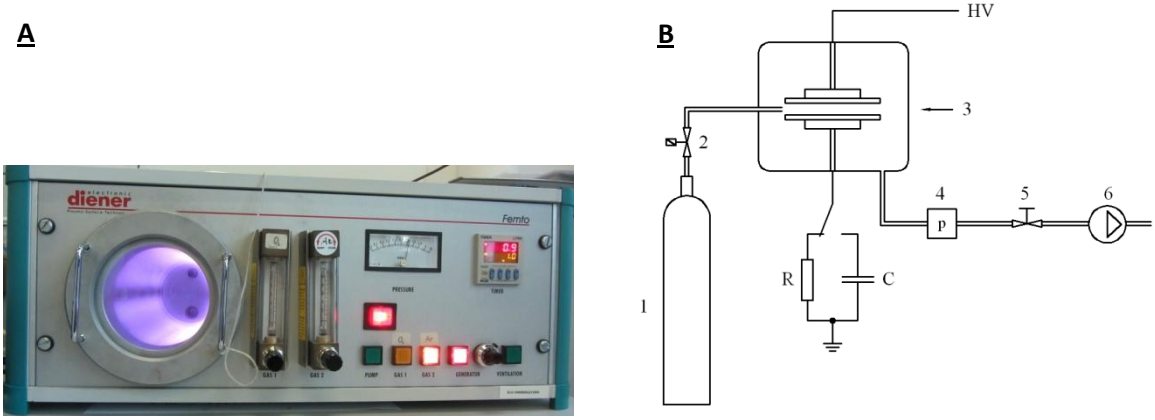

Figure 3.2: A: Plasma reactor showing the illumination caused by the emitted photo-electrons and B: the schematic representation of the used DBD set-up, which consists of the gas cylinder (1), a mass flow controller (2), a plasma chamber (3), a pressure gauge (4), a valve (5) and a pump (6).

As already indicated in the introduction, compared to wet chemical treatments, plasma treatment is characterized by a number of advantages including its solvent-free nature, its applicability onto different material geometries and its surface specific application, meaning that the bulk properties of the treated material remain unaltered. On the other hand, the greatest disadvantage of this plasma technique is 'ageing', which is the disappearance of the plasma effect as a function of time [45].
It should be mentioned that the application of plasma may also result in etching of the surface, because of the bombardment with ions from the plasma. As a result, the surface roughness might be altered due to the release of small fragments. Depending on the application, this fact may be advantageous or unwanted [44].

To create a plasma, different gasses can be selected, including Ar, O_2, N_2 and CO_2 [46]. In this work, the application of Ar and O_2 plasma treatment was mainly focused on, although, in cooperation with Prof. Rino Morent (Department of Applied Physics, University of Ghent), the effect of other plasma gasses such as air and nitrogen were also studied. The preliminary results that originated from this collaboration are represented at the end of this paragraph.

In a first step, **argon** was evaluated as a plasma activating gas for the PEG and LMA-based materials. Static contact angle measurements (SCA) clearly showed that a plasma treatment converts the hydrophobic LMA-based surfaces into more hydrophilic ones (Figure 3.3, A), as represented by a decrease in water contact angle. In case Irgacure® 2959 was used, an initial decrease of the contact angle value was followed by a plateau value (i.e. ~50°) when longer plasma treatment times were applied (i.e. 60 seconds).
For PLMA(651), a clear minimum in contact angle was reached when executing the plasma treatment for 30 seconds (± 40°), whereas a treatment time of 60 seconds caused the contact angle to increase (± 56°). It is however clear that for treatment times exceeding 60 seconds, similar contact angle values were obtained compared to PLMA(2959) (i.e. 50°).
A similar trend could be observed when PMMAPEG was used as a substrate material (Figure 3.3, B). After 30 seconds of plasma treatment, the lowest contact angle was observed (i.e. 20°) which is a 50° decrease compared to the blank value of 70°.

From literature, it is known that the functional groups which are introduced by a plasma treatment, are not stable over time and that treated surfaces tend to re-orient over time [45]. To evaluate this ageing phenomenon, plasma-treated samples were exposed to ambient air for a certain period of time and were again evaluated by SCA measurements. Figure 3.3 (C and D), clearly show that the SCA of all material surfaces increased as a function of time. In case of PMMAPEG (Figure 3.3, D), the contact angle was slightly increased after 30 minutes of air-exposure, but even after 4 hours, this increase was limited to only 8 degrees. For the LMA-based materials (Figure 3.3, C), the ageing behavior was again dependent on the type of initiator used. In case of irgacure® 651, a further decrease of the SCA was observed, even after 20 minutes of air exposure. This suggests a slower but further introduction of oxygen-containing functional groups onto the polymer surfaces. Thereafter, the SCA increased up to 68°. In case irgacure® 2959 was used as an initiator, ageing occurred immediately and after 4 hours, the SCA increased with 13°, reaching a value of 55°. For both materials (i.e. PLMA(651) and PLMA(2959)), the initial contact angle of 89° was not restored implying that the surface wettability is well maintained for all three materials evaluated.
These results indicated that no real time constraints were needed for the subsequent post-plasma modification step in aqueous media. Nevertheless, in order to minimize losses of the plasma treatment effect, all samples were typically immersed 'immediately' in the solution applied for the modification reactions. Additionally, in literature it has been described that the immersion of plasma-treated samples in an aqueous environment maintains the hydrophilicity of the samples and thereby reduces the effect of ageing. This means that the

aqueous modification solutions show affinity towards the incorporated polar groups, forcing them to stay on the surface rather than forcing them into the bulk of the material [47].

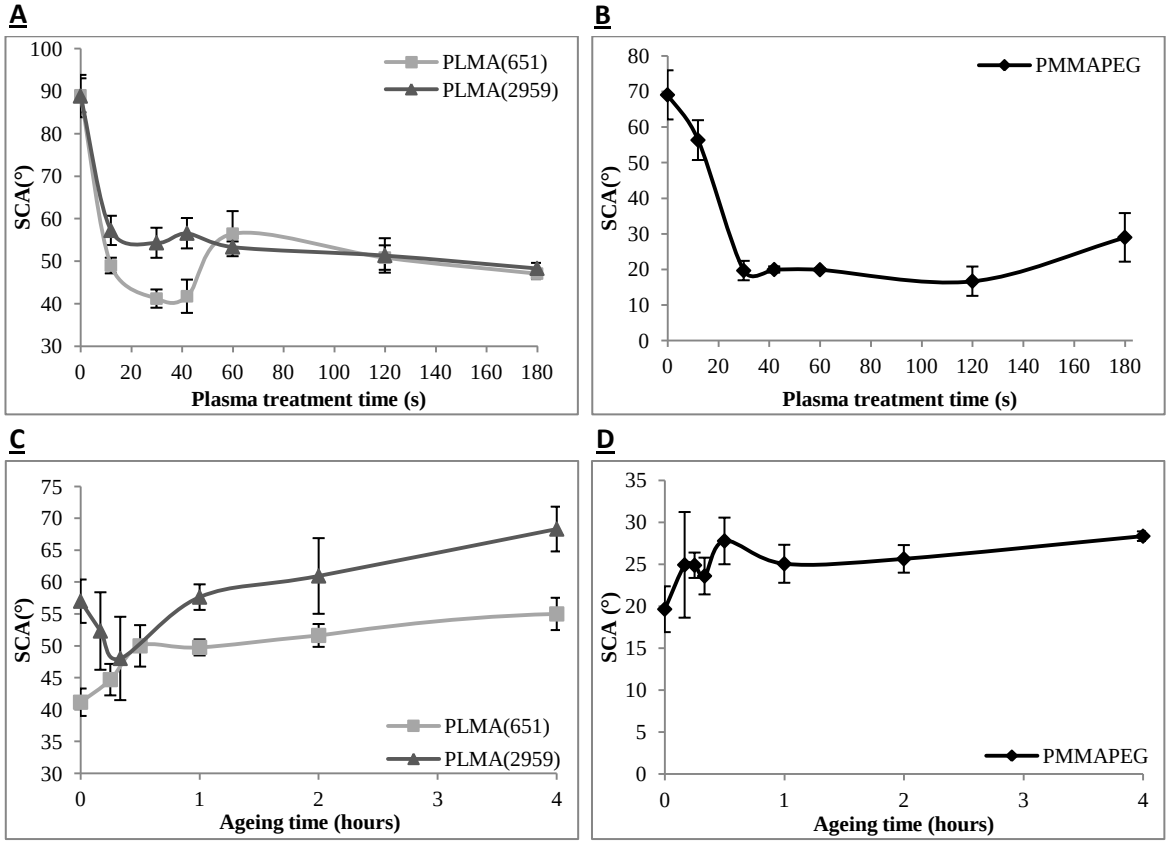

Figure 3.3: Static contact angles of Ar plasma-treated PLMA samples (A) and PMMAPEG samples (B) as a function of plasma treatment time. Furthermore, the static contact angles as a function of ageing time are displayed for Ar-plasma treated PLMA (C) and PMMAPEG samples (D).

To study the effect of an **oxygen plasma** treatment, PLMA(2959) was selected and the effect was compared with the results obtained for an argon plasma treatment (see figure 3.4). The results showed that the application of an oxygen plasma resulted in similar contact angles compared to the argon plasma treatment. One minute of plasma treatment resulted in a SCA of 53°, irrespective of the applied gas. With respect to ageing, it is clear that after oxygen plasma treatment, no further decrease of the SCA was observed, but a slight increase was immediately manifested ($p>0.05$). The results also showed that the plasma effect was slightly better maintained after oxygen plasma treatment compared to argon plasma. Indeed, after 4 hours of air exposure, the SCA remained 60° after O_2 plasma treatment, whereas for Ar plasma a value of 70° was already obtained.

In figure 3.4 (C), an overview is given of the O_2 and Ar plasma effects for the three different materials under evaluation, using a plasma exposure time of 1 minute. As previously discussed, a similar SCA was obtained for PLMA(2959) whereas for PLMA(651), a significantly lower SCA was obtained after argon plasma treatment compared to oxygen plasma treatment (i.e. a difference of 14°). A similar effect was found for the PEG-based material

and compared to oxygen plasma, a 20° lower SCA was obtained upon application of argon plasma. These results point out that the plasma-effect is highly substrate dependent.

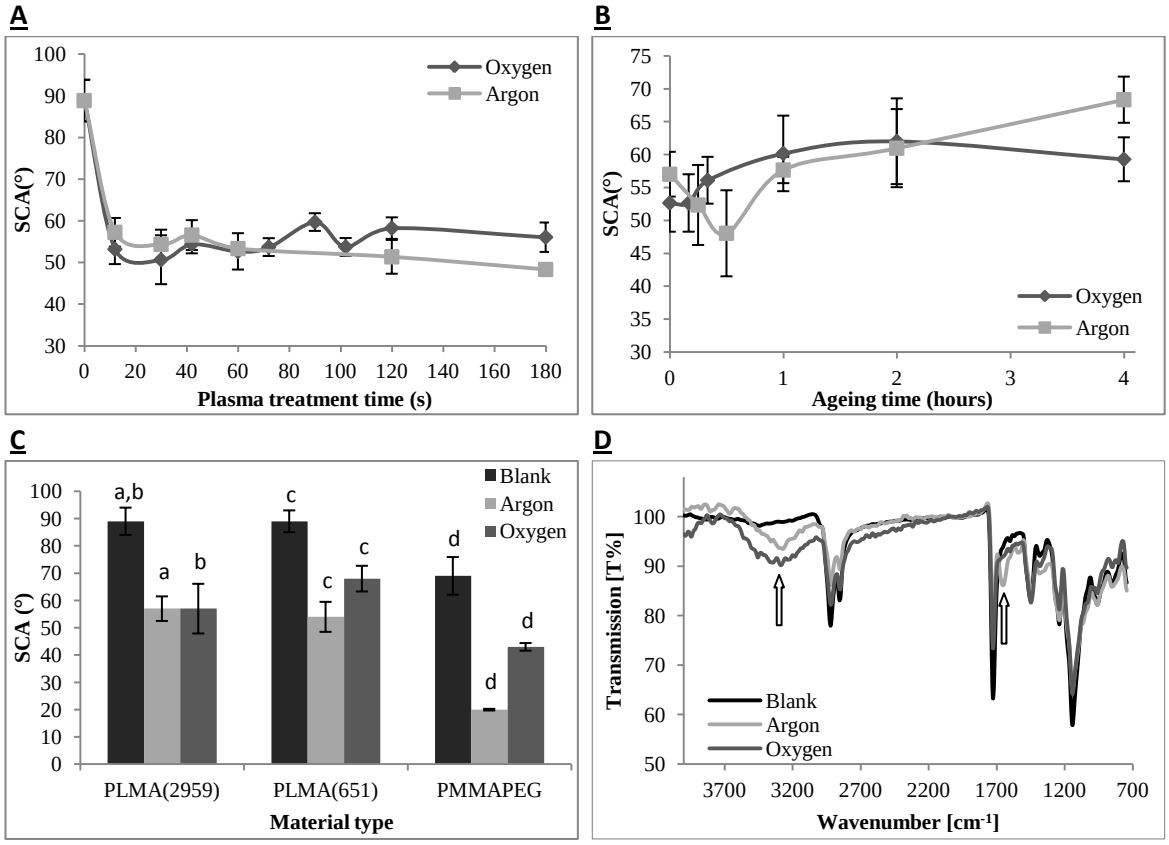

Figure 3.4: Comparison of Ar- and O_2 plasma treated PLMA(2959) samples: effect of plasma treatment time (A) and the ageing effect (B). Panel C makes the comparison between the blank and a 1 minute argon and oxygen plasma treatment and this for the three substrate materials under investigation. Conditions which were significantly different ($p<0.05$) are denoted by the same letters a,b,c,… Panel D shows IR mapping measurements performed on PLMA(2959). The annotated peaks show the appearance of OH- (3500-3200 cm^{-1}) and C=O functionalities (1665 cm^{-1}).

It is generally accepted from literature data that an O_2 plasma treatment results in the introduction of -COOH and -OH functionalities on the substrate surface whereas for Ar plasma treatment, the creation of free radicals is predominant. In the latter case, upon air exposure, these radicals can react with air species thereby introducing mainly oxygen and some nitrogen on the material surface [48]. In the present work, the presence of these functional groups was demonstrated by IR mapping on the surface (Figure 3.4, D). For both plasma gasses, a broad signal could be distinguished around 3500-3200 cm^{-1} (pointed by an arrow), which can be attributed to –OH functionalities. Furthermore, in case of argon plasma treatment, a new peak arose around 1665 cm^{-1} (pointed by an arrow in figure 3.4, D) which can be attributed to the introduction of -C=O containing functionalities.

In general, the observed decreases in SCA after plasma treatment can be explained by the introduction of these functional groups. In this respect, XPS analyses could have been

performed to gain more information on the nature of these functionalities. Further elucidation of the latter could offer interesting insight for future research.

As mentioned in the beginning of this paragraph, a preliminary study was conducted with alternative plasma gasses, including nitrogen gas and air and a comparison was made with the results obtained for argon plasma treatment. As a case study, PMMAPEG was subjected to the different plasma treatments and the SCA values were compared (see figure 3.5, A). Regardless of the chosen gas, a significant decrease in contact angle was obtained after plasma treatment. Air and argon induced a similar effect, whereas nitrogen influenced the hydrophilicity to a greater extent. To understand the cause of this effect, the elemental composition of the nitrogen-treated surfaces was studied. Preliminary XPS analysis (see figure 3.5, B) revealed that a nitrogen plasma treatment resulted in the introduction of a substantial amount of nitrogen-containing species, which are in all probability responsible for the increased hydrophilicity. Maximum amounts of 6 and 7 % of nitrogen were introduced after respectively 0.5 and 2 minutes of plasma treatment.

Because of the presence of amine functions in case of N_2 plasma treatment, the direct biofunctionalization of the surfaces could also have been considered. Nevertheless, this route was not further explored in the current work.

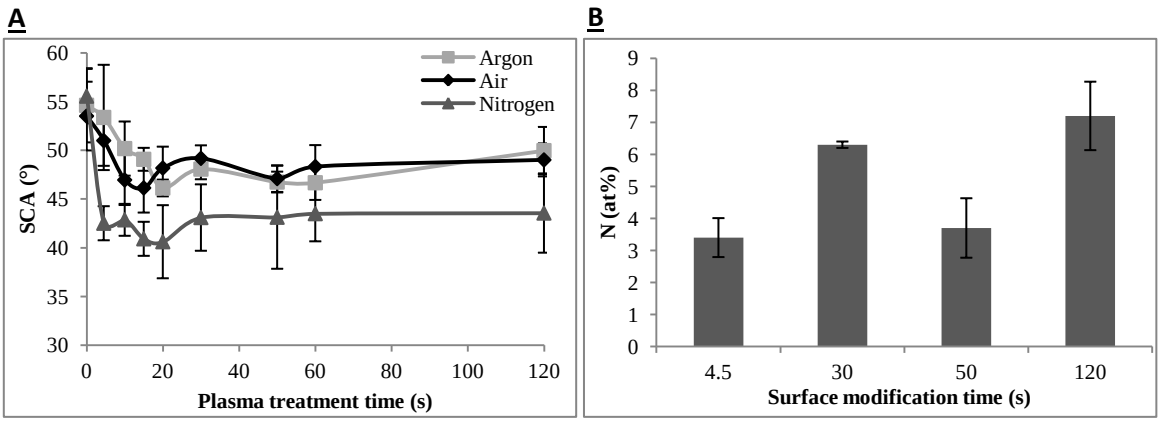

Figure 3.5: Static contact angle of air, argon and nitrogen plasma treated PMMAPEG samples as a function of plasma treatment time (A). Percentage of nitrogen introduced on the nitrogen-plasma treated samples (B).

3.3. Post-plasma grafting of 2-aminoethyl methacrylate

Apart from surface activation, functionalization of the surface was required to enable subsequent immobilisation of biomolecules (see chapter 4). In a first strategy, amine-based functionalities were introduced via a post-plasma grafting procedure. Herein, 2-aminoethyl methacrylate (AEMA) was selected as grafting monomer to introduce primary amines as reactive units. Since we aim at an activation of the polymer surface by the introduction of radicals, argon gas was selected to perform the plasma pre-treatment step.

Figure 3.6 (A) summarizes the grafting procedure which consists of two steps. First, a plasma treatment is applied on the polymer sheets to activate the surface by the introduction of radicals (see discussion in § 3.2). Upon exposure to ambient air, the created radicals immediately react with atmospheric oxygen and as a consequence, oxygen-rich functionalities are introduced on the polymer surface, such as peroxides. Based on the mechanistic model of Suzuki et al [26], UV-induced radical cleavage of these peroxides would facilitate the post-plasma grafting step. Although many literature reports refer to the above-mentioned model [26, 29, 49-50], recent electron spin resonance (EPR) studies have demonstrated that UV irradiation is producing radicals not only on the functional groups introduced by plasma, but also continuously on the polymer chain itself [51].
Independent of the exact grafting mechanism, upon grafting of AEMA, primary amine functions were introduced on the surface, enabling subsequent biofunctionalization (see chapter 4).

The presence of the primary amine functions could be evidenced by XPS measurements. As demonstrated in figure 3.6 (B), nitrogen was introduced on all surfaces after the AEMA grafting step. Since no nitrogen was present on the blank materials, these values were clear evidence of the successful immobilization. Nevertheless, it should be noted that the reproducibility (a minimum of 2 samples, measured at three different locations were included in these data) of the grafting technique was rather poor, as demonstrated by the high standard deviations. Furthermore, if one sample was considered of one specific condition, no homogeneous coatings were obtained. Places without successful modification (i.e. of 0% N) were detected and for some samples, even places of 5-6% of nitrogen were observed. It appeared that PLMA(651) resulted in the most reproducible grafting results. Generally, compared to the work of Desmet et al [29], the obtained nitrogen percentages were rather small, since for the grafting on PCL, nitrogen percentages of 6 % were reached for the same grafting conditions and for all samples. These differences clearly prove that the success of this grafting method is substrate dependent. Since the optimum value to enable the subsequent immobilization of biomolecules is unknown, it could be anticipated that a lower immobilization degree of AEMA could still be sufficient to realize this goal.
Based on these XPS measurements, an ‘optimal’ plasma treatment time was selected for each material. It should be noted that, due to the high standard deviations, no significant differences in atomic nitrogen percentage or N/C ratio were obtained when comparing the three different plasma activation times. Nevertheless, the plasma treatment time was still selected based on a maximized nitrogen percentage (mean values) and a maximized N/C ratio . In case of the PEG-based material, this maximum was reached for a treatment time of 30 seconds, whereas for the PLMA-based materials, 12 seconds was selected for future experiments.
In a next step, static contact angle measurements (SCA) were performed to further evidence the successful immobilization of AEMA. Figure 3.6 (C) shows that a significant difference was obtained between the SCA values of the plasma-treated samples and the AEMA-grafted

surfaces ($p<0.05$). More specifically, a significant increase of 41°, 11° and 27° was found for respectively PMMAPEG, PLMA(2959) and PLMA(651). After AEMA grafting, it could be anticipated that similar contact angles would be obtained, due to the presence of identical surface functionalities. Indeed, for the LMA-based materials, no significant difference was obtained in SCA after AEMA grafting ($p>0.05$), but for PMMAPEG, a significant difference was obtained when comparing its SCA (±61°) with the ones obtained for PLMA(651) (±76°). In literature, a SCA of 50° was reported for AEMA-grafted PCL samples [29]. As explained above, the grafting technique resulted in a poor reproducibility for the current materials and as a consequence, the SCA measurements are still influenced by the underlying substrate. Furthermore, a different surface roughness of the materials could also have a substantial effect on these SCA measurements.

A

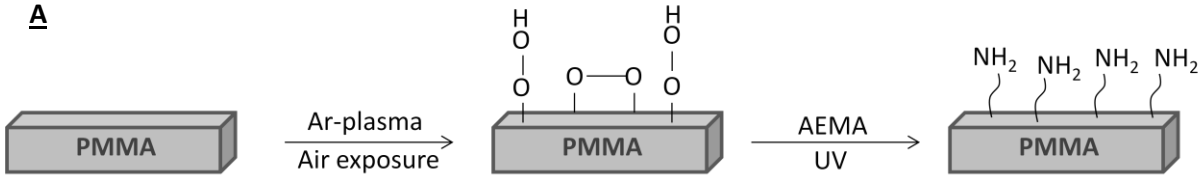

B

	PMMAPEG		PLMA(651)		PLMA(2959)	
Plasma time (s)	**N (at%)**	**N/C**	**N (at%)**	**N/C**	**N (at%)**	**N/C**
12	1.6 ± 1.8	0.027 ± 0.027	1.3 ± 0.3	0.020 ± 0.004	1.4 ± 1.8	0.020 ± 0.026
30	3.2 ± 3.0	0.047 ± 0.042	1.0 ± 0.2	0.016 ± 0.003	0.9 ± 0.5	0.012 ± 0.006
42	2.5 ± 2.5	0.039 ± 0.038	1.2 ±0.2	0.019 ± 0.004	1.2 ± 0.4	0.015 ± 0.006

C

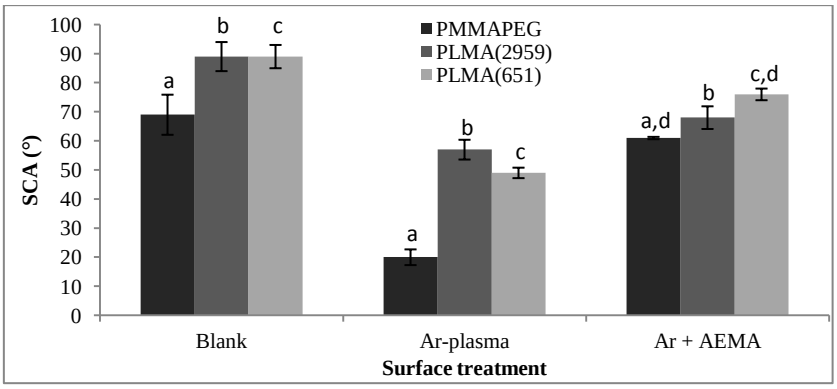

Figure 3.6: A: Post-plasma grafting technique of 2-aminoethyl methacrylate onto a polymer substrate. B: Atomic percentages and N/C ratio's of the AEMA grafted samples. C: Contact angles for the blank, argon plasma-treated and AEMA-grafted PMMAPEG and PLMA materials. Conditions which are significantly different ($p<0.05$) are denoted by the same letters a,b,c,…

3.4. Surface functionalization with polydopamine

In addition to AEMA functionalization of the surfaces via a post-plasma grafting technique, the application of a polydopamine coating as activating sublayer has also been studied. In literature, a lot of attention has been paid to this adhesive coating. In the upcoming section, a short summary is provided on the background of this polymer coating and the various adhesion mechanisms reported on to date. Next, the characteristics of the deposited PDA layers are overviewed for the two substrate materials, including PMMAPEG (§ 3.4.2.1) and PLMA (§ 3.4.2.2).

3.4.1. Background on polydopamine

During the last decades, increasing research efforts have been focussing on the study of the adhesive capabilities of gecko's and marine organisms of which mussels, barnacles and tube worms comprise common examples [38-40, 52]. In case of mussels, the so-called MAP's (i.e. mussel adhesive proteins) play a central role during the adhesion process and because of these MAP's, mussels are able to attach to virtually all types of inorganic and organic surfaces under water. Sequencing of these proteins has revealed the significant presence of two compounds [52-53]:

1. L-3,4-dihydroxyphenylalanine (DOPA), a catechol containing amino acid that is formed by post-translational modification of L-tyrosine. Depending on the protein studied, concentrations ranging from a few mol% up to 27 mol% are contained in these MAPs [54].

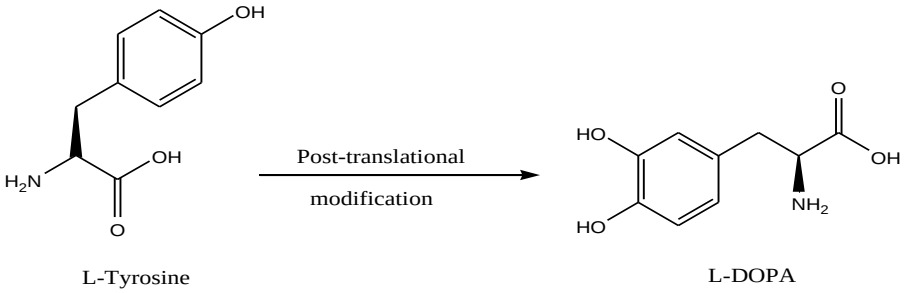

Figure 3.7: Chemical structures of L-tyrosine and L-DOPA

2. Lysine amino acids which are mostly located next to the DOPA residues.

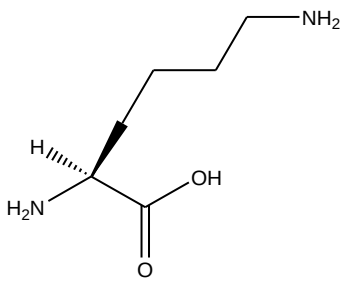

Figure 3.8: Chemical structure of L-lysine

Apart from covalent crosslinking which results in solidification of the adhesive, the DOPA residues are believed to be primarily responsible for chemisorption to surfaces under water via covalent and non-covalent interactions [41, 52, 55-56]. Once the adhesive strength of this catechol-containing residue became clear, a lot of research started to mimic this behavior by synthesizing **biomimetic copolymers**, containing these DOPA residues in order to modify material surfaces [39, 52-53, 57-62]. Examples include co-polypeptides consisting of L-Lysine and DOPA to form moisture resistant coatings [52], the introduction of DOPA into the structure of Pluronic materials to form *in-situ* bioadhesive hydrogels [57], the production of DOPA end-functionalized PEG polymers to obtain non-fouling surfaces [58-59, 61, 63-64] and the production of poly(dopamine methacrylate-co-2-methoxyethyl acrylate)[62]. Furthermore, new **bifunctional initiators** were developed to initiate a surface-initiated atom transfer radical polymerization (SI-ATRP) of methyl methacrylate-based macromonomers. Bifunctional refers to the presence of an alkyl bromine to activate surface-initiated polymerization (SIP) and to the presence of a catechol function to allow surface anchoring of the initiator [60].

Apart from these more complex mimetics, Lee et al introduced **dopamine**, also known as a neurotransmitter and hormone, as the smallest alternative to nature's adhesive protein which combines both the catechol and amine function already mentioned above [65] (figure 3.9). As pioneers, Lee et al applied this molecule as a self-polymerizing monomer to coat multiple surfaces such as metals (e.g. Au, Ag, Pt, Pd Cu, stainless steel and nitinol), oxides (e.g. SiO_2, Al_2O_3,…), semiconductors (e.g. GaAs), ceramics (e.g. glass) and synthetic polymers (e.g. polystyrene) [41]. The polydopamine (PDA) coating activates the surfaces, thereby enabling the subsequent grafting of polymer adlayers and biomolecules (see also chapter 4) [66]. Ever since, many research groups have investigated the potential of this coating to be applied on different substrates. Typical examples include titanium [59], silicon oxide [67] and its microparticles [68], stainless steel [69], carbon nanotubes [70], silanated aluminum oxide membranes [71] and different polymers including polydimethylsiloxane (PDMS) [61], poly-ε-caprolactone (PCL) [72], polyethylene (PE), poly(vinylidene fluoride) (PVDF), polytetrafluoroethylene (PTFE) [73] and polycarbonate (PC) [66]. Interestingly, the results of those studies indicated that the melanin-based polymer induced a positive effect on cell viability, attachment and spreading on the range of materials evaluated [72, 74-76].

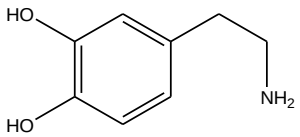

Figure 3.9: Chemical structure of dopamine

From literature, it is clear that researchers agree on the universal character of PDA and on its applicability as linker to immobilize other polymers, biomolecules or linkers. On the other hand, on the deposition behavior and structure of the PDA layers, some disagreement still exists to date. In the following paragraphs, a brief overview will be given on the existing literature regarding the reaction mechanism and structure of PDA.

To date, the exact **polymerization mechanism** remains unknown, but literature often refers to a reaction route resembling melanin formation [41, 77]. Melanins comprise a group of phenolic pigments and their formation is better known as melangonesis which is a biochemical process occurring in the skin to protect animals and humans from solar damage [78]. The mechanism of melanin synthesis is described by the Rapor-Mason pathway and consists of two main phases:

1) the conversion of tyrosine into indolequinones
2) polymerization of these quinones into melanin

Figure 3.10 summarizes the steps in this mechanism in greater detail and makes a comparison with the polymerization mechanism of dopamine proposed by Lee et al.

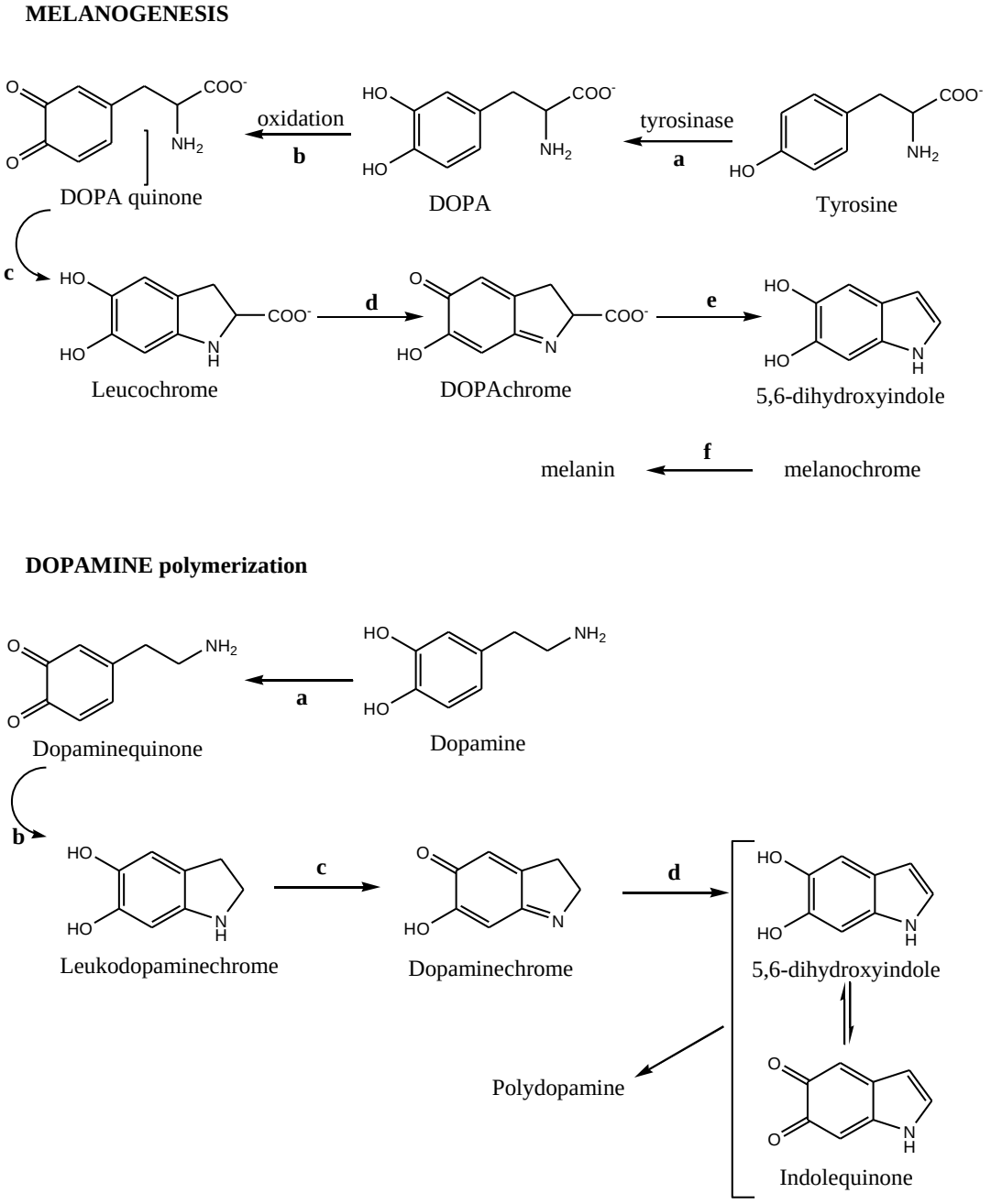

Figure 3.10: Pathway for melanogenesis [78] and polydopamine formation [41].

The greatest difference between both reaction schemes is the involvement of enzymes which catalyze several steps in case of melanogenesis. In case of dopamine, no enzymes are involved but oxidative conditions such as alkaline media and the presence of oxidants such as air-oxygen, ammonium persulfate or Cu^{2+} will be the prerequisite to enable the different oxidation steps [79-80]. In both cases, 5,6-dihydroxyindole (DHI) is formed which is suggested to be the main compound during polymerization, together with its quinone derivative [41, 78, 81]. Also other groups speculated or confirmed that intramolecular cyclization of dopaminequinone occurs with the formation of indole derivatives [69, 82]. Multistep reactions involving these indoles result in the formation of insoluble black to brownish melanin-like PDA particles which aggregate in solution, but at the same time, a tightly adherent PDA coating is formed on the immersed substrates [77].

According to Bernsmann et al, both processes are independent, which means that particles in solution do not adhere to the substrates during immersion, but instead, PDA films are formed because of the interaction of monomeric species with the material's surface [67]. They proposed a radical process similar to aniline oxidation in which radicals absorb at the surface and initiate subsequent polymerization [83]. Definitive proof of this mechanism was not delivered but also other research groups supported this idea [77] or at least confirmed the presence of radicals in the PDA structure [82, 84-85]. They also concluded that a regular supply of freshly, non-oxidized dopamine molecules is needed to enable continuous growth of the PDA layer and to obtain a controllable layer thickness [86 67]. Lee et al proposed that in case of inorganic surfaces such as metals, the catechol derivative of dopamine is forming strong but reversible coordination bonds whereas on organic surfaces, covalent bond formation is established by the quinone derivative [87-88].

Apart from the deposition mechanism, also the **structure** of PDA remains a point of discussion. Intuitively, the structure of PDA could consist of a linear linkage of dopamine units, resulting in a structure as represented in figure 3.11 (a). Nevertheless, as already mentioned before, 5,6-dihydroxyindole and 5,6-indolequinone have already been identified as very important building blocks of PDA. Generally, agreement exists about this fact, but there still remains disagreement about how these units are linked and organized and whether these are the only compounds involved. A first group of researchers strongly believes in the covalent character of this polymer, in which different tautomers of the indole and quinone compounds play a major role during the reaction (see figure 3.12) [81, 89]. In their opinion, PDA clearly resembles a melanin-like structure as displayed in figure 3.11 (b), but uncertainty exists about the number of repeating units. For eumelanins, the formation of dimers and trimers has already been suggested [85]. Conversely, others determined the formation of tetramers and pentamers as the favorable ones [90].
Liebscher et al even proposed a PDA structure consisting of dopamine, DHI and indoledione units with different degrees of (un)saturation, which are linked by C-C bonds between their benzyl groups (see figure 3.11, c) [84, 91] .

Contrary to these models, Dreyer et al did not find spectroscopic evidence for aryl-aryl coupling between the dopamine monomers and instead of a covalent polymer, they suggested a non-covalent organization of cyclized dopamine monomers. Figure 3.11 (d) displays the proposed structure of PDA in which strong, non-covalent intra- and interchain interactions exist, including hydrogen bonding, charge transfer and π-stacking [82]. More recently, it has been suggested that a combination of covalent and non-covalent linkages exist in the PDA structure. Hong et al identified a self-assembled trimer consisting of a $(dopamine)_2$/DHI complex (figure 3.11, e), which is tightly entrapped inside of a covalently bound polydopamine structure [82]. The presence of free dopamine in the polymer was also evidenced by others [81, 92].

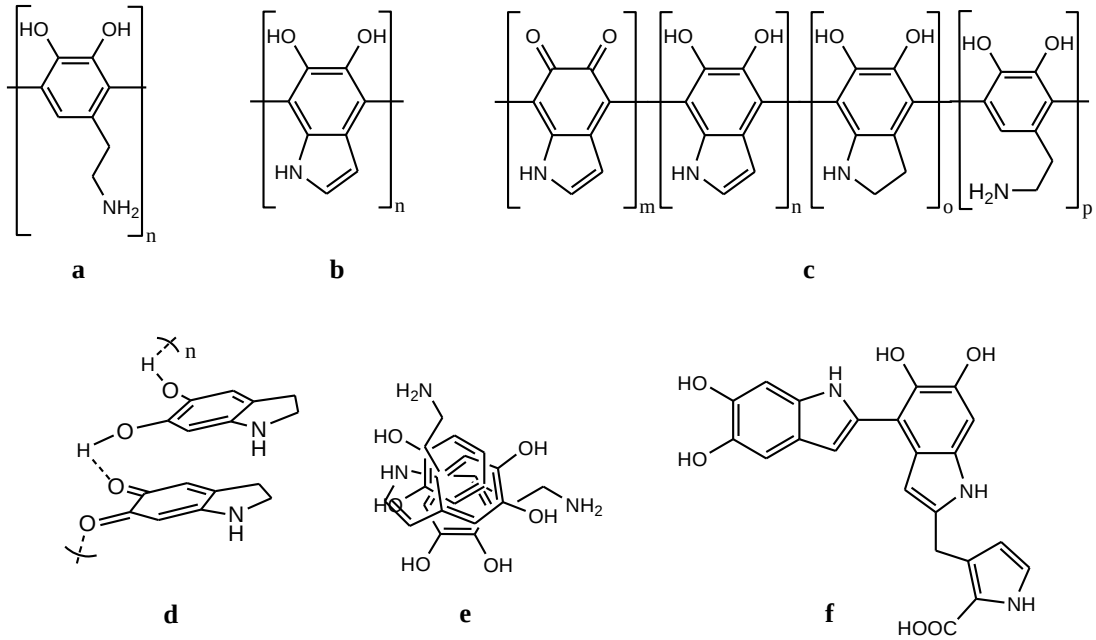

Figure 3.11: Proposed structures of PDA according to the polycatecholamine model [41] (a), the eumelanin-type model [78] (b), the poly(indole-dopamine) model [84] (c), the non-covalent organization model [82] (d), the formation of a $(dopamine)_2$/DHI complex [93] (e) and the formation of a $(DHI)_2$/PCA trimer [94] (f).

Other studies agree on the fact that covalent linkages are very important during the initial steps of PDA built-up but also that non-covalent interactions become significant at later stages [91, 95]. Liebscher et al identified the charge transfer interactions between the quinone and catechol units as the prevalent inter-chain interactions, assisted by some hydrogen bonding [84]. On the other hand, according to Arzillo et al, PDA consists of oligomers which are attached to each other to form aggregates which are organized in 2D planar sheets via π-stacks [95]. Additionally, evidence has been found that these planar sheets of varying dimensions organize in onion-like nanostructures [96].

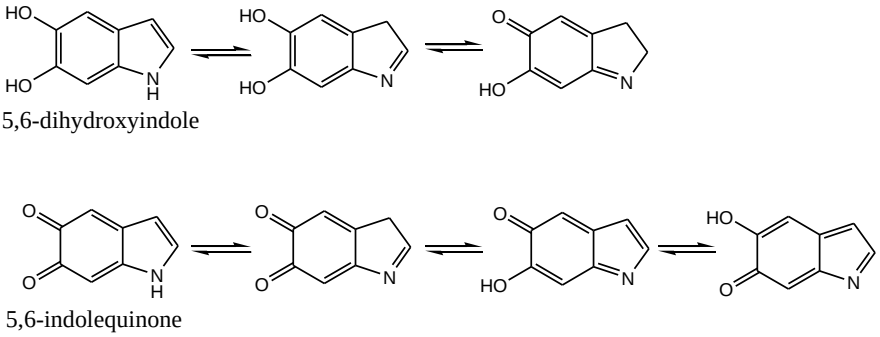

Figure 3.12: Tautomers of 5,6-dihydroxyindole and 5,6-indolequinone [81, 89]

It should be noted that the-above mentioned structural information about PDA is mainly deduced from PDA aggregates which were formed in solution. More recently, Ding and co-workers focused on the structural characteristics of deposited PDA-films for different starting concentrations of the dopamine (DA) solution. They concluded that the film thickness increased with the concentration but once a concentration of 1 g/l was applied, a decreased layer thickness was obtained. Furthermore, based on results obtained with TOF-SIMS, they were able to disprove all the previously mentioned models presented in figure 3.10 and suggested the presence of pyrrolecarboxylic acid (PCA) moieties, which are derived from oxidative degradation of indole units. From their results, the $(DHI)_2$/PCA trimer complex was identified as the major building block of PDA film formation (figure 3.11, f) [94].

It is clear that the PDA structure is very complex and that probably none of the models described in literature completely covers the true structure of this polymer to date. As a consequence, PDA can be described as a very heterogeneous material and future research will have to shed light on this topic.

Despite the uncertainty about its chemical structure, PDA possesses interesting characteristics and as a result, it has been applied for a broad range of applications. Apart from its application as adhesive coating, it is also used for the production of PDA nano/microcapsules which can be used as a reservoir for functional agents [68, 97]. Furthermore, PDA has been used as universal biomineralization route to assist hydroxyapatite crystallization on different scaffold materials [98-100]. In the world of chromatography, it is used as coating for capillary columns to determine auxins [101] and in the world of batteries, it functions as a coating for separators to improve properties such as electrolyte wetting and ionic conductivity [102].
In the present work, PDA is used as an activating sub-layer to enable the subsequent immobilization of biomolecules such as gelatin, antibodies and growth factors (see chapter 4). In a first part, the different deposition protocols are discussed followed by an in depth characterization of the deposited PDA layers.

3.4.2. PDA immobilization protocols and characterization

PMMA, PMMAPEG, PLMA(651) and PLMA(2959) were subjected to a PDA surface modification step. As described in the experimental part (see chapter 6), different immobilization protocols were used. Protocol I resembles the original deposition protocol as described by Lee et al [41]. Protocol II includes an additional step as the samples were first immersed in Tris buffer (pH 8.5), followed by the addition of dopamine (DA) in powder form. In order to evaluate the possibility to further improve the adhesion of polydopamine and the materials developed, both protocols were also combined with an oxygen plasma pre-activation step (referred to as Ipl and IIpl). The deposited layers were characterized by applying a range of characterization techniques including static contact angle (SCA) measurements, X-ray photoelectron spectroscopy (XPS), profilometry measurements, atomic force microscopy (AFM) and scanning electron microscopy (SEM) of which the results are discussed in the up-coming paragraphs.

3.4.2.1. PMMA and PMMAPEG as substrate materials for PDA deposition

The different deposition protocols were tested on PMMA and PMMAPEG, in order to select one of the protocols for the subsequent material biofunctionalization (see chapter 4). Herein, PMMAPEG should be considered as the main material of interest as this material was intended to function as the eventual glucose sensor packaging. PMMA was included in the study as reference material. In § 3.4.2.2, a similar optimization will be described for the PLMA-based materials.

In order to assess the atomic composition of the sample surfaces after PDA deposition, XPS measurements were performed. The recorded atomic nitrogen percentages indicated that a successful immobilization of PDA was accomplished for all samples, regardless of the protocol used (figure 3.13, A and B). For PMMAPEG, protocol I and protocol IIpl resulted in the highest nitrogen percentages (i.e. 5 ± 0.8 % for both protocols) and therefore, they present the preferred protocols.

Based on the O/C ratio, the data revealed that, for PMMA, no significant difference was obtained ($p>0.05$) between the blank and the different surface-modified samples (figure 3.13 C). The latter suggested the deposition of a very thin PDA film through which the substrate material could still be detected. Furthermore, it was anticipated that the O/C value of the PMMA blank would approach the theoretical value of 0.40. The deviation in signal observed for the theoretical (0.40) and experimental blank (0.30) might suggest carbon contamination during sample handling or chain migration and orientation, resulting in higher carbon percentages at the surface.

In case of PMMAPEG (Figure 3.13, D), an excellent agreement was found between the theoretical (0.45) and the experimental value (i.e. 0.46) for the blank. Furthermore, as anticipated, deposition of PDA resulted in a significant decrease of the O/C ratio ($p<0.05$), although, compared to the theoretical value of 0.25, only protocol I approached this value.

Undoubtedly, the observed changes in the chemical composition of the surface also influenced their wettability. Therefore, static contact angle measurements were performed to complement the previously described results. Figure 3.13 (E) clearly shows that, irrespective of the used protocol, the deposition of PDA gave rise to a significant decrease in static contact angle compared to the blank materials ($p<0.05$) (from 70-85° for the blank materials to 40-50° for the PDA coated ones). These data are in good agreement with literature as Lee et al reported contact angles for PDA-coated PTFE and PC of 49° and 42° respectively [41]. Statistical analysis showed that no significant difference was obtained for both materials when comparing protocol I and II. On the other hand, a significant influence could be observed in case protocol II was combined with a plasma pre-activating step ($p<0.05$). This might suggest a different orientation or composition of the formed PDA layer. Yet, if plasma treatment would induce such an effect, a significant difference would also be expected when comparing the results obtained for protocol I with and without a plasma pre-activation step. As this difference is not observed, no clear evidence of this plasma-effect could be delivered at this stage.

Based on XPS and SCA analyses, a successful PDA deposition on both PMMA and PMMAPEG was shown. Furthermore, based on the observed atomic nitrogen percentages and the match between the experimental and the theoretical O/C ratios as obtained from XPS, protocol I was selected as the preferred PDA deposition method. Interestingly, compared to the other protocols, protocol I also offered the advantage to be more time efficient.

In literature, it has been shown that the deposited amount of PDA is a function of the incubation time and that after 24 hours, a 50 nm thick layer is deposited [41]. As a consequence, this variable was also optimized for the selected deposition protocol. After 24 hours of incubation, indeed the highest amount of nitrogen was detected on the PMMAPEG surface (i.e. N/O = 0.30) (Figure 3.13F). For PMMA, a similar optimization was performed and again after 24 hours, the amount of PDA was maximized (N/O = 0.29).

Further characterization of the PDA-modified samples with SEM revealed the presence of clusters (i.e. aggregates of grape-like shaped particles) on the surfaces (figure 3.14). Intrigued by this observation, a comparison was made between the pristine polymers and the plasma treated ones. In this way, we hoped to get a better insight in the above-mentioned plasma-effect. When comparing pristine PMMA (SCA 85°) with the plasma-treated one (SCA ≈ 0°), the size of the largest clusters decreased from 6.5 µm to approximately 2 µm. Similarly, for PMMAPEG, the largest clusters sized 4 µm on the blank material (SCA 75°), while after a plasma treatment (corresponding with a SCA of 43°), this value decreased to 1.3 µm. These data suggest that plasma treatment results in a decreased cluster size, which is probably induced by a closer contact between the substrate and the dopamine solution, resulting in an increased probability for cluster formation to occur concomitant with a higher number of clusters deposited (cfr. cluster nucleation sites).

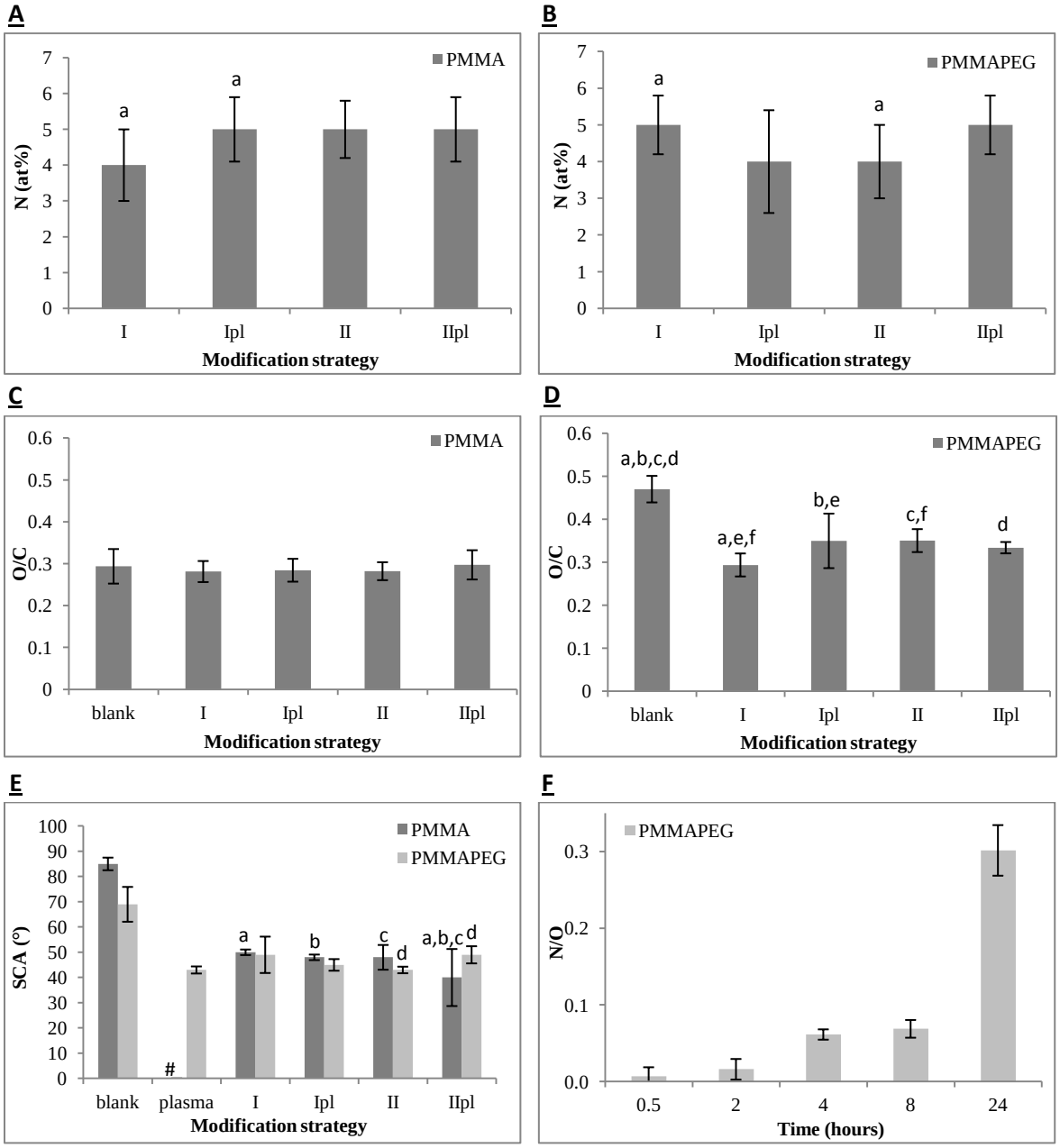

Figure 3.13: Atomic nitrogen percentages of blank and PDA-coated PMMA (A) and PMMAPEG (B) materials and the O/C ratio of the same PDA-coated PMMA (C) and PMMAPEG (D) samples, as determined by XPS. Panel (E) displays the static contact angles (SCA) determined for the blank and PDA-coated PMMA and PMMAPEG samples, applying different immobilization protocols. The value indicated by '#' refers to a contact angle approaching 0°. Panel (F) demonstrates the effect of PDA deposition time on the N/O ratios of PMMAPEG surfaces as obtained by XPS measurements. Samples which are significantly different within one graph are marked with the same letter (a,b,c,…) ($p<0.05$). For the SCA measurements, all PDA-modified samples are significantly different compared to their respective blank ($p<0.05$).

In literature, PDA coatings have already been described as showing a granular morphology on a gold surface [81], to uniform with covalently bound PDA on poly(vinylidene fluoride) (PVDF) [77] and on epoxy resins, showing a granular cover layer containing additional

aggregates with a diameter of 0.5-5µm and 100-450 nm respectively [103]. Furthermore, Giol et al noticed that dependent on the applied protocol, specific surface topographies were obtained on poly(ethylene terephtalate) (PET) [104]. Additionally, plasma pretreatment resulted in a more homogeneous PDA spreading, a finding which was also supported by Xie et al [105].

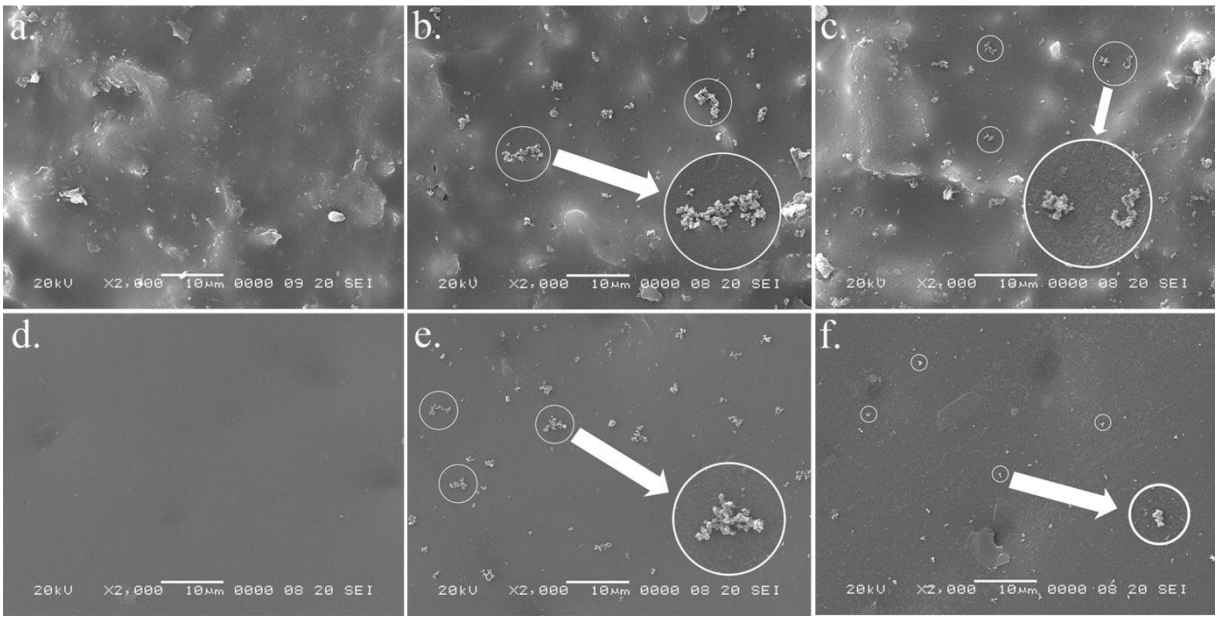

Figure 3.14: SEM images[1] of PMMA blank (a), PDA coated PMMA applying protocol I (b) and plasma + protocol I (c), PMMAPEG blank (d) and PDA coated PMMAPEG applying protocol I (e) and plasma + protocol I (f). For each coated material, several clusters are indicated and one zoom (indicative, produced via graphical software) is pointed by the arrows.

The cluster formation was further evidenced by AFM measurements. For the plasma-treated PMMAPEG samples, grain-like structures were visualized in the surface plots (figure 3.15, C). On the other hand, in the absence of the plasma treatment, a more cloud-like structure was observed (figure 3.15, B). This observation supported the SEM images, as smaller clusters were also observed in case a plasma treatment was applied.

In case of PMMA, upon application of the selected protocol (i.e. protocol I), a decrease in surface roughness manifested, going from an RMS value of 88 nm for the blank down to 45 nm for the PDA-coated samples (figure 3.16, A). It is clear that for the PMMA samples, a high surface roughness was obtained for the blank materials which can be explained by the use of a release foil during the production of the samples. Upon PDA deposition, the surface 'valleys' were filled to some extent (figure 3.16, B), which explained the observed decrease in RMS value.

[1] All SEM images were realized in cooperation with Dr. David Schaubroeck, from the Centre for Microsystems Technology (Cmst) ; Department of Electronics and information systems.

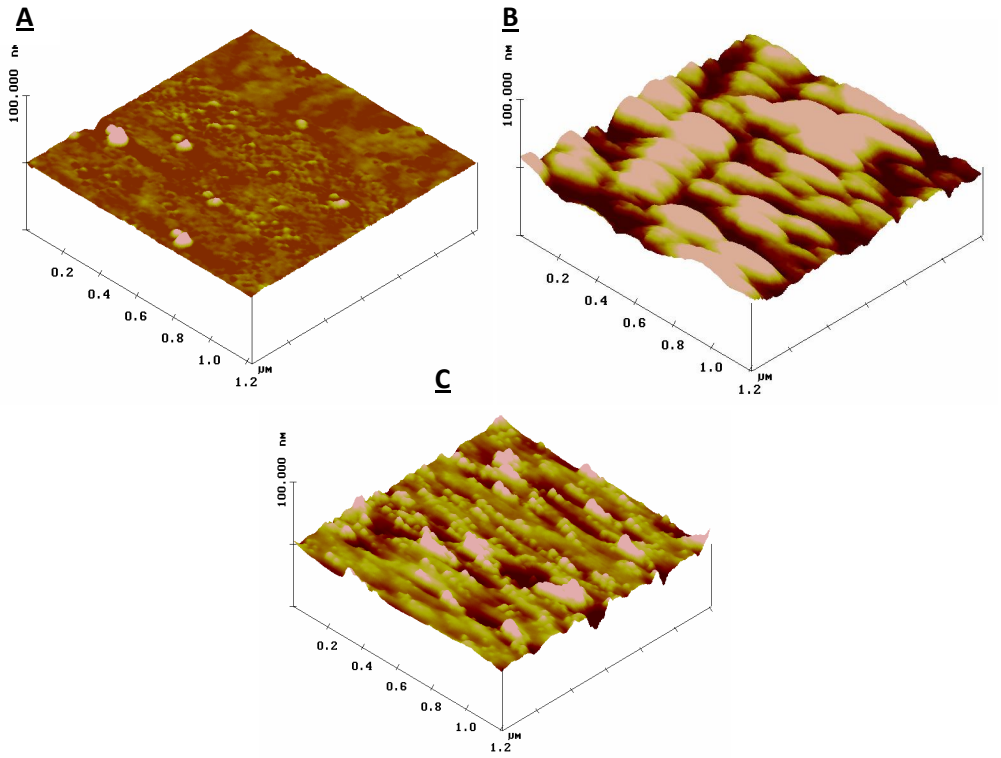

Figure 3.15: Surface plots recorded with AFM for blank PMMAPEG (RMS 0.576 nm) (A), PDA-coated PMMAPEG applying protocol I (RMS 4.459 nm) (B), PDA-coated PMMAPEG applying plasma+protocol I (RMS 4.814 nm) (C)

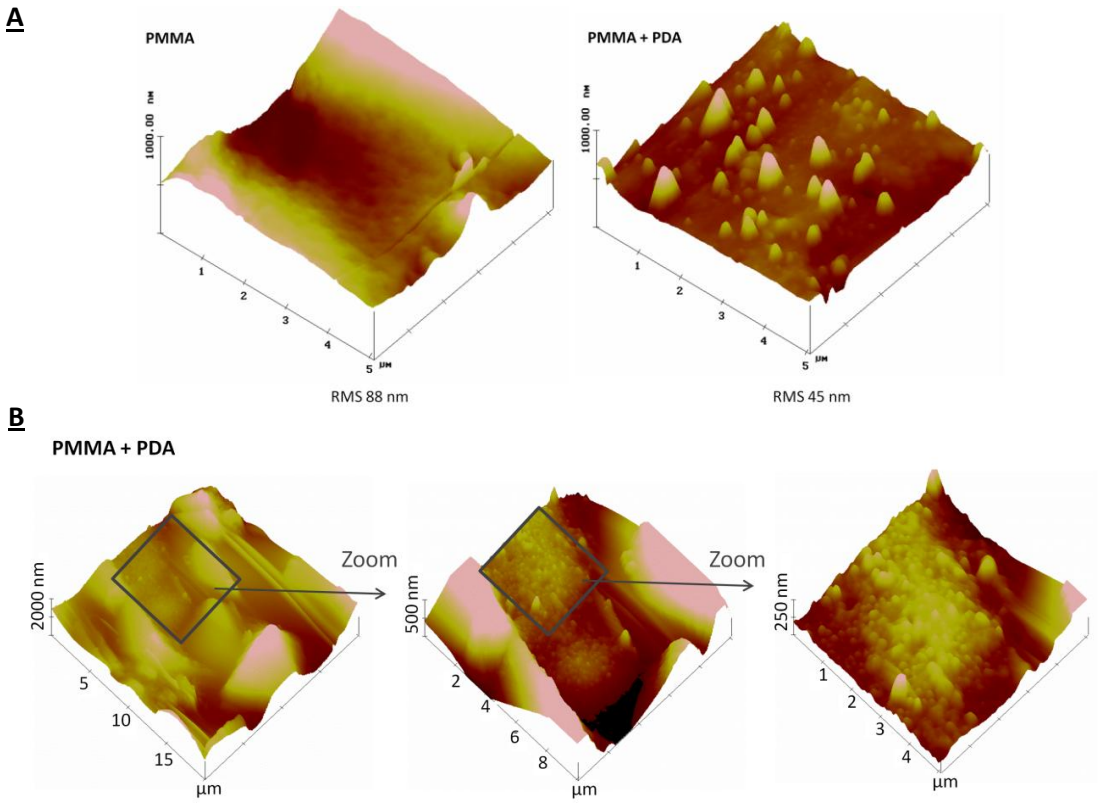

Figure 3.16: Panel A displays the AFM surface plots of the blank (left) and PDA coated PMMA (right), applying protocol I. Panel B clearly shows how the surface valleys contain PDA clusters.

3.4.2.2. PLMA as substrate material for PDA deposition

After optimization of the deposition protocol for PMMA and PMMAPEG, both PLMA(651) and PLMA(2959) were evaluated as substrate materials for PDA immobilization. Based on their hydrophobic nature, which is mainly reflected by their low swelling percentage (<0.5%), a plasma pre-treatment was in this case beneficial to activate the surface and enhance its surface wettability. For these materials, protocol I and the combination of this protocol with a plasma pre-treatment step (Ipl) were evaluated. Two plasma gasses including oxygen and argon gas, were used to study the enhancement of the PDA deposition. In the end, based on the previous findings, we anticipated that the hydrophilicity of the substrate will be crucial to enhance contact with the dopamine solution.

XPS measurements were performed to gain insight in the elemental composition of the deposited PDA layers. The presence of nitrogen in the elemental composition again confirmed the immobilization of this layer (figure 3.17, A). Furthermore, the use of a plasma pre-activation step resulted in significantly higher nitrogen percentages compared to protocol I ($p<0.05$) while the highest nitrogen percentages (up to 6%) were obtained when oxygen was used as plasma gas. It also became clear that significantly higher amounts of PDA were deposited onto PLMA(2959) compared to PLMA(651), especially in case a plasma pre-treatment step was applied.
Apart from the atomic nitrogen percentages, the O/C ratios, represented in figure 3.17 (B), were also evaluated. In case Irgacure®2959 was applied, no significant differences were obtained, whereas for PLMA(651), significant differences were obtained between the plasma treated samples and both the blank and the samples treated using protocol I. Herein, the theoretical O/C value of dopamine (0.25) was best approached by the oxygen plasma treated samples (0.29 for PLMA(651) and 0.27 for PLMA(2959)). Based on the XPS data, the latter protocol was selected as the optimal one. Again, the optimal deposition time was determined to be 24 hours (N/O= 0.28).
Next, static contact angle measurements were performed to evaluate the wettability of the different surfaces. The results (see figure 3.17, C and D) show that treatment of the blank materials with oxygen or argon plasma resulted in a significant decrease of the contact angle. In addition, the most pronounced effect was obtained for the argon plasma treatment (see also § 3.2).
All PDA coated samples showed a significant difference compared to their respective blanks, which again proved the successful immobilization. Only for the PLMA(651) samples which were pre-treated by Ar-plasma, a significant difference in SCA after PDA deposition was not observed ($p>0.05$).
In case Irgacure® 2959 was used as an initiator, similar contact angles were obtained for the different PDA deposition protocols, compared to those obtained for PMMA and PMMAPEG (between 40 and 50°). For PLMA(651), slightly higher contact angles were obtained (up to 55°). However, only in case of Ar plasma treatment, a significant difference was obtained between both PLMA(651) and PLMA(2959) after PDA deposition. Comparison of the

different PDA deposition protocols applied on PLMA(651), showed a significant difference in case protocol I was compared with plasma(O_2)+protocol I. This observation might suggest a different structure or orientation of the PDA layer in case oxygen plasma was applied, but no clear evidence was found for this. Based on the maximized atomic nitrogen percentage, the plasma(O_2)+protocol I was selected as the preferred PDA deposition protocol.
Overall, it could be concluded that the selection of initiator does affect the outcome of surface functionalization, although, only in a limited manner (maximum difference of 2% of nitrogen and less than 10° in SCA value).

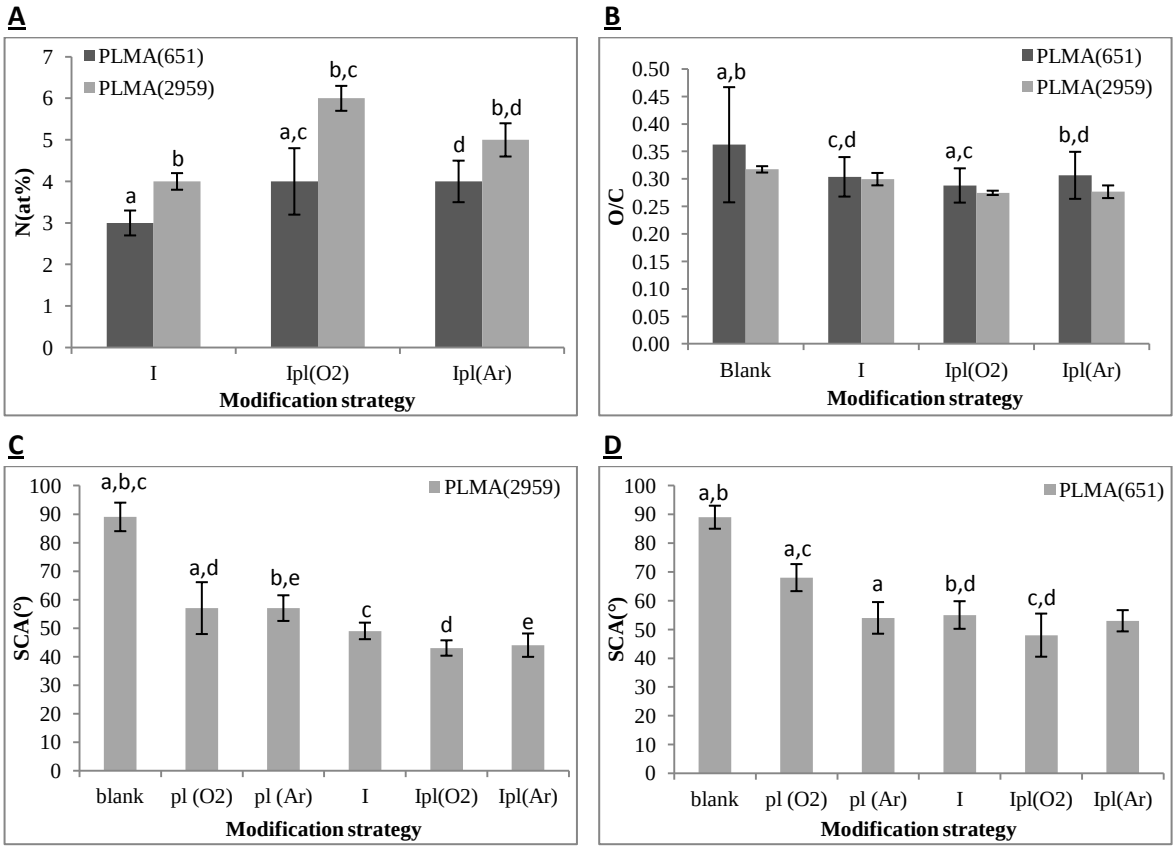

Figure 3.17: Atomic nitrogen percentage (A) and O/C ratios (B) determined by XPS of the blank and PDA-coated PLMA(651) and PLMA(2959) (via protocol I (I) and in combination with an O_2 (Ipl(O_2) or an Ar plasma pre-treatment step (Ipl(Ar))). Static contact angles measured for PLMA(2959) (C) and PLMA(651) (D) are also presented. Samples which are significantly different are marked with the same letter (a,b,c,…)

Again, SEM was used to visualize the clusters formed on the material surfaces. Similar to PMMA and PMMAPEG, the application of a plasma treatment onto PLMA(651) resulted in the formation of smaller clusters, which was probably due to a lower contact angle of the underlying surfaces (figure 3.18, A). In case of the blank material (CA 90°), the largest clusters sized 9 µm. Conversely, for the O_2-plasma treated samples (CA 68°), the largest clusters only sized 4 µm. For the Ar-plasma treated samples (CA 54°), this value even dropped to 2 µm.

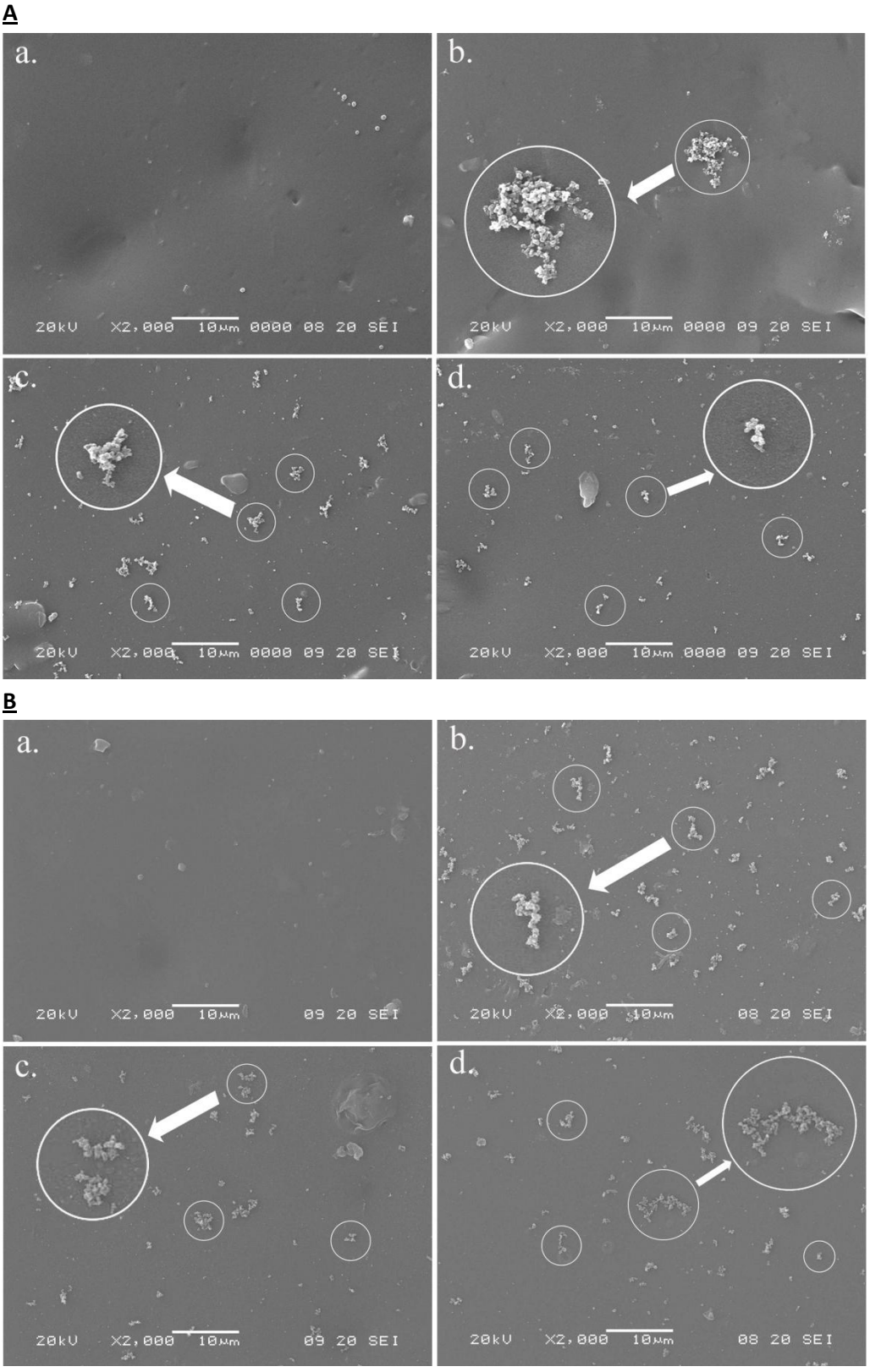

Figure 3.18: SEM images of PLMA(651) (A) and PLMA(2959) (B): blank (a), PDA coated, protocol I (b), O_2 + protocol I (c) and Ar + protocol I (d). For each coated material, several clusters are indicated and one zoom (indicative, produced via graphical software) is indicated with arrows.

Upon comparing different materials, it became clear that comparable cluster sizes were obtained because of similar contact angles. Indeed, comparison of the largest cluster size obtained for the PMMAPEG blank (CA 69°) and the O_2-plasma treated PLMA samples (CA 68°), revealed a comparable cluster size (i.e. 4 µm).

If one material is considered, the cluster size definitely decreased with a decreasing contact angle. However, this observation was contradicted when evaluating the PLMA(2959) materials (Figure 3.18, B). Herein, the largest clusters (7 µm) were observed on the argon-treated samples (CA 61°), followed by the oxygen treated samples (4 µm; CA 71°) and the blank material (2 µm, CA 89°), a trend which is exactly the opposite of the previously observed ones. It can thus be concluded that the PDA cluster formation is not solely controlled by the surface contact angle.

3.5. Conclusion

In a first part of this chapter, a plasma treatment has been evaluated for its surface activating effect. The results showed that both argon and oxygen were able to lower the contact angle of the different substrate materials due to the introduction of oxygen containing groups. Furthermore, the use of a nitrogen gas plasma enabled the introduction of nitrogen functionalities on the surface of the materials and this approach could offer future opportunities to allow for surface biofunctionalization.
In the next step, two functionalization routes were explored. First, the UV-induced post-plasma grafting of 2-aminoethyl methacrylate was studied. For both the LMA-based materials and PMMAPEG, successful grafting was shown. However, compared to literature results, the amount of immobilized AEMA was only limited. Based on the XPS results, the optimal Ar plasma treatment time was considered to be 30 seconds for PMMAPEG, whereas for the PLMA materials, this time was set at 14 seconds.
In the second case, polydopamine was evaluated as activating sublayer and regardless of the underlying substrate and the used protocol, successful immobilization was accomplished for both PMMAPEG and PLMA. The presence of the layer was confirmed by XPS as indicated by the presence of nitrogen on the surface, through SEM and AFM because of the visualization of clusters and via SCA measurements, as shown by the changed wettabilities. Based on the obtained nitrogen content present on the surface and the best agreement between the theoretical and the experimental O/C surface ratio's, the optimal PDA deposition protocol could be selected for each material, being protocol I in case of PMMAPEG and Ipl(O_2) for the LMA-based materials.
For the latter material, the effect of the initiator selection on the subsequent surface functionalization was evaluated. In case of the post-plasma grafting of AEMA, no clear influence was noticed. Conversely, in case of PDA deposition, the use of irgacure® 2959 resulted in a slightly higher nitrogen content on the surface (+2%), although no differences

were found in surface wettability. Due to this difference, it was decided to exclude PLMA(651) from the biofunctionalization studies, to be discussed in chapter 4.

3.6. References

1. Mogosanu, D. E., et al. (2014) Polyester Biomaterials for Regenerative Medicine; Chapter: Frontiers in Biomaterials: The Design, Synthetic Strategies and Biocompatibility of Polymer Scaffolds for Biomedical Application., pp 155-197, Bentham Science.
2. Lopez-Santos, C., Yubero, F., Cotrino, J., Barranco, A., and Gonzalez-Elipe, A. R. (2008) - Plasmas and atom beam activation of the surface of polymers, *Journal of Physics D-Applied Physics* 41.
3. Schulz, U., Munzert, P., and Kaiser, N. (2001) Surface modification of PMMA by DC glow discharge and microwave plasma treatment for the improvement of coating adhesion, *Surface and Coatings Technology* 142, 507-511.
4. Koschwanez, H. E., Reichert, W. M., and Klitzman, B. (2010) Intravital microscopy evaluation of angiogenesis and its effects on glucose sensor performance, *Journal of Biomedical Materials Research Part A* 93A, 1348-1357.
5. Henry, A. C., Tutt, T. J., Galloway, M., Davidson, Y. Y., McWhorter, C. S., Soper, S. A., and McCarley, R. L. (2000) Surface modification of poly(methyl methacrylate) used in the fabrication of microanalytical devices, *Analytical Chemistry* 72, 5331-5337.
6. Brown, L., Koerner, T., Horton, J. H., and Oleschuk, R. D. (2006) Fabrication and characterization of poly(methylmethacrylate) microfluidic devices bonded using surface modifications and solvents, *Lab on a Chip* 6, 66-73.
7. Soper, S. A., Henry, A. C., Vaidya, B., Galloway, M., Wabuyele, M., and McCarley, R. L. (2002) Surface modification of polymer-based microfluidic devices, *Analytica Chimica Acta* 470, 87-99.
8. Tao, S. L., Lubeley, M. W., and Desai, T. A. (2003) Bioadhesive poly(methyl methacrylate) microdevices for controlled drug delivery, *Journal of controlled release* 88, 215-228.
9. Patel, S., Thakar, R. G., Wong, J., McLeod, S. D., and Li, S. (2006) Control of cell adhesion on poly(methyl methacrylate), *Biomaterials* 27, 2890-2897.
10. Fixe, F., Dufva, M., Telleman, P., and Christensen, C. B. V. (2004) Functionalization of poly(methyl methacrylate) (PMMA) as a substrate for DNA microarrays, *Nucleic Acids Research* 32.
11. Tanahashi, M., Yao, T., Kokubo, T., Minoda, M., Miyamoto, T., Nakamura, T., and Yamamuro, T. (1994) Apatite coated on organic polymers by biomimetic process-improvement in its adhesion to substrate by NaOH treatment, *Journal of Applied Biomaterials* 5, 339-347.
12. Varma, H. K., Sreenivasan, K., Yokogawa, Y., and Hosumi, A. (2003) In vitro calcium phosphate growth over surface modified PMMA film, *Biomaterials* 24, 297-303.
13. Liu, S. Q., Ito, Y., and Imanishi, Y. (1993) Cell-growth on immobilized cell-growth factor.5. Interaction of immobilized transferrin with fibroblast cells, *International Journal of Biological Macromolecules* 15, 221-226.
14. Ito, Y., Liu, S. Q., Nakabayashi, M., and Imanishi, Y. (1992) Cell-growth on immobilized cell-growth factor. 2.Adhesion and growth of fibroblast cells on Poly(methyl methacrylate) membrane immobilized with proteins of various kinds, *Biomaterials* 13, 789-794.
15. Liu, S. Q., Ito, Y., and Imanishi, Y. (1992) Cell-growth on immobilized cell-growth factor. 4. Interaction of fibroblast cells with insulin immobilized on Poly(methyl methacrylate) membrane, *Journal of Biochemical and Biophysical Methods* 25, 139-148.

16. Ozcan, C., Zorlutuna, P., Hasirci, V., and Hasirci, N. (2008) Influence of oxygen plasma modification on surface free energy of PMMA films and cell attachment, *Macromolecular Symposia* 269, 128-137.
17. Lim, H., Lee, Y., Han, S., Cho, J., and Kim, K. J. (2001) Surface treatment and characterization of PMMA, PHEMA, and PHPMA, *Journal of Vacuum Science & Technology a-Vacuum Surfaces and Films* 19, 1490-1496.
18. Zhang, L., Wu, D., Chen, Y., Wang, X., Zhao, G., Wan, H., and Huang, C. (2009) Surface modification of polymethyl methacrylate intraocular lenses by plasma for improvement of antithrombogenicity and transmittance, *Applied Surface Science* 255, 6840-6845.
19. Suh, T. S., Joo, C. K., Kim, Y. C., Lee, M. S., Lee, H. K., Choe, B. Y., and Chun, H. J. (2002) Surface modification of polymethyl methacrylate intraocular lenses with the mixture of acrylic acid and acrylamide via plasma-induced graft copolymerization, *Journal of Applied Polymer Science* 85, 2361-2366.
20. Schulz, U., Munzert, P., and Kaiser, N. (2001) Surface modification of PMMA by DC glow discharge and microwave plasma treatment for the improvement of coating adhesion, *Surface & Coatings Technology* 142, 507-511.
21. Kitova, S., Minchev, M., and Danev, G. (2005) Soft plasma treatment of polymer surfaces, *Journal of Optoelectronics and Advanced Materials* 7, 249-252.
22. Liu, C., Brown, N. M. D., and Meenan, B. J. (2006) Dielectric barrier discharge (DBD) processing of PMMA surface: Optimization of operational parameters, *Surface & Coatings Technology* 201, 2341-2350.
23. Liu, C., and Meenan, B. J. (2008) Effect of Air Plasma Processing on the Adsorption Behaviour of Bovine Serum Albumin on Spin-Coated PMMA Surfaces, *Journal of Bionic Engineering* 5, 204-214.
24. Lim, H., Lee, Y., Han, S., Cho, J., and Kim, K.-J. (2001) Surface treatment and characterization of PMMA, PHEMA, and PHPMA, *Journal of Vacuum Science & Technology A* 19, 1490-1496.
25. Jacobs, T., Declercq, H., De Geyter, N., Cornelissen, R., Dubruel, P., Leys, C., and Morent, R. (2013) Improved cell adhesion to flat and porous plasma-treated poly-epsilon-caprolactone samples, *Surface & Coatings Technology* 232, 447-455.
26. Suzuki, M., Kishida, A., Iwata, H., and Ikada, Y. (1986) Graft copolymerization of acrylamide onto a polyethylene surface pretreated with glow discharge, *Macromolecules* 19, 1804-1808.
27. Suh, T. S., Joo, C.-K., Kim, Y. C., Lee, M. S., Lee, H. K., Choe, B. Y., and Chun, H. J. (2002) Surface modification of polymethyl methacrylate Intraocular Lenses with the mixture of acrylic acid and acrylamide via plasma-induced graft copolymerization *Journal of Applied Polymer Science* 85.
28. Kang, I. K., Kwon, B. K., Lee, J. H., and Lee, H. B. (1993) IMMOBILIZATION OF PROTEINS ON POLY(METHYL METHACRYLATE) FILMS, *Biomaterials* 14, 787-792.
29. Desmet, T., Billiet, T., Berneel, E., Cornelissen, R., Schaubroeck, D., Schacht, E., and Dubruel, P. (2010) Post-Plasma Grafting of AEMA as a Versatile Tool to Biofunctionalise Polyesters for Tissue Engineering, *Macromol. Biosci.* 10, 1484-1494.
30. Wirsen, A., Sun, H., and Albertsson, A. C. (2005) Solvent free vapour phase photografting of acrylamide onto poly(methyl methacrylate), *Polymer* 46, 4554-4561.
31. Iguerb, O., and Bertrand, P. (2008) Graft photopolymerization of polyethylene glycol monoacrylate (PEGA) on poly(methyl methacrylate) (PMMA) films to prevent BSA adsorption, *Surface and Interface analysis* 40, 386-390.
32. Ko, Y. G., Kim, Y. H., Park, K. D., Lee, H. J., Lee, W. K., Park, H. D., Kim, S. H., Lee, G. S., and Ahn, D. J. (2001) Immobilization of poly(ethylene glycol) or its sulfonate onto polymer surfaces by ozone oxidation, *Biomaterials* 22, 2115-2123.
33. Sofia, S. J., and Merill, E. W. (1997) Grafting of PEO to polymer surfaces using electron beam irradiation, *Journal of biomedical materials research* 40, 153-163.

34. Cho, S. O., and Jun, H. Y. (2005) Surface hardening of poly(methyl methacrylate) by electron irradiation, *Nuclear instruments & methods in physics research. Section B, Beam interactions with materials and atoms* 237, 525-532.
35. Aminuzzaman, M., Mitsuishi, M., and Miyashita, T. (2010) Fabrication of fluorinated polymer nanosheets using the Langmuir-Blodgett technique: characterization of their surface properties and applications, *Polymer international* 59, 583-596.
36. Ruckenstein, E., and Li, Z. F. (2005) Surface modification and functionalization through the self-assembled monolayer and graft polymerization, *Advances in Colloid and Interface Science* 113, 43-63.
37. Kharlampieva, E., and Sukhishvili, S. A. (2006) Hydrogen-bonded layer-by-layer polymer films, *Polym. Rev.* 46, 377-395.
38. Messersmith, P. B. (2010) Holding On by a Hard-Shell Thread, *Science* 328, 180-181.
39. Lee, H., Lee, B. P., and Messersmith, P. B. (2007) A Reversible Wet/Dry Adhesive Inspired by Mussels and Geckos, *Nature* 448, 338-U334.
40. Messersmith, P. B. (2008) Materials science - Multitasking in tissues and materials, *Science* 319, 1767-1768.
41. Lee, H., Dellatore, S. M., Miller, W. M., and Messersmith, P. B. (2007) Mussel-Inspired Surface Chemistry for Multifunctional Coatings, *Science* 318.
42. Gombotz, W., and Hoffman, A. (1987) Gas-discharge techniques for biomaterial modification, *CRC Critical Reviews in Biocompatibility* 4, 1-42.
43. Bogaerts, A., Neyts, E., Gijbels, R., and van der Mullen, J. (2002) Gas discharge plasmas and their applications, *Spectrochimica Acta Part B: Atomic Spectroscopy* 57, 609-658.
44. Desmet, T., Morent, R., De Geyter, N., Leys, C., Schacht, E., and Dubruel, P. (2009) Nonthermal Plasma Technology as a Versatile Strategy for Polymeric Biomaterials Surface Modification: A Review, *Biomacromolecules* 10, 2351–2378.
45. Vesel, A., and Mozetic, M. (2012) Surface modification and ageing of PMMA polymer by oxygen plasma treatment, *Vacuum* 86, 634-637.
46. Chu, P. K., Chen, J. Y., Wang, L. P., and Huang, N. (2002) Plasma-surface modification of biomaterials, *Materials Science & Engineering R-Reports* 36, 143-206.
47. Morent, R., De Geyter, N., Leys, C., Gengembre, L., and Payen, E. (2007) Study of the ageing behaviour of polymer films treated with a dielectric barrier discharge in air, helium and argon at medium pressure, *Surface & Coatings Technology* 201, 7847-7854.
48. Øiseth, S. K., Krozer, A., Kasemo, B., and Lausmaa, J. (2002) Surface modification of spin-coated high-density polyethylene films by argon and oxygen glow discharge plasma treatments, *Applied Surface Science* 202, 92-103.
49. Gupta, B., Hilborn, J. G., Bisson, I., and Frey, P. (2001) Plasma-induced graft polymerization of acrylic acid onto poly (ethylene terephthalate) films, *Journal of Applied Polymer Science* 81, 2993-3001.
50. Lee, S. D., Hsiue, G. H., and Kao, C. Y. (1996) Preparation and characterization of a homobifunctional silicone rubber membrane grafted with acrylic acid via plasma-induced graft copolymerization, *Journal of Polymer Science Part A: Polymer Chemistry* 34, 141-148.
51. De Cooman, H., Desmet, T., Callens, F., and Dubruel, P. (2012) Role of radicals in UV-initiated postplasma grafting of poly-ε-caprolactone: An electron paramagnetic resonance study, *Journal of Polymer Science Part A: Polymer Chemistry* 50, 2142-2149.
52. Yu, M. E., and Deming, T. J. (1998) Synthetic Polypeptide Mimics of Marine Adhesives, *Macromolecules* 31, 4739-4745.
53. Statz, A. R., Meagher, R. J., Barron, A. E., and Messersmith, P. B. (2005) New Peptidomimetic Polymers for Antifouling Surfaces, *Journal of the American Chemical Society* 127, 7972-7973.
54. Waite, J. H., and Qin, X. X. (2001) Polyphosphoprotein from the adhesive pads of Mytilus edulis, *Biochemistry* 40, 2887-2893.
55. Yu, M. E., Hwang, J. Y., and Deming, T. J. (1999) Role of L-3,4-dihydroxyphenylalanine in mussel adhesive proteins, *Journal of the American Chemical Society* 121, 5825-5826.

56. Burzio, L. A., and Waite, J. H. (2000) Cross-linking in adhesive quinoproteins: Studies with model decapeptides, *Biochemistry* 39, 11147-11153.
57. Huang, K., Lee, B. P., and Messersmith, P. B. (2001) Synthesis and Characterization of Self-Assembling Block Copolymers Containing Adhesive Moieties, *Abstracts of Papers of the American Chemical Society* 222, U319-U319.
58. Dalsin, J. L., Hu, B. H., Lee, B. P., and Messersmith, P. B. (2003) Mussel Adhesive Protein Mimetic Polymers for the Preparation of Nonfouling Surfaces, *Journal of the American Chemical Society* 125, 4253-4258.
59. Dalsin, J. L., Lin, L. J., Tosatti, S., Voros, J., Textor, M., and Messersmith, P. B. (2005) Protein Resistance of Titanium Oxide Surfaces Modified by Biologically Inspired mPEG-DOPA, *Langmuir* 21, 640-646.
60. Fan, X. W., Lin, L. J., Dalsin, J. L., and Messersmith, P. B. (2005) Biomimetic Anchor for Surface-Initiated Polymerization from Metal Substrates, *Journal of the American Chemical Society* 127, 15843-15847.
61. Chawla, K., Lee, S., Lee, B. P., Dalsin, J. L., Messersmith, P. B., and Spencer, N. D. (2009) A Novel Low-Friction Surface for Biomedical Applications: Modification of Poly(Dimethylsiloxane) (PDMS) with Polyethylene Glycol (PEG)-DOPA-Lysine, *Journal of Biomedical Materials Research Part A* 90A, 742-749.
62. Glass, P., Chung, H., Washburn, N. R., and Sitti, M. (2009) Enhanced Reversible Adhesion of Dopamine Methacrylamide-Coated Elastomer Microfibrillar Structures under Wet Conditions, *Langmuir* 25, 6607-6612.
63. Statz, A. R. (2009) Experimental and Theoretical Investigation of Chain Length and Surface Coverage on Fouling of Surface Grafted Polypeptoids, *Biointerphases* 4, FA22.
64. Wach, J.-Y., Malisova, B., Bonazzi, S., Tosatti, S., Textor, M., Zuercher, S., and Gademann, K. (2008) Protein-Resistant Surfaces through Mild Dopamine Surface Functionalization, *Chemistry-a European Journal* 14, 10579-10584.
65. Waite, J. H. (2008) Surface Chemistry - Mussel Power, *Nature Materials* 7, 8-9.
66. Lee, H., Rho, J., and Messersmith, P. B. (2009) Facile Conjugation of Biomolecules onto Surfaces via Mussel Adhesive Protein Inspired Coatings, *Advanced Materials* 21, 431-434.
67. Bernsmann, F., Ponche, A., Ringwald, C., Hemmerle, J., Raya, J., Bechinger, B., Voegel, J.-C., Schaaf, P., and Ball, V. (2009) Characterization of Dopamine-Melanin Growth on Silicon Oxide, *Journal of Physical Chemistry C* 113, 8234-8242.
68. Postma, A., Yan, Y., Wang, Y., Zelikin, A. N., Tjipto, E., and Caruso, F. (2009) Self-Polymerization of Dopamine as a Versatile and Robust Technique to Prepare Polymer Capsules, *Chemistry of Materials* 21, 3042-3044.
69. Yu, F., Chen, S., Chen, Y., Li, H., Yang, L., and Yin, Y. (2010) Experimental and Theoretical Analysis of Polymerization Reaction Process on the Polydopamine Membranes and its Corrosion Protection Properties for 304 Stainless Steel, *Journal of Molecular Structure* 982, 152-161.
70. Haiyuan, H., Bo, Y., Qian, Y., Yusheng, G., and Feng, Z. (2010) Modification of carbon nanotubes with a nanothin polydopamine layer and polydimethylamino-ethyl methacrylate brushes, *Carbon* 48.
71. Kang, S. M., You, I., Cho, W. K., Shon, H. K., Lee, T. G., Choi, I. S., Karp, J. M., and Lee, H. (2010) One-Step Modification of Superhydrophobic Surfaces by a Mussel-Inspired Polymer Coating, *Angewandte Chemie-International Edition* 49, 9401-9404.
72. Ku, S. H., and Park, C. B. (2010) Human endothelial cell growth on mussel-inspired nanofiber scaffold for vascular tissue engineering, *Biomaterials* 31, 9431-9437.
73. Xi, Z.-Y., Xu, Y.-Y., Zhu, L.-P., Wang, Y., and Zhu, B.-K. (2009) A Facile Method of Surface Modification for Hydrophobic Polymer Membranes Based on the Adhesive Behavior of Poly(DOPA) and Poly(dopamine), *Journal of Membrane Science* 327, 244-253.
74. Ku, S. H., Lee, J. S., and Park, C. B. (2010) Spatial Control of Cell Adhesion and Patterning through Mussel-Inspired Surface Modification by Polydopamine, *Langmuir* 26, 15104-15108.

75. Shin, Y. M., Lee, Y. B., Kim, S. J., Kang, J. K., Park, J.-C., Jang, W., and Shin, H. (2012) Mussel-Inspired Immobilization of Vascular Endothelial Growth Factor (VEGF) for Enhanced Endothelialization of Vascular Grafts, *Biomacromolecules* 13, 2020-2028.
76. Ku, S. H., Ryu, J., Hong, S. K., Lee, H., and Park, C. B. (2010) General Functionalization Route for Cell Adhesion on Non-Wetting Surfaces, *Biomaterials* 31, 2535-2541.
77. Jiang, J. H., Zhu, L. P., Zhu, L. J., Zhu, B. K., and Xu, Y. Y. (2011) Surface Characteristics of a Self-Polymerized Dopamine Coating Deposited on Hydrophobic Polymer Films, *Langmuir* 27, 14180-14187.
78. Sugumaran, M. (1991) Molecular Mechanisms for Mammalian Melanogenesis - Comparison with Insect Cuticular Sclerotization, *Febs Letters* 293, 4-10.
79. Wei, Q., Zhang, F., Li, J., Li, B., and Zhao, C. (2010) Oxidant-induced dopamine polymerization for multifunctional coatings, *Polymer Chemistry* 1, 1430-1433.
80. Bernsmann, F., Ball, V., Addiego, F., Ponche, A., Michel, M., Gracio, J. J. D., Toniazzo, V., and Ruch, D. (2011) Dopamine-Melanin Film Deposition Depends on the Used Oxidant and Buffer Solution, *Langmuir* 27, 2819-2825.
81. Zangmeister, R. A., Morris, T. A., and Tarlov, M. J. (2013) Characterization of Polydopamine Thin Films Deposited at Short Times by Autoxidation of Dopamine, *Langmuir* 29, 8619-8628.
82. Dreyer, D. R., Miller, D. J., Freeman, B. D., Paul, D. R., and Bielawski, C. W. (2012) Elucidating the Structure of Poly(dopamine), *Langmuir* 28, 6428-6435.
83. Sapurina, I., Riede, A., and Stejskal, J. (2001) In-situ polymerized polyaniline films 3. Film formation, *Synthetic Metals* 123, 503-507.
84. Liebscher, J., Mrowczynski, R., Scheidt, H. A., Filip, C., Hadade, N. D., Turcu, R., Bende, A., and Beck, S. (2013) Structure of Polydopamine: A Never-Ending Story?, *Langmuir* 29, 10539-10548.
85. d'Ischia, M., Napolitano, A., Pezzella, A., Meredith, P., and Sarna, T. (2009) Chemical and Structural Diversity in Eumelanins: Unexplored Bio-Optoelectronic Materials, *Angewandte Chemie-International Edition* 48, 3914-3921.
86. Bernsrnann, F., Ersen, O., Voegel, J. C., Jan, E., Kotov, N. A., and Ball, V. (2010) Melanin-Containing Films: Growth from Dopamine Solutions versus Layer-by-Layer Deposition, *Chemphyschem* 11, 3299-3305.
87. Lee, H., Scherer, N. F., and Messersmith, P. B. (2006) Single-Molecule Mechanics of Mussel Adhesion, *Proceedings of the National Academy of Sciences of the United States of America* 103, 12999-13003.
88. Ye, Q., Zhou, F., and Liu, W. (2011) Bioinspired Catecholic Chemistry for Surface Modification, *Chemical Society Reviews* 40, 4244-4258.
89. Il'ichev, Y. V., and Simon, J. D. (2003) Building blocks of eumelanin: Relative stability and excitation energies of tautomers of 5,6-dihydroxyindole and 5,6-indolequinone, *Journal of Physical Chemistry B* 107, 7162-7171.
90. Kaxiras, E., Tsolakidis, A., Zonios, G., and Meng, S. (2006) Structural model of eumelanin, *Physical review letters* 97.
91. Della Vecchia, N. F., Avolio, R., Alfe, M., Errico, M. E., Napolitano, A., and d'Ischia, M. (2013) Building-Block Diversity in Polydopamine Underpins a Multifunctional Eumelanin-Type Platform Tunable Through a Quinone Control Point, *Advanced Functional Materials* 23, 1331-1340.
92. Ponzio, F., and Ball, V. (2014) Persistence of dopamine and small oxidation products thereof in oxygenated dopamine solutions and in “polydopamine” films, *Colloids and Surfaces A: Physicochemical and Engineering Aspects* 443, 540-543.
93. Hong, S., Na, Y. S., Choi, S., Song, I. T., Kim, W. Y., and Lee, H. (2012) Non-Covalent Self-Assembly and Covalent Polymerization Co-Contribute to Polydopamine Formation, *Advanced Functional Materials* 22, 4711-4717.
94. Ding, Y., Weng, L.-T., Yang, M., Yang, Z., Lu, X., Huang, N., and Leng, Y. (2014) Insights into Aggregation/Deposition and Structure of Polydopamine Film, *Langmuir*.

95. Arzillo, M., Mangiapia, G., Pezzella, A., Heenan, R. K., Radulescu, A., Paduano, L., and d'Ischia, M. (2012) Eumelanin Buildup on the Nanoscale: Aggregate Growth/Assembly and Visible Absorption Development in Biomimetic 5,6-Dihydroxyindole Polymerization, *Biomacromolecules* 13, 2379-2390.
96. Watt, A. A. R., Bothma, J. P., and Meredith, P. (2009) The supramolecular structure of melanin, *Soft Matter* 5, 3754-3760.
97. Yu, B., Wang, D. A., Ye, Q., Zhou, F., and Liu, W. (2009) Robust polydopamine nano/microcapsules and their loading and release behavior, *Chemical Communications*, 6789-6791.
98. Wu, C., Han, P., Liu, X., Xu, M., Tian, T., Chang, J., and Xiao, Y. (2014) Mussel-inspired bioceramics with self-assembled Ca-P/polydopamine composite nanolayer: Preparation, formation mechanism, improved cellular bioactivity and osteogenic differentiation of bone marrow stromal cells, *Acta Biomaterialia* 10, 428-438.
99. Ryu, J., Ku, S. H., Lee, H., and Park, C. B. (2010) Mussel-Inspired Polydopamine Coating as a Universal Route to Hydroxyapatite Crystallization, *Advanced Functional Materials* 20, 2132-2139.
100. Zhou, Y.-Z., Cao, Y., Liu, W., Chu, C. H., and Li, Q.-L. (2012) Polydopamine-Induced Tooth Remineralization, *Acs Applied Materials & Interfaces* 4, 6900-6909.
101. Yin, X.-B., and Liu, D.-Y. (2008) Polydopamine-based permanent coating capillary electrochromatography for auxin determination, *Journal of Chromatography A* 1212, 130-136.
102. Ryou, M.-H., Lee, Y. M., Park, J.-K., and Choi, J. W. (2011) Mussel-Inspired Polydopamine-Treated Polyethylene Separators for High-Power Li-Ion Batteries, *Advanced Materials* 23, 3066-+.
103. David Schaubroeck, Y. V., Luc Van Vaeck, Els Vanderleyden, peter Dubruel, Jan Vanfleteren. (2014) Surface characterization and stability of an epoxy resin surface modified with polyamines grafted on polydopamine, *Applied Surface Science* 303, 465-472.
104. Giol, E. D., Schaubroeck, D., Kersemans, K., De Vos, F., Van Vlierberghe, S., and Dubruel, P. (2015) Bio-inspired surface modification of PET for cardiovascular applications: case study of gelatin, *Colloids and Surfaces B: Biointerfaces*.
105. Xie, J., Michael, P. L., Zhong, S., Ma, B., MacEwan, M. R., and Lim, C. T. (2012) Mussel inspired protein-mediated surface modification to electrospun fibers and their potential biomedical applications, *Journal of Biomedical Materials Research Part A* 100, 929-938.

Chapter 4

Cell-interactive methacrylate-based materials through surface biofunctionalization

Parts of this chapter have been published in:

Van de Walle, E.; Van Nieuwenhove, I.; Vanderleyden, E.; Declercq, H.; Gellynck, K.; Schaubroeck, D.; Ottevaere, H.; Thienpont, H.; De Vos, W. H.; Cornelissen, M.; Van Vlierberghe, S.; Dubruel, P., Polydopamine-Gelatin as Universal Cell-Interactive Coating for Methacrylate-Based Medical Device Packaging Materials: When Surface Chemistry Overrules Substrate Bulk Properties. *Biomacromolecules* **2016,** *17* (1), 56-68.

4.1. Introduction

Surface biofunctionalization differentiates from surface activation in the sense that modification of the material is performed in order to introduce a biological function. In this work, the introduction of a biological function aims at controlling the cell-interactivity of the developed materials. Even more, we aim at enhancing the vascularization around the implant.

To realize the former goal (i.e. enhancement of cell-interactivity), an often applied strategy involves the immobilization of proteins constituting the extra-cellular matrix. A very relevant protein in this respect is gelatin, which is derived from collagen by an acid or an alkaline treatment. In the former case, Gel A is obtained which is characterized by an iso-electric point (IEP) of 7-9, whereas in the latter case Gel B is formed which possesses an IEP of 4.7-5.3. The difference in IEP is the result of the different pre-treatment applied. Gelatin is a well known compound in the food industry, where it is used in desserts, confectionary, as clarification agent in beverages, but also in meat [1]. In the pharmaceutical field, it is applied in tablets, drug capsules and emulsions, but also in photography, gelatin-based emulsions have been used substantially in the past, prior to the current digital era [2-3]. In the biomedical industry, gelatin is frequently used as injectable microspheres for drug delivery [4-6], as matrix for protein release [7] but also as hydrogel-based wound dressing with the aim to realize skin regeneration [8-10]. Herein, gelatin B (Gel B) from bovine skin was selected and evaluated as biofunctional coating to enhance cell adhesion and proliferation of the implant materials developed, with the final aim of tissue integration. It should be noticed that a full immunological study has already been performed by Sirova et al indicating that Gel B is superior over Gel A from an immunological perspective [11]. With respect to the proposed glucose sensor design (see chapter 1), tissue integration includes a pre-requisite to allow for contact between the interstitial fluid (that contains glucose) and the sensor itself. In the end, the formation of a fluid pocket needs to be avoided, since this would result in the isolation of the glucose sensor from the body (see also chapter 5). This first biofunctionalization strategy (i.e., tissue integration approach; see figure 4.1) will be topic of § 4.2.

During the course of the current work, it was realized that the stimulation of blood vessel growth in the vicinity of the sensor could further enhance the success of the eventual sensor. In the end, the formation of a foreign body capsule at the site of sensor implantation would be disadvantageous as this capsule is characterized by a hypo-vascular nature. As a consequence, the permeation of glucose molecules would again be limited which is detrimental for the sensor function. Indeed, Kreutzer et al have already shown that an increased blood vessel density at the site of sensor implantation improves the *in vivo* glucose sensor function [12].

To stimulate the process of new blood vessel formation from existing ones (i.e. the second goal of this chapter), also known as angiogenesis, different approaches can be followed.

First, researchers have tried to increase the vessel density through the local release of angiogenic factors, such as basic fibroblast growth factor (bFGF) and vascular endothelial growth factor (VEGF) [13]. bFGF was recognized as the first angiogenic factor which enabled the proliferation of endothelial cells (EC) [14]. Later on, VEGF was identified as a more specific mitogen of EC which stimulates the migration of these cells to form tubular structures *in vitro* [15]. Other families of growth factors (i.e. indirect angiogenic factors) have been used to stabilize and mature the newly formed capillaries, for example, by the recruitment of smooth muscle cells. Examples include platelet derived growth factor (PDGF), angiopoietin and transforming growth factor β (TGF-β) [15-16]. Due to their complementary effects, interest has grown to develop systems enabling the delivery of multiple (direct and indirect) angiogenic factors [17].

Irrespective of the factor release targeted (single vs multiple), polymers have always played a crucial role in the process. Local release is necessary to avoid angiogenesis at unwanted sites, whereas controlled release ideally should avoid the detrimental effects which are associated with prolonged exposure of tissue towards these factors, including severe vascular leakage and reduced blood pressure [18]. Typical natural polymer matrices used for growth factor loading for tissue regeneration purposes include heparinized alginate scaffolds [19], fibrin [20], chitosan [21-22], collagen and gelatin [23-24], whereas the synthetic alternatives are offered by polyesters synthesized starting from lactide and glycolide (PLGA) and PEG hydrogels [16]. Growth factors are mainly physically embedded into the polymer scaffolds, aiming at a sustained and slow release, which is controlled by the degradation speed of the scaffold as well as the growth factor-polymer interactions. In this way, the polymer scaffold, which offers mechanical support, is systematically replaced by vascularized functional tissue.

Other studies focused on the covalent immobilization of growth factors. According to Shen et al, immobilization of VEGF in a collagen-based scaffold resulted in an increased viability of endothelial cells compared to the ones containing soluble VEGF [25]. Furthermore, it has already been suggested that immobilized VEGF could transduce cell signals for a longer time compared to soluble VEGF, which only has an *in vivo* half-life of 3 minutes due to internalization and cellular inactivation [26]. According to the authors, this observation opens perspective for the *in vivo* blood vessel formation. The positive effect of immobilization onto VEGF activity was also proven by Ito et al [27] and Chiu et al [26], but also for other growth factors, a similar effect was observed [28-29].

Since, in this work, the targeted glucose sensor is intended for long term implantation purposes, degradation of the polymer packaging would be an undesired feature. As a consequence, based on the observed positive effect of VEGF immobilization, herein, a similar approach was followed and the covalent immobilization of VEGF was studied as the first approach within the second biofunctionalisation strategy (see figure 4.1 and § 4.3).

In a second approach to promote vascularization, the mobilization of endothelial progenitor cells (EPC) towards the site of implantation was targeted. These EPC typically differentiate into mature endothelial cells and restore endothelial function after vascular injury. Herein, identification of a specific and exclusive surface marker for EPC has formed the main

challenge. The Bio-engineered Genous^{TM} stent, provided by OrbusNeich, applies CD34 as marker. To bind circulating EPC, monoclonal murine anti-human CD34 antibodies have been coupled on a 316L stainless steel (SS) coronary stent [30]. Nevertheless, Lim et al questioned the specificity of this surface marker, since other CD34 positive cells could differentiate into inflammatory cells and smooth muscle cells. As an alternative, VE-cadherin was proposed as the ideal surface marker for EPC, as this marker is only expressed on late EPC and mature endothelial cells, but not on early EPC or other leukocytes. It was proven that immobilization of anti-VE-cadherin antibodies (VE-cad AB) onto a SS stent did enhance re-endothelialization of a stent, which is the first step towards angiogenesis [31]. As a consequence, the immobilization of VE-cad AB onto the developed polymeric packaging materials was also studied in this work (see figure 4.1 and § 4.3).
In a last and third approach, both VEGF and VE-cad AB's are combined to study a potential combined effect between both of them (see figure 4.1).

In the following paragraphs, the immobilization strategies are discussed and the successful immobilization of the biomolecules is presented. Furthermore, their influence on the cell-interactivity of the materials is described[1]. Improvement of the latter property was interpreted as a first indication for their *in vivo* success to stimulate tissue integration (1st strategy) and vascularization (2nd strategy).

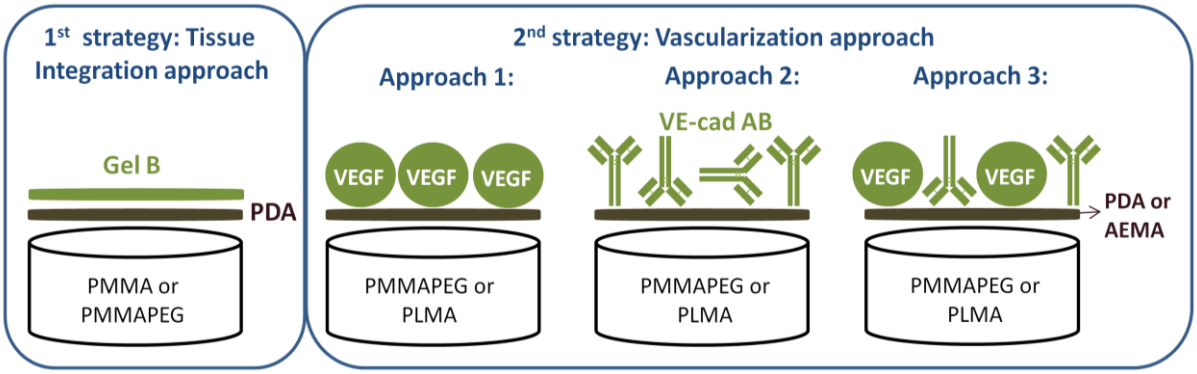

Figure 4.1: Two biofunctionalization strategies have been applied and compared. The first generation strategy includes a Gel B immobilization to stimulate tissue integration (studied on PMMA and PMMAPEG). In a second strategy VEGF, a growth factor (approach 1), VE-cad AB (approach 2) and their combinations (approach 3) are immobilized to stimulate vascularization of the future implant (studied on PMMAPEG and PLMA). For the second strategy, biofunctionalization was performed on both AEMA (only studied in case of PLMA) and PDA activated substrates (studied on both PLMA and PMMAPEG).

[1] All live/dead assays were perfomed in cooperation with Heidi Declercq and Johanna Aernoudt, from the Tissue Engineering Group of the Department of Basic Medical Sciences, under supervision of Prof. Maria Cornelissen. The immune-assays and confocal fluorescence microscopy measurements were conducted in cooperation with Prof. Winnok De Vos from the Faculty of Bioscience Engineering; Department of Molecular Biotechnology.

4.2. The enhancement of tissue integration via Gel B biofunctionalization

4.2.1. Surface immobilization of bio-active biopolymers onto PDA-coated surfaces

Messersmith et al, the pioneers of the PDA-coating, recognized this method as a versatile platform to enable subsequent coupling reactions using biologically active compounds [32]. Since the exact structure of PDA is still unclear, the exact coupling mechanism remains unknown, but it has been suggested that catechol and quinone functions, present in the PDA coating, react with nucleophiles such as amines and thiols via a Michael-type addition or a Schiff-base reaction [32]. Regardless of the exact mechanism, the successful immobilization of different biologically active compounds have already been demonstrated by different research groups, of which some examples are summarized in table 4.1.

Table 4.1: Literature examples of the immobilization of biologically active compounds onto PDA coated substrates.

Substrate material	Biological compound	Aim	Ref.*
PE*, DLC*	Bovine serum albumin (BSA)	Blood compatibility improvement	33-34
Cu, TiO_x, PC, cellulose	Trypsin	Proof of immobilization strategy	35
PE/PU*	Heparin	Blood compatibility improvement	36-37
Glass	Lysozyme, myoglobin, a-lactalbumin	Fundamental study	38
Ti	VEGF	Revascularization/bone healing	39
Gold electrode	Anti-SRB* antibodies	Selective immunosensor	40
NiTi alloy	VEGF	Endothelialization of vascular implant	41
PLCL*	VEGF/bFGF/RGD	Endothelialization of vascular implant	42-43
SS* 316L	VEGF/mPEG-NH_2	Improve biocompatibility of metal devices	44
Au, glass, Pt, In, SnO_2, LCP*	Poly-D-lysine	Neural interface design	45

*Abbreviations: PE: Polyethylene; DLC: Diamond like carbon; PU: Polyurethane; SRB: sulfate-reducing bacteria; PLCL: poly(L-lactide-co-ε-caprolactone); SS: Stainless steel; LCP: liquid crystal polymer; Ref.: References

In the present work, the PDA platform was also used to enable subsequent biofunctionalization of the developed materials. As pointed out in the introduction, in a first strategy, an improved cell-interactivity of the implant materials was targeted by means of Gel B immobilization. In a second strategy, a more specific body response was targeted, being the recruitment of endothelial cells towards the implant with the final aim to induce angiogenesis. To this end, VEGF and VE-cad AB were coupled onto PDA-functionalized polymer substrates (see § 4.3).

4.2.2. Immobilization of Gel B as biofunctional compound

Gel B from bovine skin was selected and evaluated as biofunctional coating to enhance cell adhesion and proliferation of the materials developed. In a first step, PMMAPEG was selected as substrate material to evaluate the success of the Gel B immobilization (§ 4.2.1.1). Herein, PMMA was included as reference. *In vitro* studies were conducted to evaluate the cell-interactivity and proliferation of the Gel B coated materials and a comparison was made with the blank and PDA coated samples (§ 4.2.1.2).

4.2.2.1. Surface characterization of the immobilized Gel B layer

Immobilization of Gel B onto the selected materials was facilitated by first activating the surfaces using PDA. The results presented in chapter 3, illustrated that PDA was successfully immobilized onto the selected polymers. Next, based on previous research [46], three Gel B concentrations, including 0.5, 1 and 2 w/v% were evaluated.
XPS measurements revealed that for PMMA, all three concentrations resulted in a homogeneous coating, as no significant differences ($p>0.05$) were obtained when comparing the N-content present on the surface (figure 4.2, A). However, when considering PMMAPEG, a significant difference was obtained when comparing the lowest (i.e. 0.5 w/v%) and the intermediate (i.e. 1 w/v%) concentration. As a consequence, 1 w/v% was selected for further sample preparation, as this represents the minimum concentration required to realize homogeneous coatings on both material types.
The successful Gel B immobilization was confirmed by comparison of the C1s carbon detail peaks of the PDA and Gel B coated materials. As shown in figure 4.2 (B and C), deconvolution of these peaks resulted in three different carbon signals, indicating different chemical environments (i.e. C=O, C-O/C-N and C-C/C-H). These figures suggest that deposition of Gel B resulted in an increase in carbonyl (C=O) functionalities (figure 4.2, C) compared to the PDA deposition. This can be ascribed to the presence of amide linkages in the gelatin backbone.
The presence of Gel B was further evidenced by contact angle measurements as shown in figure 4.2 (D). For both material types, PMMA and PMMAPEG, a significant ($p<0.05$) decrease in contact angle was observed when comparing the PDA and Gel B coated samples (from 50° to 20° and 28° for PMMA and PMMAPEG respectively).

As an important intermediate conclusion, it can be stated that two polymers with different mechanical properties (see chapter 2) but with a comparable surface chemistry are obtained. The comparable surface chemistry implies that both materials are characterized by similar surface wettabilities (both after PDA and GelB deposition) and atomic compositions. Nevertheless, two more parameters should be evaluated prior to *in vitro* testing: the surface roughness and the stability of the deposited layers.

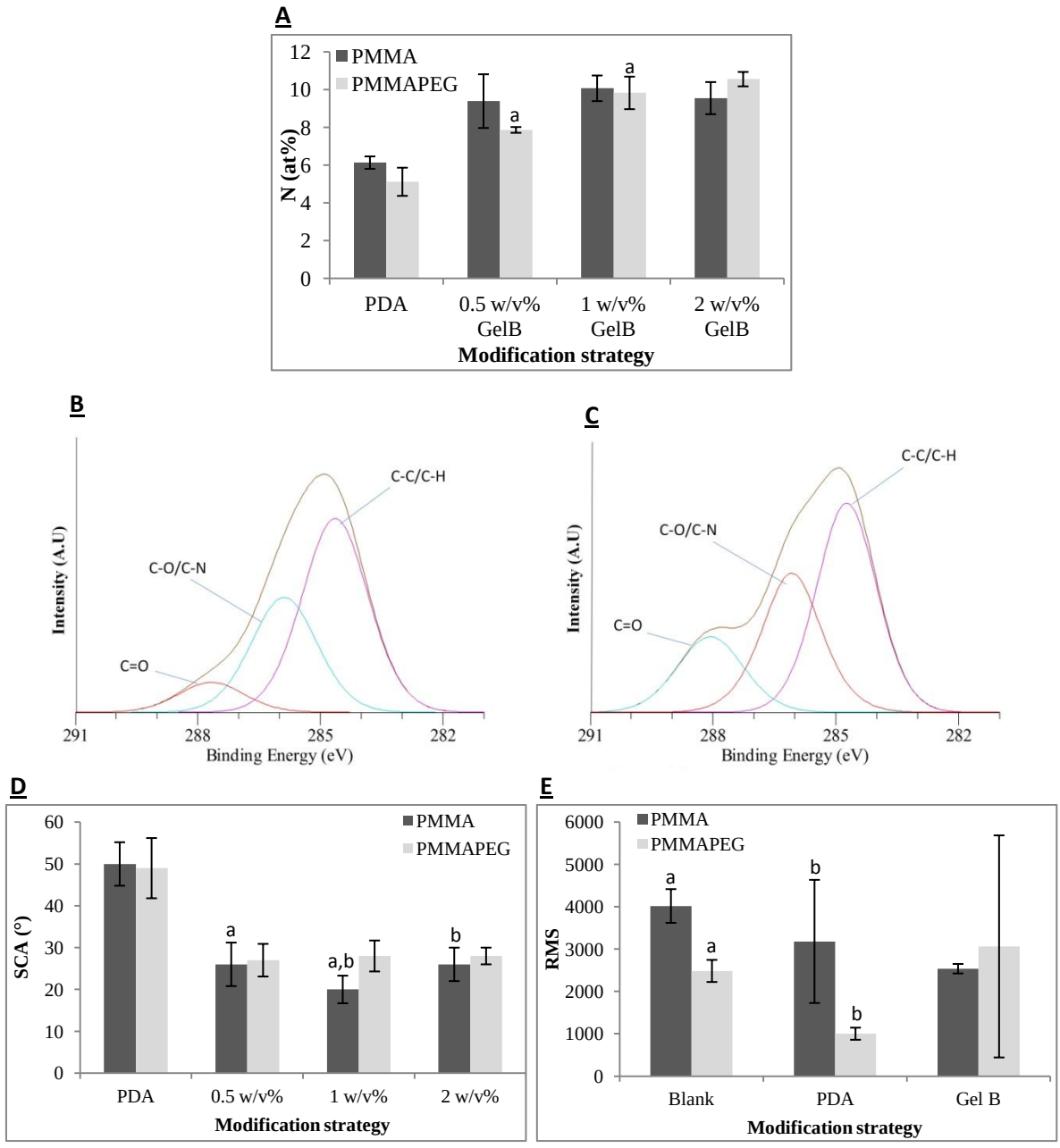

Figure 4.2: Panel A: Percentage of nitrogen determined by XPS for the PDA and Gel B modified PMMA and PMMAPEG samples. Three different Gel B concentrations were evaluated: 0.5, 1 and 2 w/v%. Panel B and C represent the carbon detail peaks obtained through XPS which reveal the different chemical environments when comparing a PDA (B) and a Gel B (C) modified surface (Herein, PMMA). Panel D shows the static contact angle values for the different surface modifications applied whilst panel E compares the root mean square (RMS) values obtained through profilometry for the blank, PDA coated and Gel B coated PMMA and PMMAPEG samples. Conditions marked by the same letters a,b,c,…are significantly different ($p < 0.05$). In figures A and D, all Gel B coated samples were significantly different compared to the PDA coated ones (not marked).

Previously, it has been demonstrated that surface roughness influences cell behavior [47]. In case of PMMA, it has been shown that the use of concave patterned films results in significantly increased cell densities compared to flat surfaces [48]. As a consequence, the surface roughness of the different (un-)modified materials was evaluated by profilometry. Figure 4.2 (E) clearly demonstrates that for both materials, no significant difference was obtained between the different surface modifications ($p>0.05$). In case both material types are compared, a significant difference was obtained in RMS value for the blank materials and the PDA coated ones ($p<0.05$), whereas for Gel B, regardless of the material, a similar surface roughness was observed. As a consequence, the observed differences (for blank and PDA functionalized materials) should be considered when interpreting the upcoming cell data.

Since implantation of the materials is targeted, it is essential to evaluate the stability of the PDA and Gel B layers in simulated *in vivo* conditions. To this end, the modified PMMA and PMMAPEG samples were incubated in PBS buffer at 37°C and as a function of incubation time, the decrease in atomic nitrogen percentage was measured. For both PMMA (figure 4.3, A) and PMMAPEG (figure 4.3, B), stable PDA layers were obtained since after incubation no significant decreases in atomic nitrogen percentage were measured ($p > 0.05$). On the other hand, after 24 hours of incubation, the Gel B modified PMMA and PMMAPEG samples respectively resulted in a 2 and 4 % decrease in atomic nitrogen percentage compared to the non-incubated samples ($p < 0.05$). Notwithstanding this decrease, the atomic nitrogen percentages remained significantly higher compared to the PDA modified samples, which proves the presence of the Gel B layer. For longer incubation times (i.e. 48 hours and 1 week), similar results were obtained compared to the samples which were incubated for 24 hours, meaning that the Gel B layers can be assumed stable after this initial incubation time. Furthermore, after 24 hours of incubation, equal nitrogen percentages are detected for both PMMA and PMMAPEG (i.e. 8-9 % N).

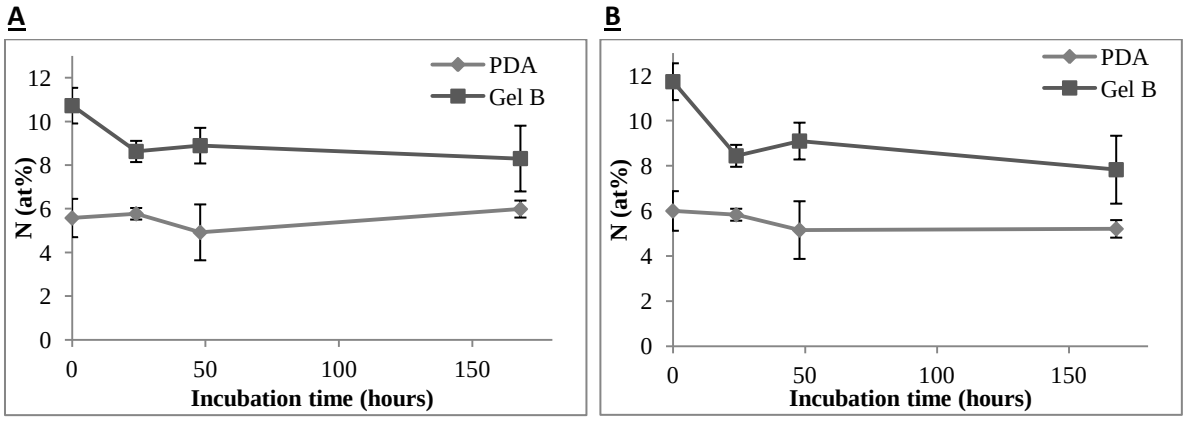

Figure 4.3: Stability testing of the PDA and PDA/Gel B modified PMMA (Panel A) and PMMAPEG materials (Panel B). The decrease in atomic nitrogen percentage was evaluated as a function of incubation time in PBS buffer at 37°C, using XPS.

4.2.2.2. *In vitro* evaluation of the Gel B modified samples

As previously mentioned, the developed implant materials are intended for long term implantations, implying eventual tissue integration. As a consequence, the *in vitro* cell-interactivity is a prerequisite.

Therefore, to gauge the cytocompatibility of the various materials under investigation, a semi-quantitative live/dead assay with human foreskin fibroblasts (HFF) was conducted. The data revealed that for the pristine surfaces, HFF attached to the PMMAPEG blank (estimated viable cell density of 1%) to a lower extent compared to the PMMA blank (estimated viable cell density of 6%) (figure 4.4, A). Using PMMA as a substrate material, deposition of a PDA layer showed a significant positive effect ($p<0.05$) on the fibroblast cell attachment (estimated viable cell density of 12%), in line with earlier findings, although to a lower extent [42, 49-51]. This was not the case for PDA-modified PMMAPEG (estimated cell viability of 2%), plausibly due to the cell-repellant properties of PEG. In the past, many studies focused on the production of antifouling surfaces applying PEG as antifouling polymer [52]. In this context, PEG grafts are mainly used to realize this aim. As a result, copolymer networks containing these PEG moieties might also induce a similar effect, as shown by the low cellular adhesion (see figure 4.4, A). However, it was anticipated that PDA deposition would render these materials cell-interactive. Indeed, it has already been suggested that an increased cell-interactivity of PDA coated materials results from the adsorption and subsequent covalent immobilization of serum proteins via Schiff-base formation and/or Michael-type addition without altering their biological function [51].

From our findings, it is obvious that the applied PDA coating on PMMAPEG is insufficient to overrule the decrease in thermodynamic stability of the serum proteins induced by PEG [53-54]. It can be anticipated that this perturbation of the serum protein's native structure prevents specific interactions occurring between the adsorbed proteins and cells and as a result, also cell adhesion [51]. Furthermore, these results suggest that cells still sense the underlying PEG-substrate, probably because of a low PDA layer thickness. Investigation of this causal effect could therefore be topic of future work.

Upon surface decoration of the PDA functionalized polymers using gel B, a more prominent effect was accomplished on the cell growth as evidenced by higher cell densities (>90 % for both PMMA and PMMAPEG) accompanied by superior cell spreading (see figure 4.4, A).

To acquire more detailed information on the attachment and spreading potential of fibroblasts, cytoskeletal cellular components were visualized (figure 4.4, B) including the F-actin fibers and focal adhesion (FA) points. Being responsible for cell shape, the actin cytoskeleton provides a direct proxy for cell spreading. The focal adhesion points, on the other hand, represent cellular connections with the extracellular matrix and thereby provide information about the cell adhesion properties. In brief, cells with larger actin-stained surface area and more focal adhesion points are better attached to the surface [55]. Bearing this in mind, the projected area and relative number of focal adhesion points per cell were quantified (figure 4.4, C).

As represented in figure 4.4 (C), higher cell areas (determined at the level of 1 cell) were obtained for the Gel B coated samples, although, for PMMA the differences were not significant ($p>0.05$) compared to the blank and PDA coated samples. For PMMAPEG on the other hand, a significantly increased cell area was observed for the Gel B coated samples when compared to the other test conditions ($p<0.05$). This increased cell area can be understood as an improved cell spreading on the Gel B coated samples. Furthermore, comparison of the two substrate materials showed that a significantly lower cell area was obtained for the PDA coated PMMAPEG samples compared to the PMMA coated ones ($p<0.05$). This again points in the direction of a PDA layer thickness which is insufficient to disguise the underlying substrate. Apart from the consequential protein repellant properties, a lower surface roughness of the PDA-coated PMMAPEG materials, as demonstrated in § 4.2.2.1, might also be a cause for the observed difference in cell area [56].

Apart from cell growth, cell attachment was studied by determining the number of focal adhesion points, counted for each cell. The results showed that in the series PMMA < PDA-coated PMMA < Gel B coated PMMA, the number of focal adhesions increased, although not significantly, as depicted in figure 4.4 (C) ($p > 0.05$). As a consequence, this result confirmed a small, yet positive effect on cell attachment when applying PDA as an activating layer. In previous research, a similar, yet more pronounced (i.e. a 14-fold increase in the overall cell area for the PDA coated materials) trend has already been observed [51]. It can be concluded that these results correspond with the live/dead results. Furthermore, in order to maximize cell adhesion and spreading, Gel B can be considered as the preferential coating for PMMA, as illustrated in figure 4.4 (A, B and C).

The PMMAPEG materials showed a somewhat different behavior. When comparing PMMAPEG and PMMAPEG-PDA, no statistical difference was obtained between the number of focal adhesion points present on the surfaces and for both conditions almost no focal adhesions were observed (figure 4.4, C). As a consequence, the application of PDA was insufficient to enhance cell adhesion.

Inferior cell adhesions were also clearly visualized by a spherical cell shape present on the blank and PDA-coated PMMAPEG materials (figure 4.4, B). Gel B immobilization on the other hand resulted in a natural rhombic-like shape of the attached cells, comparable to the cell shape obtained in case of the PMMA surfaces. This visual observation was also supported by quantification of the cell circularity, since significant differences were obtained when comparing the PDA and Gel B coated PMMAPEG samples. As a consequence, also for PMMAPEG, Gel B coatings can be considered as the preferential ones.

In previous work, the application of PDA and gelatin was studied by Sook et al on PCL-based materials. They tested PCL, PCL-PDA and PCL-gelatin to assess the bio-interactivity towards human umbilical vein endothelial cells (HUVECs). Their results illustrated that the PDA-coated samples resulted in higher cell viabilities and adhesion compared to the gelatin modified samples [50].

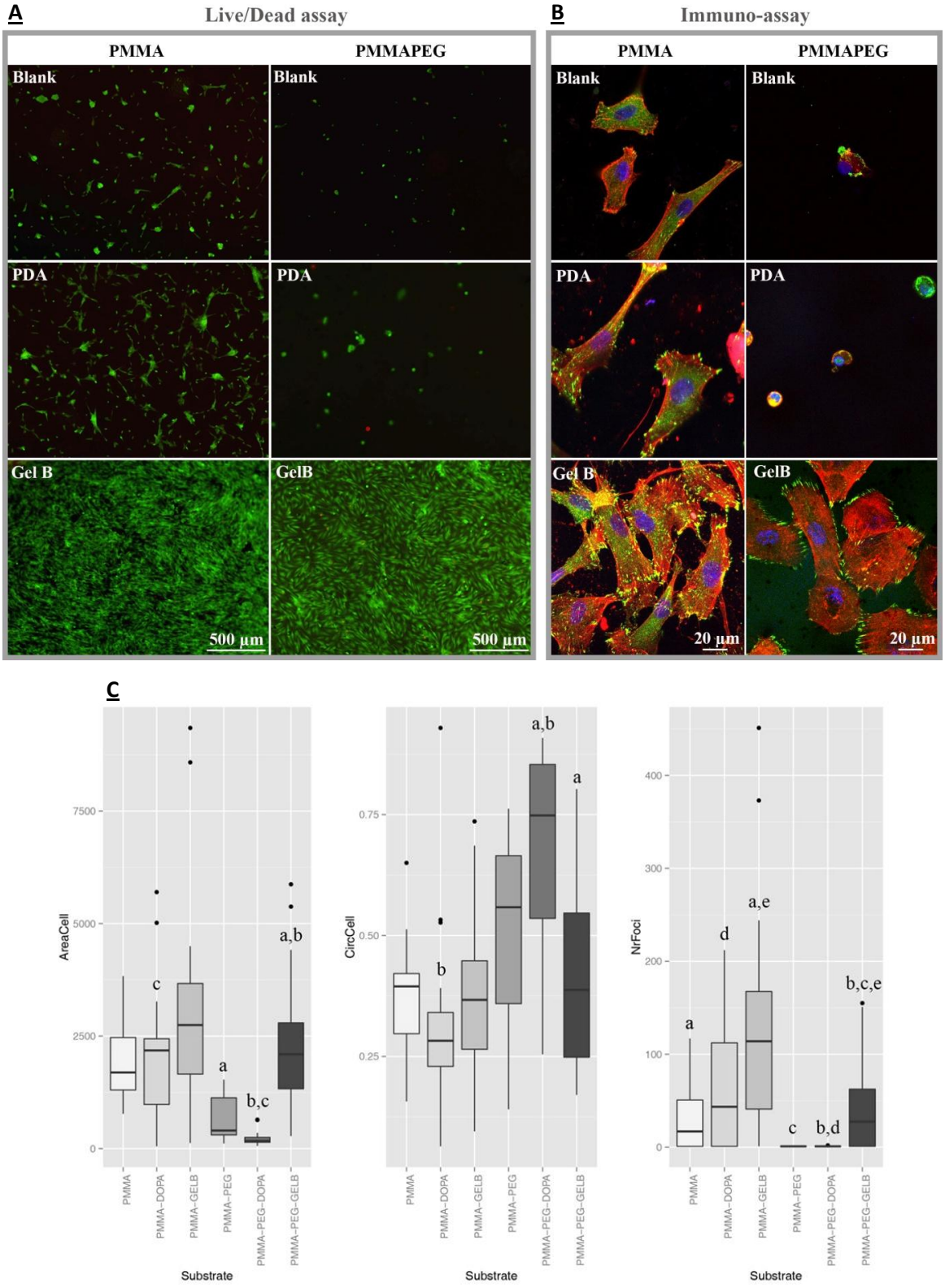

Figure 4.4: panel A: Live dead assay with propidium iodide (red color, dead cells) and calcein AM stained (green color, living cells) using HFF cells. Panel B: Immunostaining assay with HFF cells. Stainings are performed to visualize the actin filaments (red), the nuclei (blue) and the focal adhesions (green). Panel C: Cell Area, cell circularity and number of focal adhesion points obtained for the different material conditions. Samples marked by the same letters (a,b,c,…) were statistically different ($p<0.05$).

In the present work, an opposite trend was observed. However, it should be noted that herein gelatin was covalently bound to the PDA layer while in the study of Sook et al, gelatin was physically adsorbed onto the PCL fibers without applying the PDA primer layer. In this respect, Desmet et al. also confirmed that physisorption of gelatin onto PCL resulted in inferior cell-interactivity compared to chemically coupled gelatin [57]. Nevertheless, the improvement in cell-interactivity after PDA deposition was not as prominent herein compared to their study [50]. The latter clearly implies that apart from the considered cell type, the substrate material also influences cell behavior to a great extent despite a similar surface chemistry.

To further prove the universal character of the PDA/ GelB coating strategy, a preliminary live/dead assay was conducted on the same set of (un)modified materials, but upon the application of a second cell type, i.e., HUVECs. Figure 4.5 clearly demonstrates how the application of Gel B again results in an enhanced cell density as reflected by the higher cell densities compared to the blank and PDA-coated samples. It can be noted, however, that herein the application of a PDA coating does enhance the cell interactivity, although, to a lesser extent compared to the combined PDA/GelB immobilization.

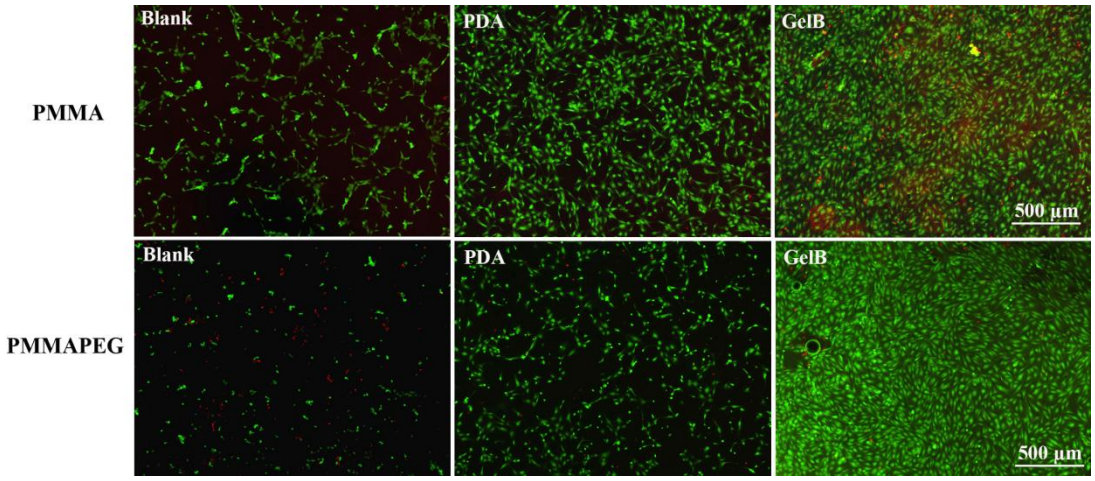

Figure 4.5: A live/dead assay was performed, using HUVECs. Dead cells are stained with propidium iodide (red) and living cells are stained with calcein AM (green).

From these *in vitro* results, it can be concluded that the combination of PDA activation and Gel B functionalization results in similar cellular responses, irrespective of the physicochemical properties of the underlying substrate. Hence, it can be stated that a universal surface modification strategy was developed.

4.2.2.3. Effect of substrate mechanical properties on cell response, using Gel B as a model

From literature, it is well known that matrix stiffness influences cell behavior [58-59]. In this respect, cells not only exert forces on the underlying substrate, but they also experience tension from their environment on which they respond through alterations in their

cytoskeleton organization, adhesion, protein expression, post-translational modifications, differentiation properties and cell-cell interactions [59-61]. It should be mentioned that these responses are cell-type dependent. In this context, increased proliferation with rise in substrate rigidity is common across many cell types, such as neurons, osteoblasts, vascular smooth muscle cells and fibroblasts [59]. Also endothelial cells behave similar to fibroblasts in the sense that increased substrate rigidity will result in increased cell spreading. Furthermore, for these cell types, it was demonstrated that soft materials (E-mod = 0.5 kPa) stimulate the existence of cell-cell contacts, whereas more rigid ones (E-mod = 33 kPa) enhance cell-substrate adhesion [62].

In order to study the influence of the mechanical properties on cell behavior, a range of PEG-based materials (see chapter 2), characterized by different elasticity moduli were selected and compared for their cell-interactive properties. The material composition together with the corresponding E-moduli and the surface composition of the selected materials are represented in table 4.2. Different mechanical properties were obtained by varying the PEG chain length (550 vs 750 g/mol) or by varying the molar composition (linear PEG vs PEG cross-linker). As a control, materials 1 and 3 (see table 4.2 for their exact composition) were included, because of their similar E-moduli. Material 5, on the other hand, was included to study the effect of a substantially lower E-modulus.

To render the selected materials cell-interactive, the PDA/Gel B coating, as described above, was applied. Regarding the experimental setup, two assumptions could be made. First, if the PDA/Gel B coating is indeed characterized by a universal character, it is expected that regardless of the different mechanical properties, a similar cell response would be provoked. Secondly, if a difference in cell response would be observed between materials 1 to 4, it can be anticipated that the latter is due to differences in the mechanical properties of the substrate materials, as similar compositions were selected (90 mol% MMA and 10 mol% PEG).

Prior to the *in vitro* assay, the success of the PDA and Gel B immobilization onto the materials was confirmed using XPS.

Table 4.2: Overview of the chemical composition and the E-moduli of the selected PEG containing materials. The atomic nitrogen percentages, as determined by XPS, after PDA deposition and Gel B immobilization are also shown. Herein, the standard deviations, shown between brackets, are a measure of the homogeneity of the coatings applied on the sample surfaces.

Material	MMA (mol%)	PEGDMA(550) (mol%)	PEGDMA(750) (mol%)	PEGMA(500) (mol%)	E-mod (MPa)	N_{PDA} (at%) (stdev)	N_{GelB} (at%) (stdev)
1	90	10	0	0	1533	5 (0.2)	10 (0.4)
2	90	0	10	0	324	4 (0.2)	9 (0.4)
3	90	8	0	2	1542	5 (0.6)	10 (0.7)
4	90	2	0	8	678	5 (0.4)	9 (0.2)
5	50	40	0	10	37	5 (0.1)	7 (0.4)

It can be concluded from table 4.2 that PDA deposition resulted in a similar nitrogen content for the different material surfaces (i.e. ±5%). In case of Gel B immobilization, the different materials also resulted in a similar nitrogen content (i.e. ±10% N) which resembled the values as described higher (§4.2.1.1). An exception was observed for material 5, since only 7% of nitrogen was detected after Gel B immobilization. Whether the somewhat higher swelling degree (i.e. 24% cfr a maximum swelling of 16%) is responsible for this fact, should be further investigated.

Evaluation of the live-dead images, presented in figure 4.6 (A), showed that after 1 day of cell contact, all materials, except material 5, resulted in high cell densities. However, for materials 2 and 4, areas of lower cell density were also observed (not shown). This observation suggests a preferred HUVECs cell growth onto more rigid materials, an observation which was also made in literature, although, in the latter case rigid materials were characterized by an E-modulus of 30 kPa [59]. After 7 days, confluent cell layers were observed on all materials, although material 5 again showed lower cell densities compared to the other materials. Furthermore, more dead cells were observed for this material. If material 1 and 3 are compared, more dead cells were present on the latter. Since both materials are characterized by similar elasticity moduli, it cannot be excluded that the introduction of PEGMA into the material's composition is responsible for this phenomenon. Since material 5 contains the highest amount of PEGMA(500), it can also be questioned whether the difference in cell behavior is caused by a difference in mechanical properties or by the presence of a higher amount of PEGMA. Additionally, for material 5, a third cause could be the less efficient Gel B immobilization (cfr. 7% N versus 10% N for the other materials).
In order to obtain more information about cell adhesion, the focal adhesion (FA) points were stained and quantified. Figure 4.6 (B) shows a representative confocal image for the different substrate materials, as well as the boxplots, which represent the distribution of the number of FA counted for different cells on a substrate material. Visual observation of the FA shape showed that for all material compositions, stable, elongated focal adhesions were obtained. In literature, a similar observation was made for acrylamide-based gels. In this study, more rigid substrates (E-mod of 30-100 kPa) resulted in mature elongated focal adhesions, whereas on more flexible substrates (~ 1kPa), the FA appeared as more diffuse dot-like structures [63]. When comparing these E-moduli to the values in our study, it is clear that all materials reveal an E-mod > 100 kPa (i.e. all materials in this study) and thus they can be considered as rigid substrates, which are characterized by an organized F-actin stress fiber structure [60]. A comparison with literature results describing similar cell types and materials characterized by an E-mod > 40 MPa would have been more relevant, but these are lacking in the current state-of-the-art. Furthermore, it should be noted that the mechanical analysis procedures generally described in literature are in great part different from the techniques applied herein (e.g. the use of rheology [64] or indentation tests [65] versus tensile testing in the current study).

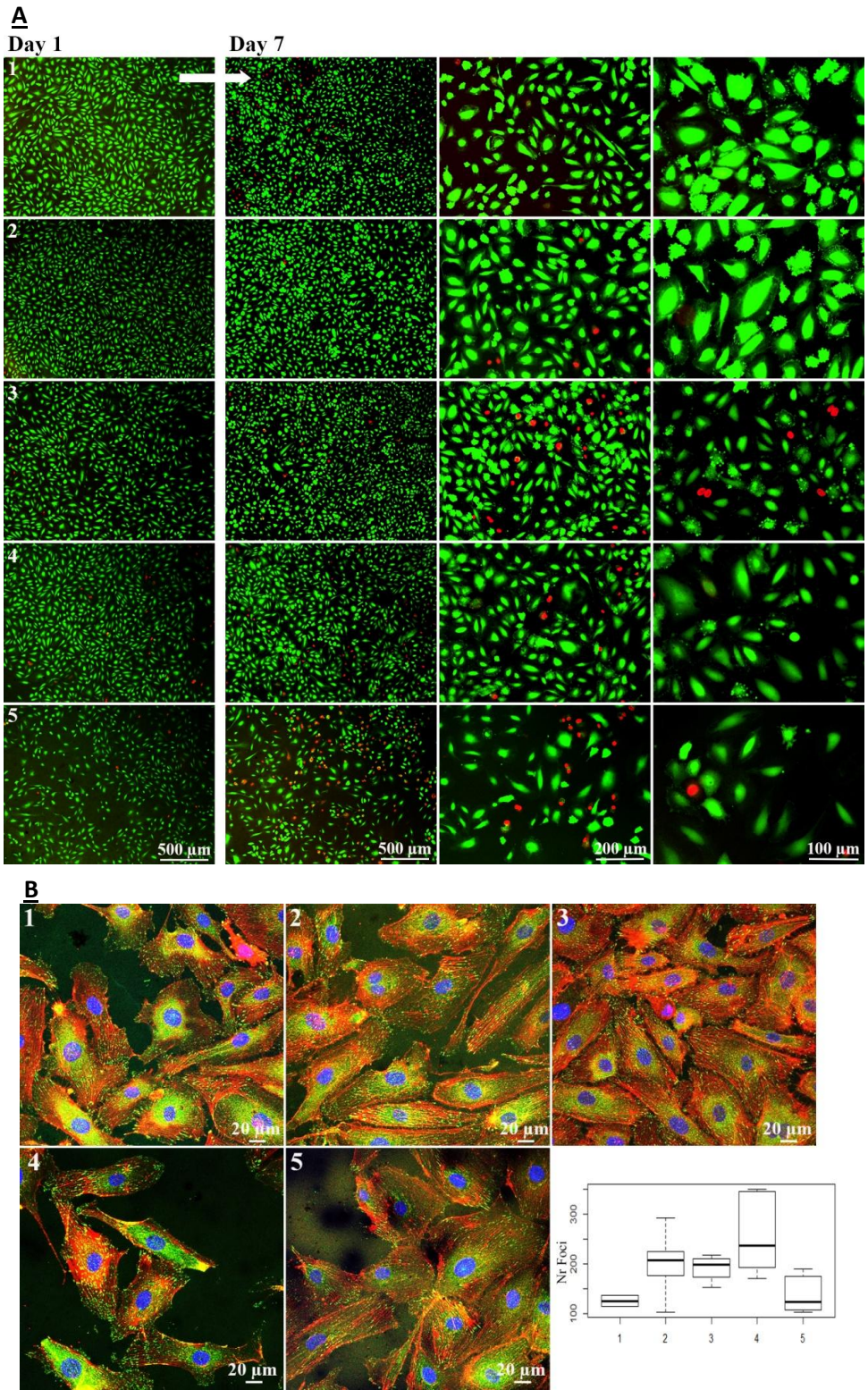

Figure 4.6: Panel A: Live dead assay with propidium iodide (red color, dead cells) and calcein AM stained (green color, living cells) HUVEC cells. Panel B: Immunostaining assay with HUVECs. Stainings are performed to visualize the actin filaments (red), the nuclei (blue) and the focal adhesions (green). The boxplots representing the FA distributions are also shown.

Apart from substrate stiffness, the presence of Gel B, will also influence cell adhesion. In this respect, a previous study has shown that a decreased density of collagen type I onto polyacrylamide gels resulted in decreased cell-matrix adhesions but in increased cell-cell connections [66]. Since Gel B immobilization resulted in a similar surface composition (cfr. XPS results) for the different materials, except for material 5, this variable could be considered as a constant.
Quantification of the number of focal adhesion points showed that materials 4 (median FA = 236), 2 (median FA= 207) and 3 (median FA = 198) resulted in the highest median number of focal adhesion points, as compared to material 1 (median FA = 126) and 5 (median FA = 124). Nevertheless, based on statistical analysis, it could be concluded that the focal adhesion distribution is the same across the different material categories ($p>0.05$).
This last conclusion again highlights the universal character of the PDA/Gel B modification.

4.3. The enhancement of vascularization via the immobilization of VEGF and VE-cad AB

In the previous paragraph, Gel B was evaluated as cell-interactive coating, in order to estimate its potential for tissue integration. As pointed out in the introduction, the stimulation of angiogenesis and vascularization (i.e., strategy 2 in figure 4.1) could further increase the glucose sensor success and therefore, the immobilization of VEGF (approach 1), VE-cad AB (approach 2) and their combinations (approach 3) were studied together with their *in vitro* response. In order to immobilize the angiogenic factors, both of the surface activation strategies, discussed in chapter 3, were considered. Dependent on the pre-activation step, i.e., PDA vs. AEMA activation, a different protocol was required for the immobilization of the biological components. As a consequence, the characterization results are discussed accordingly in § 4.3.1 (PDA-based) and § 4.3.2 (AEMA-based).
Apart from PMMAPEG, the LMA-based packaging (referred to as PLMA) was also included in this study.

4.3.1. Immobilization of VEGF and VE-cad AB onto PDA-modified surfaces

4.3.1.1. Preliminary experiments to determine the required angiogenic factor concentration

Prior to immobilization and full characterization of the immobilized compounds, the angiogenic factor concentration was selected for both VE-cad AB and VEGF.
In case of antibody immobilization, the applied concentrations reported in literature highly depend on the targeted application [40, 67-72]. In the specific case of VE-cadherin AB, only few studies have been conducted and as a consequence, a concentration range was evaluated by means of radiolabeling experiments[2]. To this end, VE-cad antibodies were radiolabeled with

[2] All radiolabeling experiments were conducted in cooperation with Ken Kersemans, from the Department of Pharmaceutical Analysis, the Laboratory of Radiopharmacy, under supervision of Prof. Filip De Vos.

the iodine isotope I^{125} according to the procedure described in chapter 6 (§ 6.1.10 and § 6.2.3.5). Furthermore, since the amino acid composition of VE-cad AB remains unknown to date, the evaluation of a concentration range was also beneficial to evaluate the feasibility of radiolabeling experiments. Figure 4.7 (A) clearly shows that upon increasing the AB concentration, an increased radio-active signal was obtained for both the blanks and the PDA coated surfaces. As a consequence, proof was delivered that tyrosine and/or histidine were present in the AB amino acid sequence and that iodination through electrophilic aromatic substitution could be considered a suitable technique for further characterization of the AB-modified surfaces (see next paragraph).

It is clear from figure 4.7 (A) that the highest radio-activity was obtained in case a starting solution of 4 µg/ml was used. As a consequence, the concentration was set at 4 µg/ml for all future experiments.
A preliminary stability test showed that incubation of the AB-modified samples in PBS-buffer (37°C) resulted in a slight decrease in signal, but overall, the modification could be assumed stable over the studied time frame (i.e. 48 hours, see figure 4.7, B). These preliminary data indicated that the immobilization of VE-cad AB was successful and that an in depth study could be initiated in this respect. The results of this study will be discussed in the upcoming paragraphs.

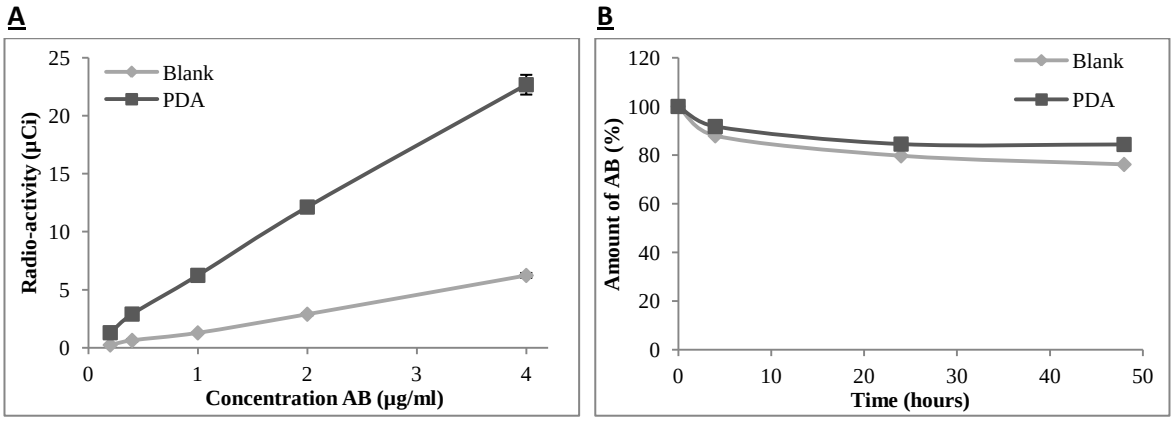

Figure 4.7: I^{125} radio-activity from VE-cad antibody (AB) deposited onto the blank and the PDA coated PMMAPEG material, as a function of the initial AB concentration (The measured radio-activity of the 0.2, 0.4, 1, 2 and µg/ml stock solutions was respectively 1, 2, 6, 12, 24 and 49 µCi) (A). The stability of the deposited AB layer was tested as a function of time, upon incubation of the AB-modified (4 µg/ml) samples in PBS buffer at 37°C (B).

In case of VEGF immobilization, the concentration of the starting VEGF solution was selected based on the most relevant literature reports, describing the covalent immobilization of VEGF with the aim of improving vascularization around an implant. In this respect, Shen et al immobilized VEGF into a collagen scaffold via EDC-chemistry [73] using 500 ng/ml and 1 µg/ml VEGF solutions. They showed that both VEGF concentrations promoted the penetration and proliferation of endothelial cells within the scaffolds, which could lead to an *in vivo*

vascularized scaffold [25]. The same research group also proved that the use of 1 µg/ml resulted in tube formation *in vitro* and in an increased blood vessel density by conducting an *in vivo* chicken chorioallantoic membrane (CAM) assay [26]. Furthermore, Shin et al applied a similar concentration of VEGF (1.3 µm/ml) onto PDA functionalized poly(L-lactide-co-ε-caprolactone) (PLCL) films. They demonstrated an enhanced proliferation and migration of HUVECs [42]. Based on these data, a VEGF concentration of 1 µg/ml was selected to perform the modification in the current study.

4.3.1.2. Characterization of the AB and VEGF functionalized surfaces

In order to study and quantify the amount of immobilized AB and VEGF, XPS measurements and radiolabeling experiments were conducted.
Table 4.3 displays the ***XPS results*** of the angiogenic factor functionalized substrate materials. Comparison of both materials (PMMAPEG vs PLMA) did not result in significant differences in the N/C ratios in case the same surface modification was considered ($p > 0.05$). For both PMMAPEG and PLMA, a significantly higher N/C ratio was obtained after AB and/or VEGF immobilization, when compared to the PDA functionalized blanks, offering a prominent proof of successful angiogenic factor immobilization.

It was anticipated that the AB and VEGF immobilized surfaces would result in similar or lower N/C values compared to the pristine AB and VEGF materials. This trend was followed for the AB functionalized PDA surfaces (N/C < 0.177), but the VEGF modified PDA surfaces resulted in significantly higher N/C ratios compared to the ones obtained for pristine VEGF (N/C = 0.110). It should be mentioned that for VEGF immobilization, the supplier's protocol stipulated that bovine serum albumin (BSA) had to be dissolved in the modification buffer to assure the stability of VEGF. As a consequence, the increased N/C ratios for the VEGF functionalized surfaces were possibly biased by the addition of this nitrogen containing compound. As mentioned in the introduction (§4.2, table 4.1), the covalent linkage of amine functions in BSA with the o-benzoquinone of dopamine has been demonstrated previously [36]. Furthermore, since BSA may also influence cell behavior, this factor should be considered when interpreting the up-coming cell data. It is known that surface adsorbed albumins offer non-fouling properties, which intervene with cell adhesion [74].

Apart from XPS, ***radiolabeling experiments*** were conducted to determine the amount of AB and/or VEGF which was deposited onto the surface. It should be mentioned that for the VEGF functionalized samples, no BSA interference could occur in this case, since VEGF was selectively labeled with ^{125}I.

For both materials, high aspecific adsorptions of AB and VEGF were measured, as shown in table 4.3. Herein, comparable amounts of antibody were deposited on both PMMAPEG and PLMA, whereas in case of VEGF, significantly higher adsorptions were determined for PMMAPEG. This phenomenon of aspecific adsorption could already be deduced from the

XPS measurements, since nitrogen was detected on most of the blank surfaces after AB or VEGF incubation. This topic will be further discussed in the upcoming paragraph. Further comparison of PMMAPEG and PLMA showed that all biofunctionalization strategies (i.e. AB vs VEGF vs combined AB/VEGF immobilization) resulted in significantly higher depositions for PMMAPEG compared to PLMA ($p<0.05$), which can be declared by the higher swelling properties of the former material.

When there is focused on one material, the following observations could be made:
In case of PMMAPEG, the successful AB immobilization was confirmed, since significantly higher amounts of AB were deposited onto the PDA functionalized surfaces (±80 ng/cm^2) compared to the blank (± 22 ng/cm^2) ($p<0.05$). VEGF immobilization, on the other hand resulted in a significantly higher amount on the blank sample (634 ng/cm^2) compared to the PDA activated one (± 507 ng/cm^2). As a consequence, due to the high aspecific adsorption, the covalently linked fraction is potentially masked, making it difficult to judge the success of VEGF immobilization at this stage.

In case of PLMA, PDA activation resulted in higher amounts of AB (29 ng/cm^2) and VEGF (286 ng/cm^2) compared to deposition onto the blank materials (16 and 174 ng/cm^2 respectively) and although a significant difference was only measured in case of the VEGF-functionalized samples ($p<0.05$), the immobilization could be considered successful.

Table 4.3: Atomic composition of the biofunctionalized PMMAPEG and PLMA surfaces. A comparison is made with the experimental composition of the pristine proteins. The amount of AB and VEGF deposited onto the different material surfaces, as determined by radiolabeling experiments is also displayed. Significantly different conditions ($p<0.05$) are denoted by the same letters a,b,c,…

Material	Modification	O (at%)	C(at%)	N (at%)	N/C	Mass (ng/cm^2)
PMMAPEG	**-**	29 (±1)	63 (±1)	0	0	-
PLMA	**-**	22 (±0)	70 (±1)	0	0	-
AB	**-**	22 (±2)	62 (±1)	11 (±0)	0.177 (±0.005)	-
VEGF	**-**	33 (±1)	59 (±1)	7 (±0)	0.110 (±0.006)	-
PMMAPEG	**AB**	31 (±0)	64 (±1)	0 (±0)	0 (±0)	22 (±7) [a]
	VEGF	30 (±1)	66(±0)	1 (±0)	0.010 (±0.005)	634 (±73) [c,d]
	PDA	21 (±2)	73 (±1)	5 (±1)	0.070 (±0.010)	-
	PDA AB	23 (±1)	65 (±1)	9 (±1)	0.132 (±0.009)	79 (±4) [a,b]
	PDA VEGF	22 (±1)	65 (±1)	10 (±1)	0.154 (±0.021)	507 (±48) [c,e]
	PDA AB VEGF	22 (±0)	65 (±1)	10 (±1)	0.160 (±0.009)	186 (±3) [f]
PLMA	**AB**	22 (±1)	71 (±1)	1 (±0)	0.019 (±0.004)	16 (±1)
	VEGF	22 (±1)	70 (±1)	1 (±0)	0.017 (±0.005)	174 (±7) [d,g]
	PDA	20 (±0)	74 (±0)	6 (±0)	0.076 (±0.004)	-
	PDA AB	21 (±0)	69 (±1)	9 (±1)	0.136 (±0.010)	29 (±11) [b]
	PDA VEGF	20 (±0)	69 (±1)	10 (±0)	0.143 (±0.003)	286 (±12) [e,g]
	PDA AB VEGF	21 (±1)	68 (±1)	10 (±1)	0.142 (±0.010)	56 (±4) [f]

Finally, if both AB and VEGF are immobilized onto the PDA coated surfaces, a lower angiogenic factor mass was determined for both materials (186 and 56 ng/cm^2 for respectively PMMAPEG and PLMA), compared to the sum of the individually immobilized factors (586 and 315 ng/cm^2 for respectively PMMAPEG and PLMA). It can be concluded that both factors influence each other and that competition exists during immobilization.

4.3.1.3. Stability study of the AB and VEGF functionalized surfaces

To study the stability of the AB and/or VEGF functionalized samples, the radio-labeled samples were incubated in PBS buffer at 37°C and were evaluated after 24 hours and 10 days. It was anticipated that upon incubation, the non-specifically bound AB and VEGF fraction would (partially) be removed from the surface, whereas the covalent fraction would act as a stable layer.
From the previous paragraph, it was concluded that significantly higher amounts of AB and VEGF were detected onto the PDA functionalized PMMAPEG surfaces compared to the PDA modified PLMA ones. This difference can possibly be explained by the higher swelling of PMMAPEG, which induces increased AB or VEGF **ab**sorption. Indeed, a 24 hours incubation of the AB and VEGF modified PMMAPEG samples resulted in respectively a 22 and 15% decrease of angiogenic factor mass, whereas in case of PLMA, the decrease was limited to respectively 7 and 4% (see figure 4.5, B and C). Furthermore, after 10 days of PBS incubation, the average decrease in angiogenic factor mass was again higher for PMMAPEG (i.e. 45% compared to the initial mean value) compared to PLMA (i.e. 26% compared to the initial mean value).
This trend was also confirmed for the combined AB/VEGF functionalized samples, since PMMAPEG resulted in a 46% decrease of angiogenic factor mass, whereas for PLMA this decrease was again limited to 21%.

Overall, it can be stated that the material composition is highly influencing the stability of the immobilized angiogenic factors. Furthermore, it can be stated that high aspecific adsorptions are manifested for both materials. Moreover, for PMMAPEG, a certain degree of absorption is also observed. The fraction of non-covalently bound factors can be regarded as a positive aspect, since during the first 10 days after implantation, a sustained release of angiogenic factors could be anticipated. As pointed out in the introduction of the current chapter, the positive effect of a controlled VEGF release on the vascularization process has already been proven [15]. Whether or not a similar effect could be anticipated for VE-cad AB release remains unclear and could be the subject of future research. In general, future research should ideally include a detailed *in vivo* assessment of this release.

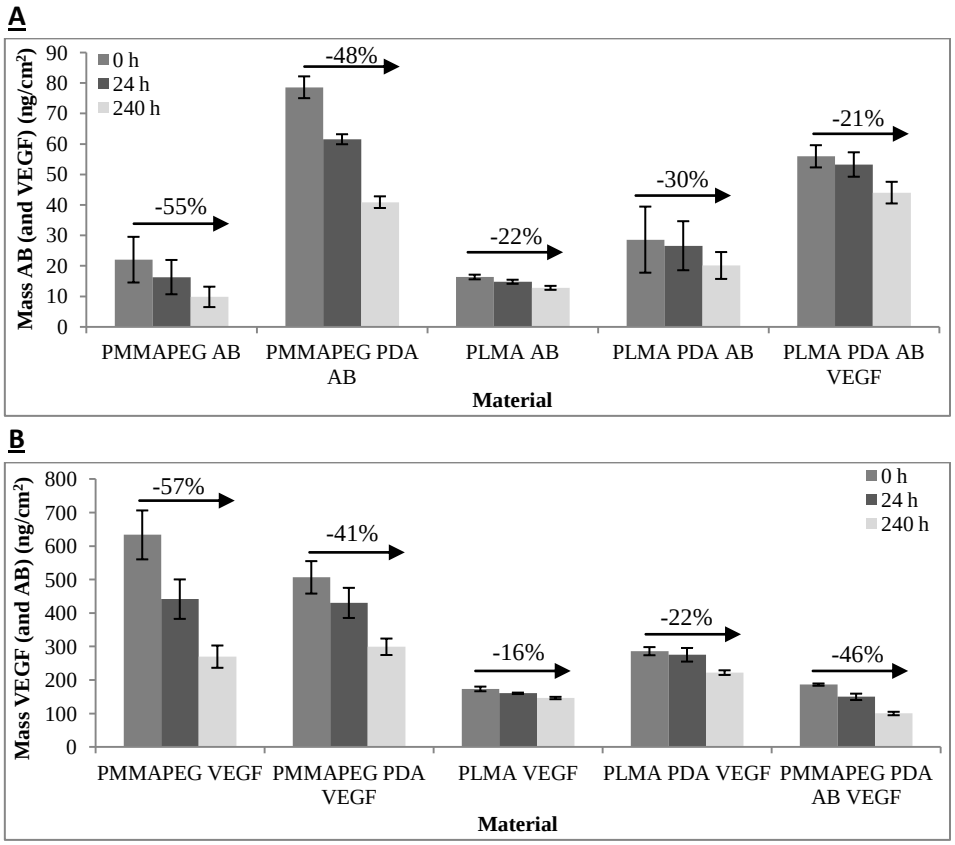

Figure 4.8: Stability study of the AB (Panel A) and VEGF (Panel B) modified PMMAPEG and PLMA surfaces by incubation of the samples during 24 hours and 10 days in PBS buffer at 37°C. Samples modified with both AB and VEGF are divided over both panels.

4.3.1.4. *In vitro* evaluation of the biofunctionalized PDA-based surfaces.

First, a qualitative live-dead assay was conducted using HUVEC. Figure 4.9 summarizes the results for both PLMA and PMMAPEG after 1 and 7 days. When comparing the blank materials, it is clear that for both time points, more cells adhered onto the LMA-based material compared to the PEG-based one. This can again be attributed to the protein repellant nature of PEG, as previously discussed (see §4.2.2.2).

For the PDA modified materials, a 24 hour cell incubation resulted in less dead cells for PLMA compared to PMMAPEG, which again shows that a PDA coating is not able to completely disguise the protein-repellant properties of PEG. Nevertheless, it can again be stated that HUVECs appear less susceptible towards the non-fouling properties of PEG, compared to HFF (cfr. figure 4.5). After 7 days of cell incubation confluent cell layers were observed for both materials, which shows that the PDA coated materials are more cell compatible compared to the blank materials.

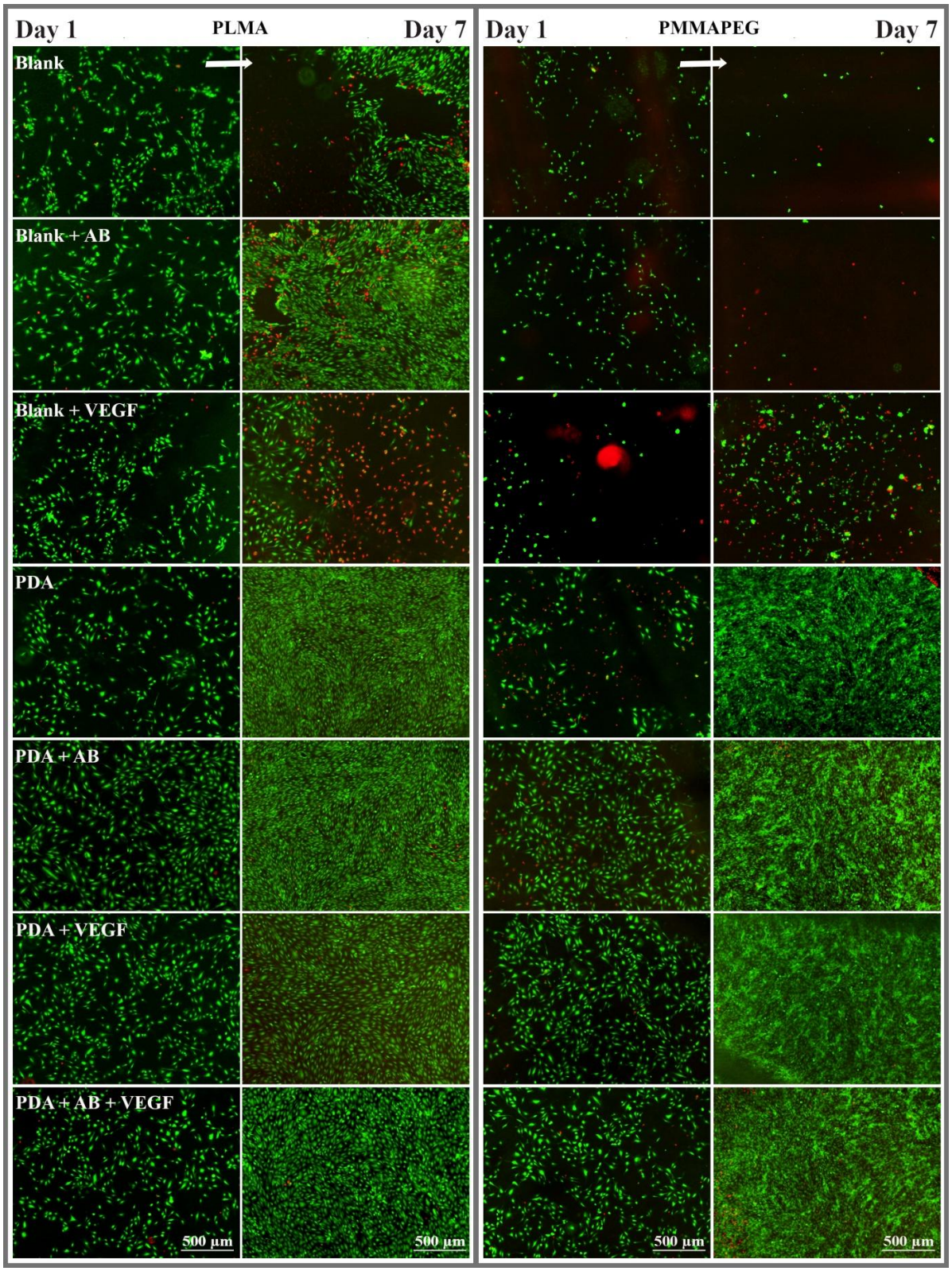

Figure 4.9: Live dead assay after 1 day and 7 days of cell incubation on the surface modified PDA-functionalized materials, including PLMA and PMMAPEG. Living cells are stained with calcein AM (green), dead cells with propidium iodide (red). Scale bare: 500 µm, for all figures.

Further biofunctionalization of the materials with VEGF and/or VE-cad AB clearly resulted in higher cell densities compared to the PDA-activated surfaces. Again, after 7 days, confluent

cell layers were evident for both material types. Since proliferation of the cells is manifested, a first proof is delivered that VEGF and/or AB functionalization of the surfaces results in an enhanced cell interactivity and cell viability. However, the assays do not allow to differentiate between the different surface functionalization strategies. As a consequence, immuno-staining assays were conducted.

Prior to this discussion, attention should be drawn to the VEGF and antibody-incubated blank materials. During radiolabeling experiments, it seemed that high amounts of VE-cad AB and VEGF adsorbed non-specifically onto the blank PMMAPEG and PLMA materials. Since almost no living cells were detected especially on the PMMAPEG surfaces, not even after 7 days of incubation, it can be concluded that the AB and growth factors are present in a non-active state. In the end, radiolabeling experiments could demonstrate the presence of AB (i.e. 40 and 20 ng/cm^2 for respectively PMMAPEG and PLMA) and VEGF (i.e. 300 and 220 ng/cm^2 for respectively PMMAPEG and PLMA) even after 10 days of PBS incubation.
In literature, similar conclusions were previously drawn in case of hydrophobic model surfaces. Wiseman et al could prove that antigen binding is not facilitated in case the deposited amount of antibody is lower than 100 ng/cm^2, because of a flat-on orientation of the AB (see § 4.2.4) [75]. As a consequence, PDA functionalisation is required to bind the antibodies and growth factors in their active state.

Immuno-staining of HUVECs, seeded on different surface-modified materials, resulted in confocal images as displayed in figure 4.10 (A). It is again very clear that both blank materials lack cell adhesive properties, as represented by a rather stretched or even bolded cell shape. Compared to the blank samples, the PDA-functionalized materials resulted in the attachment of a higher amount of cells, which are characterized by a superior non-bolded cell shape. The latter result is in line with the live/dead assay as it again points out that HUVECs are less susceptible towards PEG's repellant nature compared to HFF cells (§4.2.2.2). In case of AB and/or VEGF immobilization, nicely cuboidal-shaped HUVECs were visualized on top of the surfaces. Nevertheless, in case of VEGF immobilization, more stretched cells were observed together with lower cell densities compared to the AB functionalized ones (data not shown). Even though the latter observation was not clear from the live dead assay, visual observation of the confocal images already predicted a small preference towards the presence of VE-cad AB's on the surface. To test this hypothesis, a quantitative analysis of the focal adhesion points was performed of which the results are presented in boxplots in figure 4.10 (B). Again, cells with more focal adhesion points can be interpreted to be superiorly attached to the surface.
In case the same surface modification was considered, it can be concluded that PMMAPEG and PLMA did not result in significantly different amounts of focal adhesion points ($p>0.05$). It can thus be concluded that the studied biofunctionalization strategies result in cell responses which are independent of the nature of the underlying substrate.

If one material is considered, first PLMA, a significantly lower amount of focal adhesion points was obtained for the blank material (median FA=39), compared to the AB functionalized samples (median FA = 93) and the ones carrying a combination of VEGF and AB (median FA = 116) ($p<0.05$). If only VEGF was immobilized (median FA = 68), such a difference with the blank was not obtained, which points in the direction of our hypothesis (i.e. preference of HUVECs towards AB functionalized surfaces).

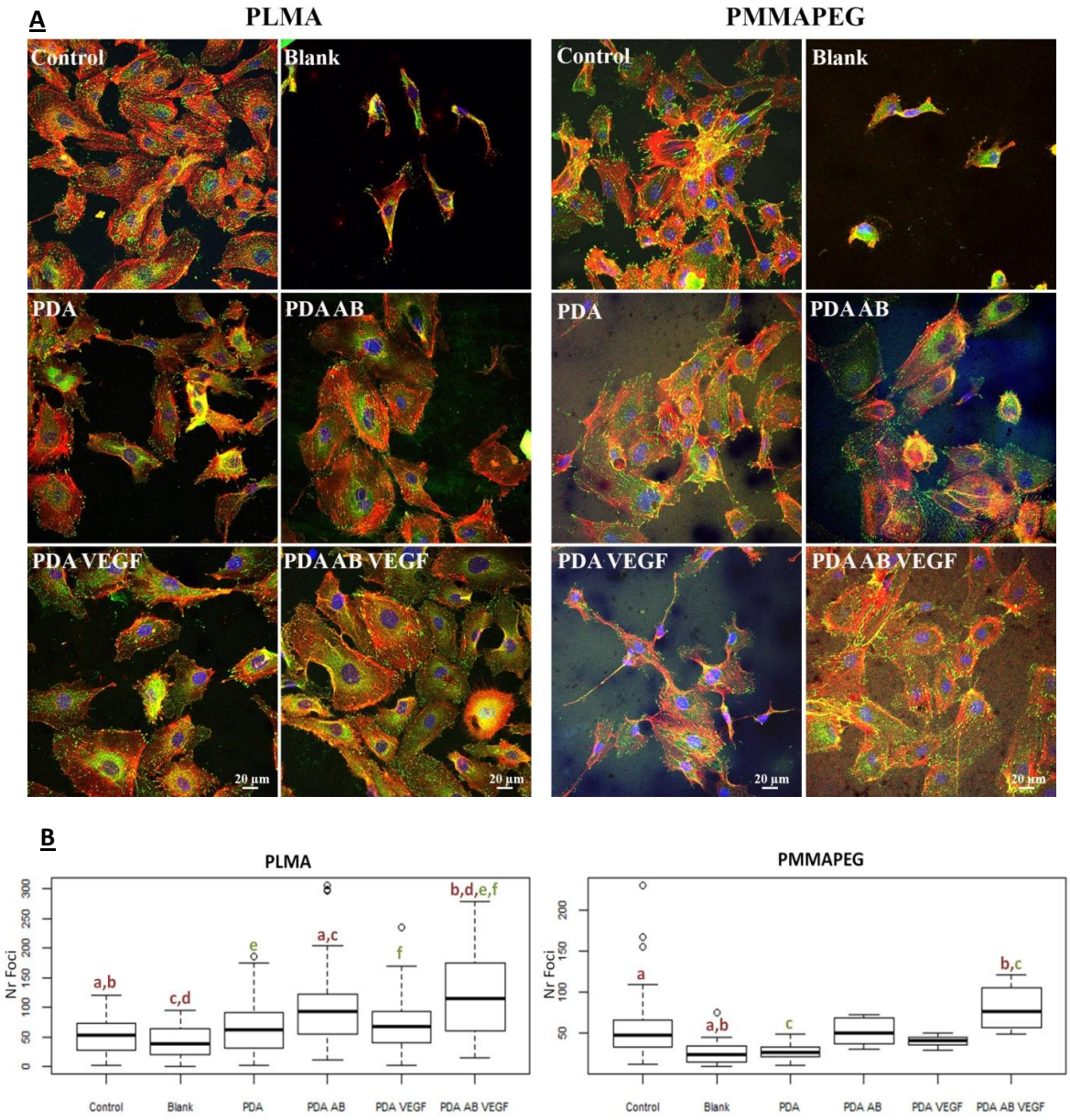

Figure 4.10: Confocal images of HUVECs, seeded onto (non-)biofunctionalized PLMA and PMMAPEG materials, for 2 days. Herein, nuclei, F-actin fibers and focal adhesion points are respectively stained in blue, red and green (scale bare = 20 µm) (A). Distribution of the focal adhesion points, counted per cell for the blank and PDA functionalized PLMA and PMMAPEG materials. Conditions which are significantly different are denoted by the same letter a, b, c,… (B)

Comparison of the different surface modifications indicated a significantly lower number of focal adhesions for the PDA coated surfaces (median FA = 63) compared to the condition where both VEGF and AB were immobilized (median FA = 116) ($p<0.05$). A similar conclusion could be made for the VEGF functionalized samples and the combination of AB and VEGF. If only AB was immobilized, no significant difference was obtained with the VEGF functionalized surfaces, nor with the combined AB/VEGF functionalized samples ($p>0.05$). As a consequence, for PLMA, it can be concluded that the combination of AB and VEGF is preferred to maximize cell adhesion, followed by the immobilization of AB as such. Immobilization of VEGF or the application of a single PDA coating is however least preferred if the stimulation of HUVEC adhesion is targeted.

For PMMAPEG, a similar evaluation was conducted and herein, a significantly higher amount of focal adhesion points was obtained for the combined AB and VEGF immobilized samples (median FA= 78), compared to the blank (median FA = 25) ($p<0.05$). The same applied for the comparison between the PDA (median of 27) coated samples and the VEGF/AB functionalized ones. However, in case the AB functionalized samples (median of 51 FA) and the VEGF functionalized ones (median of 41 FA) were compared with the PDA coated samples and the AB/VEGF functionalized samples, no significant difference could be found ($p>0.05$). As a consequence, a similar conclusion as for the LMA-based material could be made, being that the combination of AB and VEGF is preferred to stimulate HUVEC adhesion.

As a result, it was suggested that a combined, maybe synergetic effect would be provoked by the immobilization of both angiogenic factors. To study this phenomenon in more detail, a separate experiment was conducted. Herein, contrary to previous experiments, for each condition (AB, VEGF or AB/VEGF), the same total angiogenic factor concentration of 4 µg/ml was used for immobilization, as well as a fixed protocol (see chapter 6). In this way, a concentration effect or a protocol-related effect could be ruled out as variable from the experimental set-up.
Figure 4.11 clearly shows the cuboidal shaped HUVECs present on the different AB and/or VEGF functionalized surfaces. Furthermore, when the number of focal adhesion points was compared for the different samples, a significant difference was observed between the AB immobilized samples and the combined VEGF/AB functionalized ones ($p<0.05$).

Comparison of the VEGF and AB functionalized samples did however not result in significant differences. Since the only variable in the experimental setup was given by the nature of the angiogenic factors, it is clear that if both AB and VEGF are present on the surface, both factors carry responsibility for the increased cell adhesion. Furthermore, since the initial and individual concentrations of VEGF and AB in the combined angiogenic factor solutions were lower (2 µg/ml) compared to the solutions used for single angiogenic factor deposition (4 µg/ml), it can be concluded that a combined effect does exist between both VEGF and VE-cad AB, which stimulates HUVEC adhesion.

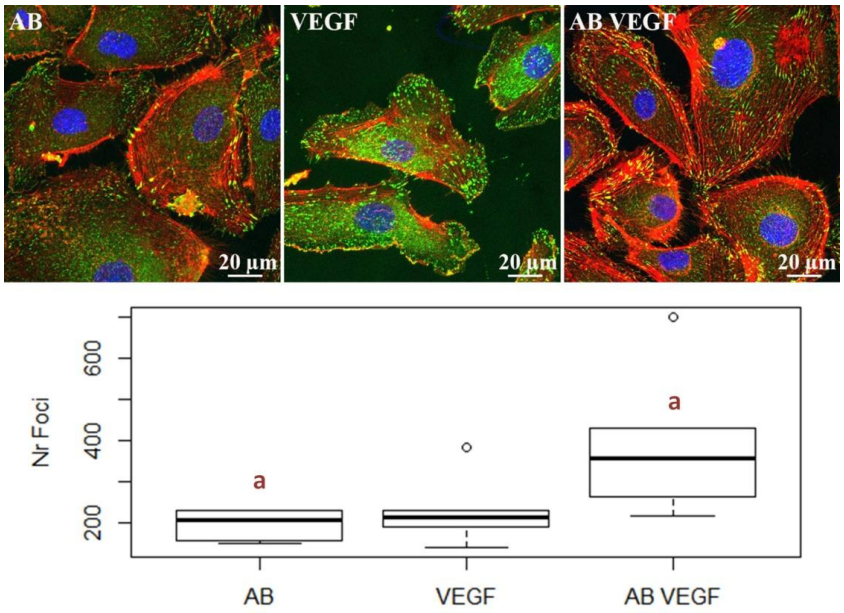

Figure 4.11: Evaluation of the combined effect of VE-cad AB and VEGF, which are immobilized onto PDA coated PLMA networks.

When translating these results into an *in vivo* situation, several assumptions can be made. In case no angiogenic factors would be immobilized, cell tests have shown that almost no adhesion of cells is manifested and as a consequence, it is suggested that the *in vivo* integration of the implant will be less efficient. This topic will be further studied in chapter 5 where the *in vivo* results are discussed. Conversely, upon immobilization of VEGF or VE-cad AB, enhanced cell adhesion was detected, implying that better body integration might be expected. To prove the latter statement, different experiments should be conducted for the different strategies. In case of single VE-cad AB immobilization, the attraction of circulating endothelial progenitor cells (EPCs) is targeted in the *in vivo* situation. After differentiation into mature endothelial cells, they will be able to contribute in the formation of new 'de novo' blood vessels via a process called vasculogenesis (see figure 4.12, A). To prove this assumption for the currently developed materials, further testing *in vitro* and *in vivo* will be necessary. To be more precise, experiments with EPCs should be conducted to evaluate their viability, and differentiation capability in case of contact with the herein developed materials.

In case of single VEGF immobilization, stimulation of angiogenesis was mainly targeted, a process wherein a new blood vessel is formed from an existing one (see figure 4.12, B). During this process, first, degradation of the basal membrane of the existing blood vessel will occur and 'tip' cells will form. These 'tip' cells consist of endothelial cells which contain long and mobile filopedia which will stretch and migrate in the direction of pro-angiogenic signals, such as VEGF, which are in this case immobilized on the implants. As a result, a sprout will form, which is the first important step towards new blood vessel formation (see figure 4.12, B). Further *in vitro* (e.g. migration studies) and extensive *in vivo* evaluations (e.g. the chick chorioallantoic assay (CAM)) will be needed to prove this theory.

Furthermore, upon combining VEGF and VE-cad AB on the surface of the implant, it can be suggested that a combined *in vivo* effect might exist. In this context, Gavard et al proved that upon VEGF stimulation, endocytosis of VE-cadherin, an endothelial cell surface marker, was stimulated [76]. Due to the internalization of VE-cadherin, cell-cell contacts are broken and thereby the endothelial barrier function is disrupted, which is needed for the initiation of angiogenesis (cfr. sprouting). Since in this work, VE-cad antibodies are immobilized, VE-cadherin bearing endothelial cells are likely to become recruited towards the implant and upon interaction with the immobilized VEGF, a similar mechanism could be induced, thereby enhancing the generation of new blood vessels via angiogenesis. Again, *in vivo* experiments should be conducted to prove the latter theory.

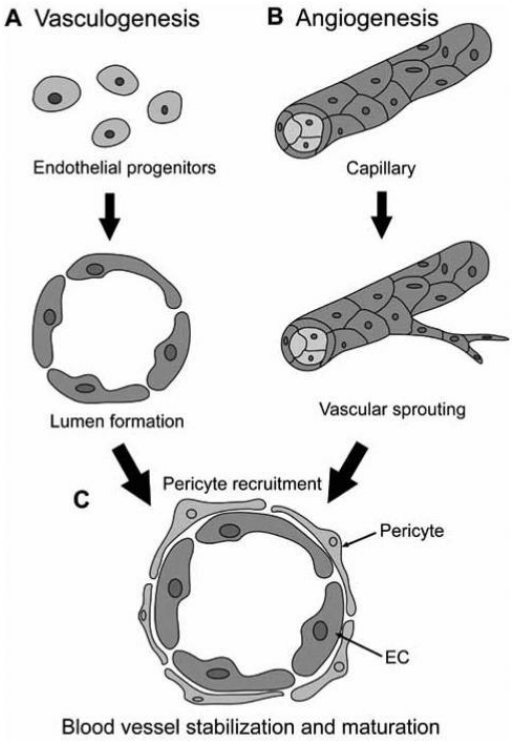

Figure 4.12: Formation of new blood vessels via vasculogenesis (i.e.'de novo') (A) or angiogenesis (via sprouting of an existing blood vessel) (B). The figure also shows the final maturation step during new blood vessel formation (C).[77]

4.3.2. Immobilization of VEGF and VE-cad AB onto AEMA-modified surfaces

Apart from PDA functionalization, primary amines were introduced onto the implant materials via a post-plasma grafting strategy, as described in chapter 3 (§ 3.3). Herein, it was proven that the post-plasma grafting of AEMA resulted in a relatively low nitrogen content on the surface (i.e. around 1%). As a consequence, due to the high cost of the biological compounds, only one material was selected to evaluate the different biofunctionalization protocols (i.e. PLMA(2959)), because of its superior physicochemical properties compared to PMMAPEG (see chapter 2).

4.3.2.1. Immobilization strategy

As a result of the post-plasma grafting of AEMA, primary amine functions were immobilized onto the substrate material, as evidenced by XPS (1% N). To enable the subsequent immobilization of AB or growth factor, carbodiimide coupling chemistry was applied to induce a nucleophilic attack of the surface amine functions towards an activated carboxylic acid group of the growth factor or antibody. As depicted in figure 4.13, this process comprised several steps. First, the carboxylic acid moiety of the AB or VEGF is activated by reaction with 1-ethyl-3-(3-dimethylaminopropyl) carbodiimide (EDC). Hereby, an excellent leaving group is generated due to the formation of an activated *o*-acylisourea intermediate. Nucleophilic attack of this activated compound by the surface amine functionalities finally results in covalent linkage of the AB or growth factor via an amide bond. The main advantage of this chemistry is its applicability in water, which enables direct bioconjugation in aqueous conditions. However, since hydrolysis of the activated intermediate includes the main competing reaction (see figure 4.13), the coupling reaction should happen fast. In this respect, the stability of the reactive intermediate can be increased by using N-hydroxysulfosuccinimide (sulfo-NHS) [78-80].

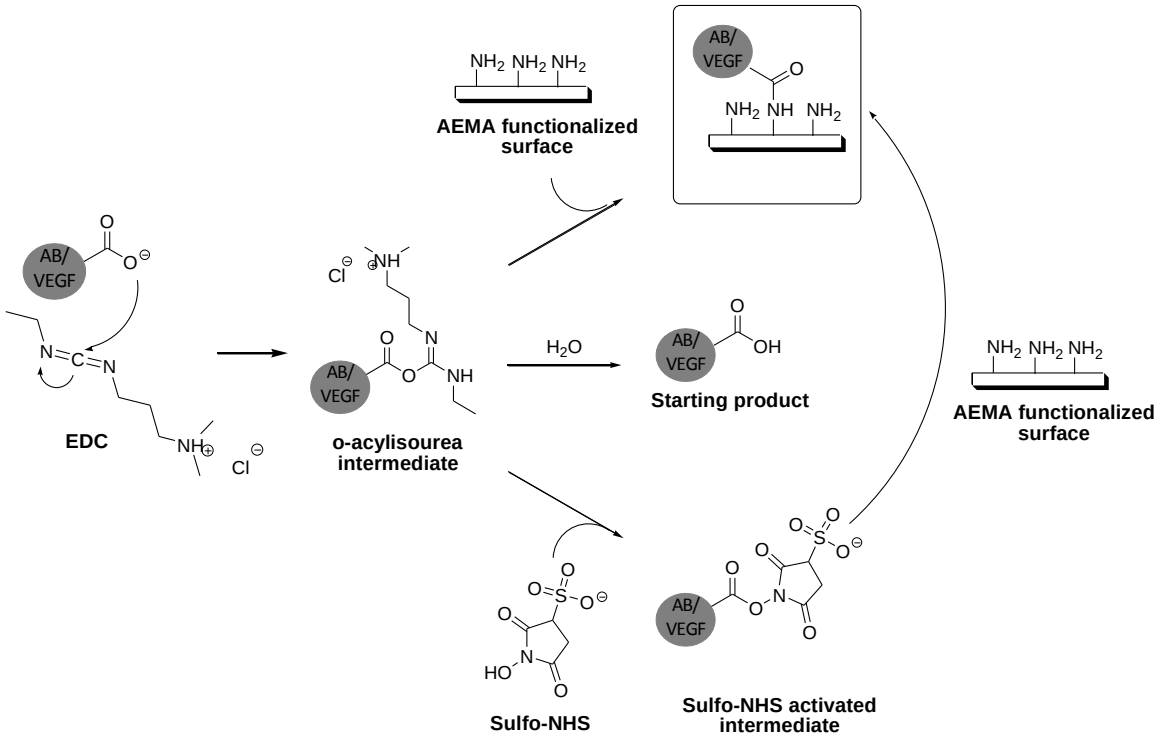

Figure 4.13: Coupling of VE-cad AB or VEGF to AEMA functionalized surfaces using EDC-chemistry, in the presence or absence of sulfo-NHS.

Because of the higher hydrolysis resistance of the sulfo-NHS activated intermediate, Staros et al proved that higher yields could be obtained for the linkage of glycine and a metalloprotein [78]. On the contrary, Vashist et al noticed that the crosslinking of antibodies with 3-aminopropyltriethoxysilane (APTES)- functionalized surfaces at a pH 7.4 was

enhanced in case EDC was used instead of EDC/sulfo-NHS [81]. Due to this finding, both conditions (i.e. use of EDC and EDC/sulfo-NHS) were evaluated in the present work. Apart from mechanism-based selections, variations in reaction conditions are also common in literature reports, such as the choice of buffer and pH. Generally, it is accepted that the EDC coupling reaction proceeds best in MES buffer at a more acidic pH (pH 4.5), although phosphate-based buffers with a neutral pH (pH 7.2) can also be used but might result in a lower coupling efficiency. In case NHS ester chemistry is used, the reaction will preferably proceed at neutral to more basic pH conditions (pH 7.2-9). Considering the practical constraints herein (modification of small sample surfaces), both reactions are conducted in the same buffer, at equal pH. Based on literature examples, two different buffers were selected, including an acidic MES buffer (pH of 6) [79, 82] and a neutral PBS buffer (pH of 7.4) [81, 83].

4.3.2.2. Characterization of the AB and VEGF functionalized surfaces

To evaluate the different protocols, ***XPS measurements*** were performed to study the elemental composition of the surface before and after angiogenic factor immobilization (table 4.4). It can be noted that compared to the AEMA functionalized surfaces (1% N), significantly higher nitrogen percentages were obtained after VEGF and/or AB immobilization (> 3% N), which is a direct proof for their presence on the surface. Furthermore, it was again anticipated that the N/C ratio of the VEGF and AB modified surfaces should again result in similar or lower values compared to pristine AB (N/C= 0.17) and VEGF (N/C = 0.11). This prediction was followed for all samples. Since BSA was again present in the VEGF modification buffer, much higher ratios could have been expected in this case (cfr. the PDA-based experiments).

If the different immobilization protocols are compared, it is clear that both for the AB and VEGF immobilization, MES buffer is preferred, since lower nitrogen percentages and N/C ratios were detected in case the modification was performed in PBS buffer. This can possibly be explained by the respective pH values of the two buffers, being 6.1 for MES and 7.4 for PBS. It is suggested that the crosslinking reaction proceeds best in more acidic conditions, which is in agreement with literature reports [83], as discussed earlier. Furthermore, similar results were obtained in case EDC was used and when EDC was combined with sulfo-NHS. This also follows the expectations, because the benefit of using sulfo-NHS could not be judged from these characterization results, but will follow from a stability test (see later on).
It can be mentioned that some degree of aspecific adsorption is again manifested, because if no EDC crosslinker was used, an increase of 1% (in case of AB) and 3% (in case of VEGF) in atomic nitrogen was observed, compared to the AEMA grafting only. Nevertheless, compared to the test samples wherein an EDC crosslinker was used, these values remain significantly lower ($p<0.05$). It should again be stressed that due to the presence of BSA in the VEGF modification buffer, it is not clear from these results whether the increase in nitrogen percentage is caused by VEGF, BSA or a combination of both.

Table 4.4: Atomic composition of the AB and/or VEGF biofunctionalized PLMA surfaces, as determined by XPS. Different immobilization protocols are compared, including variations in coupling agent and buffer (see text for the detailed discussion). The deposited masses of AB and/or VEGF are shown in the last column, as determined by radiolabeling experiments.

Material	Modification	Coupling agent	Buffer	O (at%)	C(at%)	N (at%)	N/C	Mass (ng/cm^2)
AB	-	-	-	22 (±2)	62 (±1)	11 (±0)	0.177 (±0.005)	-
VEGF	-	-	-	33 (±1)	59 (±1)	7 (±0)	0.110 (±0.006)	-
						-		
PLMA	-	-	-	22 (±0)	70 (±1)		-	-
PLMA	**AEMA**	-	**PBS**	25 (±1)	71 (±1)	1 (±0)	0.014 (±0.003)	-
	AB	-	**PBS**	22 (±1)	71 (±1)	1 (±0)	0.019 (±0.004)	15 (±1)
	VEGF	-	**PBS**	22 (±1)	70 (±1)	1 (±0)	0.017 (±0.005)	161 (±2)
PLMA	**AEMA AB**	-	**PBS**	26 (±0)	65 (±1)	2 (±0)	0.031 (±0.007)	21 (±4)
	AEMA AB	**EDC**	**PBS**	27 (±2)	64 (±1)	3 (±2)	0.046 (±0.028)	28 (±3)
	AEMA AB	**EDC**	**MES**	28 (±1)	64 (±2)	**4 (±1)**	**0.068 (±0.011)**	24 (±4)
	AEMA AB	**EDC/NHS**	**PBS**	25 (±1)	65 (±1)	3 (±1)	0.050 (±0.009)	26 (±2)
	AEMA AB	**EDC/NHS**	**MES**	27 (±1)	66 (±1)	**4 (±0)**	**0.056 (±0.006)**	21 (±2)
PLMA	**AEMA VEGF**	**/**	**PBS**	24 (±1)	65 (±3)	3 (±2)	0.053 (±0.031)	511 (±44) [a,b,c,d]
	AEMA VEGF	**EDC**	**PBS**	26 (±1)	63 (±2)	4 (±0)	0.057 (±0.007)	397 (±11) [a,e,f]
	AEMA VEGF	**EDC**	**MES**	26 (±1)	66 (±2)	**5 (±1)**	**0.076 (±0.009)**	277 (±37) [b,e,g]
	AEMA VEGF	**EDC/NHS**	**PBS**	25 (±1)	66 (±2)	3 (±1)	0.048 (±0.020)	419 (±20) [c,g,h]
	AEMA VEGF	**EDC/NHS**	**MES**	26 (±1)	66 (±1)	**6 (±0)**	**0.085 (±0.006)**	275 (±23) [d,f,h]
PLMA	**AEMA AB VEGF**	**EDC**	**MES**	26 (±1)	63 (±1)	4 (±0)	0.055 (±0.003)	164 (±12)

Next, ***radiolabeling experiments*** were performed to determine the immobilized AB and VEGF mass. The results confirmed the successful immobilization of VEGF and AB via each of the studied crosslinking mechanisms. Indeed, significantly higher amounts of AB and VEGF were measured onto the AEMA and EDC pre-treated samples compared to the AB and VEGF incubated blank samples ($p<0.05$). Furthermore, similar amounts of AB and VEGF were observed on the AEMA-coated samples compared to the PDA-coated samples (cfr. table 4.3).

In case of AB immobilization, comparison of the different AEMA-based deposition protocols did not result in significantly different AB masses present on the surface. It was expected that the addition of EDC (and NHS) would have resulted in a significantly higher amount of immobilized AB. However, due to high aspecific adsorptions, it was difficult to differentiate between the non-specifically and covalently bound portion.

Also in case of VEGF immobilization, high aspecific adsorption of VEGF onto the AEMA functionalized surfaces had manifested, since if no crosslinker was used, a significantly higher amount of immobilized VEGF was obtained ($p<0.05$). It can further be noted that in the presence of EDC, intermolecular crosslinking of VEGF could compete during surface

immobilization of VEGF. Comparison of the different EDC-chemistry based protocols showed that, coupling in PBS buffer was preferred over the use of MES buffer, since significantly higher amounts of VEGF were detected in the former case (± 400 ng/cm^2 with PBS vs ± 276 ng/cm^2 with MES) ($p<0.05$). This conclusion clearly contradicts the XPS results. Nevertheless, since the latter XPS results were biased by the presence of BSA (i.e. part of the nitrogen signal originates from BSA), the radiolabeling experiments were considered more trustworthy.

Comparable to the immobilization onto the PDA modified surfaces, dual factor immobilization resulted in lower, almost half of the deposited AB and VEGF (i.e.164 ng/cm^2), compared to the sum of their individually deposited masses (±300 ng/cm^2). It can again be concluded that both factors influence each other and that competition possibly exists during immobilization.

4.3.2.3. Stability study of the AB and VEGF functionalized surfaces

To study the stability of the immobilized angiogenic factors, the different surface modified samples were incubated in PBS buffer at 37°C and evaluated by radiolabeling experiments as a function of time. It was anticipated that upon incubation of the AB and VEGF modified samples, the systems without applied cross-linker would result in significantly higher decreases in deposited angiogenic factor mass compared to the EDC-crosslinked samples. Furthermore, it was expected that the application of NHS would result in significantly lower releases upon incubation, since NHS stabilizes the reactive intermediate (see figure 4.13), which is susceptible towards hydrolysis.
In case of the former assumption, figure 4.14 clearly shows that a similar decrease is obtained for the different crosslinker-treated samples and the ones which were not treated with a crosslinker. This suggests that, even if covalent linkage would have occurred upon application of EDC as a crosslinker, substantial amounts of aspecific adsorption could still occur. The latter suggestion could be further motivated by the limited amount of immobilized AEMA (i.e. only 1% of N detected compared to 6% in literature [84], see chapter 3).
Regarding the second assumption, upon PBS incubation, slightly lower decreases were obtained in AB and VEGF masses in case NHS was used as stabilizer, nevertheless, these decreases were not significant ($p>0.05$) compared to the other immobilization protocols. This observation shows the limited effect of NHS addition for the current experimental set-up or confirms an initial limited covalent linkage of the angiogenic factors to the surface.
If the absolute deposited masses are compared after 24 hours and 10 days of incubation, a significantly higher ($p<0.05$) amount of immobilized AB was retained for the EDC crosslinked samples (in PBS) (i.e, 20 ng/cm^2) compared to the blank (i.e. AB incubated AEMA samples without crosslinker; 17 ng/cm^2).
In case of VEGF immobilization, the same protocol (i.e. EDC crosslinking in PBS, in the absence of NHS) resulted in the highest mass retention after incubation, compared to the

other crosslinker-based protocols. Nevertheless, compared to the blank (VEGF incubated AEMA samples without crosslinker), these amounts remained significantly lower ($p<0.05$).
If these results are compared with the ones obtained for the PDA activated samples (see § 4.3.1), it can be concluded that the success of AB and VEGF immobilization onto the PDA modified samples was more pronounced compared to the AEMA activated ones. In the former case (i.e., PDA activation) higher amounts of angiogenic factors were immobilized compared to simple incubation of the blank materials in AB and VEGF solutions. As a consequence, covalent linkage was assumed in case of PDA activation. On the other hand, for the application of AEMA, such increases were not demonstrated, since simple incubation of the AEMA-modified samples into the angiogenic factor solution resulted in similar or even higher deposited angiogenic factor masses compared to the crosslinker-based (i.e. EDC) immobilizations. As a consequence, instead of covalent interactions, a preference towards aspecific adsorption was suggested. To judge the impact of this fact, cell tests had to be performed to evaluate the activity of the immobilized factors.
Similar to the angiogenic factor functionalized PDA samples, the detected sustained release could again offer interesting opportunities in the *in vivo* environment.

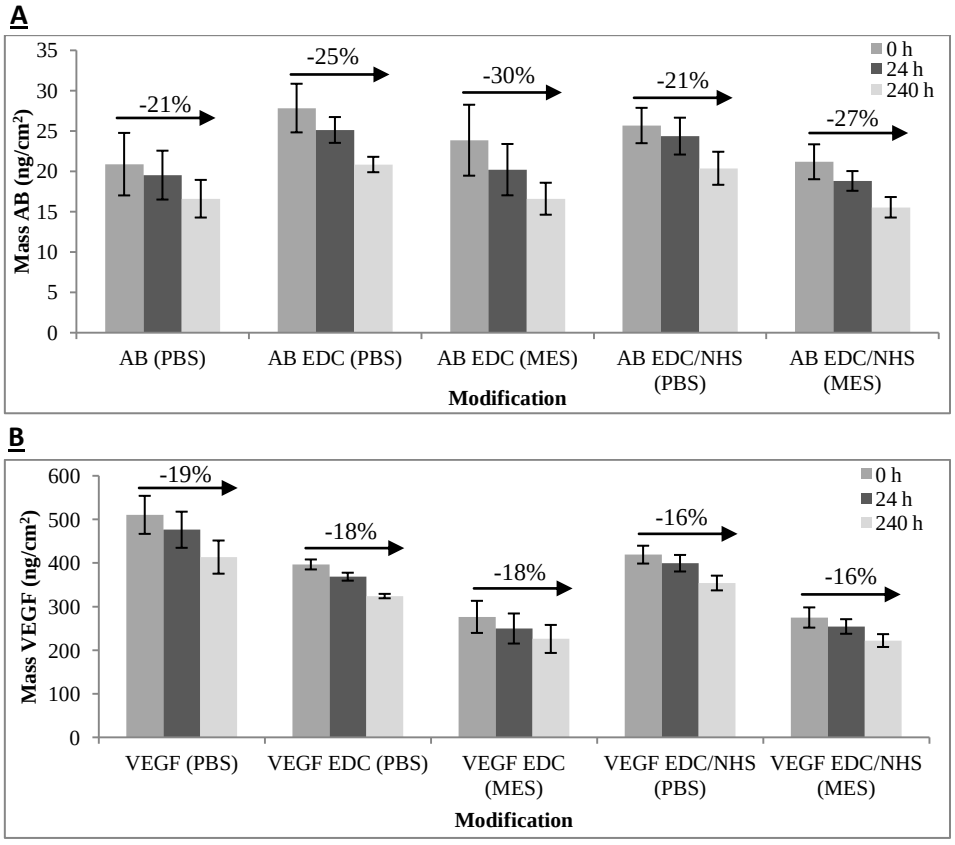

Figure 4.14: Stability study of the AB (panel A) and VEGF (panel B) modified PLMA surfaces by incubation of the samples during 24 hours and 10 days in PBS buffer at 37°C.

4.3.2.4. *In vitro* analysis of the angiogenic factor functionalized AEMA-based surfaces

Similar to previous *in vitro* evaluations, a live dead assay at day 1 and day 7 was performed to study the cell viability of HUVECs when seeded on PLMA with different surface modifications. Figure 4.15 summarizes the results obtained in case different coupling protocols were used to attach the angiogenic factors onto the AEMA functionalized surfaces. Based on a visual evaluation of the cell densities present after 24 hours, it could be concluded that almost no cells were present on the blank material and that the cell density was increased due to the application of an AEMA coating. Covalent immobilization of AB via EDC or EDC(NHS) chemistry in MES buffer resulted in higher cell densities, whereas in PBS, the cell number was much lower. Since quantification via radiolabeling revealed equal amounts of AB for the different immobilization protocols (see table 4.4), it is suggested that linkage in MES buffer resulted in a more active state of the AB.

In case of VEGF immobilization, after 24 hours of cell incubation, lower cell densities were observed compared to the AB functionalized surfaces, irrespective of the coupling protocol. The lower cell densities could possibly be attributed to the presence of BSA, which was added to the modification buffer. Similar to the PDA functionalized samples, competition will have occurred during immobilization on the AEMA coated samples and as a consequence, both VEGF and BSA were present on the surface. From previous studies with hepatocytes, it appeared that the cell adhesion, proliferation and viability significantly decreased when immobilizing BSA [33]. Therefore, also for HUVECs, a similar effect might be responsible for these lower cell densities, although further studies would be needed to elucidate the exact role of both components.
Despite of these differences seen after 24 hours, 7 days after cell seeding, both the AEMA functionalized and VEGF or AB factor containing surfaces resulted in confluent cell layers, meaning that all surfaces are characterized by a good cell compatibility. Furthermore, the HUVECs were characterized by their natural cuboidal shape, although this was less obvious in case antibodies were immobilized in PBS buffer.
As expected, the blank material resulted in a low cell compatibility, since cells did not proliferate and even after 7 days, low cell densities were still observed.

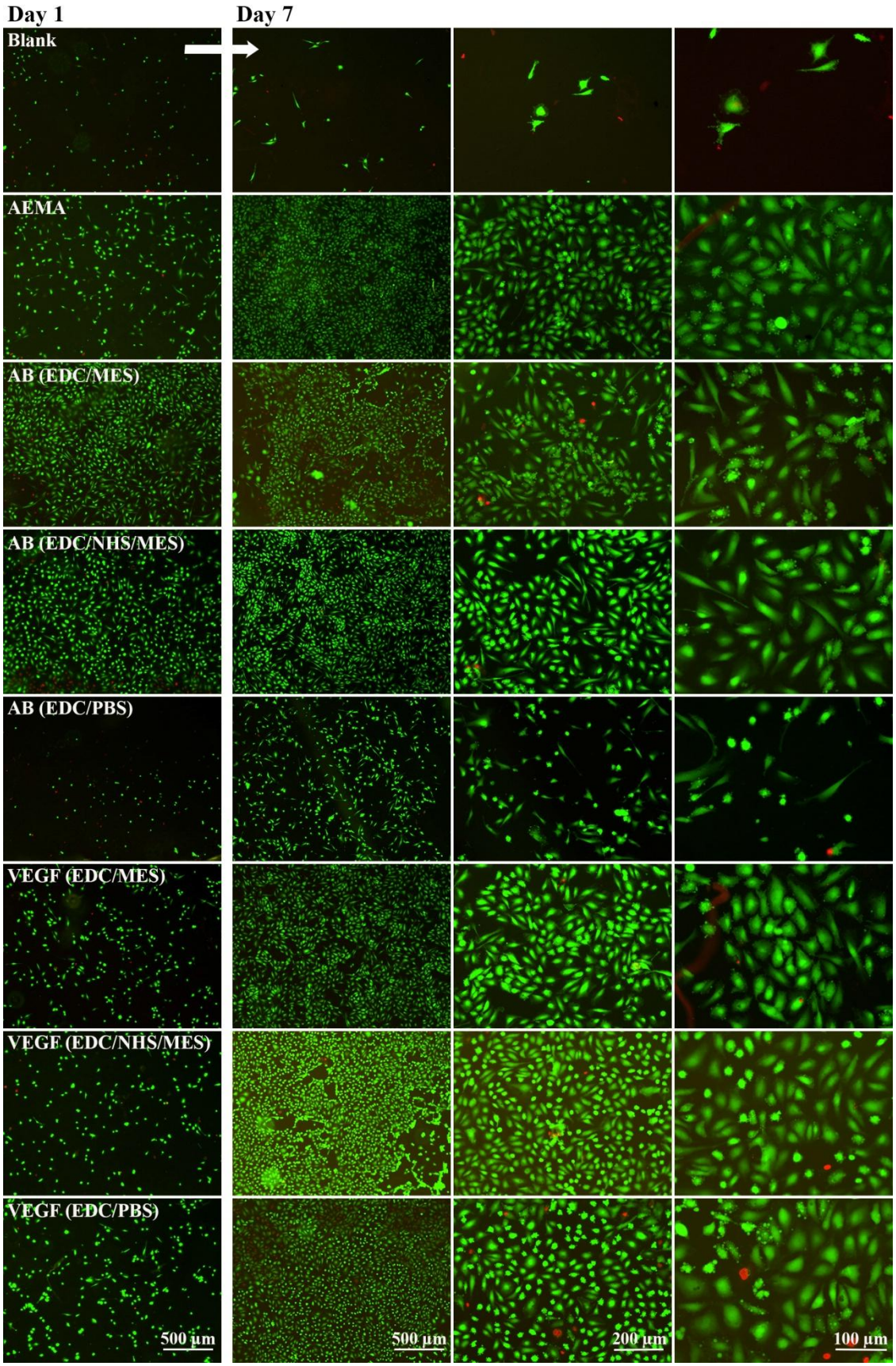

Figure 4.15: Live dead staining of HUVECs, seeded on the AEMA functionalized PLMA surfaces. Both VEGF and VE-cad AB are coupled with AEMA using EDC-chemistry.

To study the cell attachment on the PLMA surfaces in a more detailed way, immuno-assays were conducted to determine the amount of focal adhesion points present in the attached cells. From the confocal images in figure 4.16, a similar trend (compared to the live dead images) was seen for the obtained cell densities when comparing the different deposition protocols, implying that VEGF immobilization resulted in lower cell densities compared to the AB immobilized surfaces. Furthermore, the cuboidal cell shape was much more pronounced in case AB's were immobilized. VEGF immobilization resulted in more elongated, stretched cells.

In the next step, the number of focal adhesion points was quantified of which the results are presented in the boxplots of figure 4.16. AB functionalization (median FA between 70 and 80) resulted in a significantly higher amount of focal adhesion points compared to the blank (median FA= 13) ($p<0.05$), although, in case the coupling was conducted in PBS, such a difference was not obtained (median FA = 57) ($p>0.05$). When the different modification protocols were compared, no significant differences were observed and similar results were obtained compared to the positive control, which is a cell adhesive reference ($p>0.05$).
In case of VEGF immobilization, only a significant difference was obtained between the blank (median FA = 13) and in case the immobilization was performed with EDC, in MES buffer (median FA = 77). Comparison of the different VEGF immobilization protocols (median FA between 57 and 77) did not result in a significantly different number of focal adhesion points, also not compared to the cell adhesive control (79) ($p>0.05$).
Based on these cell adhesion results, it can be concluded that all immobilization protocols are suitable to maximize cell adhesion and this applies to both AB and VEGF.
On the other hand, if all *in vitro* results are considered, it can be concluded that the highest cell densities and the most natural cell morphology was obtained in case VE-cadherin antibodies were immobilized onto the PLMA surfaces and if MES was used as immobilization buffer. This follows the expectation, since more acidic conditions are generally preferred (pH 4.5) to perform the EDC coupling reaction. As a consequence, the used MES buffer in this work approaches this condition most (pH 6) [83].

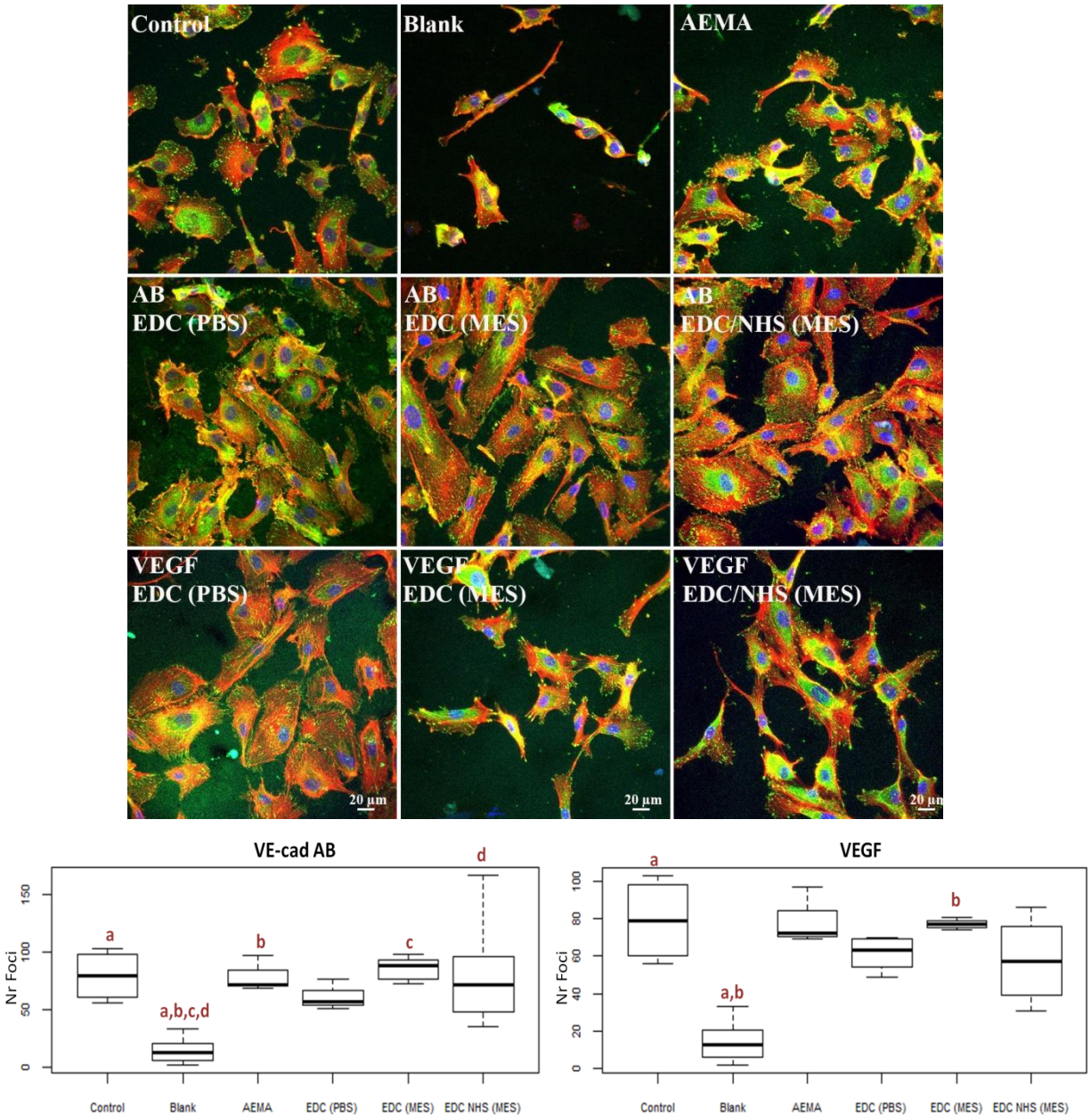

Figure 4.16: Distribution of the focal adhesion points, counted per cell after 2 days of cell contact for the blank and AEMA functionalized PLMA materials. Conditions which are significantly different are denoted by the same letter a, b, c,…

It can also be mentioned that the application of AEMA as such resulted in similar positive and equal cell responses. It should be clear that even though such positive cell responses were obtained for a single AEMA coating, the specific function of VE-cad AB and VEGF (see §4.1) will be essential to stimulate angiogenesis in an *in vivo* environment.

Similar to the PDA functionalized surfaces, it was tested whether the existence of a combined effect of AB and VEGF could be confirmed in this case. To this end, a similar experiment was conducted during which a fixed angiogenic factor concentration (4 µg/ml) and immobilization protocol (EDC/MES) was applied. Figure 4.17 shows the nicely cuboidal shaped HUVECs in case AB and AB/VEGF were immobilized. For the VEGF functionalized

surfaces, next to the anticipated cuboidal shaped cells, some cell clusters were also visible. Quantification of the focal adhesion points resulted in a higher median for the combined AB/VEGF functionalization (median FA =235), compared to the single AB (median FA = 192) or VEGF(/BSA) (median FA = 188) functionalized surfaces. However, statistical testing showed that the obtained differences were not significant ($p>0.05$). It can be concluded that based on this study, no statistical evidence for a combined angiogenic factor effect could be found.

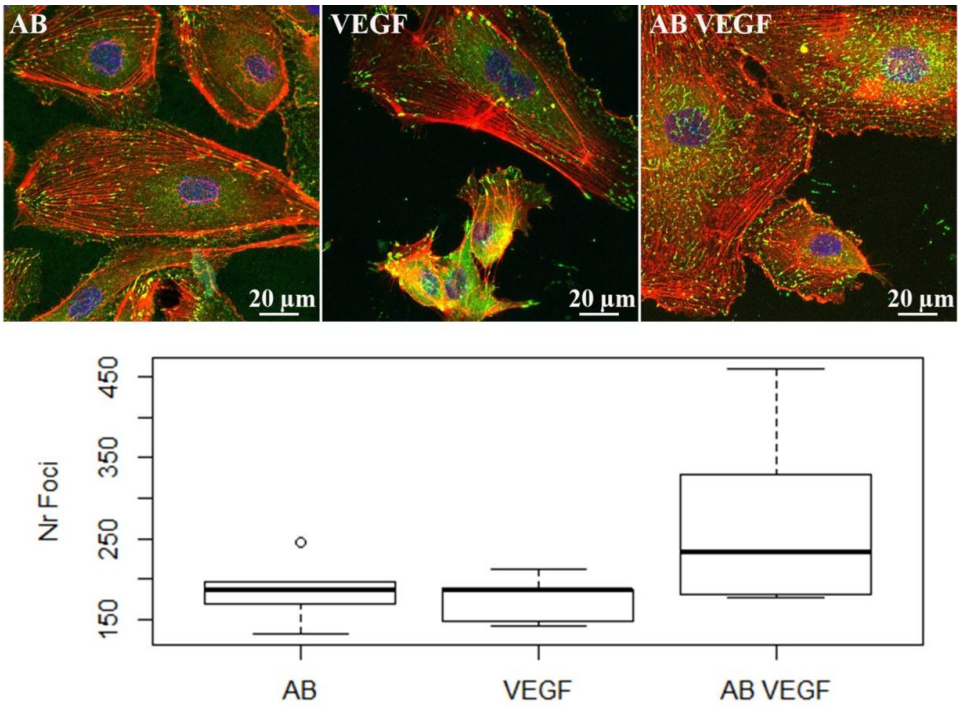

Figure 4.17: Evaluation of the combined effect of VE-cad AB and VEGF, which are immobilized onto AEMA coated PLMA networks.

To further study the impact of angiogenic factor immobilization on the cell behavior in an *in vitro* setting, future studies should focus on gene expression, during which genes related to adhesion, migration and endothelial function could be quantified. Examples include the Von Willebrand Factor (VWF), VEGFR, VEGFA, ICAM1 and ICAM2 which are factors that all contribute to angiogenesis [85]. Furthermore, two-dimensional angiogenesis assays as well as cell migration assays could be performed. In this respect, Gellynck et al (Tissue Engineering Group, UGent) already performed some preliminary tests showing that an increased AB concentration resulted in an increased blood vessel length and that a concentration of 4 µg/ml gave rise to an improved migration of HUVECs [86]. A similar evaluation could also be performed for the other angiogenic factors, including VEGF as well as the combined AB/VEGF immobilization strategy.

4.3.3. Study into the orientation of the immobilized antibodies

In the previous sections, successful immobilization of VE-cad AB was proven. It can however be questioned how these antibodies are oriented on the polymer surface. Antibodies are Y-shaped structures, which carry two Fab binding sites (antigen binding fragments) and an Fc region (fragment crystallizable region) (figure 4.18, A). In case antibodies are adsorbed onto surfaces, different orientations can occur, including the Fab-up, Fc-up, side-on and flat-on orientation [75, 87]. In case of covalent immobilization of the AB, different orientations will also be obtained due to the dispersion of the AB reactive groups (i.e. amines and carboxylic acid functions) throughout its overall structure. Optimal function of the antibody is guaranteed in case the Fab region is oriented towards the body environment. In other words, ideally, the AB should be attached onto the material surface via its Fc region. In this way, the Fab binding site will be maximally available to bind the endothelial cell's VE-cadherin. To study the orientation of the immobilized antibodies onto PLMA and PMMAPEG, radiolabeling experiments were conducted with two distinct secondary antibodies (antigens in this case). The first one specifically binds the Fab binding sites of VE-cadherin AB, whereas the second one the Fc region. In other words, a successful oriented immobilization of AB should be reflected in the results by a higher amount of bound anti-Fab secondary AB and a lower amount of anti-Fc secondary AB.
Apart from the PDA and AEMA (EDC)-based AB immobilization strategies, an alternative immobilization route, which should allow for oriented AB immobilization was included in the current study. This route, as depicted in figure 4.18 (B), consisted of four different steps. After introduction of primary amines onto the surface via the post-plasma grafting of AEMA (step 1), the amines were reacted with a (succinimidyl-6-hydrazino-nicotinamide) heterobifunctional crosslinker (S-Hynic) to introduce hydrazide functions on the surface (step 2). Next, carbohydrate moieties, which are exclusively present in the Fc part of the antibody were oxidized to aldehyde functionalities, using sodium periodate ($NaIO_4$) (step 3). In this last step, there is aimed at breaking the carbon-carbon bond between two adjacent hydroxyl functions in the sugar unit. Herein, it is important to use a $NaIO_4$ solution with a concentration higher than 10 mM. Lower concentrations will only result in the selective oxidation of sialic acid residues [83]. Finally, to couple the AB with the surface, the reactive surface hydrazide functionalities were reacted with the aldehyde functions of the oxidized AB (step 4).

The results (figure 4.18, C and D) showed that in case of PMMAPEG, high aspecific adsorptions of anti-Fab and anti-Fc VE-cad AB were manifested onto the blank material and to a higher extent compared to PLMA. For all PMMAPEG modifications, a higher amount of anti-Fc secondary AB was detected compared to the anti-Fab one, although, for the PDA functionalized surfaces, this difference was not significant. For the AEMA functionalized surfaces, significantly higher amounts of anti-Fab and anti-Fc secondary VE-cad AB's were detected compared to the PDA functionalized ones. This suggests a higher availability of the

AB binding sites in case the AB is immobilized via an AEMA-based coupling. The same conclusion could be made for the AEMA modified PLMA samples.

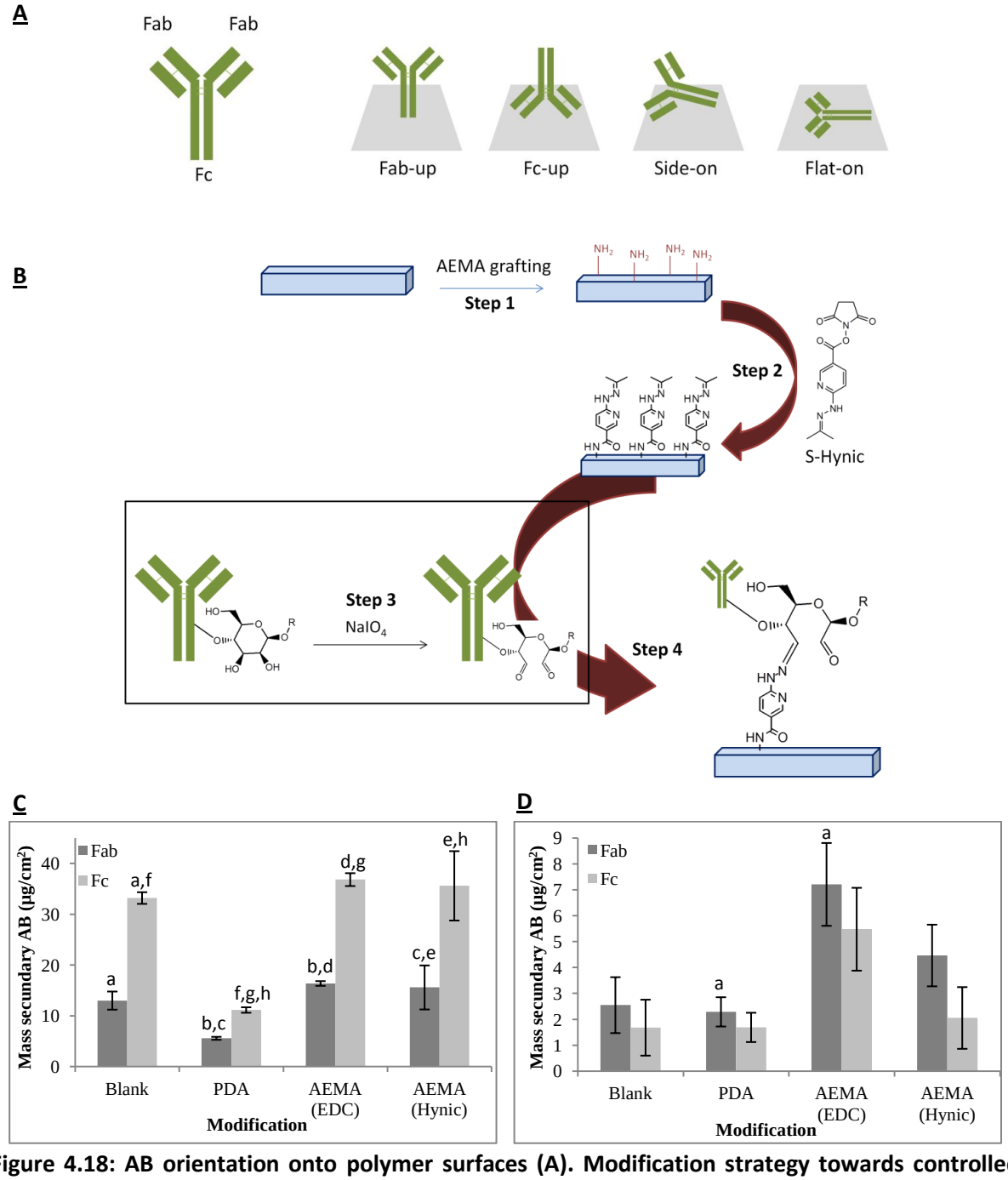

Figure 4.18: AB orientation onto polymer surfaces (A). Modification strategy towards controlled antibody orientation (B). Evaluation of the AB orientation onto PDA and AEMA functionalized PMMAPEG (C) and PLMA (D) surfaces.

For PMMAPEG, the application of the oriented AB immobilization strategy did however not result in a significant preference towards anti-Fab secondary AB binding. On the contrary, it appeared that all the modifications resulted in a preferred Fc-up orientation of the

immobilized AB's. In case of PLMA, the EDC-crosslinked AB's resulted in the highest amount of Fab-up immobilization ($p<0.05$). Furthermore, no distinct preference towards anti-Fab secondary AB bonding was experienced in case the oriented AB immobilization was executed. In case of PLMA, the Fc-up/Fab-up AB distribution is approximated by 50%/50%, whereas for PMMAPEG less than 30% of the AB's were present in the desired Fab-up orientation.
It can be concluded that the availability of the AB binding sites can still be improved. As a consequence, the evaluation of improved or alternative AB binding strategies could be the topic of future research.

4.4. Conclusion

In the present chapter, the biofunctionalization of PDA and AEMA functionalized surfaces was established.
First, a universal modification strategy was developed which enhances the cell-adhesive properties of implant materials. To this end, the combination of PDA and gelatin B was applied onto PMMA and a PEG-based methacrylate material, which is characterized by a ten-fold lower E-modulus. Application of this bi-layer system revealed similar cell-interactivities irrespective of the underlying substrate material's (physico)chemistry. Furthermore, both PMMAPEG and PMMA required a gelatin B adlayer on the PDA-modified samples to yield similar cell adhesion properties. Furthermore, if PDA/Gel B was applied onto different PMMAPEG-based materials with varying elasticity moduli, similar numbers of cell focal adhesions were obtained, which again stresses the universal character of this coating.

In the second part, VE-cad AB and VEGF were immobilized onto PDA and AEMA functionalized surfaces. In the former case, successful immobilization of both AB and VEGF was accomplished, as proven by XPS and radiolabeling experiments. Maximized HUVEC adhesion was obtained in case both angiogenic factors were immobilized and it was proven that a combined effect existed between both factors.
In case of AEMA-functionalized surfaces, similar conclusions could be drawn, although for the latter, the occurrence of a positive combined effect was not evident. In case of single angiogenic factor immobilization, increased cell densities and cell adhesions were observed if AB's were immobilized as compared to VEGF, although no statistical confirmation could be delivered for this finding. Based on XPS and radiolabeling measurements, no unambiguous preference could be observed amongst the different EDC-based immobilization protocols and it was suggested that for all conditions, the aspecific adsorption of the angiogenic factors masked the covalent linkage of these factors.
As mentioned earlier, future studies could focus on 2D angiogenesis and migration assays or gene expression during which different factors controlling angiogenesis (such as VWF, VEGF and ICAM 1), could be evaluated and quantified, in order to better simulate and understand the *in vitro* and *in vivo* response. Furthermore, the release of angiogenic factors over time,

due to the aspecific ad- and absorptions, should be further investigated in an *in vitro* and *in vivo* setting.

Based on an orientation study of the immobilized antibodies, it could be concluded that AB immobilization onto AEMA-functionalized surfaces resulted in an increased accessibility of the AB towards antigen binding, compared to antibodies immobilized onto PDA. If PMMAPEG was used as a substrate material for oriented AB immobilization, less than 30% of the antibodies were Fab-up oriented, whereas for PLMA, this amount was increased towards 50%. Based on these results, successful orientation of the antibody was not yet accomplished. Nevertheless, further investigation of the AB orientation dependent cell behavior would be an interesting topic for future research studies.

4.5. References

1. Baziwane, D., and He, Q. A. (2003) Gelatin: The Paramount food additive, *Food Reviews International* 19, 423-435.
2. America, G. M. I. o. (2012) Gelatin Handbook.
3. Karim, A. A., and Bhat, R. (2009) Fish gelatin: properties, challenges, and prospects as an alternative to mammalian gelatins, *Food Hydrocolloids* 23, 563-576.
4. Rao, K. P. (1995) Recent developments of collagen-based materials for medical applications and drug delivery systems, *Journal of Biomaterials Science-Polymer Edition* 7, 623-645.
5. Kretlow, J. D., Klouda, L., and Mikos, A. G. (2007) Injectable matrices and scaffolds for drug delivery in tissue engineering, *Advanced Drug Delivery Reviews* 59, 263-273.
6. Vandelli, M. A., Romagnoli, M., Monti, A., Gozzi, M., Guerra, P., Rivasi, F., and Forni, F. (2004) Microwave-treated gelatin microspheres as drug delivery system, *Journal of controlled release* 96, 67-84.
7. Tabata, Y., and Ikada, Y. (1998) Protein release from gelatin matrices, *Advanced Drug Delivery Reviews* 31, 287-301.
8. Ulubayram, K., Cakar, A. N., Korkusuz, P., Ertan, C., and Hasirci, N. (2001) EGF containing gelatin-based wound dressings, *Biomaterials* 22, 1345-1356.
9. Balakrishnan, B., Mohanty, M., Umashankar, P. R., and Jayakrishnan, A. (2005) Evaluation of an in situ forming hydrogel wound dressing based on oxidized alginate and gelatin, *Biomaterials* 26, 6335-6342.
10. Draye, J. P., Delaey, B., Van de Voorde, A., Van Den Bulcke, A., De Reu, B., and Schacht, E. (1998) In vitro and in vivo biocompatibility of dextran dialdehyde cross-linked gelatin hydrogel films, *Biomaterials* 19, 1677-1687.
11. Sirova, M., Van Vlierberghe, S., Matyasova, V., Rossmann, P., Schacht, E., Dubruel, P., and Rihova, B. (2014) Immunocompatibility evaluation of hydrogel-coated polyimide implants for applications in regenerative medicine, *Journal of Biomedical Materials Research Part A* 102, 1982-1990.
12. Klueh, U., Dorsky, D. I., and Kreutzer, D. L. (2005) Enhancement of implantable glucose sensor function in vivo using gene transfer-induced neovascularization, *Biomaterials* 26, 1155-1163.
13. Ward, W. K., Wood, M. D., Casey, H. M., Quinn, M. J., and Federiuk, I. F. (2004) The effect of local subcutaneous delivery of vascular endothelial growth factor on the function of a chronically implanted amperometric glucose sensor, *Diabetes Technology & Therapeutics* 6, 137-145.

14. Abraham, J. A., Mergia, A., Whang, J. L., Tumolo, A., Friedman, J., Hjerrild, K. A., Gospodarowicz, D., and Fiddes, J. C. (1986) Nucleotide sequence of a bovine clone encoding the angiogenic protein, basic fibroblast growth factor, *Science* 233, 545-548.
15. Soker, S., Machado, M., and Atala, A. (2000) Systems for therapeutic angiogenesis in tissue engineering, *World Journal of Urology* 18, 10-18.
16. Zisch, A. H., Lutolf, M. P., and Hubbell, J. A. (2003) Biopolymeric delivery matrices for angiogenic growth factors, *Cardiovascular Pathology* 12, 295-310.
17. Richardson, T. P., Peters, M. C., Ennett, A. B., and Mooney, D. J. (2001) Polymeric system for dual growth factor delivery, *Nature Biotechnology* 19, 1029-1034.
18. Hariawala, M. D., Horowitz, J. R., Esakof, D., Sheriff, D. D., Walter, D., Keyt, B., Isner, J. M., and Symes, J. F. (1996) VEGF improves myocardial blood flow but produces EDRF-mediated hypotension in porcine hearts, *Journal of Surgical Research* 63, 77-82.
19. Ho, Y.-C., Mi, F.-L., Sung, H.-W., and Kuo, P.-L. (2009) Heparin-functionalized chitosan-alginate scaffolds for controlled release of growth factor, *International Journal of Pharmaceutics* 376, 69-75.
20. Zisch, A. H., Schenk, U., Schense, J. C., Sakiyama-Elbert, S. E., and Hubbell, J. A. (2001) Covalently conjugated VEGF-fibrin matrices for endothelialization, *Journal of controlled release* 72, 101-113.
21. Ishihara, M., Obara, K., Ishizuka, T., Fujita, M., Sato, M., Masuoka, K., Saito, Y., Yura, H., Matsui, T., Hattori, H., Kikuchi, M., and Kurita, A. (2003) Controlled release of fibroblast growth factors and heparin from photocrosslinked chitosan hydrogels and subsequent effect on in vivo vascularization, *Journal of Biomedical Materials Research Part A* 64A, 551-559.
22. Park, Y. J., Lee, Y. M., Park, S. N., Sheen, S. Y., Chung, C. P., and Lee, S. J. (2000) Platelet derived growth factor releasing chitosan sponge for periodontal bone regeneration, *Biomaterials* 21, 153-159.
23. Chan, T. R., Stahl, P. J., Li, Y., and Yu, S. M. (2015) Collagen-gelatin mixtures as wound model, and substrates for VEGF-mimetic peptide binding and endothelial cell activation, *Acta Biomaterialia* 15, 164-172.
24. Takemoto, S., Morimoto, N., Kimura, Y., Taira, T., Kitagawa, T., Tomihata, K., Tabata, Y., and Suzuki, S. (2008) Preparation of Collagen/Gelatin Sponge Scaffold for Sustained Release of bFGF, *Tissue Engineering Part A* 14, 1629-1638.
25. Shen, Y. H., Shoichet, M. S., and Radisic, M. (2008) Vascular endothelial growth factor immobilized in collagen scaffold promotes penetration and proliferation of endothelial cells, *Acta Biomaterialia* 4, 477-489.
26. Chiu, L. L. Y., and Radisic, M. (2010) Scaffolds with covalently immobilized VEGF and Angiopoietin-1 for vascularization of engineered tissues, *Biomaterials* 31, 226-241.
27. Ito, Y., Hasuda, H., Terai, H., and Kitajima, T. (2005) Culture of human umbilical vein endothelial cells on immobilized vascular endothelial growth factor, *Journal of Biomedical Materials Research Part A* 74A, 659-665.
28. Ito, Y., Liu, S. Q., and Imanishi, Y. (1991) Enhancement of cell-growth on growth factor-immobilized polymer film, *Biomaterials* 12, 449-453.
29. Kim, E. J., Kang, I. K., Jang, M. K., and Park, Y. B. (1998) Preparation of insulin-immobilized polyurethanes and their interaction with human fibroblasts, *Biomaterials* 19, 239-249.
30. Beijk, M. A. M., Klomp, M., Verouden, N. J. W., van Geloven, N., Koch, K. T., Henriques, J. P. S., Baan, J., Vis, M. M., Scheunhage, E., Piek, J. J., Tijssen, J. G. P., and de Winter, R. J. (2010) Genous (TM) endothelial progenitor cell capturing stent vs. the Taxus Liberte stent in patients with de novo coronary lesions with a high-risk of coronary restenosis: a randomized, single-centre, pilot study, *European Heart Journal* 31, 1055-1064.

31. Lim, W.-H., Seo, W.-W., Choe, W., Kang, C.-K., Park, J., Cho, H.-J., Kyeong, S., Hur, J., Yang, H.-M., Cho, H.-J., Lee, Y.-S., and Kim, H.-S. (2011) Stent Coated With Antibody Against Vascular Endothelial-Cadherin Captures Endothelial Progenitor Cells, Accelerates Re-Endothelialization, and Reduces Neointimal Formation, *Arteriosclerosis Thrombosis and Vascular Biology* 31, 2798-U2141.
32. Lee, H., Dellatore, S. M., Miller, W. M., and Messersmith, P. B. (2007) Mussel-Inspired Surface Chemistry for Multifunctional Coatings, *Science* 318.
33. Zhu, L.-P., Jiang, J.-H., Zhu, B.-K., and Xu, Y.-Y. (2011) Immobilization of Bovine Serum Albumin onto Porous Polyethylene Membranes using Strongly Attached Polydopamine as a Spacer, *Colloids and Surfaces B-Biointerfaces* 86, 111-118.
34. Tao, H., Shi, Z. L., Ning, F., Neoh, K. G., Kang, E. T., and Chan, V. (2009) The effect of adhesive ligands on bacterial and fibroblast adhesions to surfaces, *Biomaterials* 30.
35. Lee, H., Rho, J., and Messersmith, P. B. (2009) Facile Conjugation of Biomolecules onto Surfaces via Mussel Adhesive Protein Inspired Coatings, *Advanced Materials* 21, 431-434.
36. Jiang, J.-H., Zhu, L.-P., Li, X.-L., Xu, Y.-Y., and Zhu, B.-K. (2010) Surface modification of PE porous membranes based on the strong adhesion of polydopamine and covalent immobilization of heparin, *Journal of Membrane Science* 364, 194-202.
37. You, I., You, S., Kang, Y., Byun, H., and Lee. (2011) Enhancement of Blood Compatibility of Poly(urethane) Substrates by Mussel-Inspired Adhesive Heparin Coating, *Bioconjugate chemistry* 22, 1264-1269.
38. Bernsmann, F., Frisch, B., Ringwald, C., and Ball, V. (2010) Protein adsorption on dopamine-melanin films: Role of electrostatic interactions inferred from zeta-potential measurements versus chemisorption, *Journal of Colloid and Interface Science* 344, 54-60.
39. Poh, C. K., Shi, Z., Lim, T. Y., Neoh, K. G., and Wang, W. (2010) The effect of VEGF functionalization of titanium on endothelial cells in vitro, *Biomaterials* 31, 1578-1585.
40. Wan, Y., Zhang, D., Wang, Y., Qi, P., and Hou, B. (2011) Direct immobilisation of antibodies on a bioinspired architecture as a sensing platform, *Biosensors & Bioelectronics* 26, 2595-2600.
41. Shen, W., Cai, K., Yang, Z., Yan, Y., Yang, W., and Liu, P. (2012) Improved endothelialization of NiTi alloy by VEGF functionalized nanocoating, *Colloids and Surfaces B-Biointerfaces* 94, 347-353.
42. Shin, Y. M., Lee, Y. B., Kim, S. J., Kang, J. K., Park, J.-C., Jang, W., and Shin, H. (2012) Mussel-Inspired Immobilization of Vascular Endothelial Growth Factor (VEGF) for Enhanced Endothelialization of Vascular Grafts, *Biomacromolecules* 13, 2020-2028.
43. Lee, Y. B., Shin, Y. M., Lee, J.-h., Jun, I., Kang, J. K., Park, J.-C., and Shin, H. (2012) Polydopamine-mediated immobilization of multiple bioactive molecules for the development of functional vascular graft materials, *Biomaterials* 33, 8343-8352.
44. Luo, R., Tang, L., Wang, J., Zhao, Y., Tu, Q., Weng, Y., Shen, R., and Huang, N. (2013) Improved immobilization of biomolecules to quinone-rich polydopamine for efficient surface functionalization, *Colloids and Surfaces B-Biointerfaces* 106, 66-73.
45. Kang, K., Choi, I. S., and Nam, Y. (2011) A biofunctionalization scheme for neural interfaces using polydopamine polymer, *Biomaterials* 32, 6374-6380.
46. Vanderleyden, E., Van Bael, S., Chai, Y. C., Kruth, J. P., Schrooten, J., and Dubruel, P. (2014) Gelatin functionalised porous titanium alloy implants for orthopaedic applications, *Materials Science & Engineering C-Materials for Biological Applications* 42, 396-404.
47. Schweikl, H., Mueller, R., Englert, C., Hiller, K.-A., Kujat, R., Nerlich, M., and Schmalz, G. (2007) Proliferation of osteoblasts and fibroblasts on model surfaces of varying roughness and surface chemistry, *Journal of Materials Science-Materials in Medicine* 18, 1895-1905.
48. Ho, Q.-P., Wang, S.-L., and Wang, M.-J. (2011) Creation of Biofunctionalized Micropatterns on Poly(methyl methacrylate) by Single-Step Phase Separation Method, *Acs Applied Materials & Interfaces* 3, 4496-4503.
49. Ku, S. H., Lee, J. S., and Park, C. B. (2010) Spatial Control of Cell Adhesion and Patterning through Mussel-Inspired Surface Modification by Polydopamine, *Langmuir* 26, 15104-15108.

50. Ku, S. H., and Park, C. B. (2010) Human endothelial cell growth on mussel-inspired nanofiber scaffold for vascular tissue engineering, *Biomaterials* 31, 9431-9437.
51. Ku, S. H., Ryu, J., Hong, S. K., Lee, H., and Park, C. B. (2010) General Functionalization Route for Cell Adhesion on Non-Wetting Surfaces, *Biomaterials* 31, 2535-2541.
52. Dalsin, J. L., Hu, B. H., Lee, B. P., and Messersmith, P. B. (2003) Mussel Adhesive Protein Mimetic Polymers for the Preparation of Nonfouling Surfaces, *Journal of the American Chemical Society* 125, 4253-4258.
53. Farruggia, B., Nerli, B., Di Nuci, H., Rigatusso, R., and Pico, G. (1999) Thermal features of the bovine serum albumin unfolding by polyethylene glycols, *International Journal of Biological Macromolecules* 26, 23-33.
54. Farruggia, B., Garcia, G., Dangelo, C., and Pico, G. (1997) Destabilization of human serum albumin by polyethylene glycols studied by thermodynamical equilibrium and kinetic approaches, *International Journal of Biological Macromolecules* 20, 43-51.
55. Geiger, B., Bershadsky, A., Pankov, R., and Yamada, K. M. (2001) Transmembrane extracellular matrix-cytoskeleton crosstalk, *Nature Reviews Molecular Cell Biology* 2, 793-805.
56. Gentile, F., Tirinato, L., Battista, E., Causa, F., Liberale, C., di Fabrizio, E. M., and Decuzzi, P. (2010) Cells preferentially grow on rough substrates, *Biomaterials* 31, 7205-7212.
57. Desmet, T. (2013) *The Surface Modification of Porous Biodegradable Scaffolds for Tissue Engineering, Produced by Rapid Prototyping.*, https://biblio.ugent.be/record/4337218, Gent.
58. Yeung, T., Georges, P. C., Flanagan, L. A., Marg, B., Ortiz, M., Funaki, M., Zahir, N., Ming, W., Weaver, V., and Janmey, P. A. (2005) Effects of substrate stiffness on cell morphology, cytoskeletal structure, and adhesion, *Cell motility and the cytoskeleton* 60, 24-34.
59. Nemir, S., and West, J. L. (2010) Synthetic Materials in the Study of Cell Response to Substrate Rigidity, *Annals of Biomedical Engineering* 38, 2-20.
60. Discher, D. E., Janmey, P., and Wang, Y. L. (2005) Tissue cells feel and respond to the stiffness of their substrate, *Science* 310, 1139-1143.
61. Wells, R. G. (2008) The role of matrix stiffness in regulating cell behavior, *Hepatology* 47, 1394-1400.
62. Reinhart-King, C. A. (2011) How Matrix Properties Control the Self-Assembly and Maintenance of Tissues, *Annals of Biomedical Engineering* 39, 1849-1856.
63. Pelham, R. J., and Wang, Y. L. (1997) Cell locomotion and focal adhesions are regulated by substrate flexibility, *Proceedings of the National Academy of Sciences of the United States of America* 94, 13661-13665.
64. Bott, K., Upton, Z., Schrobback, K., Ehrbar, M., Hubbell, J. A., Lutolf, M. P., and Rizzi, S. C. (2010) The effect of matrix characteristics on fibroblast proliferation in 3D gels, *Biomaterials* 31, 8454-8464.
65. Fioretta, E. S., Fledderus, J. O., Baaijens, F. P. T., and Bouten, C. V. C. (2012) Influence of substrate stiffness on circulating progenitor cell fate, *Journal of Biomechanics* 45, 736-744.
66. Califano, J. P., and Reinhart-King, C. A. (2008) A Balance of Substrate Mechanics and Matrix Chemistry Regulates Endothelial Cell Network Assembly, *Cellular and Molecular Bioengineering* 1, 122-132.
67. Bhatia, S. K., Shriverlake, L. C., Prior, K. J., Georger, J. H., Calvert, J. M., Bredehorst, R., and Ligler, F. S. (1989) Use of thiol-terminal silanes and heterobifunctional crosslinkers for immobilization of antibodies on silica surfaces, *Analytical Biochemistry* 178, 408-413.
68. Danczyk, R., Krieder, B., North, A., Webster, T., HogenEsch, H., and Rundell, A. (2003) Comparison of antibody functionality using different immobilization methods, *Biotechnology and Bioengineering* 84, 215-223.
69. Brogan, K. L., Wolfe, K. N., Jones, P. A., and Schoenfisch, M. H. (2003) Direct oriented immobilization of F (ab') antibody fragments on gold, *Analytica Chimica Acta* 496, 73-80.

70. Ikeda, T., Ikeda, Y., Hata, K.-i., Ninomiya, Y., Ikura, K., Takeguchi, S., Aoyagi, R., Hirota, A., and Kuroda. (2009) Oriented immobilization of antibodies on a silicon wafer using Si-tagged protein A, *Analytical Biochemistry* 385, 132-137.
71. Vashist, S. K., Dixit, C. K., MacCraith, B. D., and O'Kennedy, R. (2011) Effect of antibody immobilization strategies on the analytical performance of a surface plasmon resonance-based immunoassay, *Analyst* 136, 4431-4436.
72. Vashist, S. K., Schneider, E. M., Lam, E., Hrapovic, S., and Luong, J. H. (2014) One-step antibody immobilization-based rapid and highly-sensitive sandwich ELISA procedure for potential in vitro diagnostics, *Scientific reports* 4.
73. Chiu, L. L. Y., Weisel, R. D., Li, R.-K., and Radisic, M. (2011) Defining conditions for covalent immobilization of angiogenic growth factors onto scaffolds for tissue engineering, *Journal of Tissue Engineering and Regenerative Medicine* 5, 69-84.
74. Buddy D. Ratner, A. S. H., Frederick J. Schoen, Jack E. Lemons, (Ed.) (2004) *Biomaterials Science.*, Second edition ed., Elsevier.
75. Wiseman, M. E., and Frank, C. W. (2012) Antibody Adsorption and Orientation on Hydrophobic Surfaces, *Langmuir* 28, 1765-1774.
76. Gavard, J., and Gutkind, J. S. (2006) VEGF controls endothelial-cell permeability by promoting the beta-arrestin-dependent endocytosis of VE-cadherin, *Nature Cell Biology* 8, 1223-U1217.
77. West, J. L., and Moon, J. J. (2008) Vascularization of engineered tissues: approaches to promote angiogenesis in biomaterials, *Current topics in medicinal chemistry* 8, 300-310.
78. Staros, J. V., Wright, R. W., and Swingle, D. M. (1986) Enhancement by N-hydroxysulfosuccinimide of water-soluble carbodiimide-mediated coupling reactions, *Analytical Biochemistry* 156, 220-222.
79. Sanz, V., Conde, J., Hernandez, Y., Baptista, P. V., Ibarra, M. R., and de la Fuente, J. M. (2012) Effect of PEG biofunctional spacers and TAT peptide on dsRNA loading on gold nanoparticles, *Journal of Nanoparticle Research* 14.
80. Wissink, M. J. B., Beernink, R., Pieper, J. S., Poot, A. A., Engbers, G. H. M., Beugeling, T., van Aken, W. G., and Feijen, J. (2001) Immobilization of heparin to EDC/NHS-crosslinked collagen. Characterization and in vitro evaluation, *Biomaterials* 22, 151-163.
81. Vashist, S. K. (2012) Comparison of 1-ethyl-3-(3-dimethylaminopropyl) carbodiimide based strategies to crosslink antibodies on amine-functionalized platforms for immunodiagnostic applications, *Diagnostics* 2, 23-33.
82. Conde, J., Baptista, P. V., Hernandez, Y., Sanz, V., and de la Fuente, J. M. (2012) Modification of plasmid DNA topology by 'histone-mimetic' gold nanoparticles, *Nanomedicine* 7, 1657-1666.
83. Hermanson, G. T., (Ed.) (1996) *Bioconjugate Techniques*, Pierce Chemical Company, Rockford, Illinois.
84. Desmet, T., Billiet, T., Berneel, E., Cornelissen, R., Schaubroeck, D., Schacht, E., and Dubruel, P. (2010) Post-Plasma Grafting of AEMA as a Versatile Tool to Biofunctionalise Polyesters for Tissue Engineering, *Macromol. Biosci.* 10, 1484-1494.
85. Heng, B. C., Bezerra, P. P., Meng, Q. R., Chin, D. W.-L., Koh, L. B., Li, H., Zhang, H., Preiser, P. R., Boey, F. Y.-C., and Venkatraman, S. S. (2010) Adhesion, proliferation, and gene expression profile of human umbilical vein endothelial cells cultured on bilayered polyelectrolyte coatings composed of glycosaminoglycans, *Biointerphases* 5, FA53-FA62.
86. Gellynck, K. (2013) Glucosens; Enabling technologies for continuous glucose monitoring using implantable single-chip optical sensors, *Final IWT-report* Chapter 6.3: Task 4.2: *In vitro* biocompatibility testing of the materials.
87. Couston, R. G., Skoda, M. W., Uddin, S., and van der Walle, C. F. (2013) Adsorption behavior of a human monoclonal antibody at hydrophilic and hydrophobic surfaces, *Mabs* 5, 126-139.

Chapter 5

In vivo evaluation of a biofunctionalized methacrylate-based packaging for an optical glucose sensor

Parts of this chapter have been published in:

Gellynck, K.; Kodeck, V.; Van De Walle, E.; Kersemans, K.; De Vos, F.; Declercq, H.; Dubruel, P.; Vlaminck, L.; Cornelissen, M., First step toward near-infrared continuous glucose monitoring: *in vivo* evaluation of antibody coupled biomaterials. *Experimental Biology and Medicine* **2015,** *240* (4), 446-457.

5.1. Introduction

The previous chapter has indicated that surface biofunctionalization of the polymer packaging with growth factors and especially antibodies induced a positive *in vitro* cell response, which was reflected by high cell viabilities and cell adhesion characteristics. Due to this promising outcome, it was justified to further characterize the materials for their *in vivo* behavior. To this end, an appropriate animal model needed to be selected. Spontaneous diabetes occurs in many animal species. In addition, upon the application of experimental methods such as the administration of alloxan or streptozotocin, many animals can be made diabetic. Previously, both spontaneous and experimental animal models have been used to study the etiologies, complications, treatments and prevention of diabetes [1]. Examples of such animal models include rats, mice, dogs, rabbits and hamsters [1-3]. In the current work, based on the sensor design which includes rather large sensor implants (a maximum of 2 cm in ϕ and 6 mm thickness), small animal models such as rats and hamsters could not be considered. As a consequence, bigger mammals had to be chosen. Since goats are appreciated as social animals and as 'easy to handle', they were selected as the preferred animal model. Nevertheless, for the *in vivo* evaluation of the developed materials and their surface modifications, rats were also included in this work.

Since we aimed at developing a glucose sensor which operates for longer implantation times, all goat implantation experiments were conducted for a minimum of 1 month. Previously, the subcutaneous implantation of an enzymatic glucose sensor resulted in successful long-term *in vivo* glucose measurements. Herein, with the help of a radiotransmitter, glucose values were recorded for a sensor life time of 3-5 months in dogs [4]. Furthermore, in pigs, these values could be recorded for longer than 1 year [5]. Nevertheless, in humans, the currently applied glucose sensors such as the GlucoDay, a microdialysis-based sensor, enable continuous glucose measurements for a period of only 48 hours [6-7].

This fact clearly shows the need for new continuous glucose sensors, which operate for longer periods in an *in vivo* setting. In this work, the use of an optical sensor design is evaluated for the latter purpose.

In the upcoming paragraphs, the production of the implantable sensors will be discussed, followed by the *in vivo* evaluation of the developed blank and biofunctionalized methacrylate-based packaging materials[1]. Herein, special attention is paid to the induced tissue response and vascularization around the implanted materials. In a last step, the sensor design will be evaluated in an *in vivo* and *in vitro* setting for its glucose detection capacity.

It should be mentioned that, from a polymer perspective, only the PMMAPEG-based materials were evaluated in the forthcoming *in vivo* experiments. Interestingly, the PLMA-

[1] All implantations in goats were performed by Lieven Vlaminck, from the Department of Surgery and Anaesthesiology of Domestic Animals. The rat implantation studies and histological evaluations, on the other hand were performed by Greet De Smet, Lise De Moor and Karolien Gellynck, at the Tissue Engineering Group of the Department of Basic Medical Sciences, under supervision of Prof. Maria Cornelissen. All optical, evaluations during the *in vivo* studies were performed by Ronny Bockstaele, the project leader of GlucoSens. Furthermore, he also guided the protein and glucose analyses, in cooperation with Prof. Joris Delanghe, a clinical chemist at UZ (University hospital) of Ghent.

based materials could also have offered a good (or even superior) alternative, but at the time of the planned *in vivo* experiments, these materials were not yet available. For the same reason, only the PDA surface activation and VE-cad AB biofunctionalization strategy were included in the *in vivo* assays.

5.2. Development of a UV-transparent mold for the production of dummy and fiber-embedded donut-shaped implants

As introduced in chapter 1, the sensor design requires a donut-shaped sensor packaging. Since the polymer packaging is developed via photo polymerization, a UV-transparent mold had to be designed and applied. Due to the more complex shape of the final mold compared to the polymerization set-up discussed in chapter 2, no teflon release foil could be used to assure the release of the polymers after production. As a consequence, an appropriate UV-transparent material that does not react with the MMA-based material had to be used. Since plexiglass and polycarbonate did not perform as desired, zeonex®, a cyclic olefin-based polymer was selected (transparent disks in figure 5.1 A) for all mold designs.
In case dummy, fiber-less donuts needed to be produced, a mold design as presented in figure 5.1 was used (referred to as mold design 1). Herein, the donut-shaped central cavity was created by the assembly of two UV-transparent zeonex® discs and a stainless steel (SS) ring, which determined the outer diameter of the donut (i.e. 15 mm). The inner diameter of the donut was determined by a small stainless steel tube which was mounted between the two zeonex discs (figure 5.1, A and B). To fix the different parts, they were pressed inside a brass ring and tightened with two screw rings (figure 5.1, C). To inject the monomer/initiator solution in a proper way, syringes were mounted in both needles. Herein, the first syringe was used to inject the solution, whereas the second needle/syringe was used to remove air from the central cavity in a controlled way. After injection and UV irradiation, donut-shaped samples with an outer diameter of 15 mm and a thickness of 5 mm could be created. Depending on the diameter of the used SS tube, the diameter of the central cavity could be adjusted (1 vs. 3 mm).

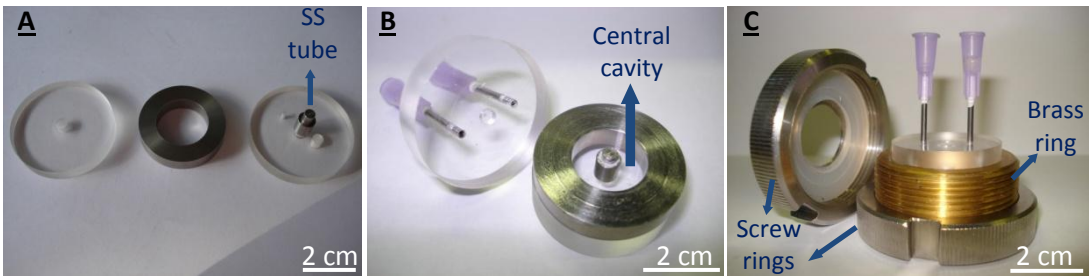

Figure 5.1: Assembly of a UV-transparent mold for the production of a dummy donut-shaped polymer packaging (mold design 1)

In case optical glass fibers needed to be embedded inside the polymer packaging, a different mold design had to be used. Figure 5.2 displays the different parts, constituting this mold (figure 5.2, A), the assembly of the mold (figure 5.2, B-D) and the final encapsulated fiber-containing implant (figure 5.2, E). Again, the central cavity of the donut-shaped implant was created by two zeonex® discs, which were separated by a stainless steel ring. Since fibers were included, space needed to be created and therefore the stainless steel ring was transversely cut. The inner diameter of 1 mm was in this case created by a SS pin which was fixed inside the zeonex® windows. In the latter design, everything was clamped by two metal rings, which also contained enough fiber space and which were tightened with screws (figure 5.2, D).

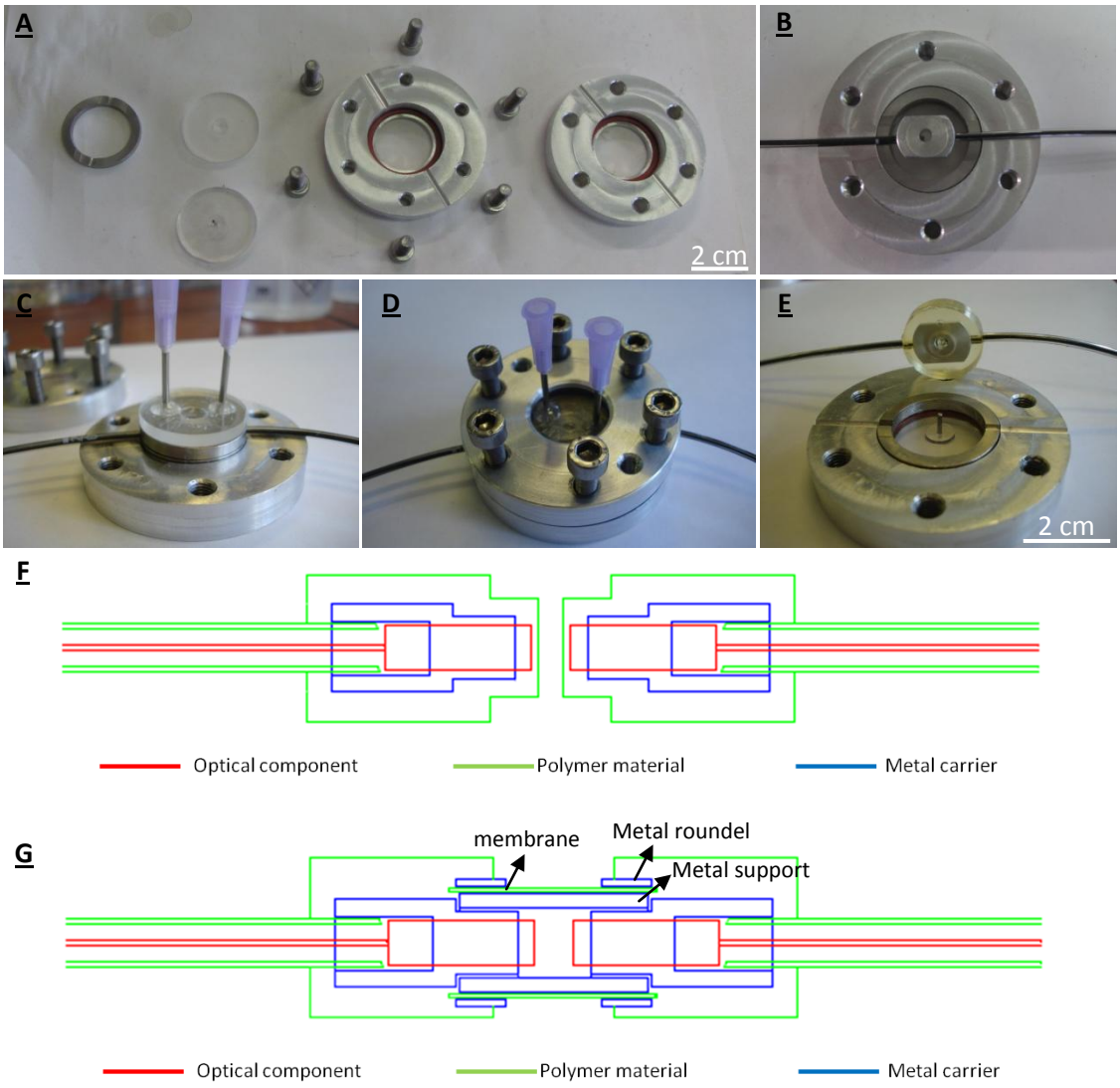

Figure 5.2: Assembly of a UV-transparent mold for the production of a donut-shaped polymer packaging, incorporating optical fibers (A-E). A cross-section of the embedded fiber construct (mold design 2) is also shown (F). Mold design 3 is identical to design 2, except for the use of PES membranes which cover the central cavity (mold design 3) (G). In this case, a metal roundel and metal perforated support were used respectively above and under the membrane as mechanical support.

Injection of the monomers and curing were conducted similarly as in the previous setup. It should be mentioned that all fibers and/or electronics, that needed to be encapsulated in the polymer packaging, first needed to be mounted and aligned onto a separate metal carrier. Otherwise, fixed positions of these compounds could not be guaranteed during the molding process. Furthermore, the fibers itself had to be protected by a poly(urethane)-based catheter, to prevent fiber fracture or damage. Application of mold design 2 resulted in implants with an outer diameter of 2 cm and a thickness of 6 mm. Due to this design, the optical light path typically consisted of 0.5 mm polymer material, followed by 1 mm air or tissue (i.e. in case of implantation) and finally again 0.5 mm polymer, before reaching the second fiber. The cross-section of the final molded implant is displayed in figure 5.2, F.

Since a central cavity was created in the previous mold designs, potential tissue in-growth and/or the influx of biological compounds such as cells and proteins might result in optical losses during glucose measurements. To study this effect, a third mold design was also included. Herein, circular polyethersulfone (PES) membranes with a molecular weight cut off at 10 kDa and a diameter of 10 mm were included [8-9]. Using this approach, low molecular weight glucose (180 Da) was able to diffuse through the membrane to reach the sensing cavity, but tissue in-growth or the influx of interfering biological compounds such as serum albumin (Mw = 67 kDa) could be prevented [10-12]. A schematic representation of the mold design is shown in figure 5.2 (G).
The production of the donuts was performed with the same mold components as represented in figure 5.2 (A). Additionally, to offer mechanical strength to the included membranes, perforated metal plates (8 mm ϕ, 0.5 mm thickness, 1 mm ϕ pores) were used as lower supports, whereas a metal roundel (10 mm outer ϕ, 5 mm inner ϕ and 0.3 mm thickness) was placed on top of the membrane. An additional advantage of this sensor design (mold design 3) included the absence of polymer in the optical path of the light beam.

5.3. Determination of the optimal implantation site: an exploratory *in vivo* study.

During a first implantation round, three different polymer formulations were implanted (2 replicates per polymer formulation) at 3 different implantation sites in three different goats. In this way, each goat was carrying 18 samples, including 6 per implantation side. The selection of the polymer networks was based on the availability of the developed packagings and on their difference in mechanical and swelling properties. An overview of the different formulations under investigation is given in table 5.1. Concerning the implantation site, subcutaneous (i.e. under the skin), intramuscular (i.e. inside a muscle) and retroperitoneal (just outside the celiac) implantations were studied and evaluated. On the other hand, intravenous (i.e. inside a blood vessel) implantations were excluded from this study because of safety and practical reasons. To be more precise, if a long-term continuous glucose sensor

would be implanted in a human blood vessel, clotting, bleeding and infection could be anticipated, which would be detrimental for the patient [13]. On the other hand, since glucose measurements in whole blood are the clinical standard, the construction of a calibration model for the interpretation of optical glucose spectra is very straightforward, because of its availability in literature. In case of glucose measurements in ISF, the biological fluid under investigation in this study, the interpretation can be more difficult. Nevertheless, it has already been shown that a clinically significant correlation exists between glucose concentrations in blood and the interstitial fluid (ISF). To be more precise, time lags of 0 (steady-state situation), 8-10 (assumed as acceptable), but also of 30 minutes have been reported and the differences are mainly due to different collection methods, experimental designs and different ISF collection sites[14-17]. The correlation can thus be assumed as unique for each sensor system and should be evaluated in detail for each example. Also in the present work, this challenge had to be tackled and an unambiguous calibration model which correlates the spectral ISF data with a glucose concentration, had to be developed. The latter was, however, beyond the scope of the current work. These aspects were tackled by co-workers at the KU (Catholic University) Leuven (under supervision of Prof. Saeys) [18].

Table 5.1: Overview of PMMAPEG formulations implanted in goats

Material	MMA (mol%)	PEGDMA (mol%)	Mn (PEGDMA) (g/mol)	E-mod (MPa)	Swelling (%)
PMMAPEG 1	50	50	550	142±40	17±1
PMMAPEG 2	50	50	750	21±1	43±1
PMMAPEG 3	85	15	550	1053±51	12±0

PMMAPEG dummy donuts (i.e. fiber-less donuts) were produced using mold design 1 (figure 5.1). The samples were implanted in three healthy, female milk goats and divided over the three implantation sites selected. After four weeks of implantation time, the donuts were explanted and the tissue clumps containing the samples were evaluated. The results showed that all samples were surrounded by a connective tissue layer. Based on the morphology of the cells and the extracellular matrix, two distinct types of these capsules could be distinguished (figure 5.3 A). In the first case (capsule 1), a sharp delineation was observed between the connective tissue capsule and both the implant and the surrounding tissue. As a consequence, the donut-shaped samples could be considered as separated from the capsule. Capsule type 1 clearly resembled a capsule characteristic for the final stage of the tissue repair process, meaning that particularly quiescent fibroblasts (i.e. fibrocytes) were present in the tissue. These fibrocytes are morphologically different from their active counterparts and are typically small, spindle-shaped cells containing a small, dark nucleus. A last characteristic of this type 1 capsule includes the presence of collagen fibres, which were visualized after hematoxylin and eosin (H&E) staining (pink color, figure 5.3, A).

In the second case (capsule 2), the connective tissue clearly resembled tissue corresponding to the active stage of the tissue repair process. Herein, a more 'ruffled' edge could be observed between the donut implant and the tissue. Furthermore, a more smooth transition

existed between the connective tissue capsule and the surrounding tissue, without clear delineations. The tissue consisted of active fibroblasts characterized by an abundant cytoplasm, a large oval pale-staining nucleus with fine euchromatic chromatin and a large nucleolus. After H&E staining, the tissue behaved less eosinophilic, which refers to a lower collagen content present in the extracellular matrix (ECM). It can be concluded that the type 2 capsule was more integrated and more preferred compared to the first one.

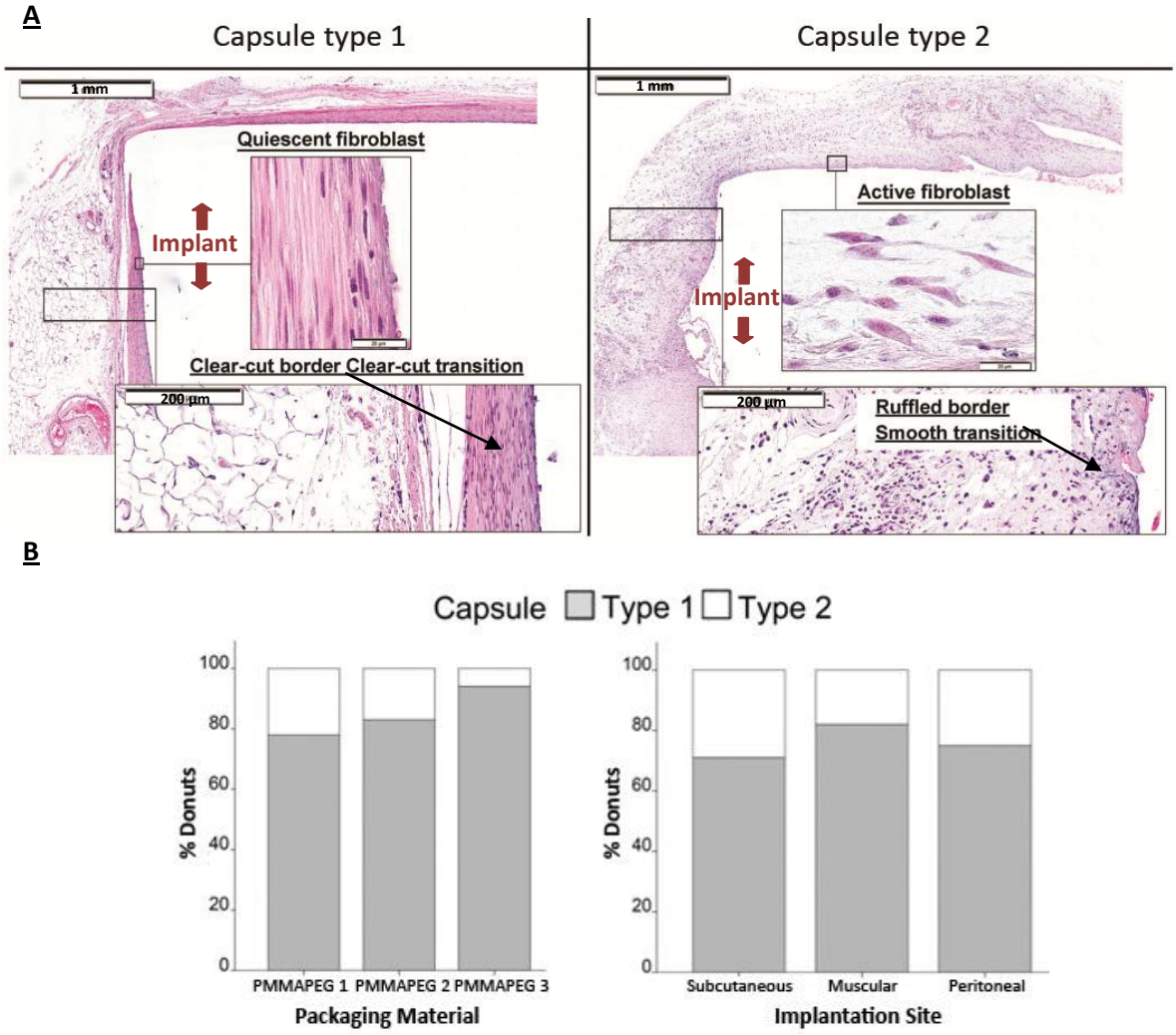

Figure 5.3: Panel A: Two types of capsule formation were observed. In case of capsule type 1, more eosinophilic fibrocytes were observed and a clear-cut border was present at the donut-capsule and capsule-tissue interfaces. On the other hand, for capsule type 2, more basophilic fibroblasts were observed, a more ruffled border was present and the capsule-tissue interface showed a smooth transition. Panel B: Distribution of the explanted samples (i.e. donuts) regarding the type of capsule surrounding them. In the left figure, the influence of the biomaterial composition is shown, whereas in the right graph, the influence of the implantation site is evaluated [19].

Apart from this general distinction, the different PMMAPEG materials were compared with regard to the type of encapsulating connective tissue. Figure 5.3 (B) shows that PMMAPEG 3 gave rise to the lowest amount of 'connective tissue capsule 2' (only 6%), followed by PMMAPEG 2 (17%) and PMMAPEG 1 (22%).

Based on this finding, PMMAPEG 1 was selected as the preferred PMMAPEG sensor packaging. Based on its physicochemical properties (see table 5.1 and chapter 2), this choice was further evidenced. Indeed, this material gave the best compromise between mechanical properties (i.e. relatively low E-modulus) and swelling behavior (i.e. low swelling %).
Concerning the implantation site, figure 5.3 (B) shows that subcutaneous implantation was preferred due to a lower amount of 'capsule 1' formation. Furthermore, from a surgical viewpoint, this selection was further supported. During the explantation process, it appeared that several of the retroperitoneal implants were migrated towards more caudally located places near the pelvic area. It is hypothesized that these migrations were caused by movement of the goat and by intestinal activity. Moreover, due to the invasive nature of these retroperitoneal implantations, its omission was more than justified.

Regarding the intramuscular implantation, some of the donuts were nicely integrated inside the muscular tissue, while others did not show any integration at all. It can be anticipated that muscle movement was responsible for this finding. As a consequence, due to the accessibility and its more reproducible nature, reflected by the appearance of mostly vascularized connective tissue, subcutaneous implantation was selected as the preferred implantation site.

5.4. *In vivo* evaluation of the surface modified PMMAPEG-based packaging material

In the next step, the pristine and surface-modified PMMAPEG materials (see chapter 3, § 3.4.2 and chapter 4, § 4.2.2) were implanted to evaluate the effect of the surface functionalization on the *in vivo* response. To this end, the nature of the tissue surrounding the implants was evaluated and particular focus was attained on the presence of blood vessels. VE-cad antibodies were immobilized to induce neo-vascularization around the implant. As a result, it could be anticipated that an increased amount of blood vessels would surround the biofunctionalized samples. Several experiments in goats and rats were conducted and will be discussed in the upcoming paragraphs.

5.4.1. *In vivo* biological experiments in goats

Similar to the exploratory *in vivo* study, donut-shaped dummy (cfr. no photonic or electronic components included) PMMAPEG implants were evaluated. More specifically, blank, PDA-modified and PDA/VE-cad AB modified (see chapter 4, §4.2.1) samples were implanted subcutaneously in three goats. In addition, VE-cad AB functionalized Gel B surfaces were included in this study. The latter combination was not fully characterized and was not mentioned in chapter 4, but at the moment of this first implantation study, it was decided by the GlucoSens partners that this condition could be considered as valuable. For the latter condition, the antibodies were immobilized onto Gel B via physisorption. Radiolabeling

experiments indicated that lower amounts of AB were immobilized onto GelB (173 ng/cm^2), compared to PDA (287 ng/cm^2). *In vivo* comparison of the latter two conditions allowed to study the effect of the used immobilization strategy on the body response.
Half of the samples were explanted after 1 month, the other half after 3 months implantation. Histological evaluation of the tissue surrounding the implants revealed that no visual differences could be observed between the different surface modifications (PDA vs PDA/VE-cad AB). However, if the blank samples were compared with the surface modified ones (figure 5.4), a more dense connective tissue could be observed for the blank samples, resembling capsule 1 (figure 5.3, A). Surface modification, on the other hand, generally resulted in superior integration, with less dense connective tissue and a smoother transition between tissues, which clearly resembled capsule 2 (figure 5.3, A).

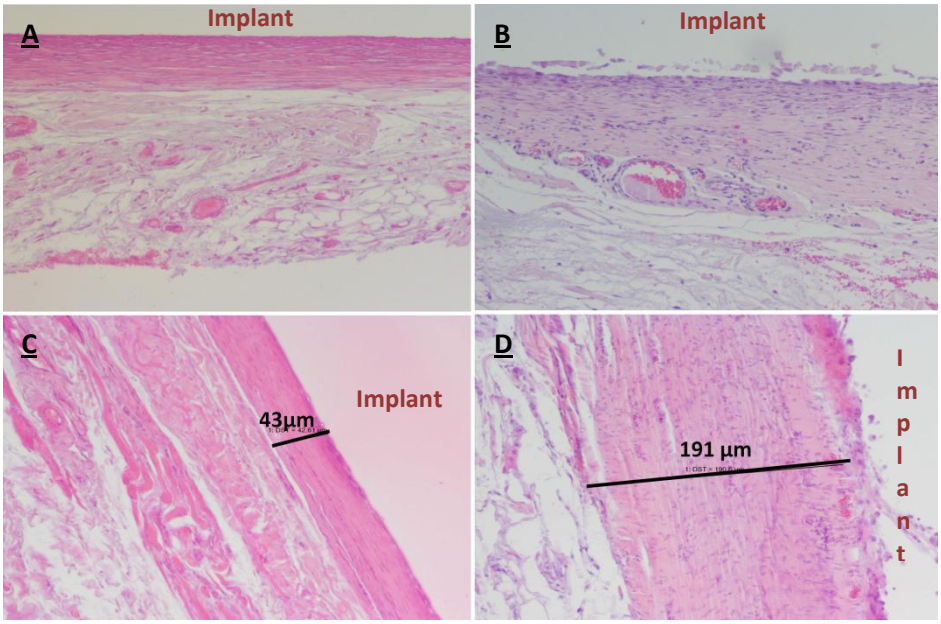

Figure 5.4 : Histological evaluation of the connective tissue surrounding the explanted unmodified (A and C) and modified (B and D) donut samples after 1 month (A and B) and 3 months (C and D) implantation. The position of the implant is indicated via 'implant'.

Nevertheless, it should be mentioned that the results depicted in figure 5.4 were not apparent for all samples. What is more, most of the samples were associated with capsule type 1, irrespective of the implantation time and the surface modification applied.
It should also be noted that, based on the presence of macrophages and lymphocytes, only minor inflammation was observed around 17% of the implants.

As pointed out in chapter 4, VE-cad AB's were immobilized on the PMMAPEG surfaces to enhance neo-vascularization via vasculogenesis. To evaluate the success of this approach, the number of blood vessels in the vicinity of the sensor were counted. Several criteria had to be met before a capillary was taken into account. In this respect, the presence of a red blood cell, an endothelial cell and a lumen were evaluated. If two of the three criteria were met and if the diameter of the blood vessel was not larger than 10 µm, the observed

structure could be classified as a capillary. Figure 5.5 (A) shows some typical examples of such capillaries.

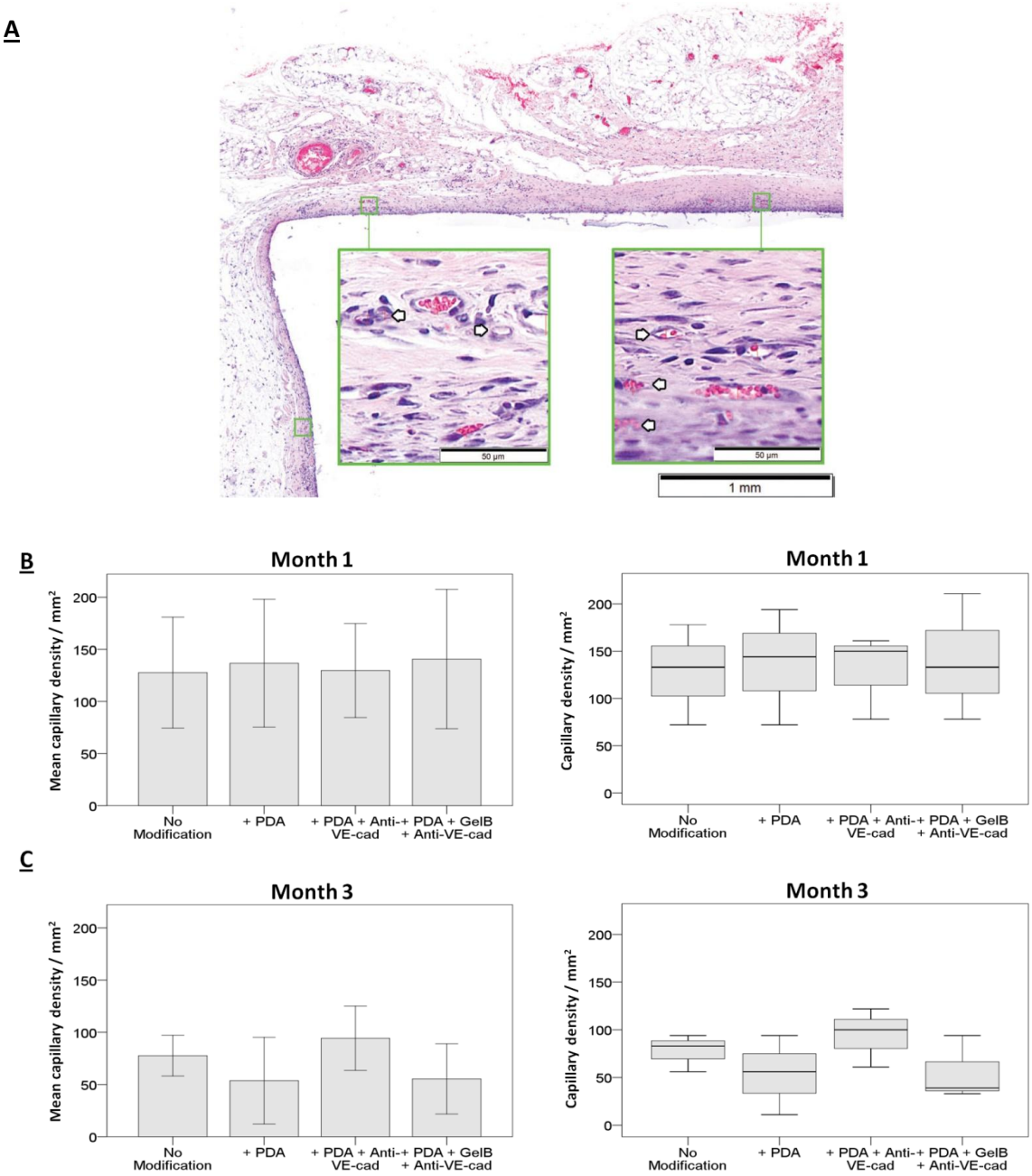

Figure 5.5: Panel A: Histological section (H&E staining) of the tissue surrounding the implant. Based on the three criteria, referred to in the text, the capillaries (indicated by arrows) could be counted. Panel B and C: Mean capillary density of the tissue surrounding the blank and modified PMMAPEG implants after 1 month (B) and after 3 months (C) implantation (left panel). The distribution of the data is represented by boxplots (right panel) [19].

The result of the evaluation of the different histological slices for the amount of capillaries is shown in figure 5.5 (B and C). After one month of implantation, no significant differences were observed for the amount of capillaries when comparing the different surface modifications applied. Furthermore, similar results were obtained for the blank, non-modified materials. After three months, based on the median capillary number, higher

amounts were counted in the vicinity of the VE-cad AB (i.e. 111/mm^2) functionalized surfaces, compared to the GelB/AB (i.e. 86/mm^2) and PDA functionalized surfaces (i.e. 83/mm^2). The latter two cases even resulted in a lower amount of capillaries compared to the blank control (i.e. 88/mm^2). Nevertheless, due to the high variation in the data distribution (see standard deviations in figure 5.5, C), none of these differences were statistically significant ($p > 0.05$).

The obtained results were in good correlation with the radiolabeling data (see higher). Indeed, the highest micro-vessel density was observed for the VE-cad AB modified samples, using PDA as functionalization platform. Based on these results, it seemed that the use of Gel B as intermediate layer did however not improve vascularization. Since the AB's were immobilized via physisorption, an enhanced availability could be anticipated. However, the obtained results showed that this effect was not manifested.

5.4.2. *In vivo* biological experiments in rats

In addition to the goat experiments, *in vivo* experiments using rats as experimental model were also performed. Since small disk samples (6 mm ϕ, 1 mm thickness) were applied in this set-up, rats could be used as animal model.

In a preliminary experiment, disks of non-modified, PDA and PDA/VE-cad AB- (4 and 40 µg/ml) modified PMMAPEG, were implanted for 28 days. After histological processing and staining with haematoxylin-eosin, the number of capillaries was counted in ten 100 µm/100 µm squares and converted to the number of capillaries/mm². Herein, the same criteria were applied to recognize blood capillaries, as indicated above (see figure 5.5, A).

In the series blank < PDA-coated < PDA/AB-coated, a slight increase in the number of capillaries was observed (figure 5.6), although, the increases were not significant ($p > 0.05$). The lower standard deviation in case of AB immobilization seemed to reveal a higher reproducibility for the capillary count. The application of a higher concentration of antibody (40 µg/ml) did, however, not augment the amount of capillaries surrounding the implant. On the contrary, a higher concentration even resulted in a significant decrease of the capillary count ($p < 0.05$). This result might be attributed to density related effects.

Based on these preliminary results, an extensive study using normal and Goto-Kakizaki rats was performed. The latter family of rats is a non-obese Wistar substrain which develops type 2 diabetes mellitus in life and which shows a congenital vascular impairment. In this study, 20 normal and 20 diabetic rats were used. Each rat contained 3 PMMAPEG-based disks, including a blank, a PDA coated sample and a PDA/VE-cad AB functionalized sample. To investigate the tissue reactions and capillary formation over time in both rat species, explantations were done 2 days, 5 days, 10 days and 25 days post-implantation. This implies that for each time point, 5 replicates were analyzed per condition (i.e. blank, PDA, PDA/VE-cad AB modified). Prior to discussing the results of capillary formation, inflammation and connective tissue formation around the implants were first evaluated.

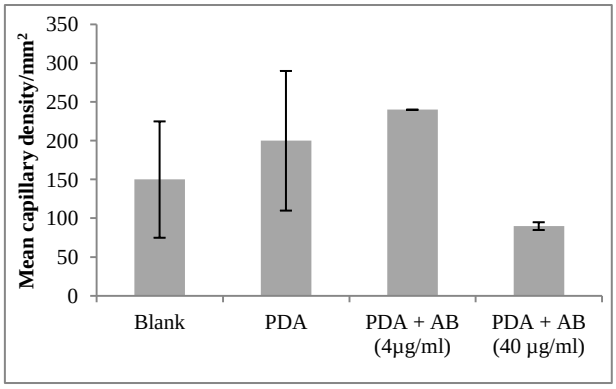

Figure 5.6: Preliminary *in vivo* test with rats. Evaluation of the number of capillaries surrounding the implanted materials after 4 weeks of implantation.

5.4.2.1. Evaluation of inflammation and connective tissue capsule formation

Similar to the goat implantation study, implantation of the test samples could evoke a body response (also see chapter 1). As previously described, this response implies that inflammation will occur and that over time, a fibrous capsule will develop around the implant.

In a first step, the inflammation of the implanted disks was studied. After 2 and 5 days, inflammation was observed by the visualization of granulocytes and macrophages. The reaction appeared equal for all conditions and it seemed that the inflammation was reduced as a function of time. Nevertheless, more inflammation was observed for the diabetic rats compared to the normal ones. In literature, similar observations have already been described for the subcutaneous [20] and the intraperitoneal [21] implantation of polyether-polyurethane sponge discs in normal and diabetic rats.

Next, the connective tissue capsule surrounding the implanted samples was evaluated for its thickness (figure 5.7). Interestingly, after 2 days, no capsule was observed yet, whereas after 5 days, measurement of the capsule thickness could be performed. Upon surface modification, the thickness of the connective tissue capsule decreased for both the diabetic and normal rats, but only for the normal rats a significant difference was obtained in case the blank (19 µm) was compared with the AB functionalized samples (15 µm) ($p<0.05$). After 10 days of implantation, similar thicknesses were obtained for the different surface modifications and this for both the normal and the diabetic rats. It can be mentioned that for both the normal and diabetic rats, the lowest capsule thickness was respectively observed for the AB functionalized surfaces (33 µm) and the control (27 µm), although, compared to the other test conditions, these differences were not significant ($p>0.05$). A similar trend was observed after 25 days. For both the normal and the diabetic rats, the thickest capsule was observed around the PDA coated samples (49 µm vs. 59 µm), followed by the AB functionalized samples (48 µm vs. 59 µm) and the controls (39 µm vs. 43 µm).

As a function of time, the capsule thus increased for both groups of rats. Statistically, for the normal rats, a significantly thicker capsule was observed after 10 days compared to 5 days of implantation for each condition (control, PDA and AB functionalized). The same applied in

case the capsules after 5 and 25 days were compared, but comparison of day 10 and day 25, only resulted in a significant difference for the PDA functionalized samples. In case of diabetic rats, comparison of the capsule after 5 and 25 days and after 10 and 25 days, resulted in a significantly thicker capsule for the longer implantation times and this for all test conditions ($p<0.05$).

Based on the data obtained after 5 and 25 days of implantation, it could be concluded that generally a thicker capsule was formed in case the samples were implanted in diabetic rats, compared to the normal rats. Nevertheless, this difference was only significant in case of PDA modification. Previous research conducted by Oviedo-Socarrás et al showed an opposite tend since the thickness of the fibrogenic capsule surrounding implants in diabetic rats (169 ± 11 µm) appeared to be significantly lower compared to the thicknesses obtained from samples in non-diabetic rats (295 ± 19 µm) [21]. Based on their experiments, they concluded that increased TNF-α (tumor necrose factor, a cytokine) levels were responsible for fibroblast apoptosis. As a consequence, decreased collagen levels were deposited by these cells, which explains the decreased fibrous capsule formation [20]. In the current study, a clearly different trend was observed. Furthermore, much thinner capsules were measured for both the diabetic (170 µm vs. 28 µm) and non-diabetic rats (300 µm vs. 33 µm) . This clearly proves that the type of material (polyether-polyurethane sponge discs vs. PMMAPEG-based materials) also influences the eventual body reaction.

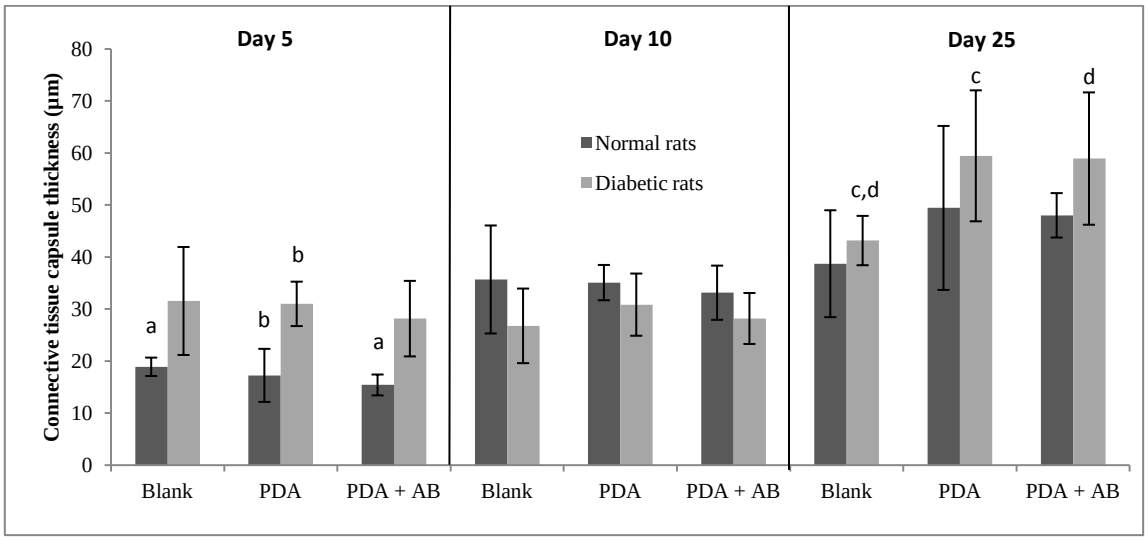

Figure 5.7: Analysis of the thickness of the connective tissue capsule after 5, 10 and 25 days of implantation in normal and diabetic rats. Conditions which are significantly different are denoted by similar letters a, b, c,… The X-axis indicates the codes of the applied surface modification. All error bars are a measure for the standard deviation, obtained after measurement of 5 replicates per condition and time point.

5.4.2.2. Evaluation of capillary formation

Apart from the fibrous capsule, the capillary formation was evaluated for the different surface modifications and the different implantation times. Herein, to count the number of capillaries, the same criteria were used as previously described (see § 5.4.1). It should be noted that no statistical analysis was performed on the obtained results due to the limited dataset (n=2) under investigation. Nevertheless, based on figure 5.8, some qualitative trends could be deduced. As a function of time, the number of capillaries increased for both groups of rats. The highest amount of capillaries was obtained for the AB functionalized samples, although, the results at day 5 contradicted this finding. At this timepoint, similar results were obtained for the different test conditions. At day 25, for both the normal and diabetic rats, a higher amount of capillaries was present around the AB functionalized samples (22 vs. 17) compared to the PDA functionalized (15 vs. 10) and the blank test condition (10 vs. 9). This finding indirectly delivered the proof that VE-cad antibodies are indeed able to attract EPC, as described by Lim et al thereby enhancing neo-vascularization [22]. From the previous comparison, it is also clear that samples implanted in diabetic rats gave rise to the formation of a lower number of capillaries compared to the normal rats. These findings are in line with the work of Oviedo-Socarrás et al, who reported on the polyether-polyurethane sponge discs [20]. They also found a lower number of blood vessels in the fibrovascular tissue from diabetic rats compared to the vessel numbers around implants from non-diabetic animals. These lower capillary numbers are most likely related to a lower number of circulating endothelial progenitor cells (EPC) which is characteristic for diabetics. It has already been demonstrated that diabetes related hyperglycemia can induce alterations to EPC, meaning that the number of EPC is reduced and that their function is impaired. As a consequence, their proliferation, adhesion and vasculogenesis is reduced. EPC originate from the bone marrow and can be mobilized into the peripheral circulation in response to tissue ischemia and cytokines such as VEGF and stromal-derived-factor-1α (SDF-1α) to contribute to endothelial repair and neovascularization at injury sites. Since diabetes is also responsible for a depleted production of SDF-1α, lower mobilizations of EPC from the bone marrow are enabled and as a consequence, lower vascularization is observed in diabetic rats [23-24].

A second explanation can be found in the mechanism of diabetic retinopathy, a disease which originates from an increased vascular permeability due to alteration of the blood-retinal barrier. It was shown that diabetes is indeed responsible for this blood-retinal barrier breakdown by the proteolytic breakdown of VE-cadherin, which is responsible for endothelial cell-cell contact. As a consequence, the quantities of soluble VE-cadherin in the body of diabetics might be increased. Since in the present work antibodies against VE-cadherin were immobilized onto the implanted materials, competition might have occurred between the soluble VE-cadherin and the circulating EPC for antibody binding. The lower AB availability for EPC could therefore be responsible for the lower degree of vascularization in diabetic rats when compared to the healthy ones [25].

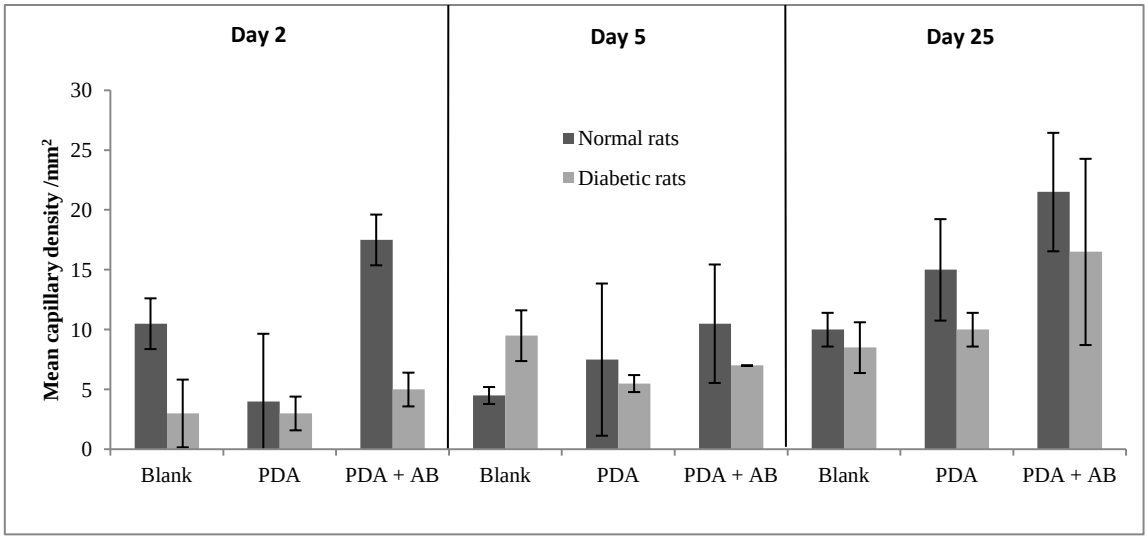

Figure 5.8: Number of capillaries counted around the implanted (non-)modified PMMAPEG samples, implanted in both healthy and diabetic rats. The evaluation was performed 2, 5 and 25 days post-implantation. The X-axis indicates the codes of the applied surface modification. All error bars are a measure for the standard deviation, obtained after measurement of 2 replicates per condition and time point.

5.4.2.3. Evaluation of capillary formation in VE-cad AB functionalized 3D scaffolds: a proof of principle

During previous experiments, the formation of a dense connective tissue capsule was observed for both the blank and the modified samples. Furthermore, a trend towards increased vascularization was observed in case VE-cad AB's were immobilized on the surface implant, but statistical confirmation could not be delivered. As a consequence, in order to evaluate and to prove the hypothesis that VE-cad AB's induce vascularization to a greater extent compared to PDA and non-modified samples, 3D printed porous PCL scaffolds, bearing identical surface chemistry were studied *in vivo*. The selection of porous scaffolds originates from previous work conducted by Koschwanez et al. They applied a porous polylactide coating on the surface of the commercialized MiniMed SOF-SENSOR (Medtronics) and they observed different tissue reactions between the sensors that contained a smooth surface versus a porous one. To be more precise, they observed threefold more blood vessels around the porous structures, combined with three times less collagen development, which resulted in a decreased thickness of the formed fibrous capsule [26].

In this work, 3D printed PCL scaffolds (6 mm ϕ, 1 mm thickness) with pores of 250 µm diameter were produced and implanted in three healthy and three diabetic rats. The same conditions as in the previous experiments were included in the study being blank, PDA-coated and PDA/AB-functionalized PCL scaffolds. For each sample condition, a duplicate was implanted per rat. In this way, samples could be explanted in duplicate at three time points, allowing for a preliminary and morphological analysis of the tissue integration and capillary formation after 4, 7 and 14 days of implantation.

After 4 days of implantation, no capillaries were observed between the struts of the plotted PCL scaffolds. Some tissue in-growth could already be observed and some inflammation was also occurring. Around the scaffold, no clear connective tissue capsule was observed (figure 5.9, A-C).

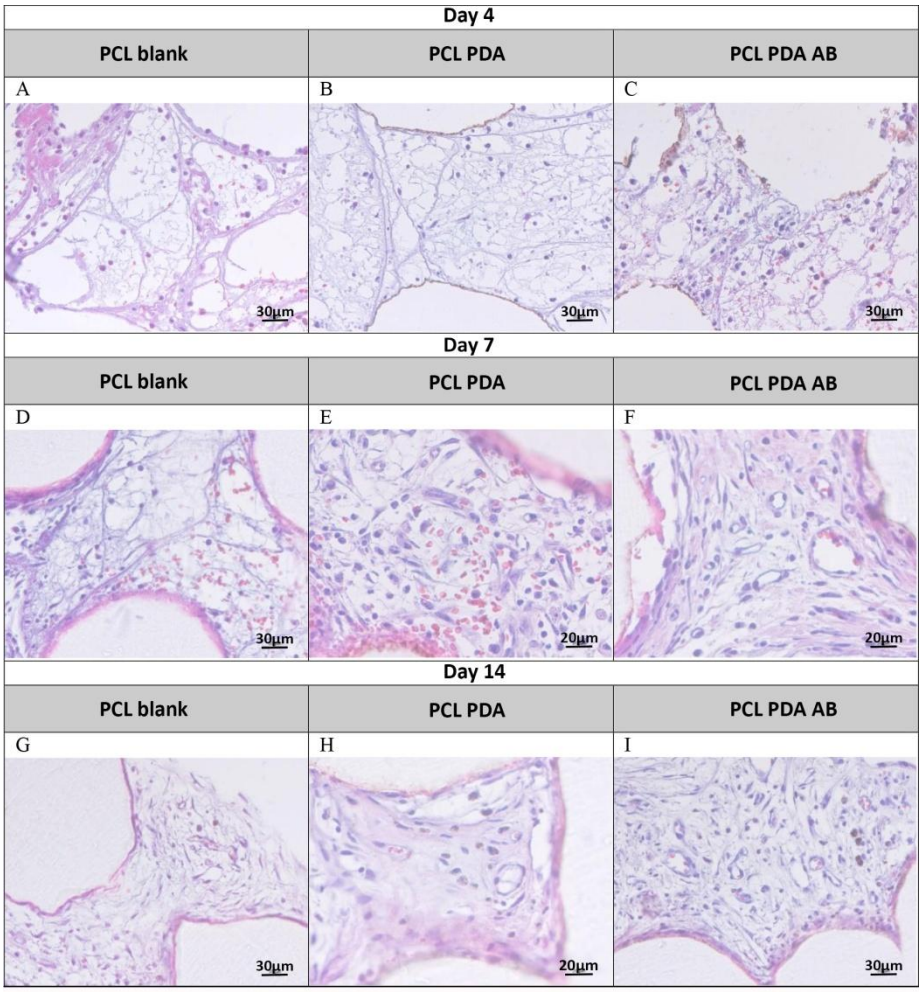

Figure 5.9: H&E staining of histological sections of PCL scaffolds. Tissue inside the scaffold, between the PCL struts and the surrounding tissue are visualized.

After 7 days of implantation, clear differences were observed between the different surface modifications. It appeared that the blank PCL scaffolds were better integrated compared to day 4 while still no connective tissue capsule was formed. Furthermore, in some areas between the struts, capillaries were spotted (figure 5.9, D). In case PDA was applied as coating, more blood vessel structures were detected compared to the blank (figure 5.9, E) and in case AB's were immobilized, blood vessels were present in all areas between the PCL struts (figure 5.9, F). In the latter case, also around the implant, a lot of capillaries were formed, even at the material border. After 14 days of implantation, the blank materials were nicely integrated in the surrounding tissue. Between the PCL struts, more capillaries were present at day 14 compared to the same condition at day 7. However, the blood capillaries were only present in certain areas (figure 5.9, G and 5.10, A). In case of PDA deposition,

more blood vessels were present compared to the blank, with less empty areas that did not contain blood vessels (figure 5.9, H and 5.10, B). In the presence of VE-cad AB, a lot of blood vessels were visualized, including the formation of many small capillaries (figure 5.9, I and 5.10, C). Again, around the implanted samples, blood vessels were observed till the border of the material (figure 5.10, D).

Based on these preliminary results, it can be concluded that the combination of a porous material structure and VE-cad AB functionalization indeed offers possibilities to provoke enhanced vascularization. Furthermore, the use of such a porous structure seems to result in a decrease or even the absence of a dense connective tissue capsule. As a consequence, for future designs of a glucose sensor packaging, the use of a porous coating, containing VE-cad AB should definitely be considered. Furthermore, the addition of dexamethasone as anti-inflammatory compound, could further decrease the inflammatory response and fibrosis around the implants [26]. Nevertheless, in the latter case, caution is needed as these drugs could also influence the immune system in a negative way (see also chapter 1, § 1.4.5).

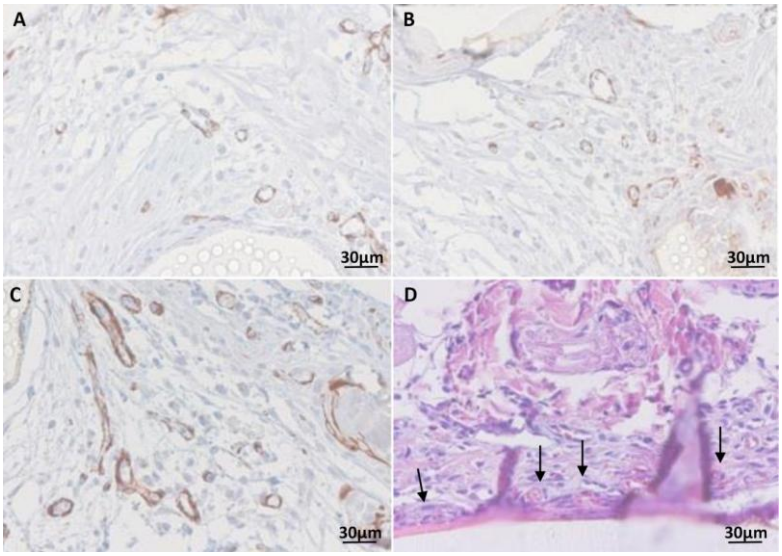

Figure 5.10: Anti-desmine staining of tissue inside the blank (A), PDA-coated (B) and AB-functionalized (C) PCL scaffolds, explanted at day 14. In case VE-cad AB was applied on the surface, blood vessels could be observed around the scaffold, even at the border of the implant (D, H&E staining at day 7, capillaries are indicated by the arrows)

5.5. Evaluation of the applied sensor design

During previous *in vivo* experiments, the main focus was on the evaluation of the chemical composition and the surface modification of the PMMAPEG-based packaging materials. Apart from that, the sensor design itself also had to be evaluated for its glucose sensing potential. To this end, the current glucose sensor concept (see figure 1.3) was tested for its optical glucose sensing capacity *in vivo.* In this work, two approaches were followed to determine glucose quantities and to evaluate the glucose sensor concepts. In a first

approach, optical transmission spectra through tissue were measured *in vivo* with the help of embedded optical fibers (§ 5.5.1). In the second approach, a commercial microdialysis probe, which is normally operational for 48 hours *in vivo*, was embedded inside the PMMAPEG packaging to see whether glucose measurements could be prolonged using the current sensor design and surface modifications (§ 5.5.2).

5.5.1. *In vivo* glucose measurements via an optical fiber-based design

5.5.1.1. Experimental set-up and *in vivo* optical measurements

In a first attempt to optically measure glucose quantities *in vivo*, an external light source and detector were connected to an implanted sensor via optical fibers. The sensor itself consisted of a PMMAPEG packaging which housed the optical fibers. Both fibers were separated by a 1 mm central cavity through which tissue and the ISF were measured. It is clear that in this approach, optical fibers passed through the skin of the animal (figure 5.11) and as a consequence, the fibers needed to be protected by a biocompatible polyurethane tubing (Braun). In this study, two variants of the sensor were fabricated. The first variant enabled direct measurement of the tissue and ISF in the central cavity and these were fabricated according to mold design 2 (see figure 5.2, § 5.2). For the second device, membranes were used to cover the central cavity in order to filter the ISF that would finally make contact with the optical beam. To this end, a commercially available PES membrane was selected and included in the mold design (cfr. mold design 3, figure 5.2, § 5.2). To insert the sensors in the animals, two incisions were made at a distance of 10 cm. A cavity was created subcutaneously and the sensor was inserted from one side. Before the insertion, the sensor was packed in a sterile drain, which was removed after the insertion. After the implantation, a metal box and protective jacket were mounted on the animal to protect the fibers and the wound of the animal (figure 5.11, B).

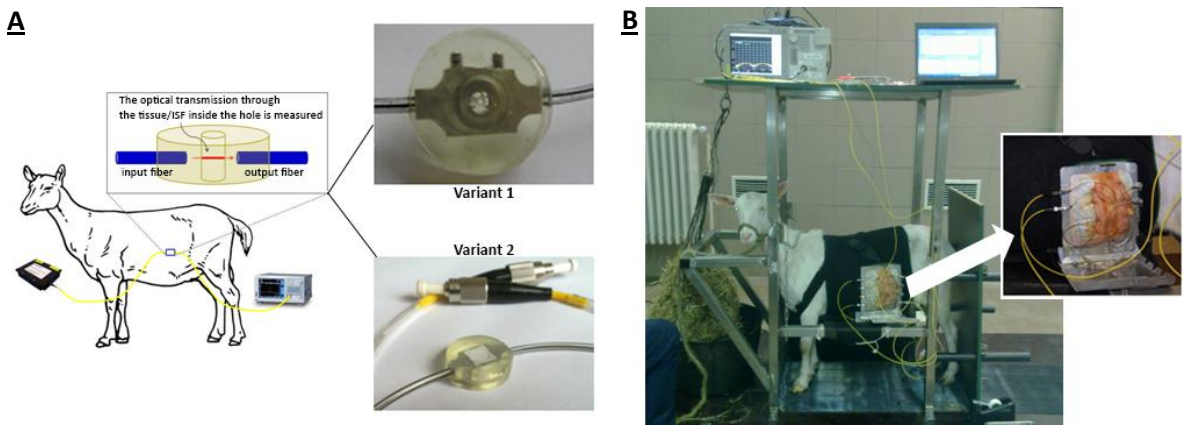

Figure 5.11: Panel A: Experimental setup to measure glucose *in vivo*. Two variants of the sensor were implanted, in the absence and presence of a membrane covering the central 1 mm hole (i.e. variant 1 and 2 respectively). Panel B: Real-life picture of the experimental set-up. A zoom is presented of the metal box surrounding the implanted sensors (B).

During the implantation period, optical measurements could be performed over a period of weeks. For the (membrane-containing) sensors, transmission spectra between 1500 and 1700 nm (first overtone band) could be recorded. Figure 5.12 (A) shows the spectra recorded with sensor variant 1 (without membranes). Herein, large variations were obtained in the optical output, which represents a large disturbance of the optical beam due to the presence of tissue inside the measurement cavity. After 3 weeks of implantation, a more stable signal was obtained which indicates that the central cavity was homogeneously filled. Overall, the variations in optical signal could not be related to spectral information of the tissue. In case a membrane was used to cover the central cavity (sensor variant 2), transmission spectra, represented in figure 5.12 (B), were typically obtained. During the first days after implantation, the central cavity of the sensor remained empty and as a consequence, no absorption could be distinguished. After 10 days, the spectrum changed to the absorption spectrum of water, which indicated that the cavity under the membrane was filled. Also in this case, variations in the signal were observed, but again these suffered from a feature-less nature. In conclusion, the optical transmission of the implanted sensors were insufficiently reproducible over time in order to perform further analysis or to develop a model for glucose concentration measurements.

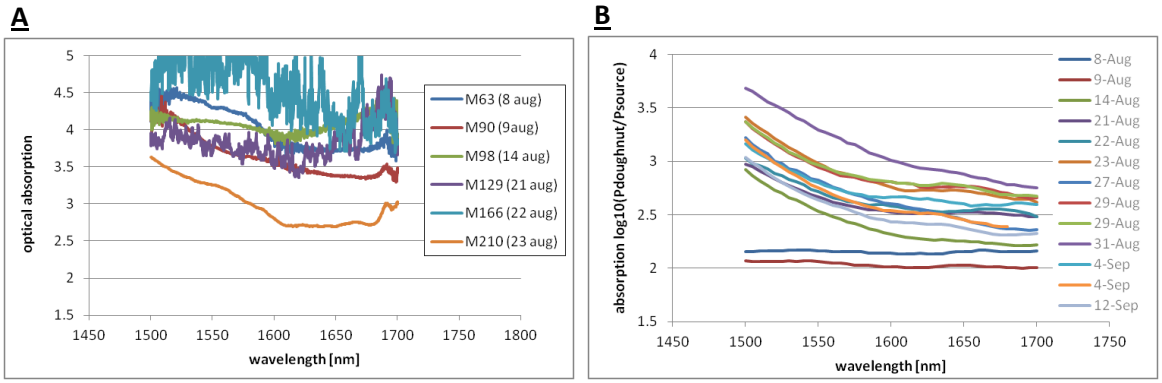

Figure 5.12: Transmission spectra of the sensor without membranes, implying that the optical beam is in direct contact with the tissue. The codes M63, M90,… refer to the codes given to each explanted donut. Furthermore, the day of explantation (e.g. 8 aug) is also mentioned (A). Transmission spectra of the sensor with membranes filtering the sample prior to contact with the optical beam (B).

From a practical point of view, a lot of sensors suffered from fiber failure as a result of external forces. Examples included movement of the mechanical protection box or fiber breakage due to movement of the goat. Furthermore, some of the fibers appeared broken close to the sensor. This indicated that the construction of a polymer tube surrounding the bare glass fiber was not reliable and did not offer sufficient protection. As a consequence, for future experiments, enforcement of the polymer cladding would be beneficial. In parallel, setups with only one fiber entry would also be preferred. In the current setup, failure of one fiber already rendered the complete sensor useless for optical transmission experiments. Finally, the protection box on the body of the animals could be further fixated

using additional tape bandages or an alternative position on the body could also be considered.

It can be concluded that the use of optically aligned fibers to measure glucose quantities is not optimal due to a lack of robustness of this system. Nevertheless, from the experiments it also became clear that the use of membranes is preferred to avoid great optical variations due to optical losses generated by tissue, grown inside the sensor cavity.

5.5.1.2. Visual evaluation of the explanted sensors

A dense and strong connective tissue capsule was formed around the sensors. What is more, even the 1 mm central cavity of the membrane-less sensors was filled with the same tissue. This observation confirms the observations made during the optical measurements (§ 5.5.1.1). Compared to the observations, described in paragraphs 5.3 and 5.4, the fiber-based sensors were characterized by inferior tissue integration and resulted in a tissue capsule which was much thicker and dense (see figure 5.13, B) compared to the fiber less implants (see figure 5.13, A). It was anticipated that these differences were caused by the movement of the optical fibers surpassing the skin of the animal, thereby influencing the healing process. In case of the membrane-based sensors, fluid was present underneath all membranes, an observation that could again be confirmed by the optical *in vivo* measurements. It is also worth noting that one of the goats developed an infection around the implanted donuts. Evaluation of the connective tissue showed an even thicker tissue layer, which clearly demonstrates the adverse body reaction (see figure 5.13, C).
It was also observed that most sensors contained cracks and that inside these cracks, clear in-growth of tissue was observed, which indicated that the cracks were probably formed in an early stage after implantation. This observation could be linked to the swelling capacity and the crosslinking density of the PEG-based materials. Furthermore, due to the incorporation of metal parts, the presence of crosslinks, in combination with material swelling, resulted in the creation of high stresses inside the sensor and as a consequence, several sensors appeared broken after explantation (see figure 5.13, B). Moreover, the mechanical impact of the movement of the goat was underestimated.
The adverse effects of material swelling were also confirmed during hermeticity testing (see chapter 2). Herein, delamination was observed between the cupper substrates and the polymer coating.
The *in vivo* results showed that swelling (even 17%) and a high crosslinking density (50 mol% PEGDMA) was detrimental to obtain a robust sensor. In this respect, the LMA-based material, described in chapter 2, could offer a superior alternative, due to its lower swelling capacity (<1%) and crosslinking density (2 mol% PEGDMA).

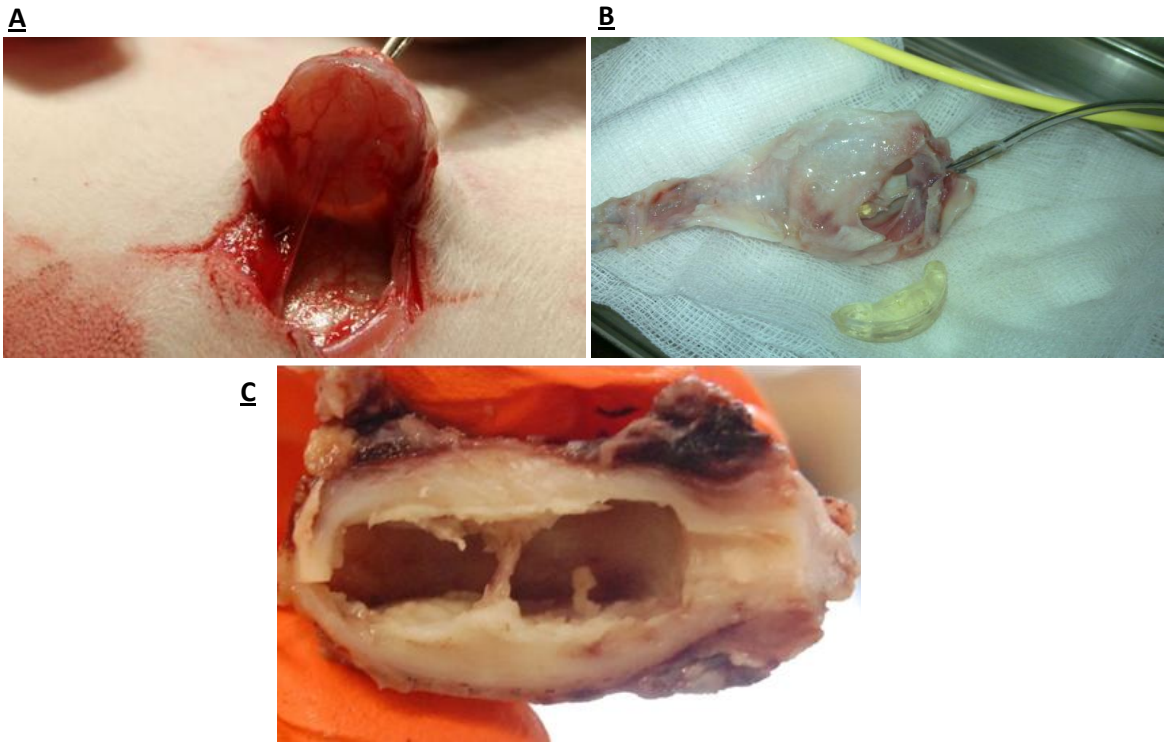

Figure 5.13: Figure A shows the vascularized tissue, surrounding a VE-cad modified fiber-less PMMAPEG sensor. Figure B shows a more dense connective tissue that is surrounding a broken PMMAPEG fiber-based sensor. Figure C shows the connective tissue that was found around an infected sensor.

5.5.2. *In vivo* glucose measurements via an embedded commercial microdialysis probe

Previous experiments indicated that as a function of time, fluid was diffusing through the membrane into the central cavity of the membrane-containing sensor setup. To study the glucose content of this fluid, a micro-dialysis probe was integrated into the sensor design and subsequently implanted subcutaneously in goats.

To this end, a CMA-7 micro dialysis probe (Aurora Bioscience) was selected, which is a flow-through dialysis probe which is in contact with its environment via a cuprophane membrane. A reference fluid is pumped through the probe via the percutaneous tubings and in this way analytes are able to diffuse from the environment through the membrane in the probe. In this way, analytes can be measured online, which is a frequently used technique for follow-up during surgical operations. Herein, the measurement of the glucose content present in the central cavity of the sensor, is targeted.

To embed the dialysis probe inside the glucose sensor design, a new molding piece had to be developed (see figure 5.14, A), containing a free space to mount the probe inside the packaging. The outer disks were produced individually, according to the principle described in mold design 1 (§ 5.2, figure 5.1). After production of the different items, they were glued together with a cyano-acrylate based glue (Loctite 4161, Henkel). Herein, no metal carrier was applied to mechanically support the membranes and all sensors were modified with PDA and functionalized with AB, in order to stimulate angiogenesis around the sensor. Again,

the sensors were implanted subcutaneously in goats. The presence of the sensors could be easily verified with ultrasound measurements, as shown in figure 5.14, (B). Based on the curvature of the membranes, it is clear that the latter experienced pressure from the body environment. Both concave and convex curvatures were observed for different sensors, but all membranes remained intact during implantation.

In order to collect the fluid inside the sensor probe, a micro dialysis pump was used to direct the glucose-containing reference fluid outside the body, where glucose was measured via a hexokinase-based glucose assay (figure 5.14, C).
For most sensors, the overall glucose yield was low, since most of the tubes of the micro-dialysis probes failed due to mechanical stresses. Only one sensor remained operational, but also in that case, only low glucose values were measured. After two months of implantation, no glucose was measured any longer. To understand the low yield of the operating sensor, the explanted sensors were further tested in an *in vitro* environment. Discussion of these results will be topic of the upcoming paragraph (§ 5.5.3).

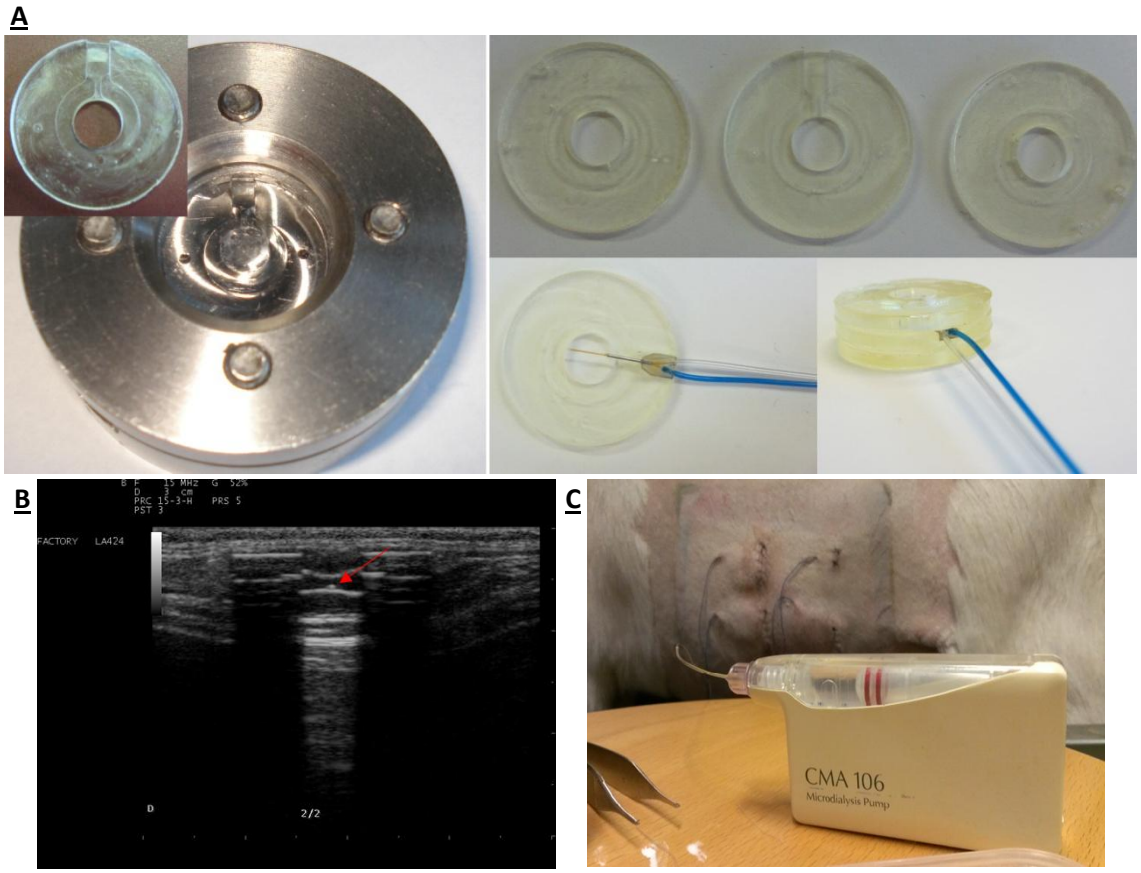

Figure 5.14: Molding piece to create the central disc, which contains open space to mount the commercial dialysis probe. Again, two membranes were applied to cover the central cavity of the sensor (not shown) (A). Ultrasound image of a sensor implanted in the goat. The membranes are clearly visible, as well as the probe (red arrow) (B). Sampling of the fluid under the membranes was done using a micro-dialysis pump (C).

5.5.3. Further evaluation of the membrane-based sensor design

From § 5.5.1, it became clear that measurements through tissue are difficult due to high optical losses. As a consequence, the use of membranes is a prerequisite to enable accurate, low noise measurements. In this respect, further characterization of the used membrane set-up was required to further elucidate the *in vivo* situation. Therefore, in a first step, dummy membrane sensors were implanted and the liquid collected under the membrane was analyzed. In this way, insight was provided in the filtering effect of the applied membrane. In a second step, the robustness of the membrane was analyzed after explantation. Implantation might have altered the physical properties of the membrane and in this respect, the change in diffusion properties of the explanted membranes was studied.

5.5.3.1. Dummy membrane-containing sensors to evaluate the filtering effect of the applied membrane

During the first experiment, dummy membrane-containing sensors were produced as demonstrated in figure 5.15 (A). Similar to the production of the 'microdialysis-probe-containing-sensor', all parts constituting the sensor, were molded individually. Next, PDA surface modification was conducted and in a last step, all different parts were glued together including the PES membrane with a molecular weight cut-off of 10 kDa. After ethylene oxide sterilization, the AB functionalization was performed, in order to prevent potential alterations in the AB's activity or function.
Prior to production, two medical device adhesives were tested including a cyanoacrylate-based glue (Loctite 4161, Henkel) and an epoxy-based-glue (Loctite M-31 CL Hysol, Henkel). Based on qualitative tensile and incubation tests, the cyano-acrylate based glue was selected as the preferred one.
For this implantation round, apart from the original PMMAPEG material (PMMAPEG 1), two other compositions were included to evaluate their *in vivo* response (PMMAPEG 4 and 5). The different material compositions and their physico-chemical properties are again summarized in table 5.2. It is clear that the selected materials were characterized by a slightly lower swelling, but also by a less brittle nature, as reflected by the lower crosslinker quantities present in the materials (= mol% PEGDMA). In this way, the impact of the mechanical properties on sensor survival could be evaluated.

Table 5.2: Composition and physico-chemical properties of the PMMAPEG-based dummy membrane sensors.

Material	MMA (mol%)	PEGDMA(550) (mol%)	PEGMA(500) (mol%)	E-mod (MPa)	Elongation (%)	Force at break (N)	Swelling (%)
PMMAPEG 1	50	50	0	142 ± 40	16 ± 3	36 ± 6	17 ± 1
PMMAPEG 4	80	16	4	486 ± 14	24 ± 6	69 ± 3	13 ± 0
PMMAPEG 5	90	4	6	1081 ± 194	10 ± 2	85 ± 12	12 ± 1

Again, all donuts were implanted subcutaneously in goats. Upon explantation of the donuts, 2 months post implantation, a good wound healing was observed and a nice thin, vascularized tissue layer was surrounding the different implants. In this case, no dense layer of connective tissue was observed, as described in § 5.5.1.2, but similar results were obtained compared to descriptions in § 5.3. It should be mentioned that the tissue closest to the membrane was characterized by a red color (figure 5.15, B). It can be anticipated that the observed blood was a remainder of the implantation process, which could not be removed by the body during the healing process.

Except for 1 sensor, which was PMMAPEG 1-based, all sensors remained intact after explantation. This indirectly proved that the ideal glucose sensor packaging should be characterized by low(er) swelling and a non-brittle nature (cfr. higher force at break and elongation percentage).

Visual observation of the explanted membranes showed some yellow discoloration after removing the tissue (Figure 5.15, C) and the central opening, under the membrane was completely filled with liquid. This liquid could be isolated (figure 5.15,D) (generally 40-50uL from each donut), but to enable analysis of the liquid content, samples had to be pooled prior to analysis. The protein content could be determined via SPE gel electrophoresis and was compared with the protein content that was observed for the liquid present on the outside of the sensor.

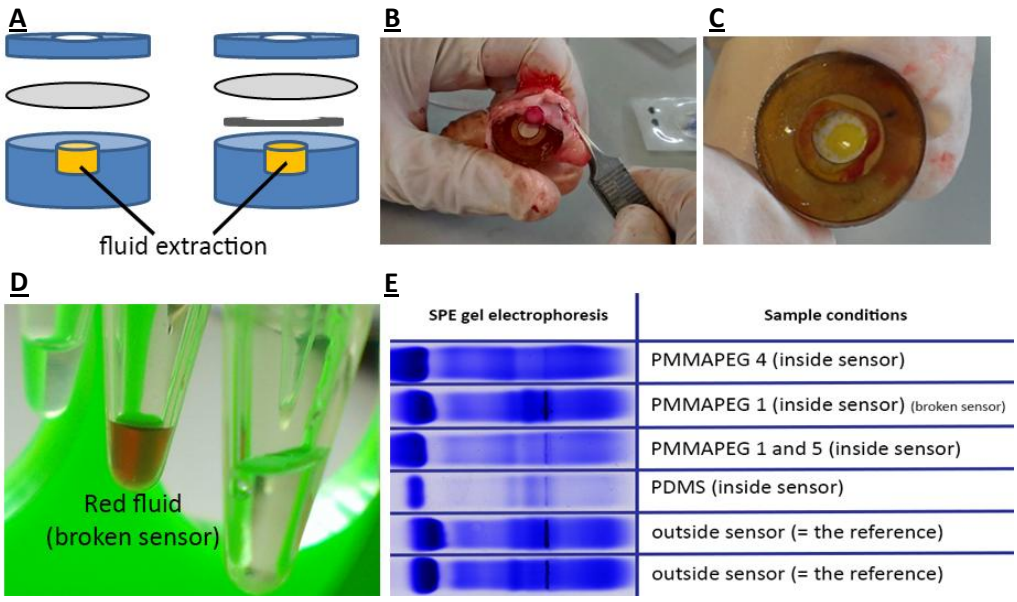

Figure 5.15: Figure A shows the design of the dummy membrane sensors. After explantation, a nice tissue layer was created around the sensors with some reddish coloration close to the membrane (B). The membrane was characterized by a yellow color (C). Figure D displays the fluid extractions from the sensor while figure E shows the SPE gel electrophoresis results obtained after 2 months of implantation. Herein, the protein profiles are compared for the inner and outer sensor liquid.

This comparison showed that some filtering could be noticed for most (except 1) of the PMMAPEG-based donuts (see figure 5.15, E). Nevertheless, compared to the PDMS donuts (protein content = 42 mg/dl) which were also included in this study as hydrophobic counterpart, the observed filtering effect was much lower (protein content inside PMMAPEG samples = 829-1812 mg/dl). The latter could be attributed to the swellable nature of the materials, which facilitated protein influx at the different material interfaces. It should be noted that during explantation, one broken sensor was yielded and as a consequence, for this sensor, a similar protein profile was obtained for the inner fluid compared to the external sensor fluid.

Apart from the protein content, glucose quantities were determined via a hexokinase-based glucose assay and UV-VIS spectrometry. The results showed that for some sensors the glucose values inside the sensor were much lower (4-18 mg/dl) compared to the reference value determined from the liquid surrounding the sensor (20-30 mg/dl). Due to this observation, the change in diffusion properties of the implanted membrane before and after implantation became a subsequent item to be evaluated.

5.5.3.2. Evaluation of the explanted membranes: a diffusion experiment

In previous experiments, glucose values lower than expected, were recorded in the fluid present in the central cavity of the sensor. As a consequence, the properties of the used membranes were further investigated. To this end, diffusion experiments were conducted. Figure 5.16 (A) displays the diffusion setup which consists of two chambers. The left one was filled with a stirring glucose solution whereas the right one contained pure water. Between the two compartments, the subject under analysis (a membrane or an explanted donut) was clamped and brought in contact with the fluids present in the compartments. In this way, diffusion of glucose could occur from the left towards the right compartment, surpassing the subject under investigation. Every 30 minutes, a 40 µl test sample was removed from the water-containing container and analyzed with a commercial Accu-check glucose sensor (Figure 5.16, B).

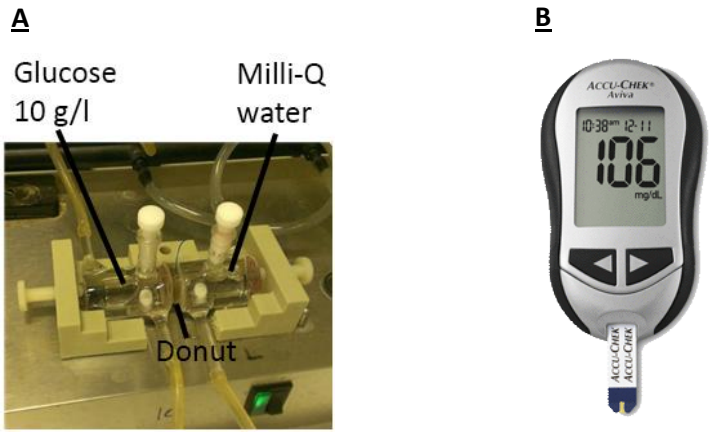

Figure 5.16: Images of the used diffusion setup (A) and the Accu-check read out system (B).

Diffusion of glucose through the explanted membranes resulted in an increased glucose value as a function of time. Indeed, after 3.5 hours of diffusion, concentrations of 97 mg/dl and 138 mg/dl were measured for respectively sensor 1 and 2 (Figure 5.17, A). Nevertheless, these values were significantly lower when compared to the ones obtained for the pristine membranes (275 mg/dl) (figure 5.17, B). These results thus showed that alterations were induced in the membrane diffusion behavior. To study the cause of this change, several diffusion experiments were conducted. First, the influence of the glue was tested on the diffusion properties of the membrane. Since the membranes were glued between the polymer disks, the glue could have potentially blocked the pores of the membranes due to capillary forces. To evaluate this assumption, the diffusion of glucose through a PES membrane glued between two polymer discs with a cyano-acrylate based glue, was tested. During the first 2.5 hours, no glucose was measured and after 4 hours, the concentration was still limited to 16 mg/dl. On the other hand, if the glued samples were incubated for 9 days in PBS buffer (37°C), much higher concentrations were detected (124 mg/dl), which were comparable to the concentrations obtained for the explanted membranes (Figure 5.18, C). As a consequence, the cyano-acrylate based glue indeed blocked the pores. In addition, as a function of time and upon incubation in PBS buffer, glucose diffusion was again facilitated. This finding suggests that no optimal adhesion exists between the glue and the different materials (i.e. the PMMAPEG material and the membrane) or that the curing parameters of the glue still need to be optimized.

As mentioned in the previous paragraph, a second epoxy-based glue was also considered for the sensor assembly. Although this glue was not selected due to inferior adhesion properties, it was also evaluated for its influence on glucose diffusion through the glued membrane constructs. Figure 5.17 (D) shows that similar concentrations were detected prior to and after incubation of the test structures (± 270 mg/dl). Furthermore, the obtained concentrations were similar to the values obtained for the blank pristine membranes. Pore blockage is thus glue-dependent, yet, for the adhesion of PMMAPEG, further optimization is required to realize functional membrane integration inside the sensor design.

Apart from glue-dependent alterations, the lower glucose concentrations in figure 5.17 (A), could also be caused by the *in vivo* residence time. As mentioned in figure 5.15 (C), the explanted membranes showed a yellowish discoloration. This observation suggested the deposition of proteins during the implantation period, which is a well-known phenomenon in literature [27-29]. More specifically, biofouling has been recognized as the main counteracting cause for the successful development of long-term implantable biosensors [11, 30] .

To prove the presence of proteins on the explanted membranes, a qualitative coomassie blue staining was performed as represented in figure 5.17 (E). This dye binds non-specifically to virtually all proteins and an increased blue intensity can thus be correlated with protein presence. Compared to the pristine membrane, a more intense blue color was observed for the explanted membranes, which indicates the presence of proteins on the latter surface. Furthermore, XPS-analysis confirmed this finding, because a higher N/C ratio was obtained

for the explanted membranes compared to the pristine membrane and the composition of the glue (Figure 5.17, F). These results were anticipated, since proteins contain a substantial amount of nitrogen in their amino acid structure.

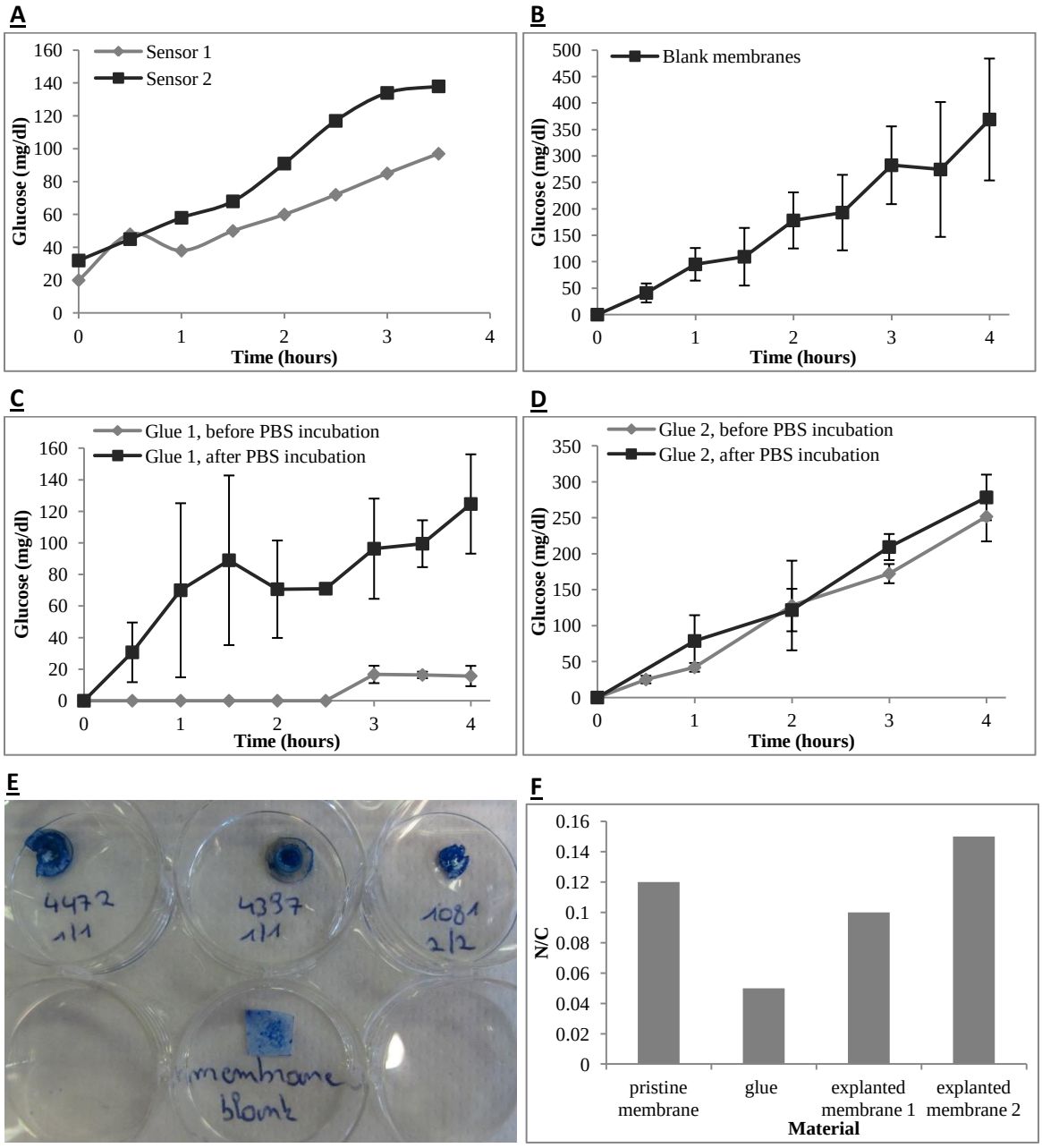

Figure 5.17: Diffusion of glucose through the explanted membranes (A), pristine blank membranes (B), membranes glued between 2 polymer discs, using a cyano-acrylate based glue (C) and an epoxy-based glue (D). In case of C and D, a comparison is made between the diffusion behavior of the glued structures before and after incubation in PBS buffer at 37°C. Panel E displays the coomassie blue stained explanted and blank membranes, whereas panel F shows the N/C ratio's, determined by XPS for the blank membranes, the glue and the explanted membranes.

To summarize, if a membrane-based PMMAPEG sensor is implanted subcutaneously, the glucose diffusion rate will be influenced by two factors. First, upon implantation, glucose

diffusion will be limited due to blockage of the membrane pores by the applied cyano-acrylate-based glue. As a function of time, partial disassembly of the sensor might occur, because of an inferior adhesion between the glue and implant material, thereby establishing glucose diffusion. Secondly, due to a body-induced reaction, biofouling will occur and as a consequence, glucose diffusion will again be delayed. It is clear that the manufacturing process of the membrane-based sensors requires further optimization. In this respect, alternative glues could be evaluated. Alternatives could be given by the MED-series provided by NuSil, as they cure in contact with most materials common for biomedical assemblies [31]. Furthermore, the use of fibrin glue could also be evaluated. Previously, it has been used extensively in plastic and reconstructive surgery in skin grafts, but also to attach PMMA intra-ocular lenses (IOL) to the sclera bed in the eye [32-33].

Regarding the applied membrane, different alternatives could also be studied such as polyacrylonitrile (PAN), polycarbonate (PC), cuprophane or cellulose acetate-based membranes [28, 34].

Transport properties of analytes towards the sensor will also be influenced by the thickness of the applied membrane. In this respect, the currently used PES membrane was characterized by a thickness of 200 µm, which might explain the slow *in vitro* diffusion of glucose, as represented in figure 5.16 (B). In electrochemical sensors, the applied membranes are mostly characterized by smaller thicknesses (< 100 µm) [4].

Furthermore, instead of using pristine polymer membranes, surface modification of the membranes could also be considered. In this respect, Wei et al have already performed PDA modification of PES membranes to subsequently biofunctionalise them. They have proven an improved blood compatibility of the membrane, but the influence of the modification on the diffusion behavior of the membrane was not included in their study [35]. As a consequence, this was studied in the current work for the PDA-VE-cad AB modified membranes.

This phenomenon was studied with the help of a diffusion setup (figure 5.16, A), as described previously. Herein, a pristine and PDA-modified PES membrane was clamped between the two diffusion cell compartments and rhodamine 6G was used as dye to study the diffusion properties of the membranes. As illustrated in figure 5.18 (B), PDA modification altered the diffusion properties in a tremendous way. As a consequence, the PDA modifications of all membrane-based sensors had to be done prior to the sensor assembly.

Alternatively, other surface modifications of the membrane could be considered for future experiments in order to reduce biofouling. Previously, Ma et al. (2007) have applied a polyvinyl alcohol (PVA) coating to enhance the membrane's antifouling properties [36]. In this respect, the plasma deposition of acrylic acid, followed by RGD peptide immobilization with the help of a hydrophilic spacer arm could also be considered [37]. In general, plasma treatment of PES membranes includes a frequently used method to improve the membrane's hydrophilicity [8].

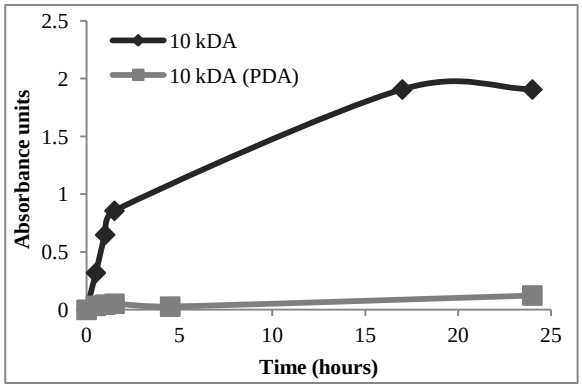

Figure 5.18: Effect of PDA functionalization on the diffusion properties of a PES membrane. A rhodamine 6G solution was used as test liquid.

5.6. Conclusions and future perspectives

In this chapter, different *in vivo* experiments were conducted in order to understand the needs of a suitable glucose sensor design.

First, it was demonstrated how an in-house-made mold enabled the production of donut-shaped implant materials. Next, a relevant and representative implantation side was selected to evaluate the different glucose sensor packagings and designs. Based on surgical implications (including site accessibility and reproducibility) and the occurrence of better integrated connective tissue capsules, subcutaneous implantation was preferred over intramuscular and retroperitoneal implantations.

Subsequently, different surface modified (i.e. blank, PDA and AB modified) implants were implanted and evaluated for their *in vivo* response. Minor inflammation was observed for a minority of the implanted samples. Generally, compared to the blank materials, a better tissue integration was observed for the surface modified materials, but no clear differences in morphology of the connective tissue could be observed between the mutual modifications. Nevertheless, higher amounts of capillaries were counted around the AB-modified samples, which were implanted both in goats and rats, but at this stage, no statistical evidence could be delivered for this phenomenon. The enhanced implant vascularization was further proven during a qualitative evaluation of porous AB-functionalized PCL scaffolds. These scaffolds gave rise to a clear enhancement of the vascularization and resulted in a tremendous decrease of fibrous encapsulation. As a consequence, for future sensor designs, the incorporation of a porous coating, bearing VE-cad AB's, should definitely be considered.

Concerning the sensor design, it was proven that *in-vivo* measurements of optical spectra using optical fibers to connect the sensors to external light sources and detectors was not successful. More specifically, the yield of the sensor was low as most of the optical fibers were broken due to the mechanical stress imposed by the movement of the animals. For

some sensors, the transmission spectra could be measured, but the transmission through tissue appeared to be too variable and therefore not feasible.
As a result, a PES membrane with a molecular weight cut-off of 10 kDa was included in the sensor design in order to filter the interstitial fluid which is in contact with the optical fibers. Optical transmission measurements became more stable compared to the non-membrane-based design, but even then the transmission remained too variable to build a multivariate analysis model.

Overall, the manufacturing approach of the membrane-based sensors requires further optimization. More specifically, because of pore blockage by the cyano-acrylate-based glue, an alternative adhesive needs to be selected to enable a robust assembly of the sensor.
Furthermore, based on the low diffusion rate of the current membrane, superior alternatives could be considered. Variations in membrane thickness or the use of a surface modified membrane could for example be tested. The latter approach would also enable a reduction in biofouling and an enhancement of the membrane's biocompatibility.

Despite of the remaining optimization needs, it can be concluded that first and important steps were taken towards the development of an implantable optical glucose sensor.

5.7. References

1. Mordes, J. P., and Rossini, A. A. (1981) Animal models of diabetes, *The American journal of medicine* 70, 353-360.
2. Rees, D., and Alcolado, J. (2005) Animal models of diabetes mellitus, *Diabetic Medicine* 22, 359-370.
3. Haghdoost, I. S., Ghaleshahi, A. J., and Safi, S. (2007) Clinicopathological findings of diabetes mellitus induced by alloxan in goats, *Comparative Clinical Pathology* 16, 53-59.
4. Updike, S. J., Shults, M. C., Gilligan, B. J., and Rhodes, R. K. (2000) A subcutaneous glucose sensor with improved longevity, dynamic range, and stability of calibration, *Diabetes Care* 23, 208-214.
5. Gough, D. A., Kumosa, L. S., Routh, T. L., Lin, J. T., and Lucisano, J. Y. (2010) Function of an implanted tissue glucose sensor for more than 1 year in animals, *Science Translational Medicine* 2, 42ra53-42ra53.
6. Varalli, M., Marelli, G., Maran, A., Bistoni, S., Luzzana, M., Cremonesi, P., Caramenti, G., Valgimigli, F., and Poscia, A. (2003) A microdialysis technique for continuous subcutaneous glucose monitoring in diabetic patients (part 2), *Biosensors & Bioelectronics* 18, 899-905.
7. Poscia, A., Mascini, M., Moscone, D., Luzzana, M., Caramenti, G., Cremonesi, P., Valgimigli, F., Bongiovanni, C., and Varalli, M. (2003) A microdialysis technique for continuous subcutaneous glucose monitoring in diabetic patients (part 1), *Biosensors & Bioelectronics* 18, 891-898.
8. Zhao, C., Xue, J., Ran, F., and Sun, S. (2013) Modification of polyethersulfone membranes–a review of methods, *Progress in Materials Science* 58, 76-150.
9. Zhang, J., Wang, Q., Wang, Z., Zhu, C., and Wu, Z. (2014) Modification of poly (vinylidene fluoride)/polyethersulfone blend membrane with polyvinyl alcohol for improving antifouling ability, *Journal of Membrane Science* 466, 293-301.

10. Gunasingham, H., Teo, P. Y., Lai, Y.-H., and Tan, S.-G. (1989) Chemically modified cellulose acetate membrane for biosensor applications, *Biosensors* 4, 349-359.
11. Wisniewski, N., and Reichert, M. (2000) Methods for reducing biosensor membrane biofouling, *Colloids and Surfaces B-Biointerfaces* 18, 197-219.
12. Uehara, H., Kakiage, M., Sekiya, M., Sakuma, D., Yamonobe, T., Takano, N., Barraud, A., Meurville, E., and Ryser, P. (2009) Size-selective diffusion in nanoporous but flexible membranes for glucose sensors, *ACS nano* 3, 924-932.
13. Jaremko, J., and Rorstad, O. (1998) Advances toward the implantable artificial pancreas for treatment of diabetes, *Diabetes Care* 21, 444-450.
14. Olesberg, J. T., Cao, C. S., Yager, J. R., Prineas, J. P., Coretsopoulos, C., Arnold, M. A., Olafsen, L. J., and Santilli, M. (2006) Optical microsensor for continuous glucose measurements in interstitial fluid - art. no. 609403, In *Optical Diagnostics and Sensing VI* (Cote, G. L., and Priezzhev, A. V., Eds.), pp 9403-9403, Spie-Int Soc Optical Engineering, Bellingham.
15. Collison, M. E., Stout, P. J., Glushko, T. S., Pokela, K. N., Mullins-Hirte, D. J., Racchini, J. R., Walter, M. A., Mecca, S. P., Rundquist, J., Allen, J. J., Hilgers, M. E., and Hoegh, T. B. (1999) Analytical characterization of electrochemical biosensor test strips for measurement of glucose in low-volume interstitial fluid samples, *Clinical Chemistry* 45, 1665-1673.
16. Sternberg, F., Meyerhoff, C., Mennel, F. J., Mayer, H., Bischof, F., and Pfeiffer, E. F. (1996) Does fall in tissue glucose precede fall in blood glucose?, *Diabetologia* 39, 609-612.
17. ThomeDuret, V., Reach, G., Gangnerau, M. N., Lemonnier, F., Klein, J. C., Zhang, Y. N., Hu, Y. B., and Wilson, G. S. (1996) Use of a subcutaneous glucose sensor to detect decreases in glucose concentration prior to observation in blood, *Analytical Chemistry* 68, 3822-3826.
18. Goodarzi, M., Sharma, S., Ramon, H., and Saeys, W. (2015) Multivariate calibration of NIR spectroscopic sensors for continuous glucose monitoring, *Trac-Trends Anal. Chem.* 67, 147-158.
19. Gellynck, K., Kodeck, V., Van De Walle, E., Kersemans, K., De Vos, F., Declercq, H., Dubruel, P., Vlaminck, L., and Cornelissen, M. (2015) First step toward near-infrared continuous glucose monitoring: in vivo evaluation of antibody coupled biomaterials, *Experimental Biology and Medicine* 240, 446-457.
20. Oviedo Socarras, T., Vasconcelos, A. C., Campos, P. P., Pereira, N. B., Souza, J. P. C., and Andrade, S. P. (2014) Foreign Body Response to Subcutaneous Implants in Diabetic Rats, *Plos One* 9.
21. Oviedo-Socarras, T., Vasconcelos, A. C., Barbosa, I. X., Pereira, N. B., Campos, P. P., and Andrade, S. P. (2014) Diabetes alters inflammation, angiogenesis, and fibrogenesis in intraperitoneal implants in rats, *Microvascular Research* 93, 23-29.
22. Lim, W.-H., Seo, W.-W., Choe, W., Kang, C.-K., Park, J., Cho, H.-J., Kyeong, S., Hur, J., Yang, H.-M., Cho, H.-J., Lee, Y.-S., and Kim, H.-S. (2011) Stent Coated With Antibody Against Vascular Endothelial-Cadherin Captures Endothelial Progenitor Cells, Accelerates Re-Endothelialization, and Reduces Neointimal Formation, *Arteriosclerosis Thrombosis and Vascular Biology* 31, 2798-U2141.
23. Westerweel, P. E., Teraa, M., Rafii, S., Jaspers, J. E., White, I. A., Hooper, A. T., Doevendans, P. A., and Verhaar, M. C. (2013) Impaired Endothelial Progenitor Cell Mobilization and Dysfunctional Bone Marrow Stroma in Diabetes Mellitus, *Plos One* 8.
24. Yiu, K.-H., and Tse, H.-F. (2014) Specific Role of Impaired Glucose Metabolism and Diabetes Mellitus in Endothelial Progenitor Cell Characteristics and Function, *Arteriosclerosis Thrombosis and Vascular Biology* 34, 1136-1143.
25. Navaratna, D., McGuire, P. G., Menicucci, G., and Das, A. (2007) Proteolytic degradation of VE-cadherin alters the blood-retinal barrier in diabetes, *Diabetes* 56, 2380-2387.
26. Koschwanez, H. E., Yap, F. Y., Klitzman, B., and Reichert, W. M. (2008) In vitro and in vivo characterization of porous poly-L-lactic acid coatings for subcutaneously implanted glucose sensors, *Journal of Biomedical Materials Research Part A* 87A, 792-807.

27. Ward, W. K. (2008) A review of the foreign-body response to subcutaneously-implanted devices: the role of macrophages and cytokines in biofouling and fibrosis, *Journal of Diabetes Science and Technology* 2, 768-777.
28. Wisniewski, N., Klitzman, B., Miller, B., and Reichert, W. (2001) Decreased analyte transport through implanted membranes: Differentiation of biofouling from tissue effects, *Journal of biomedical materials research* 57, 513-521.
29. Wisniewski, N., Moussy, F., and Reichert, W. M. (2000) Characterization of implantable biosensor membrane biofouling, *Fresenius Journal of Analytical Chemistry* 366, 611-621.
30. Gifford, R., Kehoe, J. J., Barnes, S. L., Kornilayev, B. A., Alterman, M. A., and Wilson, G. S. (2006) Protein Interactions with subcutaneously implanted biosensors, *Biomaterials* 27, 2587-2598.
31. NuSil. (2014) medical implants, adhesives; Retrieved July 20 (2015) from http://nusil.com/en/productsearch#life-sciences?segment=MedicalImplant.
32. Currie, L. J., Sharpe, J. R., and Martin, R. (2001) The use of fibrin glue in skin grafts and tissue-engineered skin replacements: A review, *Plastic and reconstructive surgery* 108, 1713-1726.
33. Agarwal, A., Kumar, D. A., Jacob, S., Baid, C., Agarwal, A., and Srinivasan, S. (2008) Fibrin glue–assisted sutureless posterior chamber intraocular lens implantation in eyes with deficient posterior capsules, *Journal of Cataract & Refractive Surgery* 34, 1433-1438.
34. Clark, L. C., and Duggan, C. A. (1982) Implanted electroenzymatic glucose sensors, *Diabetes Care* 5, 174-180.
35. Wei, Q., Li, B., Yi, N., Su, B., Yin, Z., Zhang, F., Li, J., and Zhao, C. (2011) Improving the blood compatibility of material surfaces via biomolecule-immobilized mussel-inspired coatings, *Journal of Biomedical Materials Research Part A* 96, 38-45.
36. Ma, X., Su, Y., Sun, Q., Wang, Y., and Jiang, Z. (2007) Enhancing the antifouling property of polyethersulfone ultrafiltration membranes through surface adsorption-crosslinking of poly (vinyl alcohol), *Journal of Membrane Science* 300, 71-78.
37. Di Carlo, B. V., Gottifredi, J. C., and Habert, A. C. (2011) Synthesis and characterization of composite membrane by deposition of acrylic acid plasma polymer onto pre-treated polyethersulfone support, *Journal of Materials Science* 46, 1850-1856.

Chapter 6

Experimental section

6.1. Overview of applied techniques

Previous chapters have reported on substantial characterization of both the bulk of the materials and their surface properties, using different experimental techniques. The upcoming paragraphs summarize the principles thereof. The specifications and experimental details elaborated throughout this work are summarized in a subsequent part.

6.1.1. Nuclear Magnetic Resonance spectroscopy

The synthesized materials were structurally evaluated by conventional proton nuclear magnetic resonance (^{1}H-NMR) spectroscopy. Using this technique, each proton covalently bound in a chemical structure, results in a characteristic resonance signal present in the recorded spectrum because of its characteristic spin. Depending on the chemical environment (i.e. the neighbouring atoms) of the proton, the position of the signal is alterred, yet remains characteristic for a specific environment.
In order to apply conventional ^{1}H-NMR spectroscopy, dissolution of the polymer in a deuterated solvent such as $CDCl_3$, is a prerequisite. In this work, apart from non-crosslinked materials, crosslinked polymer networks were also synthesized which are insoluble in any solvent. As a result, these were not suitable for conventional ^{1}H-NMR spectroscopy analysis. In addition, measurements in the dry state would not provide a suitable alternative since this would result in considerable line broadening because of the presence of dipolar interactions, chemical shift anisotropy (CSA) and magnetic susceptibility effects [1-3]. Conversely, if the network can be swollen in a deuterated solvent, both solvatation of the polymer chains and the chain mobility are increased. As a consequence, magic angle spinning (MAS) NMR spectroscopy can be used as a characterization technique for crosslinked, swellable networks. To this end, the sample is rapidly rotated at the magic angle of 54.7° relative to the static magnetic field (figure 6.1) in order to remove the line broadening effects. This technique thus allows to record NMR spectra of semi-solid samples, with more narrow signals as a result.

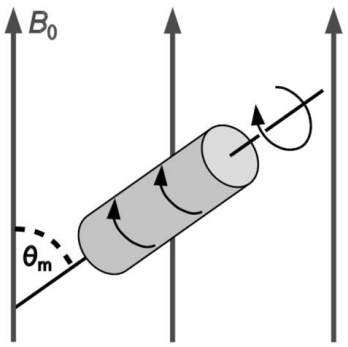

Figure 6.1: Scheme showing the concept of magic angle spinning. Within the main magnetic field (B_0), a sample (gray) is rotating with a high frequency. The rotation axis is tilted by 54,7° (i.e. the magic angle, θ_m) with respect to the direction of B_0.

6.1.2. Tensile testing

In order to evaluate the mechanical properties of the synthesized materials, tensile tests were conducted. To this end, dog bone shaped specimens (figure 6.2, A) with a length of L_0 (the gauge length) were stretched using a constant elongation rate. As a result, stress strain curves were generally recorded as depicted in figure 6.2 (B), which represents an amorphous material in the glassy state. Different regions can be distinguished in the plot. More specifically, region 1, which is the linear part of the curve, is the elastic region which follows Hooke's law, implying that the stress is proportional to the strain. As a consequence, deformations applied in this region are reversible. In region 2, a deviation from linearity can be noticed, which is due to visco-elastic effects and pseudo-plastic deformations. The maximum is defined as the yield stress. Immediately after the maximum (region 3), a drop in the stress occurs which is associated with the phenomenon of 'necking'. Herein, a decrease in cross-sectional area is created at a certain point along the length of the material which consequently propagates throughout the sample. Because of this propagation, upon increasing strength, an almost constant stress value is obtained (cfr. region 4) since the surface area of the cross-section decreased. The polymer chains align in the direction of the applied force and due to this 'cold drawing', the material is irreversibly deformed. In the final part (i.e. region 5), the stress is again increased upon increasing strain (i.e. strain hardening). At a certain point, a maximum orientation in the sample is realized, which results in a higher resistance against deformation which will finally induce rupture [4].

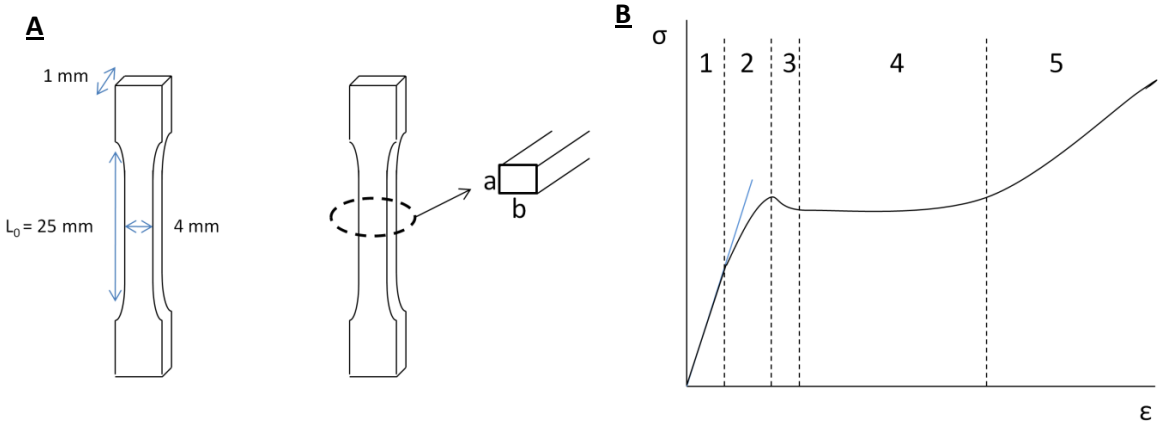

Figure 6.2: Dog bone shaped specimen with L_0 = 25 mm, used for tensile testing (A). A theoretical stress strain curve for an amorphous material in the glassy state (B).

In the present work, the technique was mainly used to compare different formulations with respect to their flexibility and elasticity. As a consequence, the E-modulus of the different materials could be determined by measuring the initial slope of the elastic part of the recorded stress (σ, MPa)- strain (ε, in %) curves (equation 2.1).

$$\sigma = E.\varepsilon \qquad (6.1)$$

Starting from the force F (expressed in Newton (N)) and the length of the sample before (L_0) and after elongation (L_e), the stress and the strain could be calculated as:

$$\sigma = \frac{F}{A_0} \tag{6.2}$$

$$\varepsilon = \frac{\Delta L}{L_0} = \frac{L_e - L_0}{L_0} \tag{6.3}$$

Herein, A_0 resembles the initial surface area on which the force is applied. Referring to figure 6.2 (A), this surface can be calculated from the cross-section of the center part of the dog bone shaped material:

$$A_0 = a.b \tag{6.4}$$

Apart from the elasticity modulus, the elongation percentage as well as the force at break were evaluated to respectively judge the 'stretchability', the brittleness and the strength of the different materials.

6.1.3. Swelling tests

In case one of the building blocks is characterized by hydrophilic character, it is very useful to quantify the swelling potential of the final materials. Given the scope of this project, swelling could have a detrimental effect on the working efficiency of the final sensor. Based on the initial dry mass (m_0) and the mass after swelling (m_t), the swelling percentage could be calculated, as pointed out in equation 6.5.

$$Swelling \quad (\%) = \frac{m_t - m_0}{m_0} * 100\ \% \tag{6.5}$$

If unreacted species are present inside the polymer network, upon incubation, they will leach out from the polymer network and form the sol fraction. Based on the dry mass of the samples after swelling (m_e), the gel and sol fractions could be calculated (equations 6.6 and 6.7).

$$Gel \quad fraction \quad (\%) = \frac{m_e}{m_0} * 100\ \% \tag{6.6}$$

$$Sol \quad fraction \quad (\%) = 100\ \% - gel \quad fraction \tag{6.7}$$

Knowledge of the gelfraction is important, because the leachable fraction might be the cause of potentially toxic effects induced during *in vitro* and *in vivo* testing. Obviously, purification of the polymers could address this issue.

6.1.4. Static Contact Angle measurements

The hydrophobic or hydrophilic nature of a material can be determined through the assessment of a static contact angle (SCA), which is a measure of the material wettability.
If a liquid drop is deposited onto a solid surface, three different interfacial forces come into play, including the solid-liquid (γ_{SL}), the liquid-vapour (γ_{LV}) and the solid-vapour (γ_{SV}) interfacial tensions. After deposition, a mechanical equilibrium will exist between the different forces and this equilibrium will determine the value of the contact angle (θ). The relationship between the different properties at equilibrium is dictated by Young's equation, as indicated in figure 6.3.

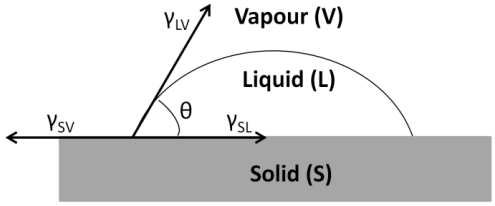

$$\cos\theta = \frac{\gamma_{SV} - \gamma_{SL}}{\gamma_{LV}}$$

Figure 6.3: Definition of the static contact angle (θ), according to Young's equation.

For high contact angle ($\theta > 90°$) values, the water droplet tends to ball up, since low affinity exists between the solid surface and the liquid. In case of low contact angles ($\theta < 90°$), the water droplet will spread due to higher affinities between the two substances. If $\theta = 0°$, complete wetting of the surface is obtained [5].

6.1.5. X-ray Photo-electron Spectroscopy

XPS is a powerful technique to determine the atomic composition of a polymer surface for an information depth of about 7 nm. Furthermore, information on the binding states of these elements, their oxidation numbers and chemical functionalities can be deduced.
To obtain this information, a solid sample is irradiated with soft X-rays under high vacuum conditions. Typically for XPS, Mg (1253.6 eV) and Al-Kα (1486.6 eV) rays are used.
Upon interaction with the surface, there is a certain probability that an electron from one of the inner shells or valence bands is excited and thereby ejected (figure 6.4). The emitted photoelectrons are detected and their number is expressed as a function of their binding energy. Based on the knowledge of the energy of the initial X-ray irradiating the surface (hv) and the detected kinetic energy of the emitted photo-electrons (E_{kin}), the binding energy (E_b) of the latter can be calculated via :

$$E_b = hv - E_{kin} - \Phi \qquad (6.8)$$

Herein, Φ represents an instrument constant, which is determined via device calibration. Since the binding energy of an electron is element-specific, information about the elemental composition (except H and He) of the surface can be obtained via this technique.

Furthermore, the binding energy will also be determined by the chemical environment of the studied atom. Due to differences in electronegativity between neighboring elements, shifts in the binding energy are represented. As a consequence, electron-withdrawing neighboring atoms will be characterized by higher binding energies, whereas electron-releasing neighbours are characterized by lower binding energies. Using peak deconvolution, the different environments of an atom can be distinguished and their relative ratios can be calculated [5].

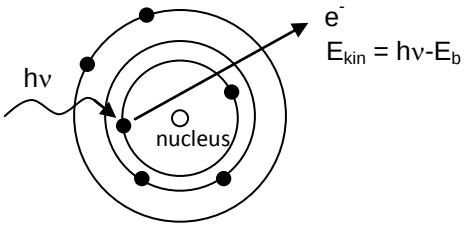

Figure 6.4: Emission of a photo-electron from the inner shell of an atom, due to the interaction of X-rays with matter.

6.1.6. Scanning Electron Microscopy

Scanning electron microscopy (SEM) is a microscopic technique which applies an electron gun to generate a high energy electron beam (5-100 keV). This beam is focused and rastered on a specimen to retrieve topographical and elemental information of a sample surface (Figure 6.5, A). Interaction of the accelerated primary electrons with the sample surface results in the production of different signals, due to the existence of different interactions. Depending on the depth of information (100 nm - 50 µm), different signals arise, each providing unique information about the sample (figure 6.5, B).

Secondary electrons and backscattered electrons are commonly used for imaging purposes. Herein, information about the sample morphology and topography is provided by detection of the secondary electrons, whereas backscattered electrons are mainly used to illustrate contrasts in composition of multiphase samples. Secondary electron-based images are created by a spatial reconstruction of the electron's intensity on a phosphor screen or a charged coupled device (CCD) detector.

The emission of secondary electrons is also accompanied by the emission of X-rays due to the relaxation of electrons that move from a higher energy state in the atom to a lower one. These X-rays are characteristic for each element and thereby, information is provided about the chemical composition of the sample surface.

Since electrons are used to generate a SEM-image, the studied samples should be characterized by electron-conducting properties. Most polymers are non-conductive and therefore, a thin conductive coating, typically gold, is applied on these samples.

Compared to light microscopy, SEM imaging is characterized by a superior lateral resolution and depth of field [5-7].

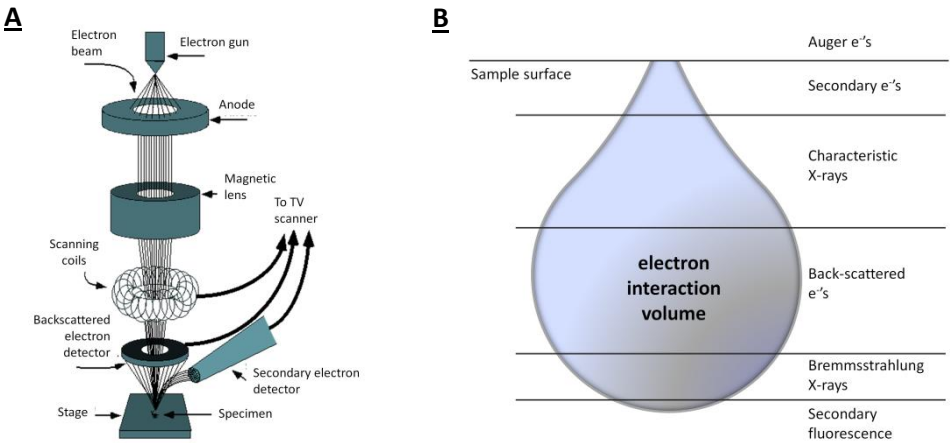

Figure 6.5: Instrumentation of a SEM device (a). Depending on the depth of information, different signals can be detected, each providing unique information about the studied sample (b)

6.1.7. Profilometry measurements

In order to study the topography of samples, profilometry measurements can be conducted. In case of contact profilometry, a finely pointed tip is moved over the sample. Herein, vertical movements of the stylus are converted into numerical information. It is a very reproducible technique, which provides a two-dimensional description of the surface. This technique only allows characterization of surface features which are larger than the stylus point diameter (µm size). Due to measuring, distortions of the surface topography might be manifested. In case the latter would impose major issues, non-contact profilometry measurements can also be conducted. In this case, no tip is used, but a laser beam is focused onto the sample surface. Light reflections are recorded and transformed into numerical information.

6.1.8. Atomic Force Microscopy (AFM)

Apart from profilometry, AFM can be used to obtain high resolution topographical information from the surface. In this case, a fine pyramidal siliciumnitride tip is mounted onto a flexible cantilever, which is attached to a piezo tube. When the tip is brought into close contact with the sample surface, interaction forces (such as van der Waals interactions and electrostatic forces) will be created between both the tip and the sample (atoms). Because of these interactions, the cantilever will undergo a deflection, which is detected by a photodiode. The latter is enabled through the use of a laser beam, which is reflected off a mirror present on the cantilever arm. Data arising from these measurements are then used as an input signal for a measuring system.

Again, the tip shape and diameter will determine the spatial resolution of the measurements. Compared to profilometry, much smaller diameters are applied. Furthermore, AFM can be considered less destructive compared to profilometry.

AFM measurements can be conducted in different modes including the contact, the non-contact and the tapping mode. In the first case, the tip is in contact with the sample and the

repulsive interaction forces are recorded, which are caused by an overlap between the electron clouds of the tip and surface. A disadvantage of this mode includes its more destructive nature, although less severe, compared to profilometry.
For both the non-contact and tapping mode, the cantilever is oscillating. In the former case, the cantilever remains close to the sample at all times (5-15 nm distance), without physical contact. Herein, imaging results from the detection of longer distance interactions, as mentioned above. In the latter case, at the lowest point of the oscillation cycle, the cantilever tip actually gets in contact with the sample. The force interaction of tip and surface influences the amplitude of oscillation and the amplitude change is translated into topographical information. The tapping mode combines the high resolution of the contact mode and the non-destructive nature of the non-contact mode.

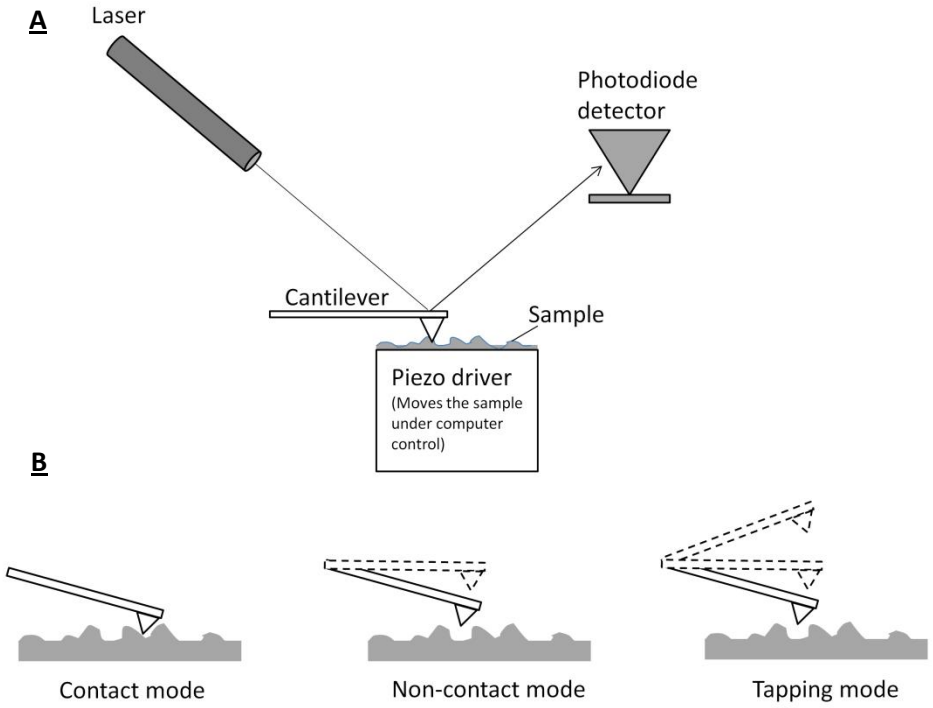

Figure 6.6: Representation of the AFM measurement principle (A) and the different measurement modes (B).

6.1.9. Infrared spectroscopy

Infrared spectroscopy is a standard technique used in organic chemistry for structure analysis, but also as an analytical technique to study the purity of compounds. Herein, organic molecules are exposed to infrared radiation and in case the light energy matches the energy of a specific molecular vibration, absorption occurs. Both the energy of the light and the amount of light absorption are molecule-specific and allow for structure elucidation.
Typically, IR measurements are performed in the mid-IR region (4000-400 cm^{-1}), but in this work interest also went to the NIR region (12820-4000 cm^{-1}), since in the final glucose sensor setup, glucose will be measured in this wavelength range.

In case IR surface mapping was conducted on the samples investigated (cfr. § 6.2.2.5), attenuated total reflectance (ATR) is measured instead of light absorption. To this end, an optically dense crystal with a high refractive index is applied. The IR beam is directed onto the crystal at an angle which exceeds the critical angle for internal reflection. This reflectance results in an evanescent wave that extends beyond the surface of the crystal into the sample held in close contact with the crystal. Due to the interactions of the IR beam with the sample, absorption of IR energy will occur and as a consequence the evanescent wave will be attenuated. Based on the attenuations, measured by the detector, the IR spectrum is generated [8].

6.1.10. Radiolabeling experiments

Radiolabeling of proteins and other molecules with a radio-active element is a frequently used method in assays, localization and for imaging applications. Typical examples of radio-active markers in biological studies are ^{14}C, ^{32}P, ^{35}S, ^{3}H, ^{125}I en ^{131}I.
Since iodination includes a common method of adding a tracer with high specific activity to a protein of interest, this method was also used in this work to label VEGF and VE-cad AB. As mentioned above, two radio-active isotopes of iodine are commonly used. The decay of ^{131}I is characterized by β- and γ-emission, whereas for ^{125}I , the decay is characterized by electron capture, followed by γ-emission. Herein, ^{131}I emits 3-10 times more energetic electromagnetic γ rays compared to ^{125}I. As a consequence, higher detection sensitivities are obtained in case the former marker is used. Nevertheless, because of its higher safety, its less damaging nature and its longer half-life (60 days cfr. 8 days for ^{131}I), ^{125}I can be considered as the most suitable isotope to label biological compounds such as ABs and growth factors [9-10].
Two methods are frequently used to perform the iodination of biological compounds. In the direct method, labeling of the biomolecule is directly done in the presence of an oxidizing agent. The indirect method makes use of an intermediate compound, which is labeled and subsequently used to label the molecule of interest. In the current work, the direct method is applied, which requires the presence of an oxidizing agent. Various oxidizing agents have already been reported such as N-chlorotoluenesulfonamide (Chloramine-T) and the complex lactoperoxidase/H_2O_2 [10]. In this work, Iodogen is used as oxidizing agent to permit the in-situ formation of an electrophilic radio-active iodine species (figure 6.7) [11-12]. This electrophilic halogen species permits reaction with molecules which contain activating groups such as activated aryl functions including aniline derivatives and phenols. As a consequence, in case of VEGF and VE-cad AB, the presence of tyrosine and histidine in their amino-acid sequence is a prerequisite to enable electrophilic aromatic substitution of the electrophilic iodine. Herein, tyrosine can incorporate two iodine-atoms whereas for histidine this number is limited to one (figure 6.7). Furthermore, to allow for the iodination reactions, neutral or more alkaline conditions should be established. At physiological pH, mainly tyrosine will be targeted, whereas at pH>9, also histidine will become susceptible towards iodination.

Nevertheless, in the latter case, the histidyl reactivity will also be influenced by other factors, such as the protein structural properties [13]. Finally, in case of acidic conditions, the protein will lose its activity, which should be avoided at all times. In this work, iodination of tyrosine was targeted.

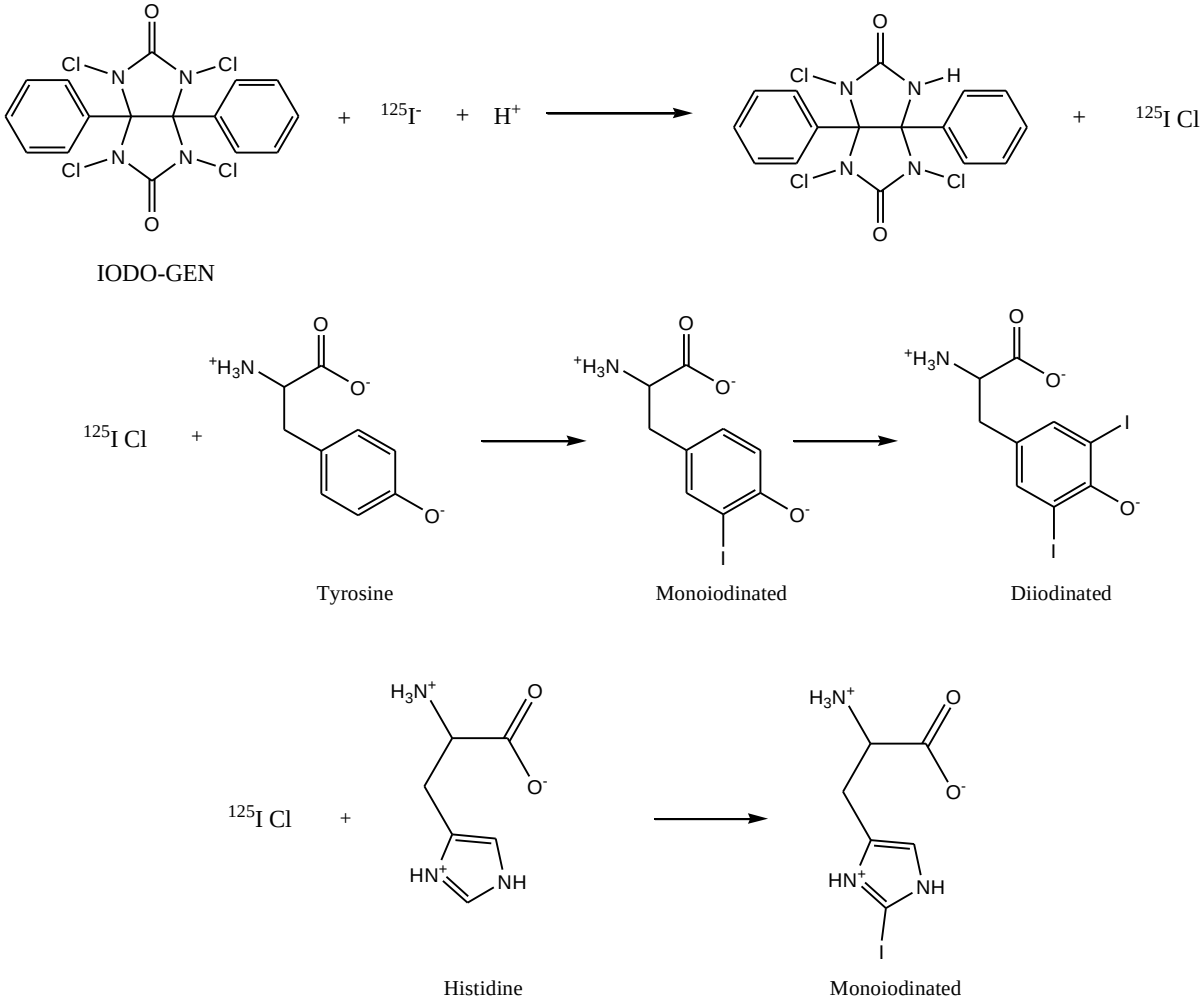

Figure 6.7: The formation of an electrophilic ^{125}I species with the help of IODO-GEN. Via electrophilic aromatic substitution, the radio-active marker is introduced in tyrosine and histidine amino acids, present in the VEGF and AB structure.

6.1.11. Fluorescence microscopy.

When a molecule is irradiated with high energy light, this energy will be absorbed by the molecule, thereby becoming excited and move from the ground state to a higher energy level. Subsequently, relaxation will occur with light emission as a consequence. Due to vibrational energy losses, the molecule will emit a photon of lower energy (i.e. with a higher wavelength) when going back from the excited to the ground state. This physical phenomenon, called fluorescence, is the basis for fluorescence microscopy imaging techniques.

In this work, two different principles of fluorescence microscopy are used including widefield microscopy and confocal fluorescence microscopy (figure 6.8).

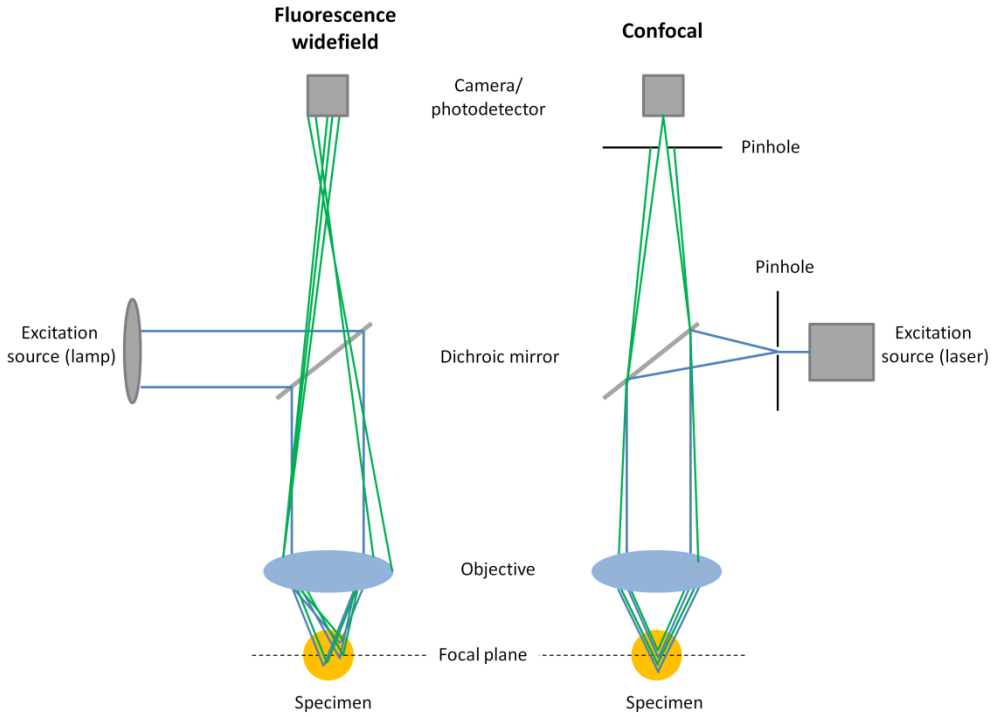

Figure 6.8: Schematic representation of the widefield and confocal fluorescence imaging process [14].

In conventional fluorescence microscopy, light of a specific wavelength (or a defined band of wavelengths), often in the ultraviolet, blue or green regions of the visible spectrum, is produced by passing multispectral light from an arc-discharge lamp or other source (e.g. a mercury or xenon source) through a wavelength selective excitation filter (not shown in figure 6.8). Next, the light is guided towards a dichromatic mirror which reflects the selected (shorter) wavelengths through the microscope's objective, in order to illuminate the sample with intense light. If the specimen is fluorescent, the emission light gathered by the objective passes back through the dichromatic mirror (transmits light of longer wavelength) and is subsequently filtered by a barrier (or emission) filter (not shown in figure 6.8), which blocks the unwanted excitation wavelengths. In this case of epifluorescence, the objective is used by both the illuminating light and the fluorescing light, in conjunction with a dichromatic mirror. In case of reflected light microscopy, a beamsplitter is used instead of a dichromatic mirror.

In contrast to widefield microscopy, where the entire specimen is illuminated, confocal microscopy only illuminates one specific spot in the sample at a time. In order to create images, one or more focused laser beam lights are scanned across the specimen. The images produced by scanning the specimen in this way are called optical sections. Apart from point illumination, the technique also makes use of a spatial pinhole in front of the detector to restrict the light reaching the detector to only the focal plane. This technique is

characterized by an improved optical resolution and contrast and it allows to collect serial optical sections of thicker specimens (so-called z-stacks) [14-15].

6.2. Experimental methods

Apart from various experimental techniques, various methods and protocols were elaborated and applied to obtain the results presented in chapters 2-5. This section summarizes the various applied methods as applied per chapter.

6.2.1. Chapter 2: Development of a flexible PMMA-based packaging for an optical glucose sensor.

6.2.1.1. Production of PMMA- and PEG-based copolymers

Methyl methacrylate (MMA; Sigma Aldrich) was distilled prior to use. Poly(ethylene glycol) monomethylether monomethacrylate (PEGMA) with molecular weights of 500 and 1100 g/mol and poly(ethylene glycol) dimethacrylate (PEGDMA) with molecular weights of 550, 750 and 1154 g/mol (Sigma Aldrich) were applied as received. In order to produce polymer sheets, an initiator (i.e. Irgacure 2959, BASF) / monomer solution (2 mol% compared to the amount of monomer double bonds) was injected in a pre-shaped silicone spacer (James Walker), which was placed between two teflon foil (Holders technology) covered glass plates. Subsequently, the samples were UV-irradiated at both sides (UV-A, 365 nm, 13 mW/cm^2, distance UV-lamps: 3 cm). Optimization of the UV irradiation times was performed by the evaluation of polymer samples obtained after different UV irradiation times by ^{1}H NMR spectroscopy (Bruker 300 MHz spectrometer). In case of PMMA, samples were dissolved in $CDCl_3$ whereas for PEGDMA, a soxhlet extraction of 24 hours in ethanol had to be performed in order to study the polymer networks. Determination of the conversion percentage of PMMA was enabled by comparing the proton integrations of the monomer double bonds (δ = 5.98 ppm and 5.44 ppm) with the sum of the O-CH_3 polymer and monomer protons (δ =3.53 ppm and 6.69 ppm respectively). In case of PEGMA, similar calculations were performed, but for PEGDMA, full conversion was assumed when the disappearance of the double bond protons in the soluble fraction was attained.
The various NMR peak annotations of the starting monomers are given below:

***MMA**: ^{1}H NMR* (CDCl3;300 MHz): δ = 6.02 ppm (1H,s, **H**$_2$C=C-), δ 5.47 ppm (1H,s, **H**$_2$C=C-), δ = 3.69 ppm (3H, s, C**H**$_3$-O-), δ = 1.83 ppm (3H, s, C**H**$_3$-C=CH_2);
***PEGMA**: ^{1}H NMR* (CDCl3;300 MHz): δ = 6.02 ppm (1H,m, **H**$_2$C=C-), δ 5.47 ppm (1H,m, **H**$_2$C=C-), δ = 4.19 ppm (2H, t, -C=OO-C**H**$_2$-CH_2-), δ = 3.64 ppm (2H, t, -C=OO-CH_2-C**H**$_2$-), δ = 3.54 ppm (28 H, m, -O-C**H**$_2$-C**H**$_2$-O-), δ = 3.44 ppm (2H, m, C**H**$_2$-O-CH_3), δ = 3.27 ppm (3H, s, -O-C**H**$_3$), δ = 1.84 ppm (3H, s, C**H**$_3$-C=CH_2).

***PEGDMA**: ^{1}H NMR* (CDCl3;300 MHz): δ = 6.02 ppm (1H,s, **H**$_2$C=C-), δ 5.47 ppm (1H,m, **H**$_2$C=C-), δ = 4.19 ppm (4H, t, -C=OO-C**H$_2$**-CH$_2$-), δ = 3.64 ppm (4H, t, -C=OO-CH$_2$-C**H$_2$**-), δ = 3.54 ppm (13H, m, -O-C**H$_2$**-C**H$_2$**-O-), δ = 1.84 ppm (6H, s, C**H$_3$**-C=CH$_2$)

6.2.1.2. Production of BuMA, EHMA and LMA-based copolymers

n-Butyl methacrylate (BuMA) and 2-ethylhexyl methacrylate (EHMA) monomers were purchased from Sigma Aldrich and purified by distillation. Lauryl methacrylate (LMA; Sigma Aldrich) was used as received. Polymer production was performed similar to the PEG-based materials, although apart from Irgacure® 2959, Irgacure® 651 (BASF) was also evaluated (see chapter 2). Optimization of the UV irradiation times was again performed by the evaluation of the polymer samples obtained after different UV irradiation times by ^{1}H NMR spectroscopy (Bruker 300 MHz spectrometer). Herein, determination of the conversion percentages was enabled by comparing the proton integrations of the unreacted methacrylate protons (δ≈ 6 ppm and 5.5 ppm) with the sum of the O-CH$_2$ polymer and monomer protons (δ ≈ 4.05 - 4.12 ppm). Again, in case a crosslinker was added to the polymer formulation, the conversions were evaluated from the soluble fractions, as obtained via soxhlet extraction. The different NMR peak annotations of the starting monomers are indicated below:

***BuMA**: ^{1}H NMR* (CDCl3;300 MHz): δ = 6.03 ppm (1H,m, **H**$_2$C=C-), δ 5.47 ppm (1H,m, **H**$_2$C=C-), δ = 4.09 ppm (2H,t, -O-C**H$_2$**-), δ = 1.88 ppm (3H, t, C**H$_3$**-C=CH$_2$), δ = 1.6 ppm (2H, quin, O-CH$_2$-C**H$_2$**), δ = 1.34 ppm (2H, sex, C**H$_2$**-CH$_3$), δ = 0.89 ppm (3H, t, CH$_2$-C**H$_3$**)
***EHMA**: ^{1}H NMR* (CDCl3;300 MHz): δ = 6.08 ppm (1H,m, **H**$_2$C=C-), δ 5.52 ppm (1H,m, **H**$_2$C=C-), δ = 4.05 ppm (2H, dd, -O-C**H$_2$**-), δ = 1.93 ppm (3H, t, C**H$_3$**-C=CH$_2$), δ = 1.61 ppm (1H, m, CH$_2$-C**H**-CH$_2$), δ = 1.43-1.30 ppm (8H, m, -C**H$_2$**-C**H$_2$**-C**H$_2$**-CH$_3$ and –CH-C**H$_2$**-CH$_3$), δ = 0.9 ppm (6H, m, CH$_2$-C**H$_3$**)
***LMA**: ^{1}H NMR* (CDCl3;300 MHz): δ = 6.07 ppm (1H,m, **H**$_2$C=C-), δ 5.51 ppm (1H,m, **H**$_2$C=C-), δ = 4.12 ppm (2H,t, -O-C**H$_2$**-), δ = 1.92 ppm (3H, t, C**H$_3$**-C=CH$_2$), δ = 1.65 ppm (2H, quin, O-CH$_2$-C**H$_2$**), δ = 1.25 ppm (18H, m, -(C**H$_2$**)$_9$-CH$_3$), δ = 0.86 ppm (3H, t, CH$_2$-C**H$_3$**)

6.2.1.3. Soxhlet extraction

All soxhlet extractions were performed for a minimum of 24 hours with ethanol as extraction solvent. Figure 6.9 demonstrates the experimental setup. A weighed sample was placed in the soxhlet chamber. Upon heating of the extraction solvent (ethanol), it is evaporated and slowly fills the soxhlet chamber. As soon as the chamber is completely filled, it is emptied via a siphon arm, in a continuous way, allowing to slowly release and enrich the soluble fraction from the solid sample.
After extraction, the solid sample was dried in a vacuum oven (40°C)

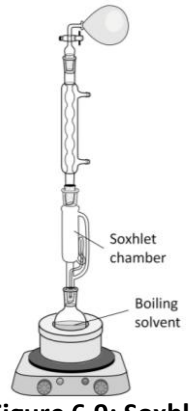

Figure 6.9: Soxhlet extraction setup

and based on the weight before and after extraction, the percentage of soluble fraction could be determined. Furthermore, identification of the soluble fraction is facilitated, by evaporating the solvent, which is collected in the round bottom flask, and by dissolving the rest fraction in $CDCl_3$. In this way, structure analysis could be performed using ^{1}H-NMR spectroscopy.

6.2.1.4. Gel Permeation Chromatography

The molecular weights and molecular weight distributions (expressed by PD, the polydispersity) of the non-crosslinked polymers were determined via gel permeation chromatography (GPC) (Waters 2695), equipped with a refractive index detector (Waters 2414). Separations were performed on a mixed D column (60 cm in length, 5 µm particle size; Polymer Laboratories), combined with a PLgel (5 µm) guard column. Chloroform was used as eluens with a flow of 1 ml/min. Prior to sample injection, all polymer solutions (10-20 mg/ml in chloroform) were filtered with 0.45 µm Chromafil®Xtra PTFE 45/25 filters (Macherey Nagel). PMMA standards with different molecular weights (5000, 20000, 50000 and 150000 g/mol; Sigma Aldrich) were used for calibration.

6.2.1.5. Tensile tests

A universal tester 10-KM (Hounsfield Test Equipment Ltd), equipped with a load cell of 100 and 1000 N was used for mechanical analysis. All measured specimens were dog bone shaped (25 mm in gauge length and 4 mm in width, according to ISO 37-2). The sample thickness was assessed using a caliper and was averaged at 1 mm. The unidirectional tension speed was 25 mm/min. For each composition, 10 measurements were performed and averaged. The elastic modulus (MPa), the elongation (%) and force at break (N) were recorded using the QMAT software.
When the influence of PBS buffer was studied on the mechanical properties, similar dog-bone shaped materials were incubated for 48 hours in PBS-buffer (10 mM, pH 7.4) at 37°C, prior to measurement.

6.2.1.6. Swelling experiments

To determine the swelling percentage of the materials, three disc-shaped samples (d = 1 mm) per condition were freeze-dried and weighed (initial mass, m_0). Subsequently, the samples were incubated for 24 hours in deionized water at 37 °C. After swelling, the samples were again weighed (m_t) and swelling degrees were calculated using equation 6.5 (§ 6.1.3).
When evaluating the polymer production of crosslinked materials (§ 2.3.3), an appropriate solvent had to be selected which is able to dissolve the building blocks. In case of MMA/PEGDMA copolymer evaluation, acetone was used and the swelling experiments were conducted in a similar way as described above.

6.2.1.7. NIR optical measurements

NIR measurements were conducted with an Agilent 680 Series FTIR (Agilent Technologies Belgium, Diegem, Belgium). Herein, the samples were fixated in the sample compartment and NIR-light (12820-4000 cm^{-1}) was transmitted through the samples. Measurements were processed by Resolutions Pro software (Agilent Technologies Belgium, Diegem, Belgium).

6.2.1.8. Hermeticity testing

Test samples consisting of copper meanders of various line widths (30, 40 and 50 µm) were covered with a PMMAPEG or PLMA network. The polymer coating was applied on the test samples in a similar way as the polymer sheets were produced. The setup is displayed in figure 6.10. A 250 µm thick spacer with a rectangular central cavity was taped over the region of the test sample that contained the cupper lines. A needle was inserted inside the spacer to allow for monomer injection and finally, the spacer was covered with a small teflon foil covered glass plate. Upon UV irradiation, the cupper meanders were covered by a 250 µm thick polymer layer.

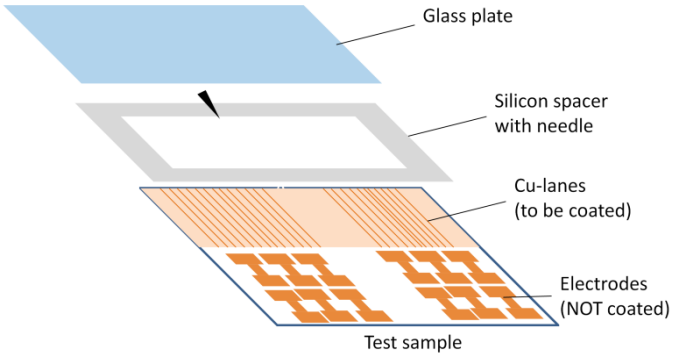

Figure 6.10: Polymerization set-up to coat the cupper lines, present in the test sample.

Next, a glass ring was glued over the Cu meanders, creating a cavity which is filled with PBS buffer (10 mM, pH 7.4) and the test samples were incubated at 37°C or 70°C. Every 3 hours, for a period of 800 hours, the resistance was measured for the various cupper line widths.

6.2.1.9. Cytotoxicity testing.

Cytotoxicity was evaluated according to the ISO10993 part 5 standards of extraction tests with MTT (3-(4, 5-dimethylthiazol-2-yl)-2,5-diphenyl-tetrazolium bromide (MTT, Merck Promega) as a detection molecule. Human foreskin fibroblasts (HFF) (American Type Culture Collection, ATCC) were cultured (37°C, 5% CO2) in a DMEM High Glucose GlutaMAX-medium supplemented with fetal bovine serum, L-glutamine, sodium pyruvate and penicillin-streptomycin (Gibco, Life Technologies, Ghent, Belgium). From an ethylene oxide sterilized polymer sheet, 0.5 g was cut and placed in 1 mL of HFF culture medium at 37°C. The extraction medium was diluted after 8 days (1:1) with HFF culture medium and then placed

on top of a monolayer of HFF. After 24 hours, the medium was discarded and replaced by 200 ml of a 0.5 mg/ml MTT containing medium, followed by an incubation for 4 hours at 37°C. The MTT-solution was discarded and replaced by 200 ml of lysis-buffer (0.1% of Triton TM-X-100 [Fluka, Sigma-Aldrich, Bornem, Belgium] in isopropanol/0.04M HCL [Chem-Lab, Zedelgem, Belgium/UCB, Brussels, Belgium]), and incubated for 30 min at 37°C. Absorbance was measured at 570 nm with KCjunior software on a Universal Microplate Reader EL800 (BIO-TEK Instruments Inc., Bad Friedrichshall, Germany). The viability was calculated as percentage of the control (i.e. no polymer extract was added).

In case of the LMA-based materials, the polymer samples were only incubated for 24 hours at 37°C in HFF medium. Different dilutions were prepared from the extraction medium, being 1/1, 1/4 and 1/8, before incubating cells for 48 hours in the diluted media.

6.2.2. Chapter 3: Surface activation and functionalization of methacrylate-based polymers

6.2.2.1. Plasma treatment

Plasma treatment of polymer sheets or discs was conducted with a cylindrical dielectrical discharge plasma reactor, Model Femto, version 3 (Diener Electronic, Germany). The O_2 or Ar gas pressure (Air liquide) was kept at 0.8 mbar and the applied power was 100 W.
In case plasma experiments were conducted at the Department of Applied Physics, a home-made device was used. Herein, the experimental set-up consisted of two circular copper plates (diameter of 7 cm) covered with glass plates, which acted as dielectric barrier. The distance between the glass plates was 7 mm and the electrodes were placed within a cylindrical enclosure made of PVC (inner diameter: 25 cm, height: 25 cm). After placing the polymer sample on the lower glass plate, the chamber was evacuated below a pressure of 2 kPa. The plasma chamber was subsequently flushed for 3 minutes with plasma gas at a rate of 5.2 slm (standard liters per minute) while keeping the pumping system switched on. After 3 minutes of flushing, the vacuum pump was turned off and the chamber was filled with helium, argon or oxygen gas (Air Liquide) at a rate of 5.2 slm. When atmospheric pressure (101 kPa) was reached, the plasma chamber was pumped down to 5 kPa while the gas flow was decreased to 0.2 slm. Subsequently, the AC power source was turned on while the pressure in the discharge chamber was maintained at 5 kPa by slightly pumping during plasma treatment [16].

6.2.2.2. Post-plasma grafting of AEMA

Grafting of AEMA onto the polymer surfaces consisted of two steps. First, the samples were treated with Ar plasma for 0.2 (optimum for PLMA), 0.5 (optimum for PMMAPEG) or 0.7 minutes. Subsequently, the activated polymer samples were placed in a quartz 6-well plate and immersed in a 1M aqueous 2-aminoethylmethacrylate (AEMA, Polysciences) solution. The latter is obtained by dissolving AEMA in degassed de-ionized water. Next, the 6-well

plate was covered with a quartz glass plate and irradiated by UV-light (λ_{max} = 350 nm) for 1 hour to enable grafting. Afterwards, the samples were rinsed with de-ionized water (3 times water exchange) and incubated overnight to remove unreacted AEMA. Finally, the samples were dried under a gentle stream of nitrogen gas and stored in a dessicator until the next modification step or analysis.

6.2.2.3. Surface functionalization with polydopamine.

In case of PMMAPEG modification, the deposition of polydopamine was established by applying and comparing two different protocols. The first protocol was described earlier by Lee et al [17]. Using this protocol (protocol I), the samples were incubated for 24 hours in a 2 mg/ml dopamine.HCl (DA) (Sigma Aldrich) solution in Tris buffer (10^{-3}M, pH 8.5; prepared from Trizma base, Sigma Aldrich). Protocol II includes an additional step as the samples were first immersed in Tris buffer (pH 8.5), followed by addition of the dopamine.HCl salt (2 mg/ml). In order to evaluate the possibility to further improve the adhesion of polydopamine onto the developed materials, both protocols were also combined with an oxygen plasma pre-activation step (1 minute, 0.8 mbar), referred to as plasma + protocol I (Ipl) and plasma + protocol II (IIpl).
In case of PLMA, protocol I was evaluated in combination with a plasma pretreatment step. Herein, two gasses were selected including Ar and O_2 gas (both 1 minute, 0.8 mbar).

6.2.2.4. SCA measurements

To determine the wettability of the modified surfaces, a SCA 20 Instrument (Dataphysics), equipped with a light source and high speed video system with CCD cameras was used. To determine the static contact angles of the (non-)modified polymer surfaces, the sessile drop method was used and for each material and condition, three samples were measured and for each sample, a minimum of three drops was recorded. For each drop, the static contact angle was determined 5 seconds after the first contact with the surface using the circle fitting of the imaging software SCA20 (version 2.1.5).

6.2.2.5. IR mapping

IR mapping was conducted with a Perkin Elmer Spotlight 400 FTIR Imaging System in combination with a Spectrum 100 FT-IR Spectrometer. The wavenumber of the light was varied between 744 and 4000 cm^{-1}. Since IR-mapping was used, the IR-light beam was scanned over the polymer surface to obtain different spectra on different locations of the material. One sample per test condition was analyzed and a spectrum was recorded for three different spots on the surface.

6.2.2.6. XPS measurements

To determine the elemental compositions, an ESCA S-probe VG monochromatised spectrometer equipped with an Al Ka X-ray source (1486 eV) was used.
Survey scans were recorded on three spots of each sample and the elemental composition of the top surface could be determined by calculating the peak areas in the obtained spectra. A minimum of two samples per test condition were measured. Furthermore, by measuring carbon details, insight on the type of chemical bonds between carbon and other elements on the surface, could be obtained.

6.2.2.7. AFM measurements

The surface roughness of the samples was characterized using atomic force microscopy (AFM). The images were obtained under ambient test conditions with a multimode scanning probe microscope (Digital Instruments, USA) equipped with a Nanoscope IIIa controller. After recording 50 µm scans in tapping mode with a silicon cantilever (OTESPA, Veeco), surface roughness analysis was enabled using the Nanoscope software version 4.43r8.

6.2.2.8. SEM measurements

SEM analysis was performed on a JEOL JSM-5600 instrument. The instrument was used in the secondary electron mode (SEI) at an acceleration voltage of 20 kV. Prior to analysis, all samples were coated with a thin gold layer (ca. 20 nm) using a plasma magnetron sputter coater. Images were recorded at three different surface areas of each sample.

6.2.2.9. Statistical analysis

The average and standard deviations were calculated for each condition tested and statistical differences were determined via a one way ANOVA-test in the 95% confidence interval, followed by a Sidak post hoc test, for multiple comparisons. IBM SPSS Statistics Version 20 (IBM Corporation, New York, United States) software package was used as statistical software and two values were considered significantly different when $p < 0.05$. Error bars represent the standard deviations in all graphs.

6.2.3. Chapter 4: Surface biofunctionalization to enhance the cell interactivity of methacrylate-based materials

6.2.3.1. Immobilization of a Gel B Layer

The deposition of Gel B (Rousselot) onto PMMAPEG was established by first applying a polydopamine coating using protocol I. Next, the samples were incubated overnight at 40°C in a gelatin B solution, by dissolving the appropriate amount of Gel B (0.5, 1 or 2 w/v%) in Tris buffer (10^{-3}M, pH 8.0). After incubation, the samples were rinsed with milliQ water and gently dried with N_2 gas.

6.2.3.2. Immobilization of angiogenic factors onto PDA-modified surfaces

Disk-shaped samples (0.8 or 1 cm in diameter, 1 mm thick) were punched from a PMMAPEG or PLMA polymer sheet. Prior to AB and/or VEGF immobilization, the sample surfaces were modified with PDA. In case of PMMAPEG, protocol I was applied whereas for PLMA, the same protocol was combined with an oxygen plasma pre-treatment step, as described previously. Next, the samples were placed in a 48 well plate and incubated overnight at 37°C, in 200 µL of the angiogenic factor solution. In case recombinant human vascular endothelial growth factor 165 (VEGF-165, Thermo Scientific) was immobilized, a solution of 1 µg/ml was prepared in Tris buffer (10^{-3}M, pH 8.5). Herein, the buffer was enriched with bovine serum albumin (BSA, Roche Diagnostics, 0.01 g/ml), as prescribed by the VEGF supplier. In case vascular endothelial cadherin antibody (BV9) (VE-cad AB, Santa Cruz Biotechnology) was immobilized, a 4 µg/mL solution was prepared in PBS buffer (pH 7.4). After incubation, all samples were rinsed three times with PBS buffer in order to remove unreacted VEGF or AB. A similar procedure was conducted on the blank materials, without PDA coating.

When both angiogenic factors were immobilized simultaneously on the sample surface, the concentrations of 1 µg/ml VEGF (in Tris buffer) and 4 µg/ml VE-cad AB (in PBS) were maintained, meaning that the overall angiogenic concentration was set to 5 µg/ml.

In case the synergetic effect of the two factors was studied, identical concentrations and immobilization conditions were used. Herein, VEGF-immobilized samples (4 µg/ml in Tris buffer pH 8.5) and AB-immobilized samples (4 µg/ml in Tris buffer pH 8.5) were compared with VEGF/AB immobilized samples with a total angiogenic factor concentration of 4 µg/ml (Tris buffer pH 8.5).

6.2.3.3. Immobilization of angiogenic factors onto AEMA-modified surfaces

Disk-shaped samples (0.8 or 1 cm in diameter, 1 mm thick) were punched from a PLMA polymer sheet. Prior to AB and/or VEGF immobilization, the sample surfaces were treated with Ar plasma during 0.2 minutes, followed by AEMA grafting as described elsewhere (see § 6.2.2.2.).

Next, for the immobilization of VEGF and AB, EDC chemistry was applied. To this end, the disk-shaped samples were placed in a 48 well-plate and incubated in 200 µl of AB or VEGF solution. Next, 10 µl of a 0.5 mg/ml 1-ethyl-3-(3-dimethylaminopropyl) carbodiimide (EDC, Sigma Aldrich) solution was added and reacted for 4 hours at room temperature. In case the sulfo-NHS mediated strategy was followed, after EDC-addition, 10 µl of a 0.7 mg/ml N-hydroxysulfosuccinimide (sulfo-NHS, Sigma Aldrich) solution was also added. After 4 hours of reaction time, all samples were rinsed with PBS buffer and incubated overnight at 37°C in order to remove the unreacted species.

The VEGF and AB solutions were prepared in two different buffer types, being PBS buffer (10 mM, pH 7.4) and MES buffer (50 mM, pH 6.1; prepared from 2-(N-morpholino)ethanesulfonic acid (MES) hydrate, Sigma Aldrich) until concentrations of

respectively 1 and 4 µg/ml were obtained. Again, in case of VEGF immobilization, BSA was added to the buffer solution (0.01 g/ml).
Similar to the PDA immobilization, when both AB and VEGF were immobilized, the concentrations of 1 µg/ml VEGF (MES buffer) and 4 µg/ml VE-cad AB (MES buffer) were maintained, meaning that the overall angiogenic concentration was set to 5 µg/ml. In case the synergetic effect was studied between both factors, VEGF-immobilized samples (4 µg/ml in MES buffer, pH 6.1) and AB-immobilized samples (4 µg/ml in MES buffer, pH 6.1) were compared to VEGF/AB immobilized samples with a total angiogenic factor concentration of 4 µg/ml (MES buffer, pH 6.1).
In case of oriented AB immobilization, the AEMA coated samples were immersed in a 0.42 mg/ml succinimidyl-6-hydrazino-nicotinamide (S-Hynic; DivBioScience, the Netherlands) solution for 2 hours at room temperature. To this end, 1 mg of S-hynic was dissolved in 200 µl DMF and diluted with PBS buffer (pH 8) to obtain the desired concentration of 0.42 mg/ml. In the meantime, in order to oxidize the carbohydrate functions of the AB, 60 µl of a 10 mg/ml sodium periodate ($NaIO_4$, Sigma Aldrich) solution was added to 250 µl of VE-cad AB (200 µg/ml) and reacted for 30 minutes. After reaction, the AB was purified with a PD-10 desalting column (packed with Sephadex™ G-25 Medium; GE Healthcare, Belgium), according to the prescribed supplier protocol and purified AB (14.3 µg/ml) was obtained and diluted (to 4 µg/ml). Finally, after 2 hours of S-Hynic incubation, the samples were rinsed three times with PBS buffer and incubated for 1 hours in 200 µl of the oxidized AB solution.

6.2.3.4. SCA and XPS measurements

All SCA and XPS measurements were conducted similarly as described in §6.2.2.4 and §6.2.2.6.

6.2.3.5. Profilometry measurements

Profilometry measurements were conducted with a stylus contact profilometer (Dektak 8) and were taken electromechanically by moving the sample under a diamond-tipped stylus with a radius of 2.5 µm. A high-precision translation stage moved the sample under the stylus according to the user-programmed scan length (7 mm), translation speed (35 µm/sec) and stylus force (3 mg). As the stage moved across the sample, surface variations caused the stylus to be translated vertically. The resultant vertical motion of the stylus is then translated into height variation information by dedicated computer algorithms. For each material and test condition, three measurements were recorded over a scan length of 7 mm with a resolution of 0.12 µm and the RMS surface roughness was determined over the same length. Averages of the three measurements were calculated, as well as the related standard deviations. Calculation of the RMS value for each scanned line was performed by applying the formula,

$$RMS = \sqrt{\frac{\sum (Z_i - Z_{avg})^2}{N}},$$

with Z_{avg} the average height (Z) value within the measured area (7 mm); Z_i being the current Z value and N the number of points recorded within the scanned area.

6.2.3.6. Radiolabeling experiments

Radio-iodination of VE-cad AB and VEGF was performed as described by Pierce Biotechnology Inc. (Rockford, IL, USA) [18]. Iodogen (1,3,4,6-tetrachloro-3a,6a-diphenylglycouril, Pierce, USA) was dissolved in chloroform to a concentration of 2 mg/ml and 100 µl was added to a 1.5 ml conical vial. Chloroform was evaporated under a gentle N_2 flow at room temperature, hereby coating the Iodogen onto the inner surface of the vial. The Iodogen coated vials were stored in a dessicator at 5°C prior to use.
To a Iodogen coated reaction vessel, the required volume of the AB/VEGF stock solution was added, immediately followed by the addition of 100 µl of a 0.01 M PBS buffer (pH 7) and 10-20 µL radio-iodide solution in 0.05 N NaOH (^{125}I; GE/Amersham Health, Eindhoven, The Netherlands). This mixture was incubated at ambient temperature under slight shaking for 15 minutes. The overall radiochemical purity (RCP) was determined using iTLC-SG chromatographic strips (Gelman Sciences) and citrate-buffer (0.068 M citrate, pH 7.4) as eluent. The concentration of AB and VEGF in the final solution was adjusted to suit the experimental conditions, specified elsewhere (see § 6.2.3.2 and 6.2.3.3) and the specific activities were calculated accordingly.
Next, disk-shaped samples (1 cm diameter, 1 mm thick) were incubated in 200 µl of the radiolabeled VEGF and AB solutions according to the immobilization protocols, described elsewhere (see § 6.2.3.2 and 6.2.3.3). After incubation, the samples were rinsed in PBS and the radioactivity was measured with a Geiger Muller teller.
In case of the AB orientation study, secondary antibodies were radiolabeled, including anti-mouse IgG (Fab specific) FITC-conjugated (Sigma Aldrich) and IgG (Fc specific) FITC-conjugated. The same procedure as described above was used. The AB modified samples were finally incubated overnight at 37°C in 200 µl of a 80 µg/ml solution of secondary AB in PBS.

6.2.3.7. Cell culture and cell seeding

Two types of cell culture were used: fibroblasts and human umbilical vein endothelial cells (HUVECs).
Human foreskin fibroblast (HFF-1) cells were cultured in DMEM glutamax medium supplemented with 10% fetal calf serum (FCS, Gibco Invitrogen), 2 mM L-glutamine (Sigma-Aldrich, Belgium), 10 U/ml penicillin, 10 mg/ml streptomycin (Gibco Invitrogen) and 100 mM sodium-pyruvate (Gibco Invitrogen). Cells were cultured at 37 °C in a humidified atmosphere containing 5% CO_2. The medium was changed 2 times a week. Normal duman dermal fibroblasts (NHDFs, Promocell) were cultured in advanced DMEM (Gibco, Invitrogen, USA), supplemented with 2 % fetal bovine serum (FBS) and 1% penicillin/streptomycin/glutamin.

HUVECs were cultured in endothelial growth medium 2 (EGM-2, Clonics®, Lonza), at 37°C. This medium was composed of endothelial basal medium (EBM-2) and SingleQuots™ (Clonics®, Lonza) containing several supplements and growth factors. The concentration of growth factors and supplements in 500 ml basal medium was: 0.5 ml human epidermal growth factor (hEGF), 2 ml human recombinant fibroblast growth factor (hFGF-β), 0.5 ml vascular endothelial growth factor (VEGF), 0.5 ml insulin-like growth factor (R3-IGF-1), 0.2 ml hydrocortisone, 0.5 ml ascorbic acid, 0.5 ml heparin, 10 ml FBS and 0.5 ml gentamicine/amfotericine (GA-1000).
Prior to cell seeding, all samples were sterilized by ethylene oxide treatment (cold cycle, AZ Sint-Jan, Brugge, Belgium). All biological compounds (Gel B, VE-cad AB and VEGF) were subsequently immobilized under sterile conditions.

Cell seeding for the *in vitro* evaluation of PDA/Gel B coated samples.
HFF-1 cells were seeded with a density of approximately 30000 cells/cm^2 in 24-well culture dishes. Cell adhesion at day 1 was evaluated after live/dead staining. NHDFs of passage number 12 were seeded on top of the films with a cell density of approximately 5000 cells/cm^2. Cytoskeletal organization was evaluated after 2 days of incubation by immunolabeling and confocal microscopy.

Cell seeding for the *in vitro* evaluation of the substrate mechanical properties
HUVECs of passage 7 were seeded on top of the PEG-based samples with a cell density of 20000 cells/cm^2. Cell adhesion at day 1 and 7 was evaluated by a live/dead assay. Cytoskeletal organization was evaluated after 2 days of incubation by immunolabeling and confocal microscopy.

Cell seeding for the *in vitro* evaluation of VEGF and AB functionalized materials
HUVECs of passage 5-10 were seeded on top of the PEG-based samples with a cell density of 10000 cells/cm^2. Cell adhesion at day 1 and 7 was evaluated by a live/dead assay. Cytoskeletal organization was evaluated after 2 days of incubation by immunolabeling and confocal microscopy.

6.2.3.8. Live dead assay

To visualize cell distribution on the polymer discs, a live/dead staining was performed. After rinsing the films, the supernatant was replaced by 1 ml PBS solution supplemented with 2 µl (1 mg/ml) Calcein AM (Anaspec, USA) and 2 µl (1 mg/ml) propidium iodide (Sigma). Cultures were incubated for 10 minutes at room temperature, washed and evaluated by fluorescence microscopy (Type U-RFL-T, Olympus, XCellence Pro software, Aartselaar, Belgium). Evaluations were done 1 day and/or 7 days post cell seeding.

6.2.3.9. Immunolabeling assay

Actin filaments and focal adhesion points were (immuno-)labeled. All steps were performed at room temperature and a washing step consisted of 3 times 5 minutes washing in PBS buffer, unless stated otherwise. After removal of the medium, the cells were washed briefly with PBS and fixed in 4 % buffered paraformaldehyde solution for 20 minutes at room temperature. After washing the samples, the cells were permeabilized with a 0.5 % Triton X-100 in PBS solution for 5 minutes. Subsequently, cells were blocked with a 50 % FBS solution in PBS for 1 hour, washed, incubated with the primary antibody, mouse anti-paxillin (Milllipore, Overijse, Belgium; 1:1000 diluted in 50 % FBS in PBS) for 1 hour and washed again. Afterwards, the cells were incubated with the secondary antibody AlexaFluor 488 goat anti-mouse IgG (A11001, Life Technologies, Merelbeke, Belgium) for 30 minutes and washed. Next, the cells were stained with a phalloidin-rhodamine (Life Technologies) solution (1:100 diluted in PBS) and a 1 µg/ml DAPI solution (Life Technologies, Merelbeke, Belgium) for 10 minutes and washed again. The samples were mounted on a cover slide prior to microscopy measurements. All immunolabeling experiments were performed in duplicate.
The samples were investigated by means of a Nikon A1r confocal microscope mounted on a Nikon Ti Body (Nikon Instruments, France) and magnified with a 40x Plan Fluor oil objective (numerical aperture 1.3). In order to obtain a representative image of each test condition, three separate regions were randomly acquired per sample.

6.2.3.10. Confocal image processing

Image processing was performed in Fiji (http://fiji.sc), a packaged version of ImageJ freeware (W.S. Rasband, U.S.A. National Institutes of Health, Bethesda, Maryland, USA, http://rsb.info.nih.gov/ij/, 1997–2014). The focal adhesion points were quantified by means of a custom-designed image processing pipeline, which is essentially based on a high-content analysis workflow described earlier [19] and available upon request. In brief, the analysis consists of a few image preprocessing steps, followed by hierarchical segmentation of nuclei, cells and focal adhesion points (FA) to allow region-specific analysis of objects. First, image hyperstacks are projected according to the maximum axial pixel intensity and corrected for lateral illumination heterogeneity and background signals by means of a pseudo-flat field correction, which consists of dividing the image by a duplicate image smoothened with a Gaussian blur of large radius (sigma = 50). A subsequent local contrast enhancement balances for more subtle intensity fluctuations. Next, nuclear regions of interest (ROIs) are segmented in the DAPI channel after filtering with a Gaussian kernel of small radius (sigma = 3), automatic thresholding according to Otsu's algorithm and watershed-based separation. Cellular boundaries are then delineated by combining a segmentation of the median filtered Phalloidin channel, using the Triangle autothresholding algorithm, with a Voronoi tesselation on the nuclear ROIs (Boolean AND operation). Finally, FA are specifically enhanced in the FA channel by means of a Laplacian operator and binarized using the Triangle autothresholding

algorithm. Segmentation of FA can be further refined by cell-dependent peak selection, which is based on preserving only those objects (presumed FA) for which the average signal surpasses a threshold (typically defined as the average signal + 1 x std of the FA channel in the cell ROI). This feature avoids detection of noise pixels and allows for accurate segmentation of FA in cells with varying background fluorescence. The resulting ROIs were used for analyzing shape (area, aspect ratio circularity) and intensity metrics of objects larger than a predefined size (> 5 pixels) on the original image.

6.2.3.11. Statistical analysis

For all experiments, except the cell tests, statistical differences were determined via a one way ANOVA-test in the 95% confidence interval, followed by a Sidak post-hoc test for multiple comparisons. In case of cell-data, the average values of various parameters such as number of focal adhesions and circularity were statistically compared by means of a non-parametric Kruskal-Wallis test. IBM SPSS Statistics Version 20 (IBM Corporation, New York, United States) software package was used as statistical software. The boxplots were generated with R statistical freeware (The R Development Core Team) [20]. Two values were considered significantly different when $p < 0.05$. Error bars represent standard deviations.

6.2.4. Chapter 5: *in vivo* evaluation of a biofunctionalized methacrylate-based packaging for an optical glucose sensor

6.2.4.1. Production of donut-shaped implants

All implants were produced according to one of the three mold designs discussed in chapter 5 (§ 5.2). In case of mold design 2, where optical fibers were included in the implants, the fibers first needed to be mounted on a separate metal carrier. In this respect, it can be mentioned that a single mode to single mode fiber setup was selected. Prior to molding, optical fibers with glass ferrules (1.8 mm, Thorlabs) were fit in two holes of a metal carrier and were optically characterized. From these measurements, it was clear that the sensor to sensor variation of the coupling efficiency was quite large, which implied that the optical overlap between the two fibers was not optimal. This was probably related to stresses inside the carrier because of drilling of the holes. Next generation carriers should be built differently to avoid these current problems. After molding, the biocompatible PUR tubing (Braun) was introduced to the carrier and an optical connector was spliced to the fibers.

6.2.4.2. Goat implantation procedure

All *in vivo* studies were approved by the Ethics Committee of the Faculty of Veterinary Medicine, Ghent University. All animal care did comply with the EC guidelines for the care and use of laboratory animals.
Adult female goats (Saanen milk goats) with ages between 3 and 6 years and a mean body weight between 50 and 70 kg were used. The goats were housed in groups with continuous

access to food and water. Twelve hours pre-operatively, the goats were deprived of food and received medication (Neopen® 1 ml/20 kg subcutaneously [Intervet, Merck & Co., Inc, Brussels, Belgium] and Ketofen 10%® 2.2 mg/kg intramuscularly [Merial, Velserbroek, the Netherlands]) to assure relevant blood values during surgery. Before surgery the goats were premedicated using xylazine (Proxylaz®, 0.2 mg/kg IM [Prodivet, Eynatten, Belgium]). Anesthesia was induced with ketamine (Ketamine 1000®, 1.1 mg/kg [Ceva Santé Animale, Naaldwijk, the Netherlands]) and midazolam (Dormicum®, 0.03 mg/kg [Roche, Woerden, Belgium]) and maintained after tracheal intubation with an O_2 in isofluorane-mixture (Isoflo® [Abbott Lab, Wavre, Belgium]). Routine monitoring (ECG, pulsoximetry, capnography, direct blood pressure, and arterial blood gasses) was performed. Ringer's lactate solution (5 ml/kg/h [Baxter]) was administered intravenously during the anesthetic period. All animals received peroperative antibiotics (Neopen® 1 ml/20 kg subcutaneously) and non-steroidal anti-inflammatory drugs (NSAID, Ketofen 10%® 2.2mg/kg intramuscular). Post-operatively, antibiotic treatment was continued for 5 days and NSAIDs were given for 3 days.

After induction of anesthesia, the animals were placed in lateral recumbency. The skin was sharply incised and the correct implantation depth was achieved through further blunt dissection before implant positioning. Incisions were sutured (if needed in several layers) with resorbable sutures (Maxon 2/0 skin, Vicryl 2/0 muscle [Ethicon, Johnson & Johnson Medical N.V./S.A., Diegem, Belgium]) and protected with a sterile self-adhesive bandage. When all samples were implanted, the goat was transported to the recovery box. The goats were closely monitored in the post-operative period.

In the ***first experimental setup***, called ***the exploratory in vivo study***, which was intended to aid design optimization, implantation site, and packaging evaluation, three goats were used. In each goat, 18 donut-shaped PMMAPEG implants were tested. These implants consisted of PMMAPEG 1, 2 and 3 of which half of the implants had an internal diameter of 3 mm, the other half, an inner donut diameter of 6 mm. Each material was implanted subcutaneously (para lumbar fossa), retroperitoneally (ventral abdominal area), and intramuscularly (gluteus muscle region) on both flanks of the animal. Animals were euthanized after 1 month and the donuts were harvested with surrounding tissue for histological analysis.

During the ***second experimental setup, the effect of the surface modifications*** was studied. Based on the results obtained in the first experiment, PMMAPEG 1 was selected and only subcutaneous implants were performed. Herein, the materials were surface modified with PDA, PDA/VE-cad AB and PDA/GelB/VE-cad AB, as described previously (§ 6.2.2.3, 6.2.3.2 and 6.2.3.1 respectively). Non-modified materials were included in the study as a control. Again donut-shaped materials were implanted in both flanks of each animal. In total, 3 samples were produced per test condition and per time point of explantation and divided over three goats. The animals were kept alive for three months. Materials were harvested after 1 and 3 months for histological processing and analysis.

The **third experimental setup** was intended to ***evaluate the in vivo measurement of glucose*** via optical fibers. 10 sensors, comprising 5 membrane-based sensors and 5 membrane-less sensors, were implanted subcutaneously in 5 goats via a similar implantation procedure as

described before. To insert the sensor, two incisions were made at approximately 10 cm distance. A cavity was created in the subcutaneous area under the skin and the sensor was inserted from one side. Prior to insertion, the sensor was packed in a sterile drain, which was removed after the insertion. After the implantation, a metal box and protective jacket were mounted on the animal to protect the fibers and the surgical site of the animal. Due to practical issues, no surface modifications were conducted on this set of implants.
During the **fourth experimental setup**, intended to ***further study the membrane-based set-up***, two types of samples were implanted. The first group consisted of CMA-7 micro-dialysis probe, incorporated into a PMMAPEG packaging (described in § 5.5.2). Two sensors were surface modified with PDA/VE-cad AB, whereas the other two weren't. The implantation procedure was similar as described in the beginning of this paragraph. The second group of samples consisted of 6 dummy membrane sensors (described in § 5.5.3). Three different compositions were studied and two replicates per composition were implanted subcutaneously, as described above. Explantations were done 1 and 3 months post the implantation date.
Prior to implantation, all implants were sterilized by ethylene oxide treatment (cold cycle, AZ Sint-Jan, Brugge, Belgium and at Maria Middelares, Gent, Belgium) and all biological compounds (Gel B, VE-cad AB and VEGF) were subsequently immobilized under sterile conditions.

6.2.4.3. Rat implantation procedure

During a first experiment, to further study the impact of surface modification on the *in vivo* response of the glucose sensor packaging, rat experiments were conducted. Herein, 20 female normal rats (Wistar rats) and 20 female diabetic rats (Goto-Kakizaki rats) were used. In each rat, three PMMAPEG 1 disks (6 mm diameter and 1 mm thickness) were implanted subcutaneously in the back of the rats. Three conditions were studied: blank samples, PDA coated ones and disks modified with PDA/VE-cad AB. Anesthesia was induced via the inhalation of 5% isofluran (Isoflo®, Abbott Lab), mixed with O_2 and was maintained during the surgery with 1 to 1.5 % isofluran. Next, the back of the rat was shaved and disinfected with Hibitane Plus® (Mönlycke Health Care). Incisions were made and after insertion of the polymer disks, these were sutured with resorbable sutures (Vicryl 4-0; Ethicon). The skin was again disinfected with Hibitane Plus® and as a painkiller, Temgesic (Reckitt Benckiser) was administered subcutaneously. Explantation of the discs and the surrounding tissue was conducted after 2, 5, 10 and 25 days from both the normal and diabetic rats.

In the course of a second experiment, porous PCL scaffolds (6 mm diameter, 1 mm thickness and 250 µm pores) were produced with a 3D-printer (Bioscaffolder®, SYS+ENG) and surface modified with PDA and PDA/VE-cad AB. In this case, 6 samples (2 per condition) were implanted subcutaneously in the back of each rat, via the same implantation procedure as described above. In total, 6 female rats (Wistar rats) were used. the discs were explanted after 4, 7 and 14 days.

6.2.4.4. Histological analysis of the explanted samples

Preparation of the sections

Donuts from the goats or disk-shaped samples from the rats, with their surrounding tissue, were placed in 4% (para)formaldehyde for 24 h at 4°C. They were dehydrated, embedded in paraffin and 7 µm sections were cut from the donut-type goat materials on a SLEE cut 4060 microtome (SLEE medical GmbH, Mainz, Germany). In case of the disk-shaped samples, explanted from the rats, 5 µm sections were cut with a microtome (Model 2040, Reichert-Jung). Sections in the middle of the implanted materials were analyzed.

Staining and analysis of the sections

Sections were stained with hematoxylin & eosin (H&E) (Hematoxylin from VWR, Leuven, Belgium and Eosin-Y w/Phloxine (Microm, Thermo Fisher, Walldorf, Germany) to screen and study the morphology of the surrounding tissue. The staining was performed with an automated staining device (HMS 740 Robot-Stainer, MICROM international) and comprised following steps: 3 x 5 minutes incubation in toluene (UltraClear), 2 x 2 minutes isopropanol, 2x2 minutes alcohol 96%, 2 minutes tap water, 1 minute milliQ water, 15 seconds haematoxyline (VWR®), 2 minutes tap water, 1 minute clarifier I (Thermo-scientific), 1 minute tap water, 1 minute bluing reagent (Thermo-scientific), 1 minute tap water, 1 minute milliQ water, 30 seconds eosine + phloxine (Thermo-scientific), 2 minutes tap water, 2 x 2 minutes alcohol 96%, 2x 2 minutes isopropanol, 2 x 2 minutes toluene, followed by 1 minute incubation in a fresh bath of toluene.

To evaluate the samples, a Jeneval light microscope (Carl Zeiss NV-SA, Zaventem, Belgium) was used. Furthermore, in case of the rat experiments, the thickness of the connective tissue capsule could be studied in this way. For each section, the thickness of the capsule was determined for the four edges surrounding the implant. Herein, the measurement was done at the position where the capsule appeared thickest. The average of these four values was calculated and used.

To study the number of capillaries in the sections, the H&E slides were scanned under a 20x or 40x objective using an Olympus BX51 microscope, and captured using dotSlide software (Olympus, Aartselaar, Belgium). Eighteen square fields per image (100 µm x 100 µm) surrounding the tissue-implant surface were manually selected, and the total number of capillaries was manually counted. The criteria applied for designating a capillary were explained in § 5.4.1.

In case of the rat experiments, pericytes, which surround mature capillaries and which contain desmine, were stained to further visualize them. To this end, after deparaffinization and an antigen retrieval pre-treatment, sections were demarcated with Dakopen (Dako) and rinsed with PBS-buffer, followed by a pre-treatment with 3% H_2O_2 solution (VWR®). Blocking was done for 30 minutes with a mixture of 10 ml PBS, 5% Normal Rabbit Serum (NRS)

(X0902, Dako), 1% BSA (Roche diagnostics) and 0.2% Tween (VWR®). Next, the sections were incubated for 2 hours in the primary antibody solution of anti-desmine (M0760, Dako, 1/200 dilution), washed with PBS (2 x 5 minutes) and incubated for 1 hour in the secondary antibody solution, which is a biotinylated rabbit anti-mouse antibody (E0413, Dako; 1/200 dilution). After rinsing with PBS (2 x 5 minutes), streptavidine-peroxidase (P0397, Dako) was added. Next, the samples were again rinsed with PBS (2 x 5 minutes) and Tris buffer (1 x 5 minutes). To render the substrate chromogenic, a mixture of 0.06% 3,3'-diaminobenzidine tetrahydrochloride (DAB, D5637, Sigma Aldrich) and 0.03% H_2O_2 in Tris-buffer was added for 10 minutes and subsequently rinsed with water for 10 minutes.

6.2.4.5. SPE gel electrophoresis

Liquid samples for SPE gel electrophoresis analysis were obtained during the explantation process. After removing the tissue from the implant material, the liquid present on top of the implant was collected and is referred to as the external fluid. Next, one membrane was removed from the donuts and the fluid present underneath was also collected and is referred to as the internal fluid. SPE gel electrophoresis was performed on both liquids with a commercially available agarose gel electrophoresis kit (Protur HiSi kit from Analis, Namur, Belgium).

6.2.4.6. Diffusion experiments

A 10 g/l D-glucose (Anhydrous, 96%, sigma Aldrich) solution was prepared and added in the right compartment of an in-house-built diffusion device, as shown and described in § 5.5.2.2. The left compartment was filled with milli-Q water (Millipore) and between the compartments, the test subject (membrane or donut-implant) was clamped and in this way contacted with the two involved stirring fluids. Both compartments were made of double-layered glass, which allowed to work at thermostatic temperatures, in this case 37°C, via a water flow supplied from a thermostatic bath.
As a function of time, samples (40 µl) were taken from the right compartment to determine the amount of glucose which diffused through the membrane or donut. Glucose quantities were determined via test strips and a commercialized glucometer (Accu-Chek Aviva, Roche). To this end, a test strip was mounted inside of the glucometer and one droplet of glucose solution was placed on the test strip, which enabled reading of the glucose concentration from the device.

6.2.4.7. Statistical analysis

Statistical significance for capillary counts were assessed by one-way ANOVA with Tukey's post-hoc test for multiple comparisons. In case the values were not normally distributed according to the Shapiro-Wilk normality test, a Kruskal-Wallis non-parametric test was performed to determine statistical significance. The threshold for significance was $p < 0.05$.

The error bars represent the standard deviation. Statistical analyses were performed using IBM SPSS Statistics Version 20 (IBM Corporation, New York, United States) software package.

6.3. References

1. Roy, A. D., Jayalakshmi, K., Dasgupta, S., Roy, R., and Mukhopadhyay, B. (2008) Real time HR-MAS NMR: application in reaction optimization, mechanism elucidation and kinetic analysis for heterogeneous reagent catalyzed small molecule chemistry, *Magnetic Resonance in Chemistry* 46, 1119-1126.
2. Li, W. (2006) Multidimensional HRMAS NMR: a platform for in vivo studies using intact bacterial cells, *Analyst* 131, 777-781.
3. Shapiro, M. J., and Gounarides, J. S. (2000) High resolution MAS-NMR in combinatorial chemistry, *Biotechnology and Bioengineering* 71, 130-148.
4. Sperling, L. H., (Ed.) (2006) *Introduction to Physical Polymer Science, 4th Edition*, Wiley.
5. Stamm, M., (Ed.) (2008) *Polymer Surfaces and Interfaces. Characterization, Modification and Applications*, First Edition ed., Springer.
6. Center, S. S. S. E. R. (2015) Retrieved July 23, from http://serc.carleton.edu/research_education/geochemsheets/techniques/SEM.html.
7. Buddy D. Ratner, A. S. H., Frederick J. Schoen, Jack E. Lemons, (Ed.) (2004) *Biomaterials Science.*, Second edition ed., Elsevier.
8. Thermoscientific. (2013) Introduction to FT-IR sample handling; retrieved 24th October 2015, from https://www.thermoscientific.com/content/dam/tfs/ATG/CAD/CAD%20Documents/Catalogs%20%26%20Brochures/Molecular%20Spectroscopy/FTIR/FTIR%20Spectrometers/BR50557_E_IntroSampHand0613M_H_1.pdf.
9. Elmer, P. (2015) Radiometric assays and detection: ^{125}I labeling of proteins; Retrieved July 25 from http://www.perkinelmer.com/Resources/TechnicalResources/ApplicationSupportKnowledgebase/radiometric/iodination.xhtml#id-125ILabelingofproteins-Choosinganiodinationtechnique.
10. Bourdoiseau, M. (1986) Iodine radiochemistry and radiopharmaceutical product labeling, *International Journal of Radiation Applications and Instrumentation. Part B. Nuclear Medicine and Biology* 13, 83-88.
11. Salacinski, P. R. P., McLean, C., Sykes, J. E. C., Clementjones, V. V., and Lowry, P. J. (1981) Iodination of proteins, glycoproteins, and peptides using a solid-phase oxidizing agent, 1,3,4,6-tetrachloro-3-alpha 6-alpha-diphenyl glycoluril (IODOGEN), *Analytical Biochemistry* 117, 136-146.
12. Farah, K., and Farouk, N. (1998) Electrophilic radioiodination of tyrosine derivatives, *Journal of Labelled Compounds & Radiopharmaceuticals* 41, 255-259.
13. Wolff, J., and Covelli, I. (1969) Factors in the iodination of histidine in proteins, *European Journal of Biochemistry* 9, 371-377.
14. Banks, P. (2015) BioTek Instruments: Development of the optical microscope; retrieved July 27, from http://www.biotek.com/resources/articles/development-of-the-optical-microscope.html.
15. Nikon. (2015) The source for microscopy education: Concepts in (confocal) fluorescence microscopy; Retrieved July 27 from https://www.microscopyu.com/articles/fluorescence/index.html.

16. Jacobs, T., Declercq, H., De Geyter, N., Cornelissen, R., Dubruel, P., Leys, C., and Morent, R. (2013) Improved cell adhesion to flat and porous plasma-treated poly-epsilon-caprolactone samples, *Surface & Coatings Technology* 232, 447-455.
17. Lee, H., Dellatore, S. M., Miller, W. M., and Messersmith, P. B. (2007) Mussel-Inspired Surface Chemistry for Multifunctional Coatings, *Science* 318.
18. Scientific, T. F. (2015) www.piercenet.com; User Guide: Pierce Pre-Coated Iodination Tubes.
19. De Vos, W., Van Neste, L., Dieriks, B., Joss, G., and Van Oostveldt, P. (2010) High content image cytometry in the context of subnuclear organization, *Cytometry Part A* 77, 64-75.
20. (2014) http://www.r-project.org/index.html, The R Foundation for Statistical Computing.

Chapter 7

Discussion and future perspectives

7.1. Discussion and future perspectives

The goal of the present research included the development of a flexible, biocompatible methacrylate-based packaging material for an implantable optical glucose sensor, which is intended for long-term continuous glucose monitoring (CGM). In this work, different steps have been elaborated, as summarized in figure 7.1.

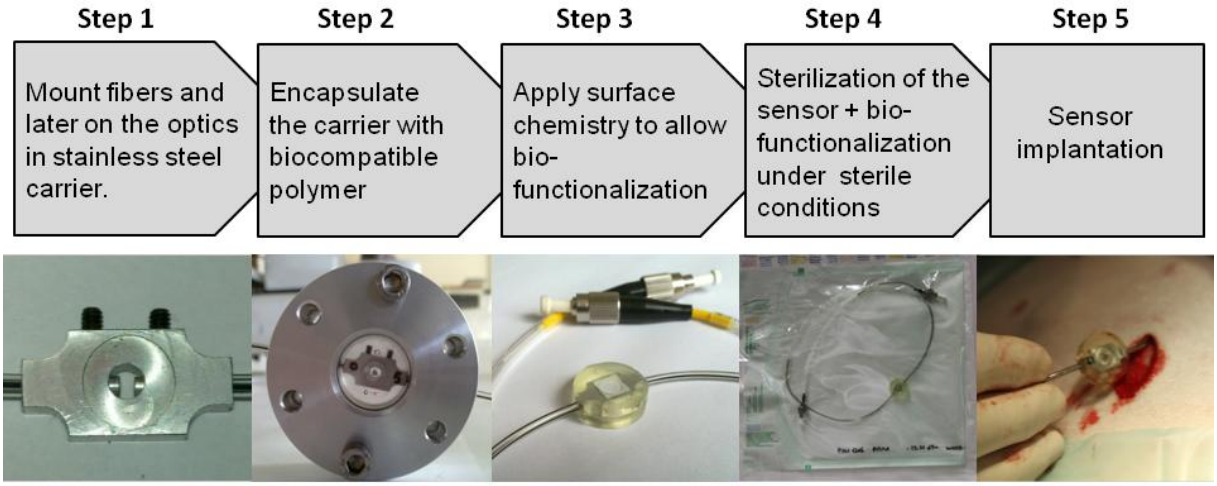

Figure 7.1: The development of a flexible methacrylate-based packaging material towards an implantable, optical glucose sensor: the different steps that should be performed in order to realize this goal. *Ronny Bockstaele is greatly acknowledged for* providing the c*oncept of this figure*

In a first step, all optical components should be mounted on a pre-assembly carrier to assure optical alignment. In the current work, optical fibers were still used and it was shown that some difficulties were associated with this concept. Due to external forces, fiber failure was apparent for most of the implanted sensors, despite the use of a biocompatible polyurethane tubing to protect the optical fibers. Future designs should encounter this problem e.g. by applying a more stiff tubing, by using only one fiber entry and/or by optimizing the eventual protection on the animals themselves. For the latter, the protection box could be fixed more tightly or could also be mounted on the back of the goats. Using this approach, the implants and fibers will be less attainable for the animals. It can further be highlighted that the concept of using optical fibers is only a preliminary set-up, since at the final approach, a wireless sensor is pursued. Nevertheless, this intermediate concept is required to evaluate the overall feasibility.

After assembly of the different optical components, the sensor is ready to become encapsulated in a polymer packaging. As indicated in chapter 1, the packaging material should fulfill certain characteristics. First, a certain flexibility and softness of the packaging were targeted. In this respect, the most ideal mechanical properties a subcutaneous packaging should show, were attempted to become identified. To this end, upon application of poly(ethylene glycol) monomethylether monomethacrylate (PEGMA) and/or poly(ethylene glycol) dimethacrylate (PEGDMA), a broad range of MMA-based copolymers

was developed (see chapter 2) with E-moduli ranging from 10 to 1600 MPa. To evaluate the impact of the E-modulus on the cell behavior, different materials, characterized by various E-moduli, were selected and treated with a similar surface chemistry. Nevertheless, the different E-moduli could not be differentiated on a cellular level (see chapter 4). Whether the mechanical properties were responsible for this fact or the applied surface chemistry, should be the topic of future research. Although it was not possible to identify the ideal range of packaging E-moduli, it can be anticipated that E-moduli in the range of those of skin (100 kPa-100 MPa [1]), could offer excellent candidates. In this respect, the developed PLMA-based material (55.5 mol% MMA, 45.5 mol% LMA and 5 mol% PEGDMA(550)) could be an interesting candidate (E-mod = 6 MPa). Nevertheless, this material was not yet studied in an *in vivo* setting, since it was only available at the end of the current PhD. Based on the mechanical properties of the PMMAPEG-based materials, also within this range, a selection could be made, but due to the high swelling of these materials (up to 250%), a somewhat higher E-modulus (E-mod = 142 MPa) was selected as potential glucose sensor packaging (i.e. combining 50 mol% MMA and 50 mol% PEGDMA), since it formed the best compromise between the E-modulus and swelling (17%). Regarding this latter property, it was also questioned how much swelling would be tolerated in the final sensor concept. Based on the experiments conducted with the PMMAPEG-based material (associated with a swelling of 17%), it was concluded that swelling should be eliminated to the greatest extent possible, especially in case of highly crosslinked materials. The *in vivo* experiments showed that some of the implanted donuts were broken inside the goats which was attributed to stresses created due to a combination of high swelling and crosslinking degree (50 mol% of crosslinker) of the studied material. Furthermore, because of swelling, poor adhesion of the PMMAPEG polymer onto the metal substrates was demonstrated during hermeticity testing. It can be noted that the PLMA-based material could again offer a superior alternative, since its swelling was limited to only 0.6%, which is even less than PMMA itself (i.e. 2%).

Regarding the optical properties of the materials, a minimized swelling would further limit the interference of water during the NIR optical measurements of glucose. Nevertheless, optical evaluation of the PMMAPEG and PLMA-based materials in the near-IR region showed that too high absorptions were present to allow for sensitive glucose measurements. Future research should thus focus on the alternative glucose sensor concept, i.e. the evanescent glucose sensor as described by Ryckeboer et al [2] (also see figure 7.2). In this concept, the polymer material is excluded from the light path.

Finally, the packaging material should preferably act as a hermetic barrier, in the sense that it should prevent contact of body fluids with the electronics and contact of leached electronic species with the body. Both materials, PMMAPEG and PLMA were evaluated and turned out to be unsuitable for this purpose, thus future experiments should further elaborate on the optimization of the latter property. For short term implantations (i.e. months), the combination with parylene C could be evaluated while long term implantations (i.e. years) could include the application of ALD (Atomic Layer deposition) to form an intermediate layer between the electronics and the polymer.

Apart from the PLMA-based material, also other polymers could in the future be evaluated as glucose sensor packaging, as long as they fulfill the above-mentioned criteria (i.e. E-mod between 100 kPa and 1000 MPa; swelling close to 0%, transparency in the near IR would be recommended, fulfillment of a hermetic barrier layer would be a plus). In this context, Kodeck et al already explored the use of PDMS (E-mod= ± 1 MPa), but due to ageing of the bulk material (the E-modulus increased as a function of time), further optimization is necessary. It can be noted that determination of the impact strength of the developed materials could also give valuable information. Indeed, upon impact, it should not break inside the body.

In a third step, after encapsulation of the sensor compounds in the polymer packaging, the surface properties of the packaging material had to be tailored. Initial cell tests (see chapter 2) showed that the bulk materials lack cell-interactivity. Since tissue encapsulation and vascularization around the sensor are required, excellent cell compatibility is needed. If inert materials would be selected, no cells or proteins would adhere in an *in vivo* setting and as a consequence, isolation of the implant from the body would be the result. This would also imply that no glucose would diffuse towards the sensor resulting in inaccurate glucose measurements. However, upon implantation of a sensor, a foreign body response will typically occur, associated with aspecific protein adsorption as well as random cell attachment. In the current work, we aimed at controlling this foreign body reaction by attracting the desired cell type, through surface biofunctionalization.
Prior to biofunctionalization, activation of the surface (step 3 in figure 7.1 and chapter 3) had to be established, since no chemical functionalities were available to immobilize these bio-molecules. To this end, two strategies were evaluated, including the deposition of a polydopamine (PDA) coating and the immobilization of 2-aminoethyl methacrylate (AEMA) via post-plasma grafting. For both PMMAPEG and PLMA, the conditions were optimized and for the latter hydrophobic material, the use of an O_2 plasma treatment seemed beneficial to maximize PDA deposition. It was shown that the use of PDA resulted in homogenous and reproducible coatings, whereas for the AEMA grafting, this was not the case. In this perspective, the use of PDA could be considered as the most promising. Furthermore, the application of a nitrogen plasma as pre-activation step could also offer future opportunities, since preliminary experiments showed the presence of nitrogen groups (up to 7%) on the surface. If the subsequent immobilization of bio-active compounds such as VEGF or VE-cad AB would be enabled via this strategy, it would offer a reagent-less, less time-consuming and cheaper alternative.

For the biofunctionalization of the materials (step 4 in figure 7.1 and chapter 4), different approaches were evaluated in an *in vitro* setting. In a first strategy, a universal modification strategy was developed to enhance the cell interactivity of polymer materials, via the anchorage of a thin gelatin layer onto the PDA modified substrates. The universal character was proven since increased cell densities and cellular focal adhesion points were observed

for both the PDA/gelatin modified PMMAPEG and PMMA samples. For the first material, this includes a remarkable result, since PEG is recognized as a protein-repellant and non cell-interactive polymer, yet gelatin was able to mask these properties. Since cell-interactivity was established via the immobilization of a combined PDA/Gel B layer, first steps were taken to assure contact between the sensor and the surrounding body environment by means of tissue integration. The latter fact was however not proven in an *in vivo* setting and could be included in future experiments. In future research, the use of recombinant gelatin could also be explored, since it could offer enhanced immunological properties compared to bovine skin derived gelatin.

During the course of this research, it was however realized that tissue integration as such would not suffice. In the end, blood glucose has to be supplied towards the sensor and as a consequence, angiogenesis should preferably be stimulated in the vicinity of the sensor. In this respect vascular endothelial growth factors (VEGF), vascular endothelial cadherin antibody (VE-cad AB) and their combinations were anchored onto the AEMA and PDA modified PMMAPEG and PLMA-based surfaces. In this work, successful immobilization was demonstrated and the number of focal adhesions, counted for each adhering HUVEC was the highest for the combination of VEGF and AB. Furthermore, in case PDA was used as activating sublayer, it was proven that the immobilization of both angiogenic factors resulted in a positive combined effect, as represented by the significantly increased cell adhesion properties of the materials. These results thus gave a first *in vitro* indication of successful and desired cell (i.e. HUVECs) attachment. Nevertheless, to prove the potentially stimulated angiogenesis, future experiments should be conducted. In this respect, the culture of endothelial progenitor cells (EPC) onto the substrates and the evaluation of their differentiation potential into mature endothelial cells could also provide valuable information. Furthermore, since in the *in vivo* environment, multiple cell types will be present, co-culture studies could also be conducted, e.g. in the presence of fibroblasts. The latter cell type secretes matrix components that could act as scaffold and enable endothelial cells (EC) to form tubules with a lumen. Furthermore, it has already been demonstrated that EC behave differently in a tubular structure in the presence of accessory cells such as pericytes and smooth muscle cells [3]. It would thus be interesting to also include these cell types in future *in vitro* assays.

Chapter 4 further demonstrated that part of the immobilized growth factors and antibodies were released over time. Extensive studies exploring the impact of this observation would be an interesting topic for future research. Indeed, the beneficial effect of a controlled and slow release of growth factors such as VEGF was already proven. Also in the present work, further elaboration on a method to render the release controllable, e.g. by the encapsulation of VEGF-containing microspheres inside the packaging material (see figure 7.2, B) could be promising. Furthermore, the *in vivo* lifetime of the biomolecules should be evaluated in detail.

As mentioned in step 4 of figure 7.1, prior to biofunctionalization, a sterilization step should be included to enable implantation of the sensor. In this work, the influence of sterilization was not included yet but its effect on the material properties should definitely be included in future research. The ethylene oxide sterilization process could influence the reactivity of the activation layers (i.e. PDA and AEMA) and thus the success of the biofunctionalization. Furthermore, in case of incomplete coverage of the material surface by the activation layer, the unmodified spots could also be characterized by altered surface properties and e.g. act as more hydrophilic substrates. This could increase the amount of aspecific adsorption of the biomolecules.

In a last part of this work (chapter 5), a selection of the developed (un-)modified materials as well as the glucose sensor concept were evaluated in an *in vivo* environment.
Herein, blank, PDA and PDA/VE-cad AB modified PMMAPEG samples were implanted in goats. The most promising condition, i.e. the combined immobilization of VEGF and AB, was not included in this study, because it was only developed at the end of this PhD. It was observed that subcutaneous implantation resulted in the development of a fibrous capsule around all of the donut-shaped implants. The highest mean capillary formation around the implant was found for the PDA/VE-cad AB functionalized samples, although no statistical evidence could be delivered. Since the evaluation of capillary formation is rather complicated on 2 D surfaces, future experiments could focus on alternative test approaches. These could include the chorioallantoic membrane assay (CAM) in a chicken embryo, which is a low cost and more straightforward method compared to mammalian models. Furthermore, this test could be used to further evaluate the impact of material optimization (e.g. concentration of VEGF, AB,…) onto the process of angiogenesis. Other *in vivo* models include implantation in the avascular cornea of rabbits or the dorsal skinfold chamber. Nevertheless, for all of these assays, porous material structures are required. In this work, preliminary tests have been performed with porous PCL scaffolds which were surface-treated with the PDA/VE-cad AB coating and it was demonstrated that enhanced vascularization and a decreased thickness of the fibrous capsule was formed compared to the unmodified PCL samples after implantation in rats. Furthermore, the use of a porous structure also seemed to have a positive influence on the results (i.e. decreased thickness of the fibrous capsule and an increased number of blood vessels). The future glucose sensor concept could thus consider the use of such a porous polymer structure (see figure 7.2).
Finally, future research could also focus on the evaluation of potential tumor formation. Since tumor formation is characterized by the process of uncontrolled angiogenesis, angiogenesis around the glucose sensor should occur in a controlled manner, without rendering it pathological. To initiate this cancerous state, preneoplastic cells should be maintained in the vicinity of the sensor. These cells would be an interesting marker to include in future assays. Nevertheless, it should also be emphasized that the rarity of human foreign body associated tumors suggests that cancer-prone cells are rather infrequently associated with the foreign body reactions towards implanted human medical devices [4].

During the *in vivo* experiments, the sensor design was also evaluated. It was concluded that glucose measurements through tissue via an optical fiber setup was impossible. As a consequence, coverage of the central cavity of the donut shaped sensor with a membrane was necessitated. Since biofouling of the applied PES membrane was demonstrated as well as its slow diffusion kinetics, further improvements should be considered during future work. Furthermore, an improved or adjusted assembly of the different sensor compounds should be investigated, as already discussed earlier in the current chapter.
For future *in vivo* experiments, goats could still be used as a representative animal model, especially in case the evaluation of the final glucose sensor is pursued. Nevertheless, for further optimization concerning polymer selection and biofunctionalization strategies, normal and diabetic rats would be preferred as they enable a faster screening.

Based on all previous considerations, a first indication for a future assembly of the evanescent glucose sensor is indicated in figure 7.2 (A). Herein, the impermeable layer could represent a parylene C coating or an ALD layer. From a technical perspective, future challenges include the incorporation of the membrane into the polymer packaging as well as ensuring good adhesion between the polymer and the impermeable layer.

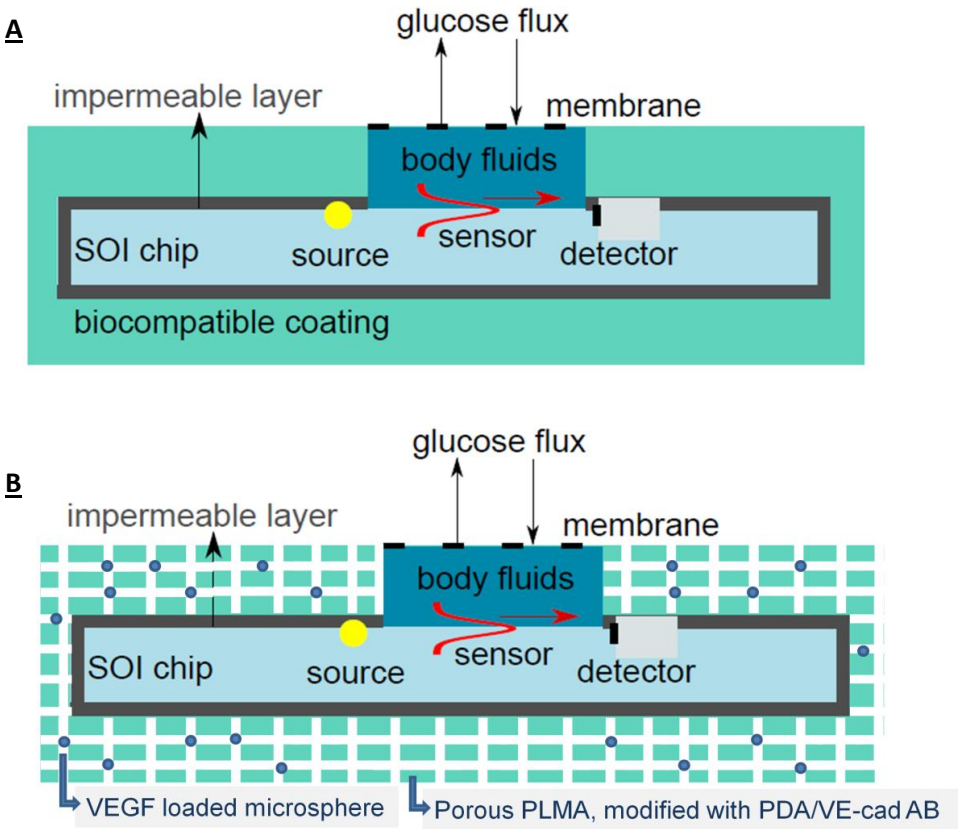

Figure 7.2: The future sensor concept as proposed by Ryckeboer et al [2] (A) and the adjusted version based on the performed research (B).

If the above mentioned conclusions would be integrated, the sensor concept could be adjusted according to figure 7.2 (B). Herein, the sensor components are again coated with an impermeable ALD layer, followed by their incorporation into a porous PLMA scaffold. Herein the scaffold could be modified with VE-cad AB (and/or VEGF) and could incorporate VEGF-loaded microparticles to enable their controlled release. This approach would be technically more challenging, since the application of a porous polymer packaging would ask for more advanced techniques such as 3D printing. The latter technique would also require alternative production methods for the PLMA starting material. Also in this case, integration of the membrane and sufficient adhesion properties of the different layers could pose some difficulties.

It can be concluded that first steps were taken in the development of an implantable glucose sensor packaging. Furthermore, new challenges are identified and could be the topic of promising forthcoming research.

7.2. Future opportunities

Apart from their application as glucose sensor packaging, some of the developed materials could also be considered as stent coating material. In this area of research, there is still a need for new coatings that cover the stent before and after expansion and which are able to reduce thrombosis and restenosis, once implanted in the human vein [5-7].
In this respect, some of the non-crosslinked, PEG based materials (cfr. chapter 2, table 2.3) offer great potential due to their high elongation percentages (up to 600%). Preliminary tests[1] already showed a uniform coverage of the stent by dipcoating it in a polymer solution. Figure 7.3 clearly shows how the stent's surface topography disappears after coating with a PEG-based material. Nevertheless, further optimization is required (cfr. concentration of the polymer solution, speed of dipcoating, solvent choice, etc.) to control and optimize the layer thickness and to avoid an excess of material in the stent bridges (indicated by the circle in figure 7.3).
Concerning the biocompatibility of the stent, re-endothelialization of the outer side of the stent is required and as a consequence, the application of the above-described biofunctionalization strategies (VEGF, AB immobilization) could also be applied in this case. On the other hand, the inner side of the stent contacts the blood stream, so a protein-repellant coating should ideally be applied in order to avoid thrombosis and restenosis of the stent. In this respect, the non-modified PEG-materials could also be examined, because based on this work and other studies, the anti-biofouling character of PEG has already been demonstrated.

[1] In cooperation with Matthieu De Beule, from the Faculty of Engineering and Architecture, Department of Electronics and Information Systems.

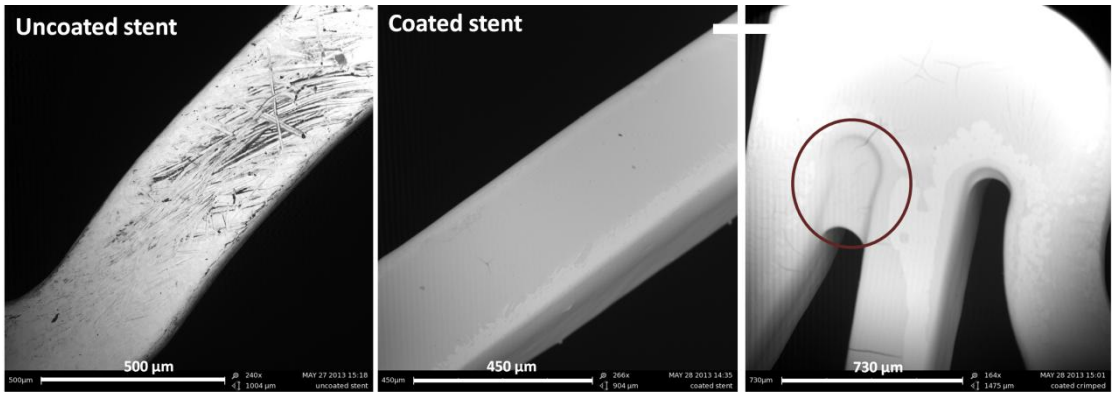

Figure 7.3: A stainless steel stent was coated with a polymer layer consisting of 94 mol% MMA and 6 mol% PEGMA(1100) (i.e. material 6 in chapter 2), via dipcoating (50 mm/min) from a polymer solution (5 wt% in THF).

7.3. References

1. Nemir, S., and West, J. L. (2010) Synthetic Materials in the Study of Cell Response to Substrate Rigidity, *Annals of Biomedical Engineering* 38, 2-20.
2. Ryckeboer, E. (2014) Spectroscopic detection of glucose with a silicon photonic integrated circuit, Ghent University.
3. Staton, C. A., Reed, M. W., and Brown, N. J. (2009) A critical analysis of current in vitro and in vivo angiogenesis assays, *International journal of experimental pathology* 90, 195-221.
4. Mikos, J. S. T. A. G. (2008) *Biomaterials: The Intersection of Biology and Materials Science*, Pearson/Prentice Hall, 2008.
5. Kraitzer, A., Kloog, Y., and Zilberman, M. (2008) Approaches for prevention of restenosis, *J. Biomed. Mater. Res. Part B* 85B, 583-603.
6. Mauri, L., Hsieh, W. H., Massaro, J. M., Ho, K. K. L., D'Agostino, R., and Cutlip, D. E. (2007) Stent thrombosis in randomized clinical trials of drug-eluting stents, *N. Engl. J. Med.* 356, 1020-1029.
7. Hopkins, C. G., McHugh, P. E., and McGarry, J. P. (2010) Computational Investigation of the Delamination of Polymer Coatings During Stent Deployment, *Annals of Biomedical Engineering* 38, 2263-2273.

Chapter 8

Nederlandstalige samenvatting

8.1. Inleiding

Uit cijfers van de internationale diabetes federatie (IDF) bleek dat er wereldwijd in 2013 meer dan 382 miljoen mensen leden aan diabetes en er wordt verwacht dat dit aantal zal verdubbelen tegen 2035 [1]. Diabetes is een ziekte die gekenmerkt wordt door een afwijkende glucose huishouding. Bij een gezonde patiënt zullen te hoge bloed glucose waarden (hyperglycemie) bestreden worden door de aanmaak van insuline, maar in het geval van diabetici is het lichaam ofwel niet in staat insuline aan te maken (diabetes type I) of niet in staat om adequaat te reageren op de aanmaak van dit hormoon (diabetes type II) [2]. Het is een niet-geneesbare ziekte, maar het is reeds bewezen dat een strikte en continue opvolging van de bloed glucose waarden zou resulteren in gereduceerde medische kosten doordat de patiënt in staat zou zijn om normale glucose waarden te handhaven, wat verder ook de kans op complicaties (zoals oog-, nier-, zenuw- en vasculaire ziekten) doet verminderen. Het spreekt voor zich dat de ontwikkeling van glucosesensoren bij diabetes management een cruciale rol speelt.

Vandaag de dag bestaat er reeds een hele reeks glucosesensoren die zeer stabiel, accuraat en gevoelig zijn *in vitro*, maar indien implantatie wordt beoogd om continue monitoring toe te laten, daalt hun betrouwbaarheid en stabiliteit dramatisch na een aantal dagen als gevolg van o.a. aspecifieke proteïne-adhesie [3].
In het kader van huidig doctoraatswerk werd een glucose sensor ontwikkeld, bestaande uit een ‘single chip’ optische, nabij infrarood (NIR) gebaseerde sensor, die een ‘silicon photonics’ geïntegreerde spectrometer bevat, alsook een NIR lichtbron, met als doel lange-termijn en continue opvolging van glucose mogelijk te maken. Het principe van de sensor wordt geïllustreerd in figuur 8.1 en komt neer op de detectie van glucose in de centrale opening van het donut-vormig implantaat.

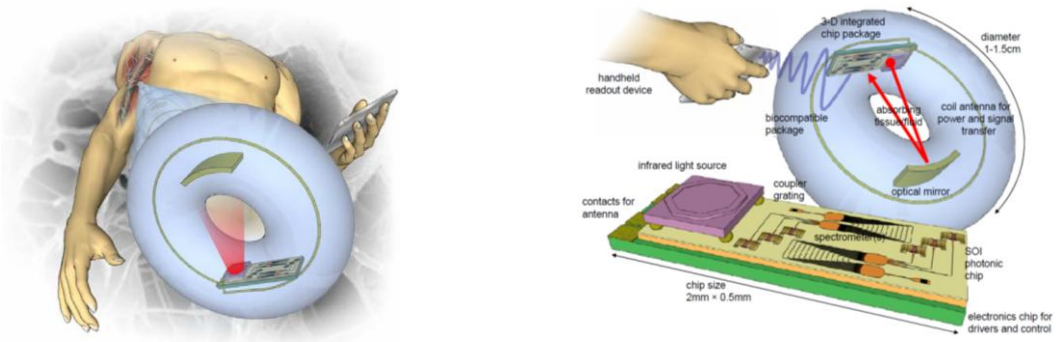

Figuur 8.1: NIR-gebaseerde glucose sensor, die verpakt is in een donutvormig biocompatibel polymeermateriaal.

Aangezien de implantatie van de sensor beoogd wordt, is er nood aan de ontwikkeling van een flexibele en biocompatibele verpakking, wat het uiteindelijke doel vormt van huidig doctoraatswerk.

8.2. Ontwikkeling van een methacrylaat-gebaseerd verpakkingsmateriaal

Voor de ontwikkeling van het verpakkingsmateriaal werd uitgegaan van poly(methyl methacrylaat) (PMMA), een materiaal dat gekarakteriseerd wordt door zijn biocompatibiliteit. In het verleden werd het reeds aangewend voor meerdere biomedische toepassingen zoals lenzen, heup-, bot-, en tandimplantaten [4-6]. Aangezien de subcutane implantatie van het verpakkingsmateriaal beoogd wordt, is een zekere flexibiliteit van de verpakking vereist om het comfort van de patiënt te verzekeren. Bovendien is een beperkte zwelling van de verpakking nodig om delaminatie van de verpakking en de sensor componenten te vermijden. Bijgevolg werden verschillende MMA-bevattende copolymeren geproduceerd via een UV-geïnduceerde fotopolymerisatie (zie figuur 8.2) met behulp van Irgacure® 2959 of 651 als foto-initiator. De bekomen materialen werden geëvalueerd voor hun mechanische en zweleigenschappen.

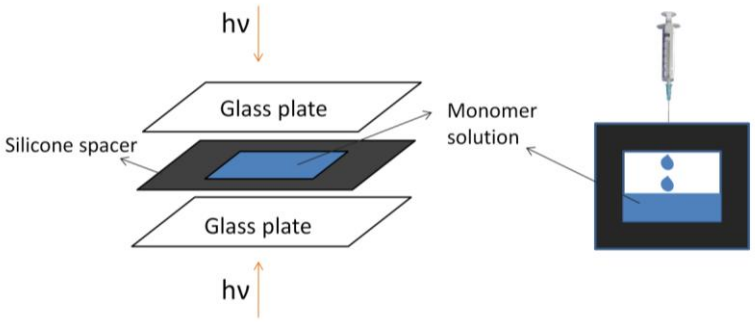

Figuur 8.2: UV-polymerisatie set-up. In de originele opstelling werd ook teflon aangebracht op de glasplaten om het polymeer vlot te kunnen verwijderen.

In een eerste strategie werd MMA gecombineerd met proteïnen afstotende poly(ethyleen glycol) gebaseerde reagentia, waaronder poly(ethyleen glycol) monomethylether monomethacrylaat (PEGMA) en poly(ethyleen glycol) dimethacrylaat (PEGDMA). Door het moleculair gewicht van de PEG keten te variëren alsook de samenstelling van het polymeer, werd een reeks polymeren gesynthetiseerd met uiteenlopende mechanische (E-moduli variërend van 10 tot 1600 MPa) en zwellingseigenschappen (zwellingspercentages variërend van 2 tot 250%). Het beste compromis tussen mechanische eigenschappen en zwelling werd vertoond door PMMAPEG, bestaande uit 50 mol% MMA en 50 mol% PEGDMA(550). Bijgevolg werd dit materiaal als eerste kandidaat verpakkingsmateriaal geselecteerd.

In een tweede strategie werd een hydrofoob materiaal ontwikkeld, bestaande uit 55.5 mol% MMA, 45.5 mol% lauryl methacrylaat (LMA) and 5 mol% PEGDMA(550). Ten opzichte van de PEG-gebaseerde materialen werd een nog lagere E-modulus (6 MPa) bereikt, alsook een verwaarloosbare zwelling (0.6%) (zie figuur 8.3). Bijgevolg werd dit materiaal (PLMA) als tweede kandidaat geselecteerd. Voor deze laatste kan er nog opgemerkt worden dat de keuze van initiator (Irgacure®2959 versus Irgacure® 651) geen significante invloed had op de mechanische of zwellingseigenschappen van het uiteindelijke materiaal. Desalniettemin

werd deze variabele meegenomen om zijn invloed na te gaan op de oppervlakmodificatie resultaten.

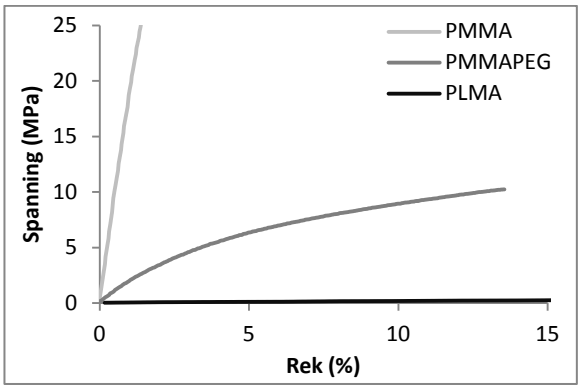

	zwellings %	stdev
PMMA	2	0.2
PMMAPEG	17	0.2
PLMA	0	0.2

Figuur 8.3: Weergave van een typische trek-rek curve (links) alsook de zwellingseigenschappen van de geselecteerde materialen PMMAPEG en PLMA (rechts). PMMA fungeerde als referentie.

Additionele testen toonden aan dat beide materialen voldoende optische transparantie in het NIR golflengtegebied vertoonden en een minimale celtoxiciteit (< 30%). Daarentegen vormden zij geen voldoende diffusiebarrière om corrosie van de onderliggende electronica tegen te gaan, wat impliceert dat in het finale sensor concept, een additionele coating, zoals paryleen C, zal moeten worden aangewend.

8.3. Activatie van de polymeeroppervlakken

In een tweede luik van dit onderzoek werd de focus gelegd op de optimalisatie van de biocompatibiliteit van de materialen door het uitvoeren van oppervlakmodificaties. Om biofunctionalisatie mogelijk te maken, dienen de inerte materiaaloppervlakken in eerste instantie geactiveerd te worden, wat betekent dat functionele, reactieve groepen ingevoerd worden.

In dit werk werden twee 'activatie-routes' verkend, waaronder de 'post-plasma grafting' van 2-aminoethyl methacrylaat (AEMA) en de depositie van een polydopamine (PDA) laag.

In geval van 'AEMA grafting' werden twee opeenvolgende stappen uitgevoerd. De eerste stap omvatte een plasmabehandeling m.b.v. Ar gas. Hierdoor werd in de tweede stap, de UV-geïnduceerde grafting van AEMA mogelijk gemaakt (zie figuur 8.4). De bekomen resultaten illustreren dat plasma behandeling een sterke daling van de contacthoek tot gevolg had, doordat zuurstof bevattende functionaliteiten ingevoerd werden op het oppervlak. Verder toont figuur 8.4 de succesvolle grafting van AEMA aan door de aanwezigheid van een stikstofpiek, bepaald via X-stralen foto-electron spectroscopie (XPS), alsook door een stijging van de contacthoek t.o.v. de plasma behandelde stalen. Aangezien geen significant verschil werd aangetoond tussen de twee PLMA gebaseerde materialen, werd PLMA(651) geëlimineerd uit de vervolgstudie.

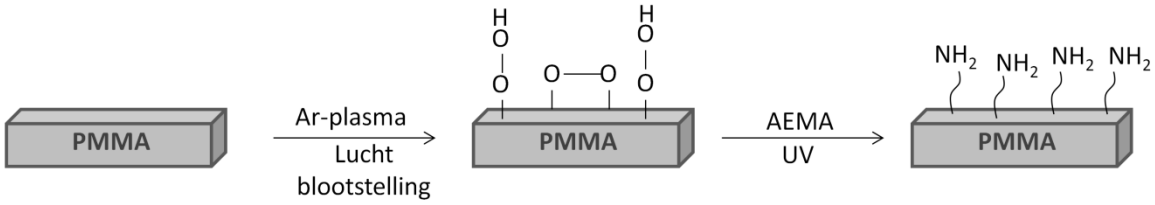

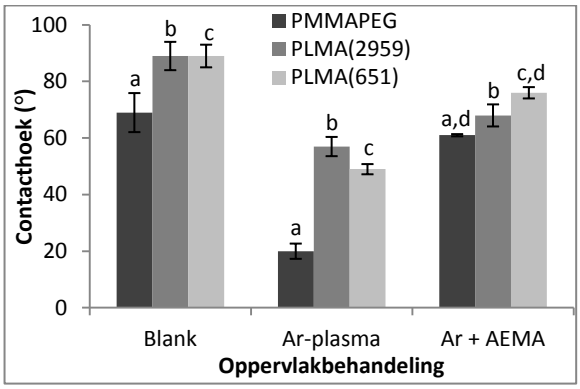

XPS	N (at%)	N/C
PMMAPEG	3.2 ± 3.0	0.047 ± 0.042
PLMA(651)	1.3 ± 0.3	0.020 ± 0.004
PLMA(2959)	1.4 ± 1.8	0.020 ± 0.026

Figuur 8.4: Schematische voorstelling van de 'post-plasma grafting' techniek van AEMA. De contacthoeken van de blanco, Ar-plasma behandelde en AEMA gecoate stalen worden weergegeven, alsook de atomaire stikstof percentages en N/C verhoudingen van de AEMA behandelde stalen. Condities die significante verschillen opleverden zijn aangeduid d.m.v. dezelfde letters a,b,c,…

In geval van PDA modificatie werden verschillende depositie protocols geëvalueerd en op basis van XPS metingen bleek het klassieke protocol van Messersmith et al [7], de pioniers van deze strategie, het meest effectief te zijn voor PMMA en PMMAPEG modificatie. Voor de PLMA materialen bleek de combinatie van dit protocol met een voorafgaande O_2 plasma behandeling te resulteren in verhoogde PDA depositie. De succesvolle modificatie werd aangetoond via verschillende technieken zoals statische contacthoekmetingen (SCA; daling van CA na PDA coating), XPS (verhoogd N%), 'raster elektronen microscopie' (SEM; aanwezigheid van clusters) en 'atomaire kracht microscopie' (AFM; invloed op oppervlak ruwheid). De belangrijkste resultaten zijn samengevat in figuur 8.5.

Door de aanwezigheid van de oppervlakfunctionaliteiten kon er in een volgende stap overgegaan worden naar biofunctionalisatie van de materialen. Hierbij werden biologisch actieve componenten geïntroduceerd op het materiaaloppervlak, met het oog op het sturen van de celrespons en de uiteindelijke lichaamsrespons.

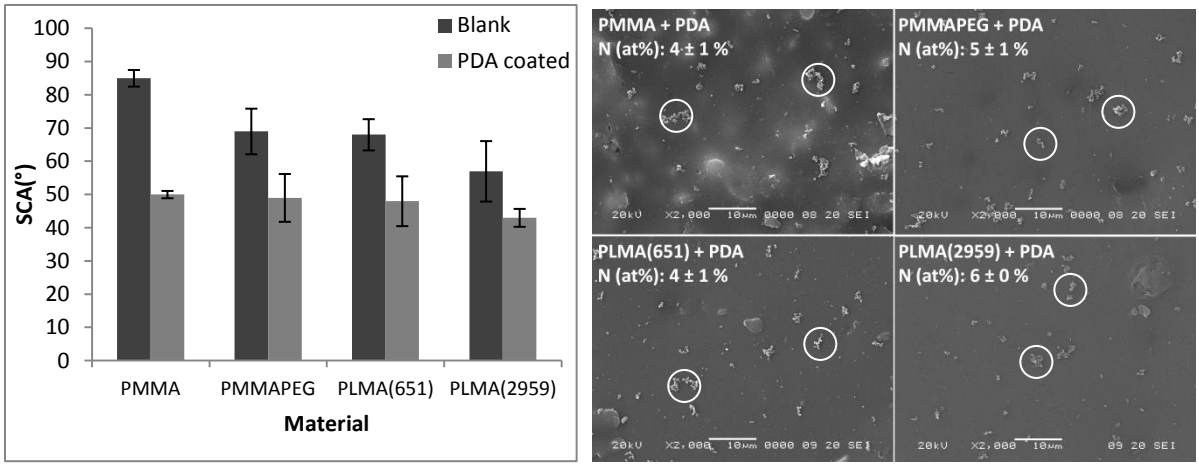

Figuur 8.5: Overzicht van de contacthoeken van de blanco materialen en de PDA gecoate materialen (links). In de SEM-figuren (rechts) zijn de PDA clusters zichtbaar (vbn. aangeduid door cirkels). Bovendien bewijzen de verhoogde stikstof percentages het succes van deze modificatiestap.

8.4. Biofunctionalisatie van de verpakkingsmaterialen en hun *in vitro* evaluatie

In een eerste stap werd een universele modificatiemethode ontwikkeld om de celinteractiviteit van implantaten te verhogen. Hiervoor werd gelatine geïmmobiliseerd op de PDA gefunctionaliseerde PMMA en PMMAPEG oppervlakken. Succesvolle immobilisatie werd aangetoond m.b.v. XPS (N% tot 10 %) en SCA (daling in CA van 20-30° t.o.v. PDA modificatie). *In vitro* celtesten hebben verder aangetoond dat de applicatie van enkel PDA niet in staat is om de proteïne-afstotende eigenschappen van PEG te maskeren. De combinatie van PDA en GelB daarentegen resulteerde in hoge celdensiteiten voor zowel PMMA als PMMAPEG, alsook in een hoog aantal focale adhesiepunten, wat verankeringspunten zijn van de cel met het substraat (zie figuur 8.6).

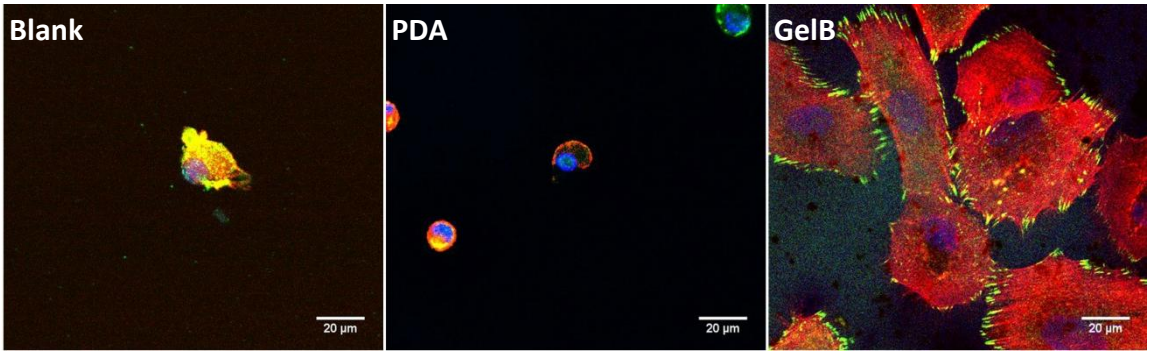

Figuur 8.6: PMMAPEG wordt gekarakteriseerd door een proteïne-afstotend karakter. PDA immobilisatie resulteerde in een onvoldoende maskering van deze materiaaleigenschap, terwijl de combinatie van PDA/GelB resulteerde in hoge celdensiteiten en een groot aantal focale adhesiepunten (groen).

Bij vergelijken van een reeks PEG-gebaseerde materialen met verschillende mechanische eigenschappen, werden opnieuw gelijkaardige celresponsen verkregen. Dit wijst er op dat de combinatie van PDA en GelB in staat is om materialen met verschillende fysicochemische eigenschappen te laten resulteren in een gelijkaardige celrespons.

In het kader van de glucose sensor zou de *in vivo* stimulatie van angiogenese, of dus het proces van bloedvatvorming, een gunstig effect hebben op de werking van de sensor [8]. Voldoende bloedvaten zouden immers de diffusie van glucose toelaten naar de sensor, wat nodig is om representatieve glucosemetingen te garanderen.
In deze context werd de immobilisatie van een vasculaire endotheliale groeifactor (VEGF) [9] en/of vasculair endotheliaal cadherine antilichaam (VE-cad AB) [10] op de AEMA en PDA gefunctionaliseerde oppervlakken bestudeerd.
Succesvolle immobilisatie werd bevestigd m.b.v. radiolabeling experimenten en XPS. 'Live dead assays' met 'humane vasculaire endotheliale navel cellen' (HUVECs), een van de celtypes waaruit een bloedvat is opgebouwd, toonden aan dat de aanwezigheid van VEGF, AB of beide aanleiding gaf tot verhoogde celdensiteiten, celviabiliteiten, alsook tot een verhoogde celadhesie (bepaald via telling van de focale adhesiepunten) en dit voor beide activatiestrategieën (i.e. PDA versus AEMA functionalisatie). Uit de resultaten bleek dat de AB geïmmobiliseerde stalen aanleiding gaven tot een betere celinteractiviteit, hoewel significante verschillen niet aangetoond konden worden. Het meest markante resultaat werd geleverd indien beide factoren (AB en VEGF) samen geïmmobiliseerd werden op het oppervlak. Deze conditie resulteerde in significant hogere adhesieresultaten t.o.v. de individuele immobilisatie van de factoren (zie figuur 8.7). VEGF en VE-cad AB vertoonden dus een gezamenlijk effect op de celrespons.

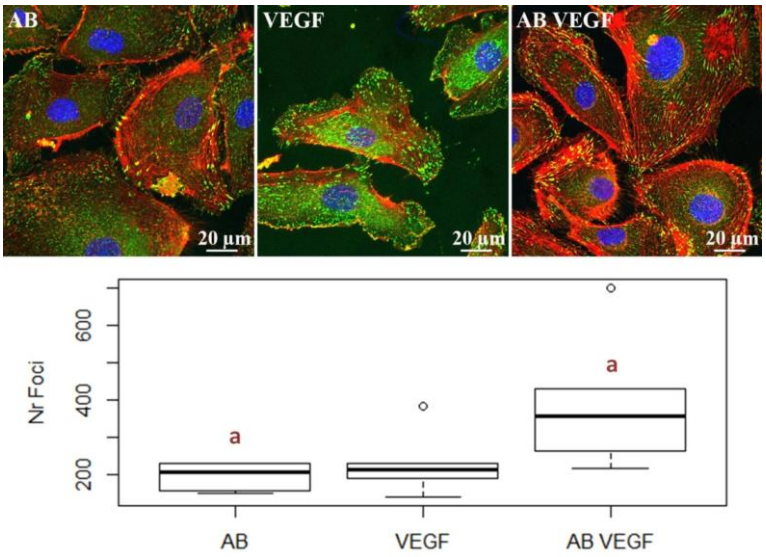

Figuur 8.7: Immuno-assay studies toonden aan dat er een gecombineerd effect bestaat tussen VEGF en VE-cad AB, hetgeen weerspiegeld werd door een significant hogere adhesie (= hoger aantal focale adhesiepunten, voorgesteld door de groene kleuring) t.o.v. de individuele factor immobilisatie.

8.5. *In vivo* evaluatie van de methacrylaat gebaseerde glucose sensor verpakkingen

In een laatste deel van dit werk, werden een aantal *in vivo* experimenten uitgevoerd in geiten en ratten. Om de productie van donut-vormige 'dummy' sensoren mogelijk te maken, werd een mal ontwikkeld die tevens de incorporatie van optische vezels toeliet.
Implantatie van deze dummy sensoren (zonder optische vezels) bevestigde dat subcutane implantatie bevoordeligd werd t.o.v. intramusculaire of intraperitoneale implantatie. Verder werd aangetoond dat de blanco stalen aanleiding gaven tot de vorming van een zeer dens fibreus kapsel, terwijl de gemodificeerde stalen (zowel PDA als PDA/VE-cad AB gemodificeerde stalen) aanleiding gaven tot de vorming van een dikker, maar minder dens fibreus weefselkapsel. Verder werd in het geval van VE-cad AB modificatie een hoger aantal capillairen geteld in de nabijheid van de sensor, hoewel significante verschillen met de blanco en PDA gemodificeerde stalen niet konden worden aangetoond. Wanneer gelijkaardige oppervlakmodificaties uitgevoerd werden op een poreuze poly(ε-caprolacton) (PCL) matrix, resulteerde VE-cad AB immobilisatie daarentegen in de afwezigheid van een fibreus kapsel, maar in een sterke vascularisatie, zelfs tot aan de rand van het implantaat (zie figuur 8.8, C). Dit laatste resultaat illustreerde duidelijk de toegevoegde waarde van porositeit van het verpakkingsmateriaal op de stimulatie van angiogenese [11].

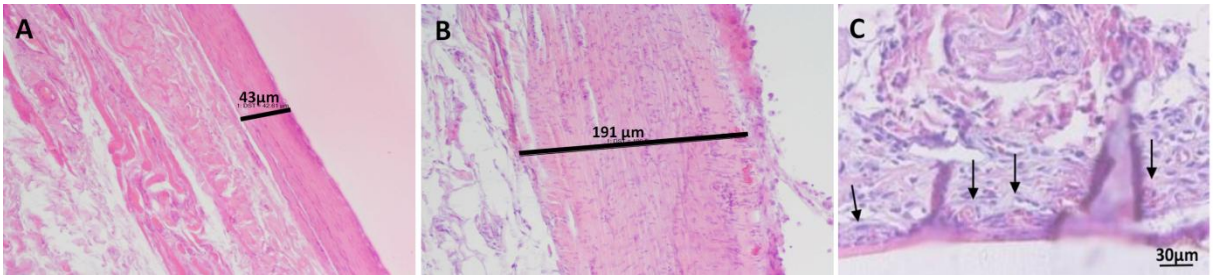

Figuur 8.8: Fibreus kapsel gevormd rondom blanco sensoren (43 µm dik) (A), PDA en PDA/AB gemodificeerde sensoren (191 µm dik) (B) en poreuze PDA/AB gemodificeerde PCL scaffolds (C). In figuur C worden de capillairen, gevormd aan de rand van de scaffold, aangeduid met pijlen.

Naast evaluatie van de oppervlakmodificaties, werd het huidige glucose sensor concept getest door implantatie van 'dummy' sensoren in geiten. Hierbij werden optische vezels, die verbonden waren met een externe laser en spectrometer, geïncorporeerd in het donut-vormige verpakkingsmateriaal. Uit deze implantatiestudie bleek dat de mechanische stabiliteit van de meeste sensoren onvoldoende was. Voor een aantal sensoren kon een transmissiespectrum opgemeten worden, maar door optische verliezen bleek transmissie doorheen weefsel niet de beste optie te zijn. Bedekking van de centrale opening met een polyethersulfon (PES) membraan liet meer stabiele optische metingen toe, hoewel de signalen nog steeds te variabel waren om een multivariabele analyse van de spectra uit te voeren.

Uit *in vitro* analyse van de geïmplanteerde membraan donuts bleek dat verdere optimalisatie van het membraan-donut concept nodig was. Hierbij dient verder aandacht besteed te worden aan de montage van de verschillende sensor onderdelen, alsook aan de bestrijding van 'biofouling' van het membraanoppervlak.

8.6. Conclusie

In dit doctoraatswerk werd een methacrylaat-gebaseerde flexibele verpakking ontwikkeld voor een optische glucose sensor. Naast het optimaliseren van de bulkeigenschappen, werd de sensor-weefsel 'interface' gefinetuned d.m.v. oppervlakactivatie en biofunctionalisatie. Uitvoeren van deze strategie resulteerde in een verbeterde *in vitro* celrespons, maar *in vivo* overheerste naast bloedvatvorming vooral de vorming van een fibreus kapsel. Toekomstig onderzoek zou in dit geval vooral kunnen focussen op de combinatie van de ontwikkelde oppervlakchemieën met een poreus verpakkingsmateriaal. Verder werden de eerste stappen genomen naar een functionele implanteerbare glucose sensor, niettegenstaande verdere optimalisatie van de sensor assemblage noodzakelijk is.

8.7. Referenties

1. Federation, I. D. (2014) Diabetes: facts and figures, retrieved 20 September 2015, from http://www.idf.org/worlddiabetesday/toolkit/gp/facts-figures.
2. Seino, Y., Nanjo, K., Tajima, N., Kadowaki, T., Kashiwagi, A., Araki, E., Ito, C., Inagaki, N., Iwamoto, Y., Kasuga, M., Hanafusa, T., Haneda, M., Ueki, K., and Comm Japan Diabet Soc, D. (2010) Report of the Committee on the Classification and Diagnostic Criteria of Diabetes Mellitus, *Journal of Diabetes Investigation* 1, 212-228.
3. Koschwanez, H. E., and Reichert, W. M. (2007) In vitro, in vivo and post explantation testing of glucose-detecting biosensors: Current methods and recommandations, *Biomaterials* 28, 3687-3703.
4. Apple, D. J., and Sims, J. (1996) Harold Ridley and the invention of the intraocular lens, *Surv. Ophthalmol.* 40, 279-292.
5. Vargas, K. F., Borghetti, R. L., Moure, S. P., Salum, F. G., Cherubini, K., and de Figueiredo, M. A. Z. (2012) Use of polymethylmethacrylate as permanent filling agent in the jaw, mouth and face regions - implications for dental practice, *Gerodontology* 29, E16-E22.
6. Webb, J., and Spencer, R. (2007) The role of polymethylmethacrylate bone cement in modern orthopaedic surgery, *Journal of Bone & Joint Surgery, British Volume* 89, 851-857.
7. Lee, H., Dellatore, S. M., Miller, W. M., and Messersmith, P. B. (2007) Mussel-Inspired Surface Chemistry for Multifunctional Coatings, *Science* 318.
8. Klueh, U., Dorsky, D. I., and Kreutzer, D. L. (2005) Enhancement of implantable glucose sensor function in vivo using gene transfer-induced neovascularization, *Biomaterials* 26, 1155-1163.
9. Shen, Y. H., Shoichet, M. S., and Radisic, M. (2008) Vascular endothelial growth factor immobilized in collagen scaffold promotes penetration and proliferation of endothelial cells, *Acta Biomaterialia* 4, 477-489.
10. Lim, W.-H., Seo, W.-W., Choe, W., Kang, C.-K., Park, J., Cho, H.-J., Kyeong, S., Hur, J., Yang, H.-M., Cho, H.-J., Lee, Y.-S., and Kim, H.-S. (2011) Stent Coated With Antibody Against Vascular Endothelial-Cadherin Captures Endothelial Progenitor Cells, Accelerates Re-Endothelialization, and Reduces Neointimal Formation, *Arteriosclerosis Thrombosis and Vascular Biology* 31, 2798-U2141.
11. Koschwanez, H. E., Yap, F. Y., Klitzman, B., and Reichert, W. M. (2008) In vitro and in vivo characterization of porous poly-L-lactic acid coatings for subcutaneously implanted glucose sensors, *Journal of Biomedical Materials Research Part A* 87A, 792-807.